



University
of Glasgow

Martines, Elena (2006) *Surfaces with periodic nano-features: physical properties and biocompatibility*.

PhD thesis

<http://theses.gla.ac.uk/3900/>

Copyright and moral rights for this thesis are retained by the author

A copy can be downloaded for personal non-commercial research or study, without prior permission or charge

This thesis cannot be reproduced or quoted extensively from without first obtaining permission in writing from the Author

The content must not be changed in any way or sold commercially in any format or medium without the formal permission of the Author

When referring to this work, full bibliographic details including the author, title, awarding institution and date of the thesis must be given

**Surfaces with periodic nano-features.
Physical properties and biocompatibility**

Elena Martines

For the degree of PhD at the University of Glasgow, UK

May, 2006



Centre for Cell Engineering
Division of Infection and Immunity
Institute of Biomedical and Life Sciences
University of Glasgow, G12 8QQ
United Kingdom

Acknowledgements

I would like to thank all my supervisors, in chronological order. First of all, Prof. Adam Curtis for giving me the opportunity of completing this work, for being a constant source of advice and support, and for being an extraordinary example throughout these years. Prof. Chris Wilkinson, for intermittent but valuable guidance, Prof. Hywel Morgan, for fundamental discussion and for help during the most difficult times of this project, and finally Dr. Nikolaj Gadegaard.

Three people in particular need my most special thanks: Dr. Mathis Riehle, for his constant and indispensable guidance and encouragement, Dr. Kris Seunarine, for fabricating all the nanostructures necessary for this work, and Dr. Lucia Csaderova: when I did not have a desk, Lucia let me sit next to her fridge for a year. When I did not have cells, she did. When I did not have food, she fed me. And when she could not help, we had a great laugh. I don't think that I would have gone all this way without her.

Thanks to Andrew Hart and Gregor Aitchison for cells, photography and the good laugh. Thanks to Dr. Matt Dalby and Dr. Catherine Berry for advice on the biology, and Dr. Jesus De La Fuente for practical advice (and salsa?!). Thanks to Ann Macintosh, Margaret Mullin, the IBLS Mechanical Workshop, Mary Robertson, Davie McCloy, and the early Keiran McGhee.

Thanks to Jean-Christophe, Clair, Jordi and Craig for being my beloved foster-family all this time, and putting up with me during the last year, and (Craig) making me all those cups of tea! I will miss you all a lot.

Finally, I would like to thank my parents, for watching patiently while I try to find my own way, far, far away from home.

I hereby declare that the research reported in this thesis is my own work, except otherwise stated, and that it has not been submitted for any other degree.

Elena Martines

Table of contents

Abstract	8
1 Introduction.....	8
2 Super-hydrophobicity and super-hydrophilicity of regular nanopatterns	17
2.1 Introduction.....	18
2.2 Materials and methods	23
2.2.1 Fabrication of silicon nanopatterns	23
2.2.2 Surface modification of silicon nanopatterns.....	24
2.2.3 Replication of silicon nanopatterns into PCL: Thumb-Embossing.....	24
2.2.4 Sample characterization.....	24
2.3 Theoretical Models	26
2.3.1 Hydrophobic surfaces	26
2.3.2 Hydrophilic surfaces.....	27
2.4 Results	28
2.4.1 Sample characteristics.....	28
2.4.2 Contact angles	32
2.5 Discussion.....	34
2.5.1 FTA measurements	34
2.5.2 Hydrophilic silicon nanopatterns	35
2.5.3 Hydrophobic silicon nanopatterns.....	36
2.5.4 PCL replicas	41
2.6 Conclusion	42

3 The DLVO force between a micro-sphere and regular sub-micrometric patterns: a Surface Element Integration study. 44

3.1	Introduction.....	45
3.2	Theoretical background.....	47
3.2.1	The van der Waals force	48
3.2.2	The electric double-layer force.....	49
3.2.3	Surface potential and ζ -potential	52
3.2.3	The DLVO theory	52
3.2.5	The Derjaguin approximation	53
3.2.6	Other non-DLVO forces	54
3.3	Surface Element Integration (SEI)	54
3.4	Modelling	56
3.5	Results	59
3.5.1	Flat control: SEI and DA	60
3.5.2	Nano-pits and nano-pillars: SEI	60
3.5.3	Small asperities 20d20h. SEI and Suresh's model.....	66
3.6	Discussion.....	68
3.7	Conclusion	70

4 Cell reaction to nano-pillars 71

4.1	Introduction.....	72
------------	--------------------------	-----------

Part I. Cells on regular nano-pillars

4.2	Materials and Methods. I.	76
4.2.1	Fabrication of the nanopatterns	76
4.2.2	Cell culture	77
4.2.3	Cell staining and Imaging	78
4.2.4	Data analysis	80
4.3	Initial results: why pillars and not pits.....	82
4.4	Results. I.....	85

4.4.1	Samples	85
4.4.2	Cell counts, morphology and surface coverage	88
4.4.3	Actin/Vinculin staining	96
4.4.4	Protein coating	99
4.4.5	Further work on hTERT	103
4.5	Discussion. I.	109
4.5.1	Fabrication	109
4.5.2	Cell culture	109
<u>Part II. Cells on irregular nano-pillars</u>		
4.6	Materials and Methods. II.	115
4.6.1	Fabrication and preparation of the replicas	115
4.6.2	Cell culture	115
4.7	Results. II.	116
4.7.1	Fabrication	116
4.7.2	Cell culture: hTERT	119
4.7.3	Cell culture: B.End3	122
4.7.4	Cell culture: BHK21	123
4.7.5	Cell culture: comparison between regular and irregular nanopatterns. HTERT and B.End3	125
4.8	Discussion II. Regular or irregular nanopatterns?	127
4.9	Conclusion	128
5	Cell flow on nano-pits	129
5.1	Introduction.....	130
5.2	Materials and Methods.....	130
5.2.1	Fabrication of the nanopatterns	130
5.2.2	Fabrication of the flow chamber	132
5.2.3	Flow apparatus.....	134
5.2.4	Cell culture	136
5.3	Results	137

5.3.1	Nanopatterned replicas.....	137
5.3.2	Flow chamber and flow apparatus.....	137
5.3.3	Cell adhesion.....	138
5.4	Discussion.....	138
5.4.1	Flow apparatus.....	138
5.4.2	Initial cell adhesion.....	139
5.5	Conclusion	141
5.6	Appendix: fluid dynamics.....	141
5.6.1	Reynolds number	142
5.6.2	Entrance length	143
5.6.3	Wall shear rate	143
5.6.4	Wall shear rate of blood in vessels.....	144
6	Final discussion	145
7	Conclusion.....	150
8	Appendix. Solutions.....	151
9	Bibliography.....	153
10	Publications.....	166

Abstract

The behaviour of animal cells *in vitro* is affected by both the chemistry and the shape of the surface (“topography”) to which they adhere. Culturing animal cells on nanopatterns of different shape, dimensions and chemistry considerably modifies cell attachment, spreading, proliferation, migration and gene expression. However, despite this ever-increasing amount of information, very little is known about how nanotopography alters the surface phenomena that underlie cell attachment and behaviour.

This work was primarily aimed at elucidating the influence of nanopatterning on some physical properties of the substrate. The contact angle of water on nanopatterned silicon was measured, and the predicted DLVO (Derjaguin-Landau-Verweey-Overbeek) interaction between a nanopatterned silica plate and a microsphere was calculated. After the physical measurements, the silicon nanopatterns were replicated into a biocompatible polymer, and further experimental investigations of the response of biological cells to nano-pillared samples were carried out. Finally, in the last chapter a flow system was designed, in order to determine the influence of a nano-pitted interface on the initial adhesion of cells subjected to hydrodynamic forces.

Surface texture has a great influence on both the wetting and the interfacial properties of the substrate. In this thesis, I show that the contact angles on nano-topographies are linked to the geometry and chemistry of the pattern by defined analytical rules. Contact angle measurements also proved that air-trapping can happen at a nanopatterned biomaterial surface. On the other hand, a SEI (Surface Element Integration) study predicts that the adhesion of a microsphere onto a plate should be strongly favoured by nanopatterned regular protrusions, and that the shape of the protrusions is a determining factor in this process.

My results on cell behaviour confirm previous observations that some particular nano-patterns can inhibit the proliferation of fibroblasts *in vitro*. It is also shown how cell-specific this response can be, and possible explanations for this behaviour, including air-trapping at the interface, are discussed.

1 Introduction

Many cells adhere to the *extracellular matrix* (ECM) throughout most of their lifetime. This close contact with the matrix exerts an extraordinary control on the behaviour of cells, determining whether they move or stay put, proliferate or remain quiescent, and even live or die. The interactions of the cells with the extracellular matrix and with each other play a major role in embryogenesis (Danen, 2003) and the maintenance of tissue integrity (Gumbiner, 1996).

Impairment of these interactions (i.e. the ability of cell to attach) are found in numerous pathological conditions, including tumor invasion and metastasis (Rovenski, 1998).

Figure 1 illustrates how cells adhere to their surrounding environment. The effects of the extracellular matrix are thought to be primarily mediated by Integrins, a family of cell adhesion molecules that are specific transmembrane receptors, which attach the cells to the matrix and mediate mechanical and chemical signals from it (DeMali, 2003, Giancotti, 2003, Gillespie, 2001, Hynes, 2002, Zamir, 2001). Integrins mediate trans-membrane connections between ECM proteins such as Collagen, Laminin, and Elastin on the outside and the cell cytoskeleton on the inside. The *cytoskeleton* is a system of protein filaments crisscrossing the cytoplasm and forming, together with the many proteins that attach to them, a system of “ropes” and “motors” that gives the cell mechanical strength, controls its shape, and drives and guides its movements; the network of Actin *filaments* shown green in Figure 1 is one of the many cytoskeletal components. Katz *et al.* (Katz, 2000) established that the physical state of the extracellular matrix (and not only its molecular composition) can regulate Integrin-mediated cytoskeletal assembly and tyrosine phosphorylation to generate two distinct types of cell-matrix adhesions: *fibrillar adhesions*, which are enriched in Tensin, and “*classical*” *focal contacts* (as observed by Izzard *et al.* (Izzard, 1976)) which contain high levels of Paxillin and Vinculin. They propose that the rigidity of the extracellular matrix is one of the mechanisms that control the molecular organisation of adhesion sites, a hypothesis that was later extended to include the control of cell locomotion (Pelham, 1997, Lo, 2000, Kaverina, 2002). Also, Vinculin-containing *focal complexes* (Geiger, 2001) are a further category of cell-matrix adhesions: these are small, dot-like adhesions that are present mainly at the cell edge, and that can be associated with cell migration or serve as precursors of focal adhesions.

When cells are cultured *in vitro*, they do not usually form adhesions directly with the substrate, but rather with the proteins that are adsorbed onto the material. Upon the first contact of growth medium with a biomaterial, proteins adsorb on its surface, forming a distribution or arranging in clusters to which cells adhere (Castner, 2002). It is becoming clearer that the clustering of Integrins, rather than their average distribution, is the main factor determining the ability of cells to attachment and migration (Arnold, 2004, Maheshwari, 2000). Finally, another significant factor in cell growth is the influence of external mechanical forces due to e.g. flowing extracellular fluids (Tsuruta, 2003, Bongrand, 1994, Bongrand, 1995).

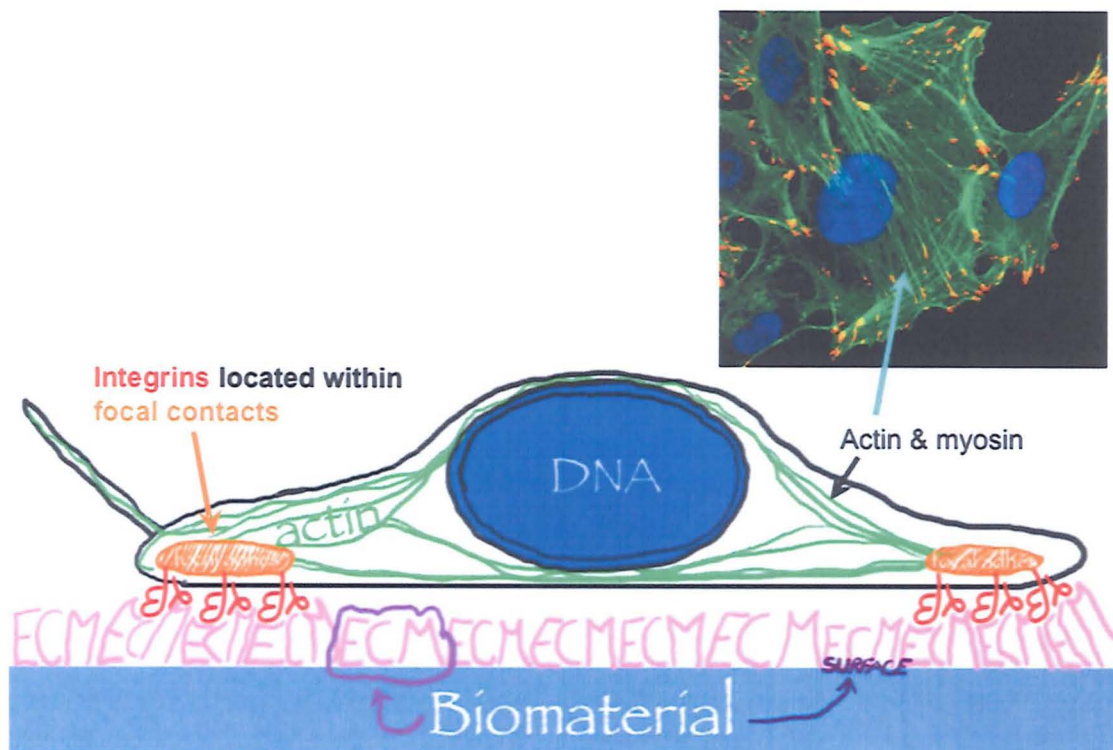


Figure 1. Schematic cross-sectional drawing of a cell adhering to the extra-cellular matrix. The adsorbed ECM molecules are detected by integrins, who upon binding organise focal complexes and focal contacts on the inside. The latter in turn recruit actin and, in conjunction with motor proteins such as myosin, allow the cells to distort the ECM. The inset on the top-right corner shows a fluorescence microscope image of human fibroblasts, stained for F-actin (green), and Vinculin-containing focal adhesions (orange) as well as the DNA highlighting the nuclei (blue). Drawing courtesy of M. Riehle, inset M Dalby.

Although the molecular machinery of cellular adhesions mediates attachment, migration and signalling to and from the ECM, it has equally important roles in the creation and organisation of the ECM. Cells secrete, deposit, and destroy the matrix in the intercellular space thus molding it to their requirements (Sawhney, 2002). One example for this is that cells can markedly and selectively rearrange ECM proteins, such as Fibronectin, on substrates and assemble them into cell-surface bound fibrils (Avnur, 1981, Geiger, 2001, Pompe, 2005).

The ECM can also provide a topographical template that guides the cell during its locomotion: this phenomenon is termed *contact guidance*. The term was introduced by Paul Weiss in 1934 when he showed that nerve cells extend their neurites along the fibres in an oriented fibrin clot (Weiss, 1934). Contact guidance was first observed by Harrison (Harrison, 1910) in the earliest experiments of cell culture using cells cultured on fine spider silk fibres. Weiss (Weiss, 1945) suggested that the phenomenon might be explained by the oriented adsorption of macromolecules produced by the cells or derived from serum onto the fibres. In 1964, Curtis & Varde (Curtis, 1964) measured the orientation and contact inhibition of chick heart primary fibroblasts on cellulose acetate replicas of diffraction gratings and on silica fibres. They found that on fibres in the range

10-30 μm the cells oriented and experienced increasing contact inhibition, with these effects dying out at larger diameters. Dunn & Heath (Dunn, 1976) extended this approach by culturing chick heart fibroblasts on silica ridges (angles 1° - 32°): their work was probably the first to be combined with observations of the cytoskeleton. They observed a reduced ability of the cells to move over a ridge with increasing angle, and that cells at times aligned to the boundaries. They suggested that the underlying mechanism was the limited bendability of the F-actin microfilaments, which caused the alignment of the cytoskeleton, thus of the cell through mechanical restriction. In 1979 Ohara & Buck (Ohara, 1979) proposed an alternative theory that seems at first sight to be diametrically opposite to that of Dunn & Heath: they suggested that the focal contacts were aligned to the fibres or grooves: since focal contacts are connected to the cytoskeleton, this might well align the cells on the substratum. However this theory explains how a cell will continue to respond to topography once this has started, but does not explain how the response initiated.

Detailed studies on the relationship between surface topography and cell behaviour were made possible as methods of micro- and nano-fabrication, adapted from the electronics industry, offered a very wide range of very precisely specified topographies that could be utilised in cell behaviour experiments (Wilkinson, 2001). Several reviewers have summarized the methods and the effects of micro- and nano-scale patterning on cell adhesion (Chehoudi, 1995, Curtis, 1997, Curtis, 1998a, Curtis, 1998b, Curtis, 2001, Flemming, 1999).

Cell behaviour on micromachined grooves was studied by Brunette *et al.*, who showed that porcine epitheliocytes (Brunette, 1986b) and human fibroblasts (Brunette, 1986a) aligned to the groove boundaries. In later studies, Cheroudi *et al.* tested these topographies *in vivo*, showing that micro-grooved implants impeded the growth of epithelial cells on percutaneous devices (Chehoudi, 1988, Chehoudi, 2002), and directed bone mineralization (Chehoudi, 1997). Earlier, Clark *et al.* (Clark, 1987) had observed that the reaction of cells to single step cues and microgrooves is cell-type dependent, and that cell alignment increased with groove depth (Clark, 1990); on the other hand, Dunn & Brown (Dunn, 1986) indicated groove width as the main factor in cell alignment, explaining the phenomenon with the mechanical restriction of the cytoskeleton. Read *et al.* (Read, 1997) observed that infection-structure differentiation of cereal rust fungi could be induced by microgrooves. Wojciak *et al.* (Wojciak, 1995) claimed that microgrooved substrata promoted the healing of rat tendons *in vitro*, and showed (Wojciak-Stothard, 1995a) that Actin condensed at the boundaries of the groove, maintaining the orientation of the cell before microtubule spreading. They also showed (Wojciak-Stothard, 1995b) that macrophages were activated on microgrooves, and that their movement was faster and more persistent than on the flat control. Rovenski *et al.* (Rovenski, 1999) cultured fibroblasts and epitheliocytes on metallic grids; they showed that the reaction was cell-type dependent and hypothesised that the alignment was controlled by microtubule

organisation. Li *et al.* (Li, 2001) studied the migration of endothelial cells in microgrooves, showing that the cells aligned and migrated faster in the direction of the groove, with focal adhesions oriented in the direction of migration. Turner *et al.* (Turner, 2000) cultured astroglial cells on micropillars (width 0.5-2 μm , height 1 μm , pitch 1-5 μm). They showed that the cells were more confluent on the pillars (70% more cells than on the flat control), although they did not create adhesions with the bottom of the surface.

With the rapid improvement of fabrication techniques, surface textures at the nano-scale could be fabricated, and the influence of nanotopographies on cell behaviour was studied. The fabrication of nano-patterned substrates can be achieved with high precision techniques like photolithography and electron beam lithography (EBL). EBL yields a lateral resolution as high as 5-10 nm, but unfortunately, although very precise, it is also expensive and time consuming, especially if large areas need to be patterned. To overcome these inconvenients, it is possible to replicate the substrate topography by embossing a master mold into polymers (Casey, 1997), which also allows the combination of the topography with different surface chemistries.

In 1991, Clark *et al.* (Clark, 1991) proved that BHK,¹ MDCK² and chick embryo neural cells aligned on nanometrically wide and deep quartz grooves, and that their degree of alignment and elongation was cell type-dependent. Wojciak-Stothard *et al.* (Wojciak-Stothard, 1996) cultured macrophages on micrometrically-wide grooves and ridges of depth between 30 and 282 nm (in fused silica), and concluded that cells on the nanometrically deep grooves were activated as they showed higher phagocytic activity. More recently, Stavridi *et al.* (Stavridi, 2003) showed that poly- ϵ -caprolactone nano-grooves (width 450 nm, depth 190 nm) attracted more platelets and induced faster platelet coagulation in a parallel-plate flow chamber. When *nano-pillars* started to be fabricated (Casey, 1997), Curtis *et al.* (Curtis, 2001) could observe that the number of animal cells on regular silicon nano pillars decreased with time; however, when the nano-pillars were randomly arranged this effect was less pronounced. Gallagher *et al.* (Gallagher, 2002) cultured rat epitenon fibroblasts³ on nano-pits made of poly- ϵ -caprolactone, and observed that the cells on the nano-pits had smaller focal adhesions and smaller spreading area; by coating the substrates with Poly-L-Lysine, they could conclude that surface chemistry did not override the effects of nanotopography.

¹ Baby hamster kidney cells: fibroblastic cells.

² Madin-Darby canine kidney: polarised kidney epithelial cells with microvilli.

³ a fibroblastic cell line extracted from the Epitenon sheath that surrounds the flexor tendon of Sprague-Dawley rats.

Dalby *et al.* (Dalby, 2004) cultured human fibroblasts on nano-columns (height 160 nm, diameter 100 nm, average pitch 230 nm), showing that after 3 h the Actin cytoskeleton was less organised on the nanopattern, and that the focal adhesions were smaller and very faint compared to the flat control. The effects of nano-pillars and nano-pits on cell adhesion are discussed in more detail in Chapter 4. For now suffice it to say that a variety of cell reactions to nanotopographies have been reported, from alignment to increased migration speed, from apoptosis to enhanced spreading, engulfing of the asperities, modified gene expression, elongation, inhibited proliferation; and these in turn depended on the cell type and on the shape, dimensions, regularity and chemistry of the surface textures (Flemming, 1999).

The responses of cells to nanotopographies have raised several questions concerning the nature of these interactions, since the size of the surface features is at least two orders of magnitude smaller than the cells. Mechanical restriction is not a possibility at this scale. M.J. Dalby (Dalby, 2005) has suggested that topographically-induced mechanotransduction might be a reason for decreased cell growth. Another potential explanation could be a change in protein adsorption and activity due to the surface patterns (Denis, 2002, Riedel, 2001). The dependence of cell adhesion, spreading, proliferation and differentiation on the surface energy and, in turn, on the protein adsorption/conformation on a substrate is a very complex subject, even without considering any additional topographical factors. Studies on protein-resistant surfaces (Ostuni, 2001) indicate that the water shell on the surface plays an important role (Herrwerth, 2003), which can be expressed in terms of hydrophobicity-hydrophilicity at the macroscopic scale (Vogler, 1998). However, an unequivocal relation between cell behaviour, surface energy and protein adsorption has not been established yet (Lim, 2004, Ostuni, 2001, Vogler, 1998, Garcia, 1999, McClary, 2000, Spijker, 2002, Ruardy, 1997).

The nanopatterns might also influence cell attachment by simply reducing the surface area available for focal adhesion formation. This in turn, could be due to the inability of the cells to form adhesion sites with the bottom surface between asperities (with heights of order 100 nm). Alternatively, it could be due to the presence of nano-bubbles (nano-cavities) of air trapped in-between asperities, which would shield the adsorption of proteins on the substrate from the growth medium, and on which the cells cannot form adhesions. One way of investigating the occurrence of air-trapping on a substrate is to determine its wettability by contact angle measurements (Figure 2). The wettability of a substrate depends primarily on the surface energy of the material, i.e. on its chemical composition. The relation between the surface energies of the three phases and the equilibrium static contact angle θ_Y is formulated by the Young-Dupre (Young, 1805) equation (eq 1):

$$\cos\theta_Y = \frac{\gamma_{SV} - \gamma_{SL}}{\gamma_{LV}} \quad (1)$$

where γ_{IJ} is the surface tension of the interface IJ, and the letters S, V, L designate the solid, vapour and liquid phase respectively. If $\gamma_{SV} < \gamma_{SL}$ the surface will be hydrophobic, i.e. $\cos\theta > \pi/2$. If $\gamma_{SV} > \gamma_{SL}$ the surface will be hydrophilic, i.e. $\cos\theta < \pi/2$. However, other criteria for defining hydrophobicity and hydrophilicity have been suggested (Vogler, 1998).

Eq 1 assumes that the surface is ideal, i.e. chemically and topographically homogeneous, and yields the ideal equilibrium (or *Young*) contact angle θ_Y of a static drop (Figure 2a). However, during the wetting of chemically and/or topographically heterogeneous surfaces not a single, but a range of metastable static contact angles can form at the edge of the interface. These can be observed during

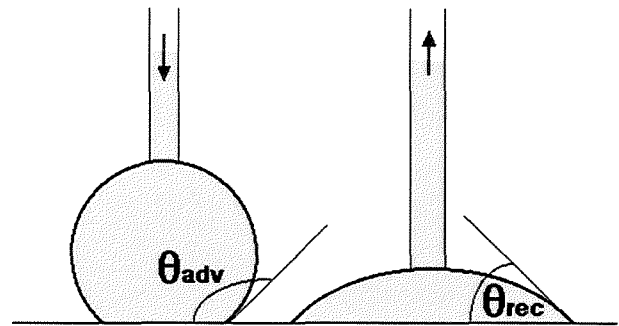


Figure 2. Dynamic contact angle measurements.

dynamic contact angle measurements (Figure 2b), where the advancing angle θ_{adv} is the maximum static angle and the receding angle θ_{rec} is the minimum static angle. The contact angle *hysteresis* $\Delta\theta$ is the difference between these two boundaries ($\Delta\theta = \theta_{adv} - \theta_{rec}$). If the energy barrier between metastable states can be overcome, for instance by vibrating the surface (Meiron, 2004), the ideal contact angle can be measured. Surface roughness is observed to affect the contact angle, but differently according to the wettability region. On rough hydrophilic surfaces, the Wenzel model predicts the contact angles to be smaller than the corresponding Young angle (Quere, 2002); however, recent evidence (Abdelsalam, 2005) shows that on substrates with $\theta_Y \approx 70^\circ$, air-trapping in the roughness can increase the contact angle. On hydrophobic surfaces, as the roughness increases, first the hysteresis increases significantly; then both advancing and receding angles suddenly increase while the hysteresis nearly vanishes. These two regimes are called, respectively, *Wenzel* and *Cassie-Baxter* regime (Figure 3), and will be discussed in more detail in Chapter 4. The Cassie-Baxter regime corresponds to the onset of air-trapping amongst the surface asperities.

A parallel consideration has to do with the influence that nanopatterning might have in determining the *potential energy of interaction* between a structured plate and a microsphere, as previously suggested by Curtis *et al.* (Curtis, 2001). The influence of surface roughness on the interparticle forces has raised much interest in recent years. Not only the adhesion of spheres on a rough surfaces has been

investigated (Gotzinger, 2004, Yu, 2004), proving that the adhesion force is affected by surface roughness, but also several authors have measured the force-distance relation between a smooth sphere and a rough surface (Bowen, 2000, Bowen, 2002, Drechsler, 2004, Hoek, 2003), hence supporting the suggestion that surface roughness is a major factor affecting the deposition of colloidal particles on collector surfaces (Elimelech, 1990). The *DLVO theory* (Verwey, 1948) is used to calculate the interaction energy as a function of the separation distance between particles, by summing the Van der Waals interaction and the electric double-layer repulsion. The DLVO theory has several limitations (Ninham, 1999); nevertheless, it is the basis of modern colloidal science, and it can be treated analytically for simple geometries (e.g, plate-plate and sphere-plate interactions). However, the cells are viscoelastic, fluid-like structures bounded by a highly charged lipid membrane: they can neither be equaled to a drop of water, nor to a solid particle. Besides, “while the intermolecular forces between biological molecules are no different from those that arise between any other types of molecules, a biological interaction is usually very different from a simple chemical reaction or physical change of a system. [...] Biological interactions do not occur in a linear, stepwise fashion, but involve competing interactions, branching pathways, feedback loops, and regulatory mechanisms; in addition, they are essentially ‘dynamic’ rather than ‘static’: biological systems are never at thermodynamic equilibrium, and are not, rigorously speaking, closed systems.”(from: Leckband & Israelachvili (Leckband, 2001)) For all the aforementioned reasons, it is impossible to derive conclusions regarding cell adhesion from measurements of interactions between solid particles.

Problem formulation

There is a need for designing prosthetic devices whose surface triggers a specific cell response, by giving control over the phenotype and activity of the cells, or by reducing inflammation around the implant. For this reason, tissue engineers are interested in understanding cell adhesion onto artificial biomaterials, since a better knowledge of cell behaviour can be used in clinical applications.

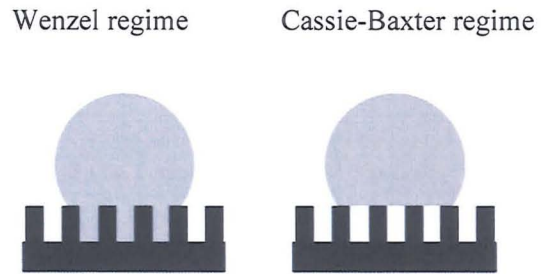


Figure 3. Schematic of Wenzel's and Cassie-Baxter wetting regimes.

However, despite the increasing amount of literature on the effect of nanopatterned surfaces on cell behaviour *in vitro*, there is no unequivocal understanding of the influence of nano-textures on animal cells. There are many reasons for this, including the difficulty of accurately controlling the feature dimensions at this scale, the fact that biological experiments are subject to a high degree of variability and the interdisciplinarity required to succeed in “biological surface science”. The use of nanofabrication technology for medical purposes is waiting for unifying concepts that could finally lead to the predictability and application of nanotopography-induced cell behaviour, in order to improve prosthetic implants or other medical devices that involve prolonged contact with living cells. The way to such knowledge needs to go through physical chemistry and colloid and surface science. Therefore, on one hand investigating the effect of nanotopography on cells needs to become more systematic and rigorous, especially since the modern fabrication techniques allow increasingly good control over surface features. On the other hand, there is a clear need to understand how the nanotopography affects other surface properties, like the occurrence of air-trapping, the deposition of colloidal particles or the adsorption of proteins. The present study has to be understood in this dual context: first and foremost, this work was aimed at elucidating the influence of nanopatterning on some physical properties of the substrate, such as the contact angle of water on silicon (Chapter 4), and the predicted DLVO interaction between a plate and a microsphere (Chapter 3). Subsequently, the nanopatterns were replicated in a biomaterial, and further experimental investigation of the response of biological cells to nanotopographies (Chapter 4 and Chapter 5) were carried out, following the work initiated by J. Gallagher and Dalby *et al.* (Dalby, 2004, Gallagher, 2002). By gaining a better understanding of some physical phenomena at the nano-scale, a first step is done towards a causal formulation of the effects of nanopatterns on the behaviour of biological cells.

2 Super-hydrophobicity and super-hydrophilicity of regular nanopatterns

In this chapter, the hydrophilicity, hydrophobicity and sliding behaviour of water droplets on nano-asperities of controlled dimensions (Figure 4) was investigated experimentally. It will be shown that the “hemi-wicking” theory for hydrophilic silicon samples successfully predicts the experimental advancing angles of water and that the same patterns, after silanization, become superhydrophobic in agreement with the Cassie-Baxter and Wenzel theories.

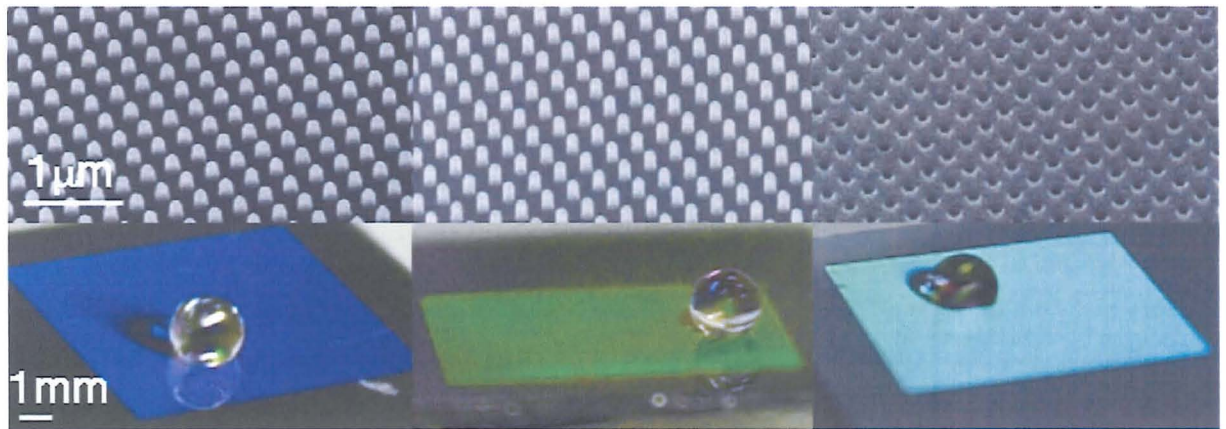


Figure 4. Top row: nanopatterned silicon surfaces; from left to the right: 1) Pillars “P22”: diameter 157 nm, height 239 nm, spacing 300 nm. 2) Pillars “P21”: diameter 156 nm, height 286 nm, spacing 300 nm. 3) Pits “H90”: diameter 105 nm, depth 116 nm, spacing 300 nm. Bottom row: Nikon D1 pictures showing a 5 μ l drop of water deposited on the nanopatterns. The interference colours on the surface indicate the presence of the above-corresponding nanopattern on a square area of 1 cm^2 . It can be seen that P22 and P21 make the drops round up, i.e. these surfaces are “superhydrophobic”.

2.1 Introduction

The wettability of solid surfaces is a subject that has raised great interest in the past decades. The surface energy of a sample will determine if a drop of a given liquid, when deposited on it, will assume a bead-like shape (indicating that the liquid is being repelled by the surface), or if it will spread and wet the substrate. Roughening the surface enhances its repellent or wetting properties (Bico, 2002), resulting in “superhydrophobic” or “superhydrophilic” textures (this nomenclature applies if the liquid considered is water, as is the case in this work). These structures raise great interest for potential applications, e.g. in the development of self-cleaning surfaces, or in wettability-driven microfluidics (Blossey, 2003, Grunze, 1999).

Many authors have contributed to the fabrication and understanding of *superhydrophobic* surfaces (Bico, 1999, Furstner, 2005, Lafuma, 2003, Lau, 2003, Marmur, 2004, Miwa, 2000, Nakae, 1998, Onda, 1996, Oner, 2000, Patankar, 2003, Patankar, 2004b, Quere, 2003, Shibuichi, 1996, Yoshimitsu, 2002). Öner&McCarthy(Oner, 2000) describe a superhydrophobic surface as one where the *advancing angle* θ_{adv} is very high (generally $>150^\circ$), and the *receding angle* θ_{rec} is such that the drop exhibits low *hysteresis* $\Delta\theta$ ($\Delta\theta = \theta_{adv} - \theta_{rec}$), as illustrated in Figure 2.

Water drops form beads and can roll off superhydrophobic surfaces, cleaning them in the process, by picking up surface contaminants. This phenomenon has been termed the “Lotus effect” (Figure 5), since it is very pronounced on the leaves of the Lotus plant (*Nelumbo nucifera*) (Barthloot, 1997, Furstner, 2005, Neinhuis, 1997). These leaves exhibit a double-structured roughness, where sub-micrometric wax crystals cover a larger micrometric structure; even though multi-scale roughness has been proven to enhance water repellency (Herminghaus, 2000, Otten, 2004, Shirtcliffe, 2004, Shirtcliffe, 2005). it has been suggested that the small scale roughness plays an important role (Patankar, 2004a).

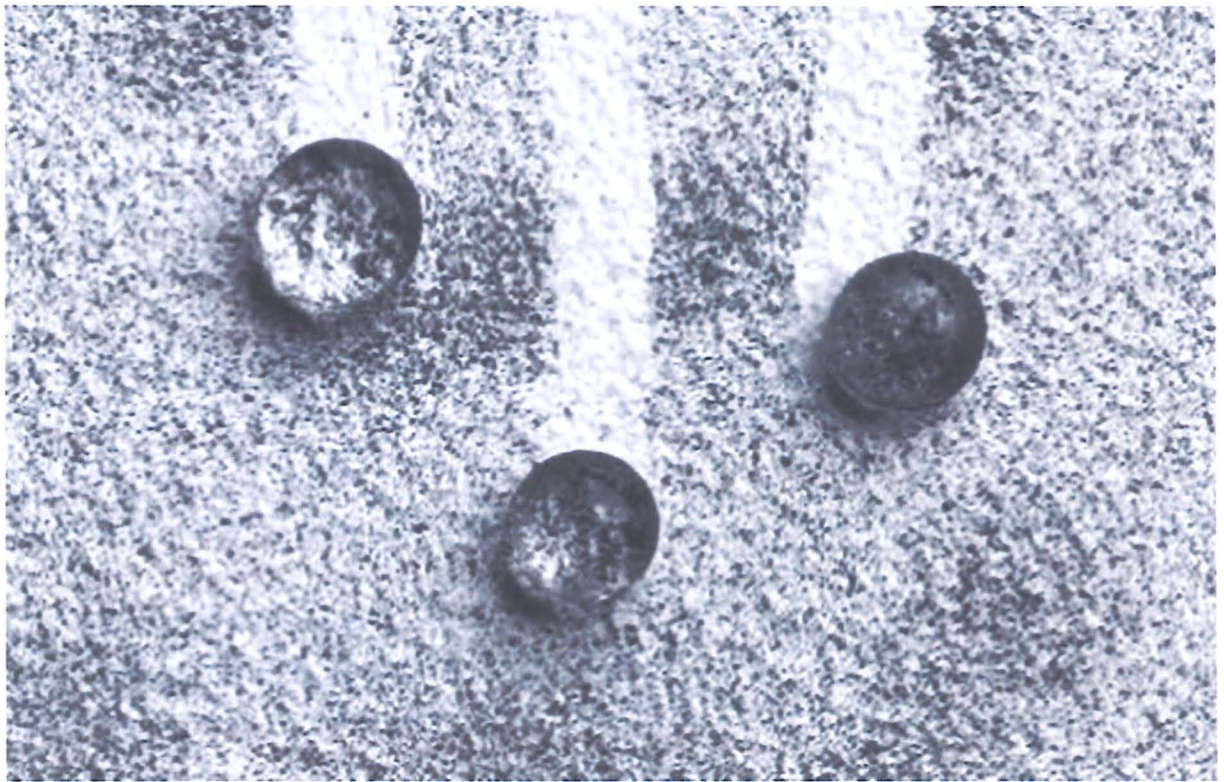


Figure 5. The Lotus effect. Image from <http://www.sto.at/htmger/pre033.htm>.

The wings and eyes of some insects (e.g. the cicada *Psaltoda claripennis* (Ashton, 1921) shown in Figure 6, and the termites in the family *Rhinotermitidae*) are also covered with nanometric structures that are thought to ensure water-repellency, besides providing an anti-reflective coating and improving the mechanical properties of the wings (Watson, 2004); unlike the



Figure 6. *Psaltoda Claripennis*. Picture from <http://152.98.200.7/ins-info/Psa.htm#Clanger>.

irregular topography of leaf wax crystals, these surfaces are covered with ordered arrays of rounded protrusions (Figure 7). Finally, complete wettability, although uncommon, can be found among insect-capturing plant leaves (Bohn, 2004).

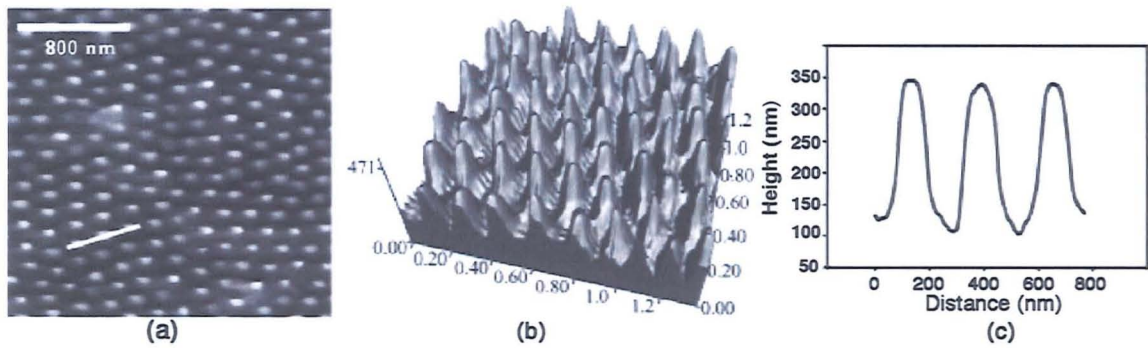


Figure 7. From Watson *et al.*²⁵. (a) AFM image of a cicada wing array obtained with a high aspect ratio tip; (b) 3-D representation of the same structure; (c) profile along the close-packed axis of the structure.

The effect of surface roughness on hydrophobicity has been explained by two different theories. According to the model developed by *Wenzel*, it is assumed that the space between the protrusions on the surface is filled by the liquid (Wenzel, 1936) (Figure 8a). This model predicts that both hydrophobicity and hydrophilicity are reinforced by the roughness, according to the following relation:

$$\cos\theta_W = r \cos\theta_Y \quad (2)$$

where θ_W is the apparent contact angle on a rough surface, θ_Y is the ideal contact angle of water (Young's angle as defined by eq 1 in Chapter 1) on a smooth surface of identical chemistry and r is the roughness factor, which is defined as the ratio of actual surface area over the projected surface area.

The approach developed by *Cassie & Baxter* on the other hand assumes that air is trapped by the asperities (Cassie, 1944), so that the drop sits on a composite surface made of air and solid (Figure 8b); the relation between the apparent contact angle θ_{CB} and the ideal angle θ_Y is in this case described as:

$$\cos\theta_{CB} = r_f f \cos\theta_Y + f - 1 \quad (3)$$

where r_f is the roughness factor of the wetted area, and f is the area fraction of the projected wet area. The product $r_f f$ is often called the solid fraction ϕ_S .

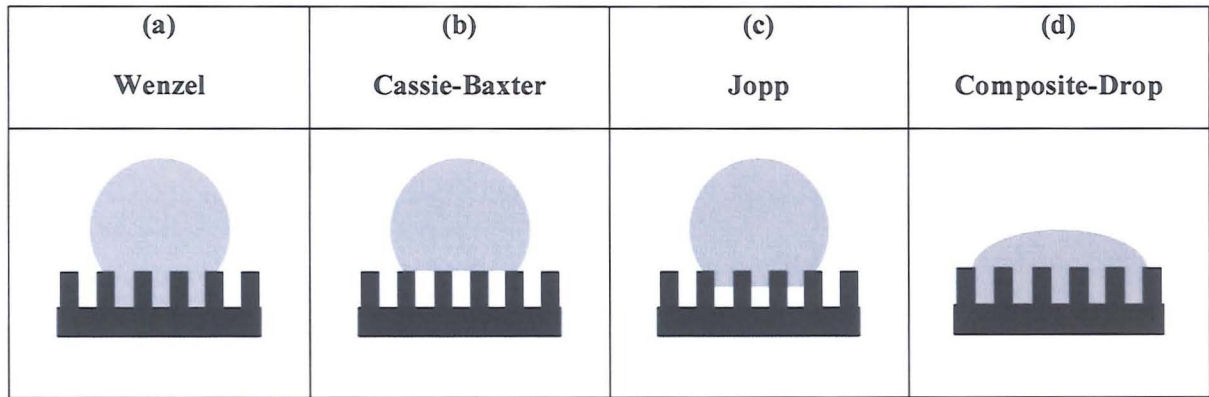


Figure 8. Schematic of roughness-filling by an advancing water drop according to the different models considered in this work: Wenzel model, Cassie-Baxter model, Jopp's simulation and the Composite-Drop mode

Both Wenzel and Cassie-Baxter relations were originally formulated for static drops at equilibrium; yet since it was shown that low-rate advancing angles and static angles are essentially identical (Kwok, 1996), eq 2 and eq 3 can also be applied to advancing angles. Fewer attempts have been made to model the receding angles, since the Cassie-Baxter and Wenzel models do not apply in this case; starting from Roura *et al.*'s method (Roura, 2002), Patankar derived a model that should predict the receding angles by assuming that a film of water is left behind the receding drop (Patankar, 2003), as shown in Figure 9.

It has been shown (Cheng, 2005, He, 2004, Lafuma, 2003, Quere, 2003) that a droplet can be in either a Cassie-Baxter or a Wenzel state on a rough hydrophobic surface depending on how it is formed. The transitions between the two states have been studied theoretically (Jopp, 2004, Marmur, 2003, Patankar, 2004b) and current research is focussed on tuning the wettability of substrates by selectively inducing such transitions (Gleiche, 2000, Krupenkin, 2004, Lee, 2005, Shiu, 2004).

Since the advancing angles predicted by the Cassie-Baxter and Wenzel theory can both be very close to the experimental values, the receding angles can be used as a qualitative indication of the state of the drop: if θ_{rec} is high (i.e. the hysteresis is low), the drop will be in a Cassie-Baxter ("slippy") mode; if θ_{rec} is low, the drop will be in a Wenzel ("sticky") state. This means that obtaining a stable Cassie-Baxter drop, with very high advancing and receding angle, is the ultimate goal for achieving super-hydrophobicity by tailoring surface topography.

Contact angle *hysteresis* is thought to be due to the pinning of the contact line by surface heterogeneities, both chemical and topographical (Chen, 1999, Oner, 2000); the drops pass through a number of metastable energy states which give rise to phenomena like "slip-stick" behaviour or complete pinning: Lam *et al.* (Lam, 2002) showed that liquid sorption/retention is a cause of

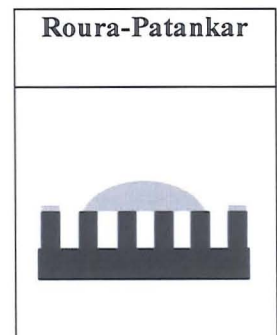


Figure 9. Schematic illustration of a receding water drop on a hydrophobic substrate, leaving a film of water behind its path.

hysteresis, since the receding contact line moves on a wet substrate, unlike the advancing drop. For this reason, only advancing angles should be used for calculations of surface energy. Decker *et al.* (Decker, 1996) and Meiron *et al.* (Meiron, 2004) vibrated drops on surfaces with chemical and topographical heterogeneities, respectively, and showed that if treated in this way the drops would overcome the energy barriers between the metastable states and thus a more reliable “ideal” contact angle could be measured.

The adhesive behaviour of water on rough surfaces can also be assessed by *sliding angle* measurements (Miwa, 2000, Onda, 1996, Yoshimitsu, 2002). The sliding angle is defined as the critical angle α where a water droplet begins to slide down an inclined plate: a high sliding angle indicates a “sticky” Wenzel state, while a low sliding angle suggests a Cassie-Baxter regime (i.e. the drop will easily roll off a slightly tilted substrate)

(Quere, 2003). Petrie *et al.* (Petrie, 2004) showed that a Cassie drop on a rough surface slides at higher speed than on a flat surface, and they explain the phenomenon with the decreased friction caused by the air trapping.

Much less work has been dedicated to the study of *superhydrophilic* (or more generally, superwetting) surfaces (Bico, 2001, Bico, 2002, McHale, 2004). Assuming that no air is trapped in the roughness of the hydrophilic surface, the Wenzel model still applies, along with another one called the “hemi-wicking” or “Composite-Drop” model (Quere, 2002), where the drop is assumed to be sitting on a composite surface made of solid and water. However, it has recently been observed that surfaces that exhibit low hydrophilicity ($\theta_Y \approx 70^\circ$), when roughened, follow Cassie-Baxter’s rather than Wenzel’s or the “hemi-wicking” laws (Abdelsalam, 2005); this behaviour indicates that air trapping can occur even on materials that are not defined as “hydrophobic” if the surface is properly structured, as already suggested by Herminghaus (Herminghaus, 2000).

All the above-mentioned theories for both hydrophobic and hydrophilic rough surfaces have been tested by preparing surfaces structured on the micrometer scale (Bico, 1999, Bico, 2001, Furstner, 2005, Miwa, 2000, Oner, 2000, Onda, 1996, Shirtcliffe, 2005, Yoshimitsu, 2002). Only few studies have been recently done on nanotopographies (Abdelsalam, 2005, Burton, Lau, 2003, Suh, 2005), mainly because of the difficulty and expense of fabrication.

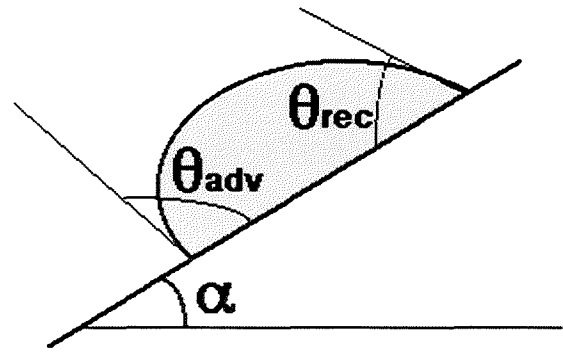


Figure 10. Schematic of a sliding water drop, on a substrate tilted at an angle α (“sliding angle”).

In this study, ordered arrays of nano-pits and nano-pillars have been fabricated in silicon, and their dynamic wettability before and after chemical hydrophobisation was investigated. Afterwards the hydrophobic silicon masters were embossed into poly- ϵ -caprolactone sheets, and contact angles were measured on these replicas.

My model structures resemble the natural sub-micrometric features that ensure the water-repellency of biological surfaces like the Lotus leaf and some insect wings. Because of the accurate geometrical characterization of our nanopatterns, the validity of the analytical models currently available for predicting the wettability of rough surfaces can be verified, for both the hydrophilic and the hydrophobic case.

2.2 Materials and methods

2.2.1 Fabrication of silicon nanopatterns

Nanopatterns with increasing solid fraction (two samples with *nano-pits* and four with *nano-pillars*) were fabricated in silicon wafers (4 in., $\langle 100 \rangle$, p-doped, 525 ± 50 μm thick) across an area of 1 cm x 1 cm. All the masters were fabricated by Dr K. Seunarine.

2.2.1.1 Nano-pillars

A 2 nm titanium layer was evaporated on the silicon (Plassys evaporator), and the samples immediately spin-coated with a 60%NEB31A3-40%EC solvent (Sumitomo Chemical Co Ltd) at 3krpm for 60 seconds (150 nm thick coating). After a pre-exposure bake at 90°C for 2 mins, the wafers were exposed in the e-beam writer (Leica Microsystems EBPG 5) with the desired pattern. After a post-exposure bake at 85°C for 2 mins, the samples were developed in Microposit MF CD-26 for 20 s and rinsed with reverse osmosis (RO) water; the titanium was etched (1 part HF:26 parts RO water) for approximately 2-3 s, and the samples rinsed in RO water. The silicon was then dry-etched using STS-ICP (Surface Technology Systems–Inductively Coupled Plasma) with C4F8 and SF6 (unswitched gasses) at an etch rate of 100 nm/min, and finally Piranha-cleaned for 5 mins.

2.2.1.2 Nano-pits

The silicon wafers were spin-coated with 40%ZEP520A at 5 krpm (100 nm thick coating) and baked at 180°C for 1 hour. The samples were then exposed in the e-beam writer, developed in o-xylene for 60 s and dry etched as for the pillars. Finally, the surfaces were Piranha-cleaned for 5 mins.

2.2.2 Surface modification of silicon nanopatterns

Prior to the measurements of contact angles on the hydrophilic nanopatterns, all the samples were cleaned with an O₂ plasma for 15 min (BP80 RIE, flow rate 20 sccm, pressure 30mT, RF power 100W); the contact angles on these surfaces were measured within 24 hours.

Subsequently, the same patterns were hydrophobised with octadecyltrichlorosilane (OTS) by modifying the procedure of Rosloznic *et al.* (Rosloznic, 2003): all samples were sonicated for 10 s in 1:1 water-ethanol and 10 s in IPA, then rinsed in chloroform and blow-dried in N₂. After a 15 min O₂ cleaning (BP80 RIE, flow rate 20 sccm, pressure 30mT, RF power 100W), they were sonicated for 10 s in chloroform and 10 s in IPA, rinsed in 1:1 water-ethanol, rinsed in RO water and blow dried. The clean samples were then placed in a ceramic slide holder, which was gently tilted on the side at 90°, so that the patterns were facing down. This technique ensured that if any OTS clusters formed in the solution, they had less chances of being deposited on the patterned surfaces. The tilted holder was placed in a glass beaker filled with a 0.001% solution of OTS (Sigma) in heptane (Sigma). After 3.5 hours the holder was sonicated three times for 1 min in copious amounts of heptane, then rinsed in IPA, 1:1 water:ethanol, RO water and finally blow dried.

2.2.3 Replication of silicon nanopatterns into PCL: Thumb-Embossing

Poly- ϵ -Caprolactone (PCL) pellets were purchased from Sigma. Sheets of polymer (of thickness \approx 0.5 mm) were prepared by placing pellets spaced on a square grid (at a distance of 1 cm from each other) between two glass plates; then the plates were clamped using 4 bulldog clamps, and the assembly was kept for more than 3 hours at 70°C in an oven. At this temperature the PCL melted and formed a sheet. On cooling down, the polymer was easily separated from the glass and the sheet was cut into squares (0.7 cm X 0.7 cm).

The silicon masters were placed on a hot plate at 85 °C, and a square of PCL was placed on top of the patterned area. When the polymer had melted, a glass slide was pressed on it for a few seconds, in order to force the PCL into the nanopattern. The sandwich (master/PCL/slide) was immediately transferred into RO water for cooling. On cooling, the polymer came off both surfaces. The polymers were blow-dried with N₂.

2.2.4 Sample characterization.

2.2.4.1 Scanning Electron Microscopy.

The silicon surfaces were imaged with a Hitachi S4700, prior to and following hydrophobisation. After contact angle measurements, they were cleaved and their SEM profiles were used to measure the dimensions of the asperities with ImageJ (Rasband, 1997-2005). The PCL replicas were imaged after being sputter-coated with 20 nm of gold-palladium in a sputter coater (Emscope, Ashford,

UK). To measure the depth of the PCL pits, the replicas were plunged in liquid nitrogen, together with two glass slides (glued to make a thick base) and a scalpel blade. The frozen samples were placed on the cold glass base, and the scalpel was hammered on the sample from the back side. This resulted in a cleavage of the patterned surface. After sputter-coating and imaging, it was possible to use the SEM profile to measure the dimensions of the embossed nano-pits, and the diameter of the embossed nano-pillars.

2.2.4.2 Dynamic Contact Angle Measurements.

Images of the advancing and receding contact angles of filtered Milli-Q water were captured at a rate of 2 images/s with a long-distance objective connected to a CCD camera (Sanyo), and analysed with the FTÅ200 software (First Ten Ångstroms, v2.0). The FTA setup consists of a vertical syringe that is controlled by a stepper-motor through the FTA software. The drops are imaged with a long-distance objective connected to a CCD camera (Figure 11). The back illumination is also computer-controlled. The software recognizes the drop profile and calculates the contact angle from the left and right side of the drop. In practice, achieving a fully automated and correct analysis was often difficult: in this case, it was possible to define the drop profile manually, and use the software to calculate the angle.



Figure 11. FTA apparatus.

Water drops were deposited and taken up through a 30-gauge flat-tipped needle mounted on a Hamilton syringe, at a rate of 0.25 $\mu\text{l/s}$; the maximum volume of the drops was 5 μl on hydrophobic substrates, and 4 μl on hydrophilic ones. The values reported are averages of at least 5 measurements made on different areas of the sample. All measurements were performed at room temperature on a vibration-free platform.

2.2.4.3 Sliding Angle Measurements.

For sliding angle measurements on the hydrophobic samples, water drops of weight ranging from 5 to 40 mg were gently deposited on a horizontal plate fixed on a goniometer (Figure 12), by means of a calibrated micropipette. The goniometer was rotated slowly until the drops started to slide. The sliding angle was determined on at least 4 different locations/sample.

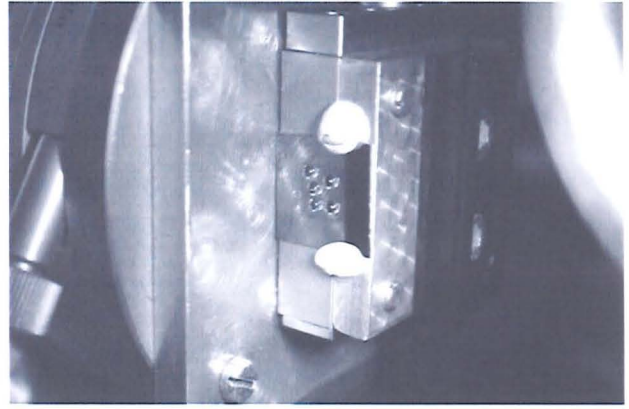


Figure 12. Sliding angle setup. The image shows pinned drops at 90° on a pitted sample.

2.3 Theoretical Models

2.3.1 Hydrophobic surfaces

In order to be able to test which model would best explain the experimental findings, the measured angles were compared with the advancing and receding angles predicted by several models (i.e. Cassie-Baxter, Wenzel, Composite-drop and Jopp's models for advancing angles, and Roura-Patankar's model for receding angles on hydrophobic surfaces). To do so, the equations of each model (eq 2 and 3) were re-formulated in order to obtain the theoretical apparent contact angle θ as a function of the geometric parameters of the surface. As a result, the formulas differ for cylindrical and hemispherical-top asperities. Note that the term "asperities" here is generally used to refer to both pillars and pits.

For vertical structures with a flat top, assuming that the water does not invade the roughness, the roughness factor of the wet area is 1 ($r_f=1$) and the solid fraction is equal to the projected wet area fraction ($\phi_S=f$, defined in 2.1). In this work, ϕ_S always refers to the solid fraction of cylindrical pillars $\phi_S=\pi d^2/4l^2$, where d is the base diameter of the cylinders, and l is their centre-to-centre pitch. The Cassie-Baxter and Wenzel formulas were applied to different geometries.

1) The Cassie-Baxter relation was calculated for two cases:

$$\text{- Cylindrical asperities:} \quad \cos\theta_{CB-c} = -1 + \phi_S(\cos\theta_Y + 1) \quad (4)$$

$$\text{- Hemispherical-top pillars (Bico, 1999):} \quad \cos\theta_{CB-h} = -1 + \phi_B(\cos\theta_Y + 1)^2 \quad (5)$$

where ϕ_B is the ratio of the area of the pillar bases over the total area. In this case, $\phi_B=\phi_S$ since the walls of the pillars are vertical.

2) Wenzel's relation was calculated for two cases:

- Cylindrical asperities: $\cos\theta_{w-c} = r \cos\theta_Y$ (6)

- Hemispherical-top pillars: $\cos\theta_{w-h} = \left[1 + 4\phi_S \left(\frac{h}{d} - 0.25\right)\right] \cos\theta_Y$ (7)

The receding angle of composite drops was also calculated, by assuming that a receding drop leaves a film of water behind (Roura, 2002). In this way Patankar (Patankar, 2003) derived eq 8 to predict the receding angles on asperities with a flat top ($r_f=1$). Thus, eq 8 was applied to cylindrical pillars:

$$\cos\theta_{rec-c} = 2\phi_S - 1$$
 (8)

In the case of hemispherical asperities, eq 8 becomes:

$$\cos\theta_{rec-h} = \phi_S(2 + 2\cos\theta_Y + \sin^2\theta_Y) - 1$$
 (9)

The model developed by Jopp *et al.*(Jopp, 2004) was also tested with my experimental results (Figure 8c). Their calculation uses a minimization of the Gibbs free energy of a drop (G) on a hydrophobic surface, as indicated by Marmur (Marmur, 2003), but it also takes into account the volume of liquid that can penetrate into the surface asperities. The formula yields the penetration depth of water z and contact angle θ that correspond to an energy minimum:

$$G = \left(1 - \frac{V_p}{V_0}\right)^{\frac{2}{3}} (2 - 3\cos\theta + \cos^3\theta)^{\frac{2}{3}} \left[2 - 2\cos\theta - (r_f f \cos\theta_Y + f - 1)\sin^2\theta\right]$$
 (10)

where V_p is the volume of the roughness that is filled by the liquid, V_0 is the total volume of water. Both V_p and V_0 are functions of the geometric parameters of the surface and the penetration depth z .

2.3.2 Hydrophilic surfaces

The Composite-Drop (or “hemi-wicking”, see Figure 8) and the Wenzel formulas for different geometries were derived.

1) The Composite-Drop relation was calculated for two cases:

- Cylindrical asperities (Quere, 2002): $\cos\theta_{comp-c} = 1 + \phi_S (\cos\theta_Y - 1)$ (11)

- Hemispherical-top pillars: $\cos\theta_{comp-h} = \phi_S (2\cos\theta_Y + 3\cos^2\theta_Y - 1) + 1$ (12)

2) Wenzel’s relation was applied to the case of cylindrical asperities, as in eq 6.

2.4 Results

2.4.1 Sample characteristics

2.4.1.1 Silicon nanopatterns

SEM images of all the nanopatterns are shown in Figure 13. Immediately after fabrication the patterns showed perfectly cylindrical nano-pillars and nano-pits (Figure 13, top row), except for sample P12, where the tall pillars had a cusped top.

The different patterns were named after their solid fraction percentage (H designates a hollow pattern i.e. pits, P a protruding pattern i.e. pillars). For instance, P22 indicates a pillared sample where 22% of the apparent area is wet by a drop, assuming the asperities to be cylindrical and air to be trapped inside (this corresponds to the flat circular tops of cylindrical pillars being wet, with a planar air-water interface over the roughness). Table 1 shows the dimensions of the silicon nanopatterns (base diameter d , height h , centre-to-centre pitch l).

After hydrophobisation (Figure 13, middle row) the edges of the pillars were rounded, probably because of sonication. In particular, the sample P22 has pillars with a hemispherical top (Figure 13g-i), and the others look like cylinders with smooth edges, except P12 whose shape was unchanged after coating (Figure 13p-r). The pitted samples (Figure 13a-f) had a cylindrical profile. The contact angle measured on the OTS-coated flat silicon was $114 \pm 1^\circ$, which indicates that a monolayer was formed (a contact angle for total coverage was reported to be 115°) (Rozlosnik, 2003).

	H90	H83	P22	P21	P13	P12
d (nm)	105 ^a	138 ^c	157 ^e	156 ^g	124 ⁱ	117 ^k
h (nm)	116 ^b	141 ^d	239 ^f	286 ^h	268 ^j	792 ^l
l (nm)	300	300	300	300	300	300

Table 1. Dimensions of the silicon nanopatterns. All dimensions were measured with ImageJ (± 5 nm). In case of hollow asperities (H), h indicates the depth. In case of pillars (P), h indicates the maximum distance from the base to the top. (^a) is the total number of averaged values: (^a) 16, (^b) 20, (^c) 6, (^d) 6, (^e) 7, (^f) 8, (^g) 8, (^h) 8, (ⁱ) 15, (^j) 17, (^k) 16, (^l) 16.

2.4.1.2 PCL replicas

Table 2 shows the dimensions of the PCL replicas (base diameter d , height h). The pitch was assumed to be 300 nm. The different patterns were named after their “source master” (e.g. H83-r was replicated from the hydrophobic master H83). The SEM images of the replicas and their SEM profiles are shown in Figure 14 and Figure 15. It was not possible to measure the height of the

replicated pillars (H90-r and H83-r) from their profiles, because the nano-pillars at the edge collapsed during the cutting.

	H90-r	H83-r	P22-r	P21-r	P13-r	P12-r
d (nm)	170±14 ^a	196±11 ^b	130±9 ^c	147±8 ^e	118±9 ^g	88±11 ⁱ
h (nm)	NA	NA	214±23 ^d	275±18 ^f	242±43 ^h	757±57 ^j

Table 2. Dimensions of the PCL replicas. All dimensions were measured with ImageJ from SEM images. In case of hollow asperities (H), h indicates the depth. In case of pillars (P), h indicates the maximum distance from the base to the top. (n) is the total number of averaged values: (a) 62, (b) 38, (c) 97, (d) 50, (e) 125, (f) 46, (g) 132, (h) 14, (i) 92, (j) 20.

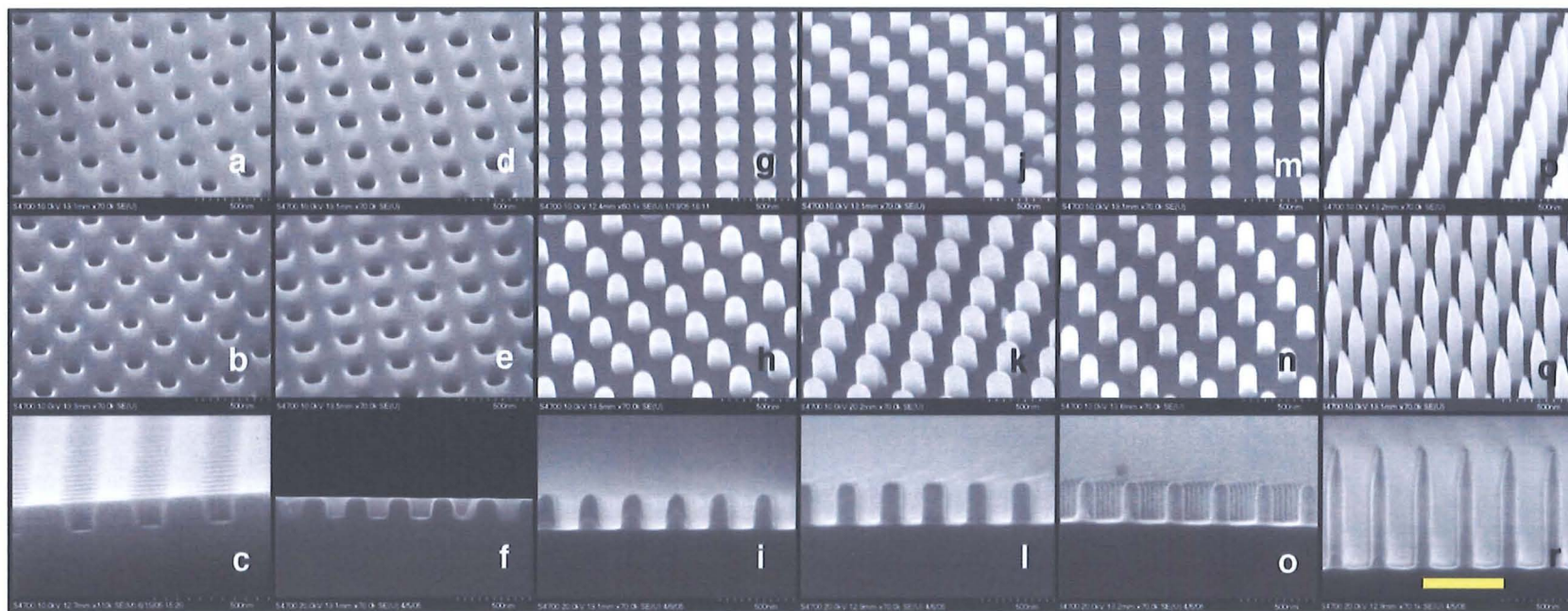


Figure 13. SEM images of silicon nanopatterns. The top row shows the hydrophilic patterns, the middle row shows the OTS-coated hydrophobic patterns, and the bottom row shows the cleaved patterns. a-c) H90; d-f) H83; g-i) P22; j-l) P21; m-o) P13; p-r) P12. The cleaved profiles were imaged with a 90° tilt, the other images were taken at 45° . The scale bar is 500 nm.

PAGE

NUMBERING

AS ORIGINAL

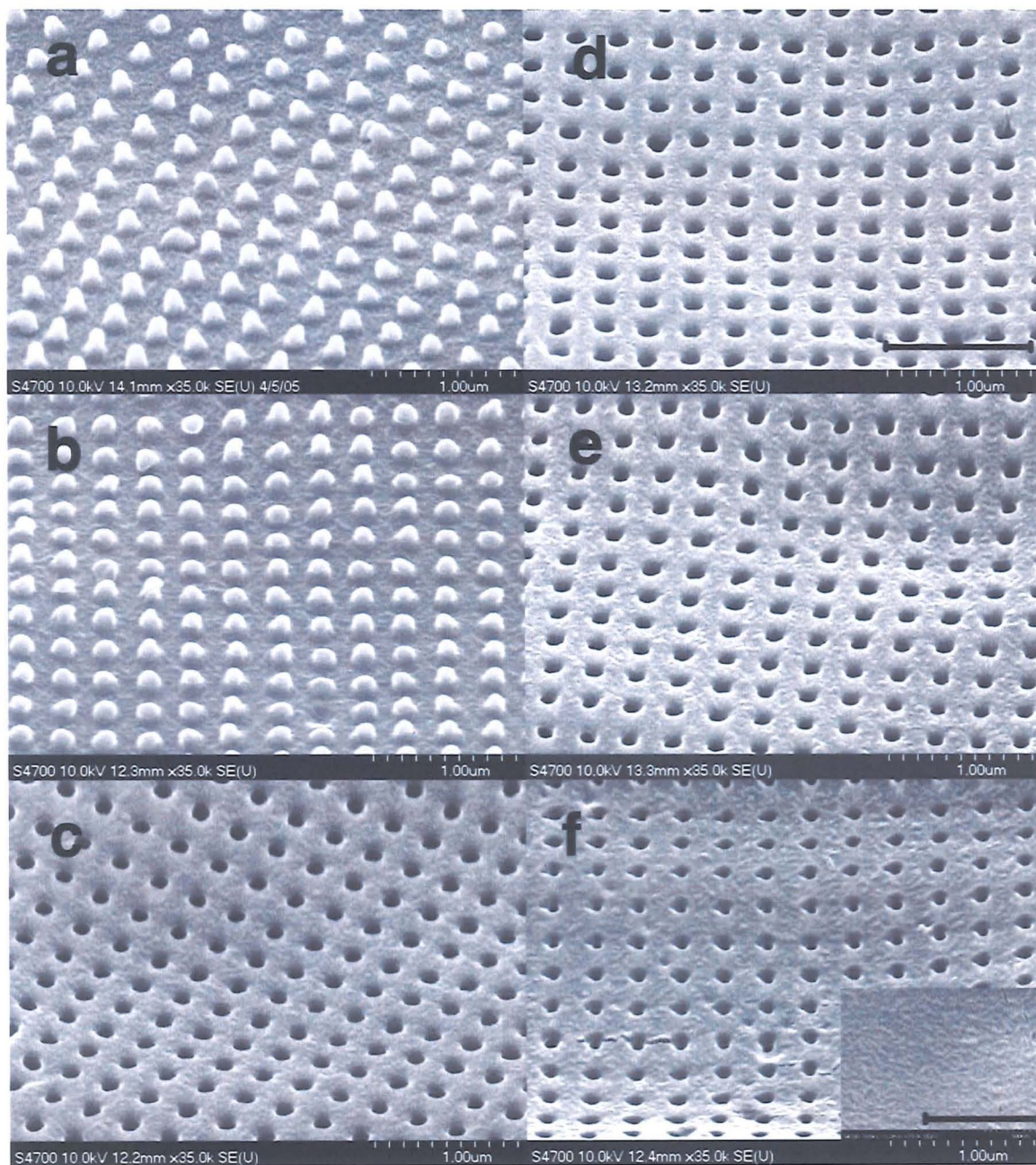


Figure 14. SEM images of PCL replicas. a) H90-r; b) H83-r; c) P22-r; d) P21-r; e) P13-r; f) P12-r; the insertion shows the roughness on a flat replica. Tilt: 45°. Bars: 1 µm.

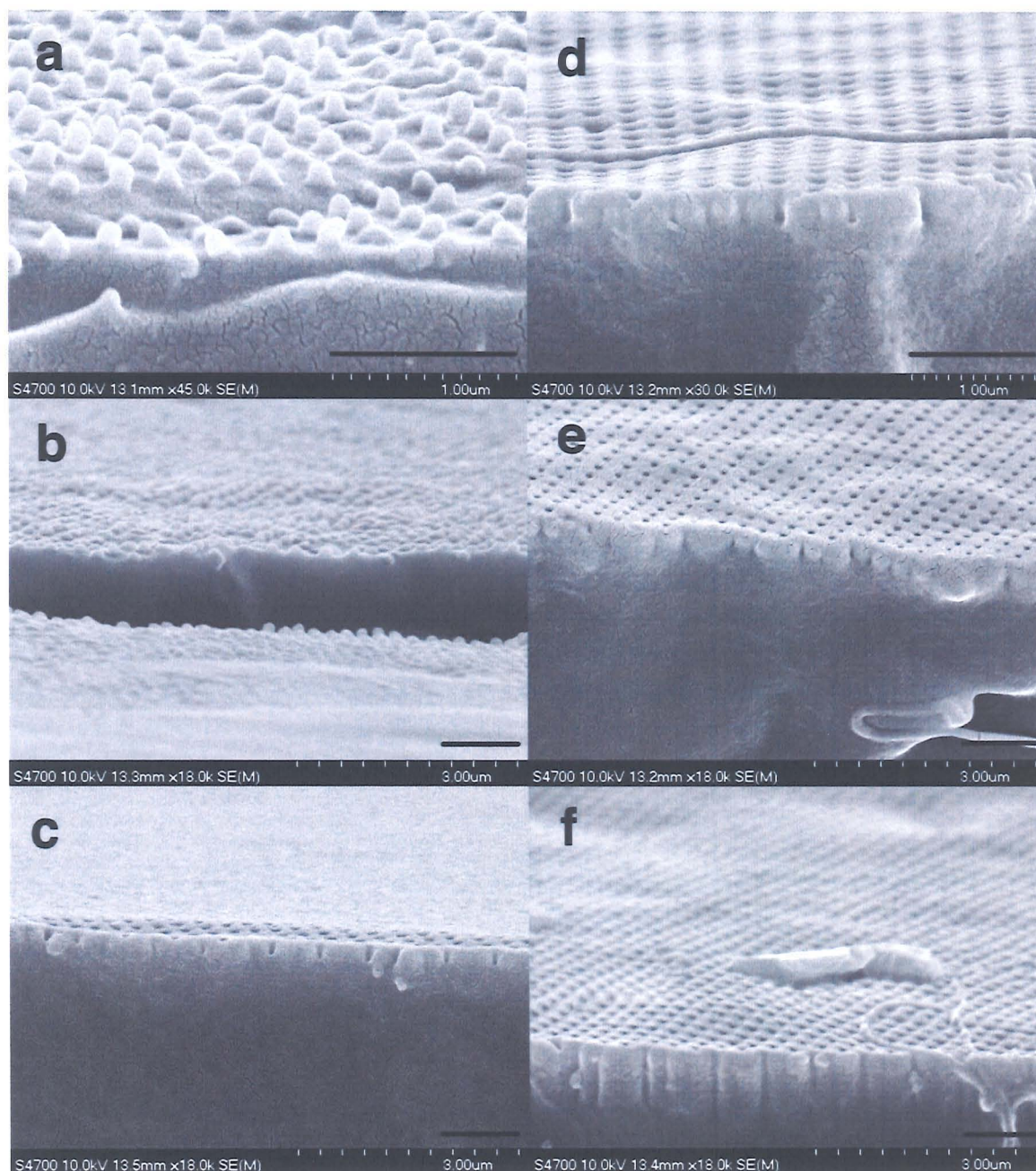


Figure 15. SEM profiles of the PCL replicas. a) H90-r; b) H83-r; c) P22-r; d) P21-r; e) P13-r; f) P12-r. Tilt: 90°. Bar: 1 μm .

2.4.2 Contact angles

2.4.2.1 Silicon nanopatterns

The experimental advancing and receding angles (θ_{adv} and θ_{rec}) on both hydrophilic and hydrophobic silicon nanopatterns are shown in Table 3. The contact angle measured on the flat hydrophilic control ($\theta_Y=35\pm 1^\circ$) was taken as Young's angle for the hydrophilic substrates, while the contact angle measured on the flat hydrophobic control ($\theta_Y=114^\circ\pm 1$) was taken as Young's

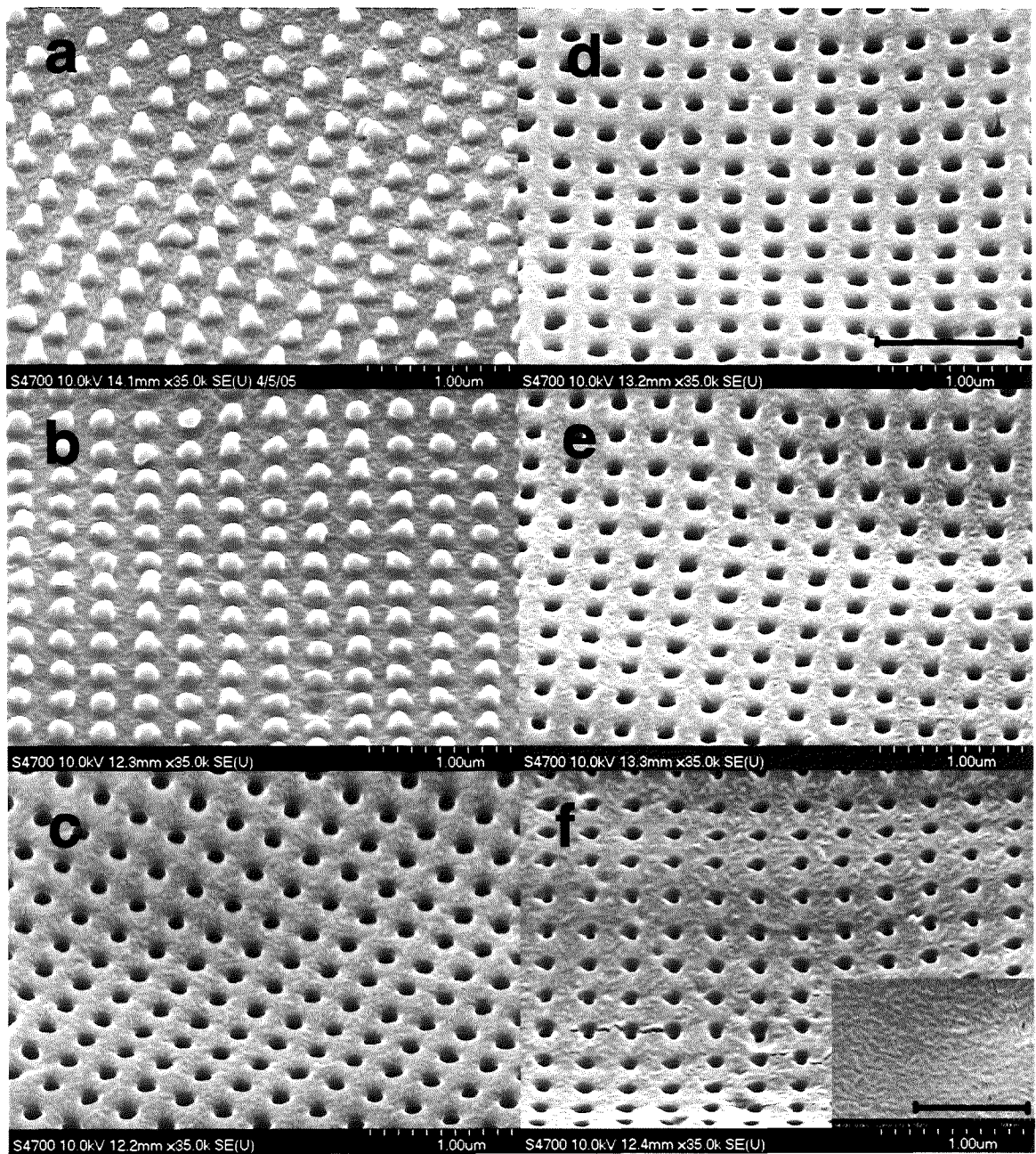


Figure 14. SEM images of PCL replicas. a) H90-r; b) H83-r; c) P22-r; d) P21-r; e) P13-r; f) P12-r; the insertion shows the roughness on a flat replica. Tilt: 45°. Bars: 1 μm.

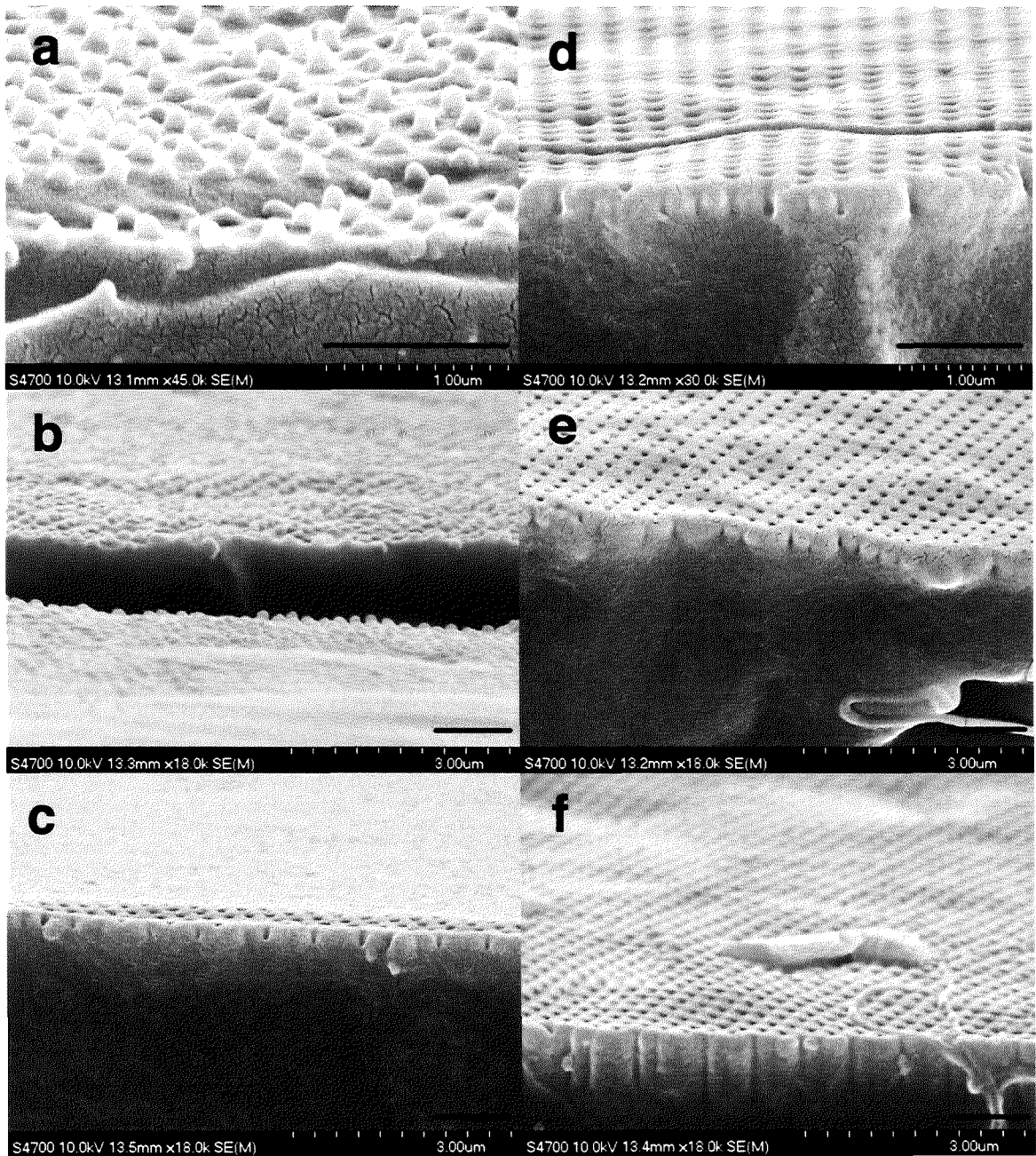


Figure 15. SEM profiles of the PCL replicas. a) H90-r; b) H83-r; c) P22-r; d) P21-r; e) P13-r; f) P12-r. Tilt: 90°. Bar: 1 μm .

2.4.2 Contact angles

2.4.2.1 Silicon nanopatterns

The experimental advancing and receding angles (θ_{adv} and θ_{rec}) on both hydrophilic and hydrophobic silicon nanopatterns are shown in Table 3. The contact angle measured on the flat hydrophilic control ($\theta_Y=35\pm 1^\circ$) was taken as Young's angle for the hydrophilic substrates, while the contact angle measured on the flat hydrophobic control ($\theta_Y=114^\circ\pm 1$) was taken as Young's

angle for the hydrophobic substrates. The receding drops on the hydrophilic substrates were pinned ($\theta_{rec}=0^\circ$), as predicted by Quere (Quere, 2002).

		Flat	H90	H83	P22	P21	P13	P12
Hydro	$\theta_{adv}(^\circ)$	114±1 ^a	125±2 ^c	129±3 ^e	155±2 ^g	159±2 ^h	161±2 ^j	164±2 ^l
	$\theta_{rec}(^\circ)$	100±3 ^b	92±2 ^d	89±2 ^f	0	140±2 ⁱ	150±2 ^k	163±2 ^m
Phobic	Model		W-c	W-c	W	CB-h	CB-h	CB-h
Hydro	$\theta_{adv}(^\circ)$	35±3 ⁿ	36±3 ^o	35±3 ^p	12±3 ^q	19±3 ^r	11±3 ^s	0
	$\theta_{rec}(^\circ)$	0	0	0	0	0	0	0
Philic	Model		Comp-c	Comp-c	Comp-c	Comp-c	Comp-c	Comp-h

Table 3. Experimental angles of water on hydrophobic (5 μ l drop) and hydrophilic (4 μ l drop) nanopatterns. Advancing and receding angles are shown, along with the best theoretical agreement ("Model"): (W) Wenzel, (CB) Cassie-Baxter, (Comp) Composite-Drop, with (-c) cylindrical and (-h) hemispherical top. Results are mean±standard deviation. (ⁿ) is the total number of averaged values: (^a) 451, (^b) 367, (^c) 137, (^d) 114, (^e) 182, (^f) 138, (^g) 147, (^h) 185, (ⁱ) 126, (^j) 170, (^k) 90, (^l) 207, (^m) 75, (ⁿ) 91, (^o) 52, (^p) 57, (^q) 93, (^r) 67, (^s) 78.

The sliding angles of water on the hydrophobic nanopatterns were also measured, using the method described in 2.2.4. The results are plotted in Figure 19.

2.4.2.2 PCL replicas

The experimental advancing and receding angles (θ_{adv} and θ_{rec}) on the PCL replicas are shown in Table 4. The Young's angle for these substrates was taken as the advancing angle measured on the flat control ($\theta_Y=77^\circ\pm 2$). The advancing angles on the pillared replicas (H90-r and H83-r) exhibited slip-stick behaviour, which made the measurements unreliable.

	Flat	H90-r	H83-r	P22-r	P21-r	P13-r	P12-r
$\theta_{adv}(^\circ)$	77±2 ^a	NA	NA	95±3 ^c	95±1 ^e	NA	84±2 ^g
$\theta_{rec}(^\circ)$	56±2 ^b	NA	NA	44±2 ^d	28±3 ^f	NA	37±10 ^h
Model	-	-	-	CB	CB	-	CB

Table 4. Experimental angles of water (5 μ l drop) on PCL replicas. Advancing and receding angles are shown, along with the best theoretical agreement ("Model"): (W) Wenzel, (CB) Cassie-Baxter. Results are mean±standard deviation. (ⁿ) is the total number of averaged values: (^a) 211, (^b) 129, (^c) 157, (^d) 70, (^e) 95, (^f) 27, (^g) 68, (^h) 37.

2.5 Discussion

2.5.1 FTA measurements

It has been shown by Kwok *et al.* (Kwok, 1997) that the drop-shape-analysis yields excellent results for use in surface energy measurements. In their setup (ADSA, Automatic Drop Shape Analysis) a hole is drilled through the sample, such that the water can be pumped from below the surface of interest. Whilst the disadvantage of the FTA setup is that the needle can interfere with the drop profile, the ADSA setup would have required completely different equipment, which was not available. However, during the present measurements a "needle-effect" (a change

in the angle with the drop radius) was only observed when the drop volume was very small, i.e. at the beginning of the advancing phase and at the end of the receding phase. To ensure that the advancing and receding angles were constant i.e. meaningful, it was specifically checked that the values of the angles used for the averaging did not increase/decrease when the drop radius increased/decreased (Kwok, 1997). When the contact line was advancing or receding only from one side, the angle from the other side was not considered.

Figure 16 shows examples of drop profiles as visualized on the FTA setup. The effect of nanotopography on the drop shape on hydrophilic and hydrophobic silicon, and subsequently on the advancing angles, is evident.

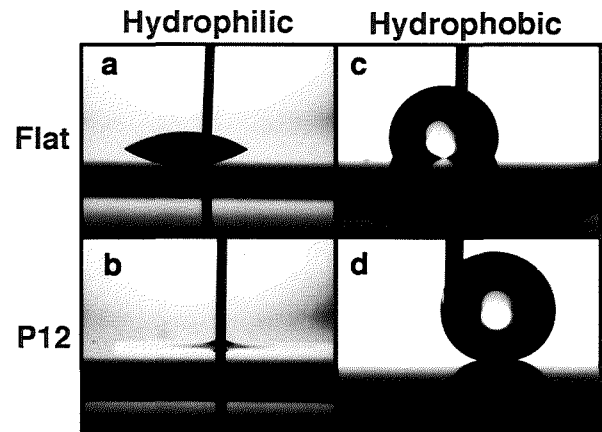


Figure 16. Drop profiles of advancing drops as visualized in the FTA. a) flat hydrophilic; b) P12 hydrophilic; c) flat hydrophobic; d) P12 hydrophobic.

2.5.2 Hydrophilic silicon nanopatterns

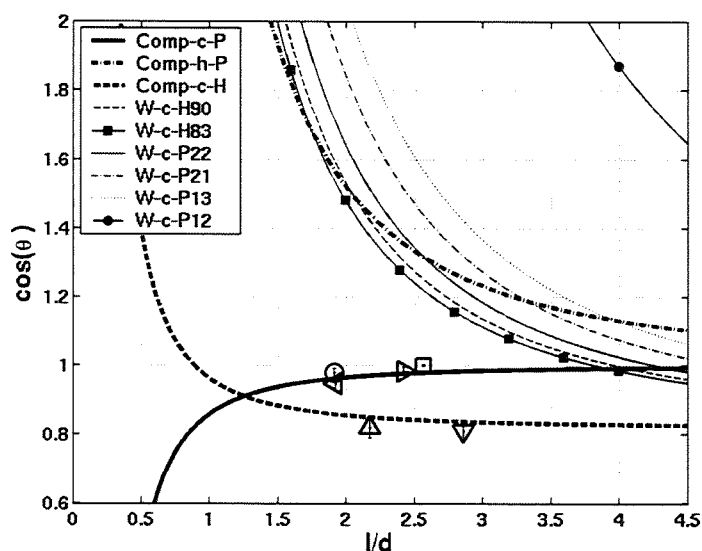


Figure 17. Plot of the apparent advancing angles of a 4 μl drop of water on hydrophilic patterns as a function of structure geometry. Composite drop (Comp-) and Wenzel (W-) curves for cylindrical (-c-) and hemispherical (-h-) asperities are shown. The Wenzel curves were plotted for cylindrical asperities only. The composite drop curves for pillars P and pits H are different because of a different dependence on l/d . Individual points indicate experimental data: (Δ) H90; (∇) H83; (\circ) P22; (\triangleleft) P21; (\triangleright) P13; (\square) P12.

The experimental advancing angles of water on hydrophilic silicon along with the theoretical predictions are plotted in Figure 17. Since all the structures (except P12) were perfectly cylindrical, the Wenzel and Composite-Drop curves were plotted for this geometry; the Composite-Drop curve for hemispherical-top pillars is also shown for comparison with the experimental advancing angle on P12.

Figure 17 shows that the Composite-Drop formula for cylindrical asperities is in excellent agreement with the experimental values. It should be noted that both the Wenzel formula for cylinders and the Composite-Drop formula for hemispherical tops (eq 12) always predict an unattainable angle corresponding to $\cos\theta > 1$, which can be understood as complete wettability. Therefore, one of the two models will apply to sample P12, where $\theta_{adv} = 0^\circ$. Because the pillars on sample P12 had a cusped top, the Composite-Drop formula for hemispherical tops should be more relevant. Since the Composite-Drop relation does not depend on the aspect ratio of the features, this formula predicts that hemispherical-top pillars will always be superhydrophilic. The topography-induced superhydrophilicity of sample P12 was due to the high aspect ratio h/d of the protrusions, which acted as a reservoir for the fast spreading of the liquid front (Quere, 2002), a spreading much faster than on the flat surface (McHale, 2004). In this context it would be interesting to investigate the effect of height variation on the reservoir-effect of such structures.

2.5.3 Hydrophobic silicon nanopatterns

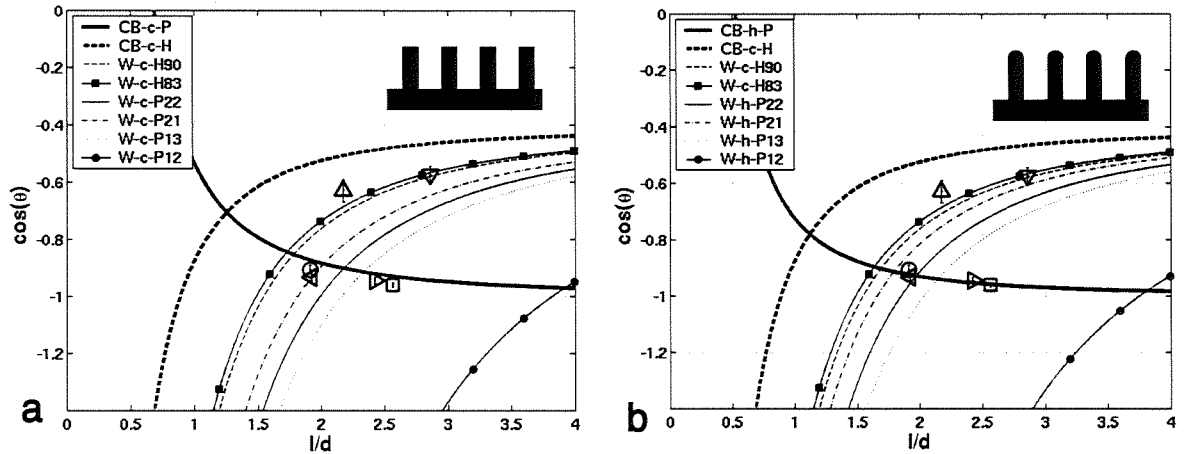


Figure 18. Plot of the apparent advancing angles of a 5 μl drop of water on hydrophobic patterns as a function of structure geometry. (a) Cassie-Baxter (CB-) and Wenzel (W-) curves for cylindrical asperities (-c-). (b) Cassie-Baxter (CB-) and Wenzel (W-) curves for cylindrical asperities (-c-) and cylinders with hemispherical tops (-h-). The CB and W curves for pits H90 and H83 are the same (W-c-H) in (a) and (b), while the CB and W curves for pillars are different: in (a) the pillars (P) are modelled as cylinders; in (b) as cylinders with hemispherical tops. Note that the dependence of the CB curve on l/d for pillars and pits (CB-c-H and CB-c-P) is different. Individual points indicate experimental data: (Δ) H90; (∇) H83; (\circ) P22; (\diamond) P21; (\triangleright) P13; (\square) P12.

The experimental advancing angles of water on hydrophobic silicon, along with the theoretical predictions, are plotted in Figure 18. Since the end-geometries of the hydrophobised pillars were somewhat in between cylindrical and hemispherical, the Cassie-Baxter and Wenzel curves were plotted for both geometries (eq 3, 5 in Figure 18a, and eq 4,6 in Figure 18b), while the pits were always modelled as perfect cylinders (eq 3, 5).

The present results are discussed within the framework of Patankar's criterion for designing superhydrophobic surfaces (Patankar, 2003). Briefly, this method consists of obtaining a stable Cassie-Baxter drop by fabricating structures which, given the highest possible aspect ratio h/d , have a dimensionless spacing l/d such that $\cos\theta_{CB} > \cos\theta_W$, or a value of $|\cos\theta_W - \cos\theta_{CB}|$ as high as possible; the first condition ensures that a Cassie-Baxter drop will have lower energy than a Wenzel drop for the given geometry; the second condition means that even if $\cos\theta_{CB} < \cos\theta_W$, the energy barrier between the two states should be as high as it can possibly be to avoid transitions from a metastable Cassie-Baxter drop to a lower-energy Wenzel state.

The sliding angles in Figure 19 were used as a means to test the deductions derived from Figure 18 concerning the “state” of the drops (i.e. Cassie or Wenzel). The radii of all the droplets was less than the capillary length, which is 2.7 mm for water, so that the force exerted by gravity was negligible: the smaller the radius of the drops, the more the Laplace internal pressure pushes the liquid inside the surface asperities. For this reason, when increasing the drop size, the internal Laplace pressure of the drop decreased, thus decreasing the pressure exerted by the drop on the substrate (Lafuma, 2003). However, there can be a competitive effect of gravity to push the water inside the texture when the weight of the drop increases. For drops of these sizes (5-40 mg) the contact line energy is negligible (Quere, 2004).

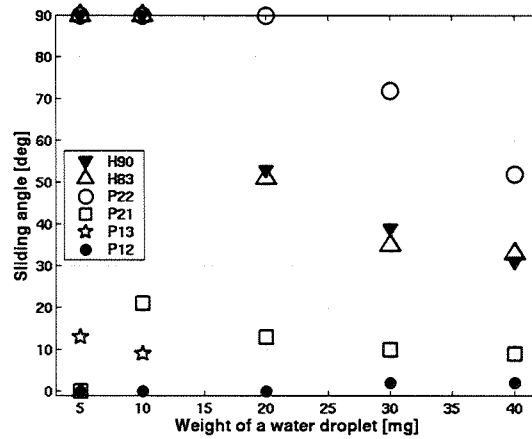


Figure 19. Mean sliding angles α of water droplets on hydrophobic patterns as a function of drop weight.

The points at 90° indicate pinned drops.

The experimental values of the advancing angles on the pitted samples (H90 and H83) were in agreement with their respective Wenzel curves for cylindrical pits (same W-c-H in both Figure 18a-b). This was supported by sliding angles measurements, where 5-10 mg drops were completely pinned (Figure 19 and Figure 12). This result goes against theoretical expectations: since the Cassie-Baxter curve for pits (CB-c-H) is always at a lower energy than the Wenzel one (W-c-H) (i.e. $\cos\theta_{CB-c-H} > \cos\theta_{W-c-H}$), the drops were expected to be in a Cassie-Baxter state, yet they are clearly in a Wenzel state. However, the Cassie-Baxter regime for pits is stabilized only for $l/d < 1.54$ (H90) and $l/d < 1.48$ (H83), which are the critical values at which the corresponding Wenzel angles becomes unattainable ($\cos\theta_w < -1$); it is therefore possible to obtain a higher energy Wenzel configuration with H90 and H83 nano-pits. On the other hand, this predicts the occurrence of stable Cassie drops on pitted surfaces with a high density of pits of large diameters.

The best agreement with the experimental data for pillars was found with the models using a hemispherical top (Figure 18b), even when the tops were not perfectly hemispherical (e.g. as in Figure 13l). This underlines the importance of the curvature of the edges in determining the advancing angles. For this reason, from this point onwards only the plot in Figure 18b will be discussed, and the experimental contact angles will be compared with the Cassie-Baxter and Wenzel models for hemispherical-top pillars.

Samples P22 and P21 had practically the same ϕ_s , but different roughness r . Their experimental advancing angles were close to the intersection between the Cassie-Baxter curve for pillars and their Wenzel curves. In this case the receding angles should allow to distinguish if the drops were in either a Wenzel or in a Cassie-Baxter state. On receding, the water droplets were pinned on P22 ($\theta_{rec}=0^\circ$), since the receding angle never attained a steady state. The sliding angle measurements showed that drops of up to 20 mg were pinned on this substrate (upper 90° values in Figure 19). This result suggests that P22 is in a Wenzel state; this could be explained by the fact that P22 is the shallowest of the four protruding patterns, and it has truly hemispherical edges: both factors make the Cassie-Baxter regime more unlikely to happen, since sharp edges and a high aspect ratio are important conditions to ensure air trapping (Bico, 1999). However, a receding angle of 0° was unexpected; between the possible reasons a differential hydrophobisation of the bottom surface compared to the top of the asperities cannot be excluded, because it could have affected the receding angles on the Wenzel samples; still, only P22 showed this behaviour. Öner&McCarthy (Öner, 2000) showed that the receding angles depended on the three-phase contact line structure, while the advancing angles were unaffected by it. Therefore, the unusual pinning on sample P22 might be due to the curvature of the hemispherical tops (see Figure 13i) since the contact line could be pinned by greater solid-liquid contact, and indeed a hemispherical top will have more solid-liquid contact than a flat top with the same height ($\Delta\phi_s=4\%$ for P22).

Unlike P22, sample P21 had a high receding angle, showing that it was in a Cassie state. Its closeness to the “critical point” (i.e. the intersection between the Cassie-Baxter and Wenzel curves) would imply that a transition to the Wenzel state would need very little energy; this hypothesis was confirmed by tilting angle measurements, which showed a sudden jump from 0° to 21° when the drop weight was increased from 5 mg to 10 mg. The increased weight forced the water inside the texture, and the 10 mg drop transitioned to the Wenzel state.

For sample P13 a Wenzel state would have had a lower energy, but the energy barrier to overcome is bigger than in P21. In this case, an increase in drop weight from 5 to 10 mg caused a decrease in sliding angle, confirming the Cassie-Baxter state of the 5 μl droplet.

Sample P12 had the best water-repellent configuration, since not only the Cassie-Baxter state was at lower energy than the Wenzel state and the energy barrier between the two was very high, but the Wenzel angle corresponding to this geometry was unattainable ($\cos\theta_w < -1$). Tilting angles on P12 were $0\pm 2^\circ$ throughout the whole range of drop weights, making it impossible to deposit a drop smaller than 30 μl . This finding is coherent with Patankar’s prediction that a forest of nano-pillars would be the most effective water-repellent structure (Patankar, 2004a), confirming that for a given spacing l , increasing the aspect ratio h/d will stabilize the Cassie-Baxter regime, as discussed by Patankar (Patankar, 2004a) and illustrated by Yoshimitsu *et al.* (Yoshimitsu, 2002) Sample P12 also

acted as superwetable when its surface was hydrophilic: this similarity not only shows that roughness with the highest possible aspect ratio h/d will enhance dramatically the wetting properties of a surface, whether hydrophilic or hydrophobic; it also entails the ambivalence of topography-enhanced wetting/dewetting, as already highlighted by McHale *et al.* (McHale, 2004).

Having verified the validity of the Cassie-Baxter model for our submicrometric structures, Patankar's (Patankar, 2004a) suggestion that the epicuticular wax crystalloids on the Lotus leaf (200 nm-1 μ m) play a significant role in repelling water droplets was investigated. This hypothesis was tested by applying the Cassie-Baxter formula for hemispherical tops to our superhydrophobic surfaces (P21, P13 and P12), assuming an ideal contact angle of cuticular wax $\theta_Y=100^\circ$ (Holloway, 1969): the Cassie-Baxter formula predicts apparent contact angles of 150° , 155° and 157° , respectively. This result is only indicative, since the morphology of the wax crystalloids is very different from our model structures: however, it shows clearly that nanotopography alone is able to increase the contact angle of water from 100° to over 150° , making the surface superhydrophobic without the need of an underlying microstructure. Thus, Patankar's hypothesis was confirmed by showing that roughness at this scale might stabilize or even be the primary cause of the hydrophobicity of dual-scale topographies. Since our model topographies resemble the naturally-occurring ordered arrays of nanometric structures shown by Watson *et al.* (Watson, 2004) on the wings of the cicada and the termite, it would be very interesting to compare the present results with experimental contact angles of such insect wings. Unfortunately, this data is not available at present.

The model of Jopp *et al.* (Jopp, 2004) for advancing hydrophobic angles (eq 10) was also tested. The results are shown in Table 5. As it can be seen, most of the predicted regimes are not in agreement with the experimental measurements. Figure 20 shows a plot of the Gibbs energy of the drop on sample H83, as a function of the penetration depth of water and the contact angle.

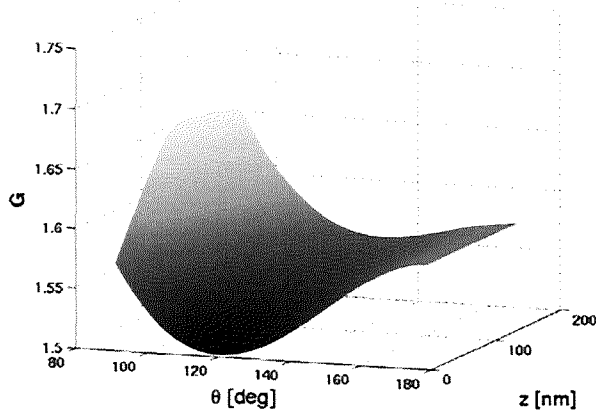


Figure 20. Normalized Gibbs free energy of a 5 μl drop of water on H83 pits as calculated by Jopp's method. The energy minimum can be seen for an angle $\theta=120^\circ$ and a penetration depth $z=0$, corresponding to the top of the surface. This plot predicts a Cassie-Baxter regime of a 5 μl drop of water with contact angle $\theta=120^\circ$ on sample H83, which disagrees with the present experimental results.

	H90	H83	P22	P21	P13	P12
$\theta_{\text{adv-exp}} (^\circ)$	114 \pm 1	125 \pm 2	129 \pm 3	155 \pm 2	159 \pm 2	161 \pm 2
Regime-exp	W	W	W	CB	CB	CB
$\theta_{\text{Jopp-cyl}} (^\circ)$	118	120	151	151	151	158
$\theta_{\text{Jopp-hem}} (^\circ)$	-	-	148	153	145	160
Regime-cyl	CB	CB	CB	CB	W	CB
Regime-hem	-	-	W	W	W	W

Table 5. Static contact angles as predicted by the model of Jopp *et al.*, in the case of cylindrical and hemispherical pillars. The first row shows my experimental results, the second the corresponding regime as confirmed by receding angles and sliding angles. θ_{Jopp} is the static angle predicted by Jopp's minimization for cylindrical (-cyl) and hemispherical (-hem) asperities, with the two bottom rows detailing the roughness-filling regime predicted by the energy minima (CB: Cassie-Baxter; W; Wenzel). Jopp's predictions are not in agreement with my experimental observations.

Finally, it was verified if the theoretical predictions by Roura-Patankar model for receding angles on surface roughness agree with experimental values. The experimental receding angles of the Cassie-Baxter drops (P21, P13 and P12) were plotted with eq 8 and eq 9 (Figure 21). The results show a trend similar to the theoretical curves for cylindrical and hemispherical-top pillars, but no quantitative agreement.

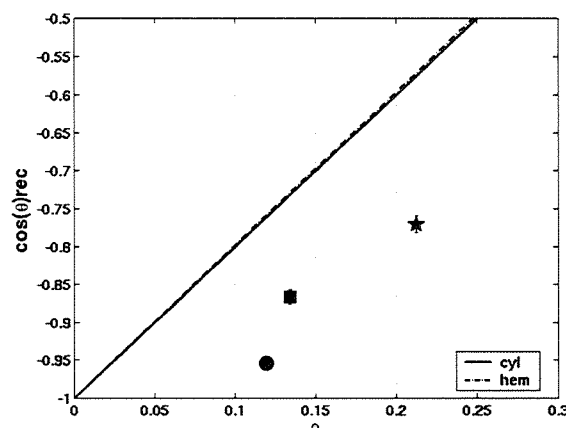


Figure 21. Receding angles of water on hydrophobic patterns as a function of the solid fraction ϕ_s .

The experimental values ((★) P21; (■) P13; (●) P12) are plotted with eq 7 (“cyl”) and eq 8 (“hem”).

2.5.4 PCL replicas

The advancing angles measured on the PCL nano-pits are plotted in Figure 22, together with the angles predicted by the Cassie-Baxter and Wenzel models. The nano-pits were modelled as cylinders. Data on the nano-pillars are not available due to experimental difficulties in measuring both the dimensions (it was impossible to image useful profiles) and the contact angles (stick-slip effects made the measurements unreliable). The advancing angles of water on the nano-pitted PCL replicas are discussed within the framework of Patankar’s criterion, despite this material being considered hydrophilic ($\theta_y=77^\circ < 90^\circ$). The reason for this choice is apparent from Figure 22: the experimental advancing angles on samples P22-r, P21-r and P12-r are in agreement with the Cassie-Baxter curve for cylindrical pits (Figure 22-left), even more so if the dimensions of the nano-pits are assumed to be the exact negative of the master dimensions (Figure 22-right). This could be because measuring the dimensions of the PCL replicas was more difficult and less precise than for the masters, for several reasons: the PCL could have been deformed during the cleaving, or during SEM examination.

The Cassie-Baxter state was constantly metastable, since all the Wenzel curves in this case correspond to a lower energy configuration. These results confirm a hypothesis by S. Herminghaus (Herminghaus, 2000), who claimed that given the appropriate steepness of the asperities, a free liquid surface can be formed, resulting in air-trapping (i.e. increased hydrophobicity) even on hydrophilic surfaces. Abdelsalam *et al.* (Abdelsalam, 2005) made a hydrophilic surface hydrophobic by patterning it with close-packed hemispherical pits of 500 nm; even though they explain the phenomenon by a particular curvature of the liquid-vapour interface on the pores, it is interesting to note that the Young’s angle on their gold substrates is 70° , which is comparable to the contact angle of PCL (77°). This calls for considerations on the definition of

hydrophilicity and hydrophobicity. So far in this thesis the defining criterion has been the contact angle θ , then $\theta_{\text{hydrophilic}} < 90^\circ$ and $\theta_{\text{hydrophobic}} > 90^\circ$. However, it has been pointed out (Hayashi, 2002, Vogler, 1998) that if the defining criterion is the structural force between surfaces, the hydrophobic/hydrophilic boundary should correspond to an angle of 62° - 65° , which is coherent with the observations reported herein. This suggests that the modeling approaches for hydrophilic surfaces, expecting a Wenzel trend when $\theta_r < 90^\circ$, will fail with substrates of $65^\circ < \theta_r < 90^\circ$, since air-trapping, although metastable, is possible in this case. This possibility should be better investigated.

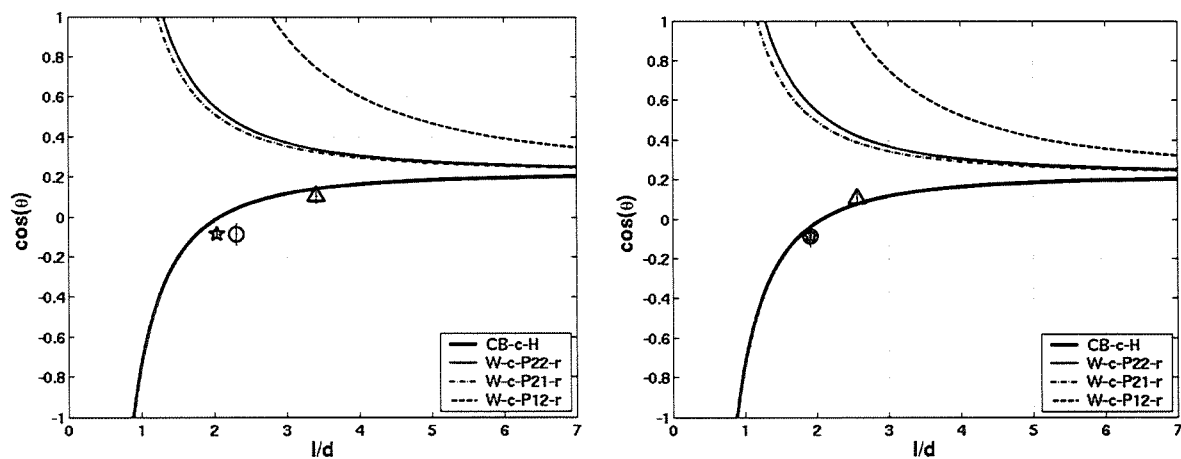


Figure 22. Plot of the apparent advancing angles of a 5 μl drop of water on PCL replicas as a function of structure geometry. Left: The nano-pits dimensions measured with ImageJ from SEM images. Right: The nano-pits dimensions are assumed to be exactly the negative of their corresponding silicon masters. The Cassie-Baxter (CB-) and Wenzel (W-) curves for cylindrical asperities (-c-) are shown. Individual points indicate experimental data: (O) P22; (☆) P21; (Δ) P12.

2.6 Conclusion

Regular nanopatterns were fabricated in silicon wafers, and the behaviour of water droplets on these surfaces was evaluated before and after chemical hydrophobisation.

From these results it can be concluded that the Composite-Drop (“hemi-wicking”) model successfully predicts the advancing angles on hydrophilic patterns. Analogously, the Cassie-Baxter and Wenzel models gave accurate estimates of the advancing angles on hydrophobic patterns. These models are very sensitive to even small variations in the asperity profile, and it is shown that if the edges of the cylindrical pillars are not sharp, a geometry considering a hemispherical-top rather than a flat one will predict the advancing experimental angles more accurately; it is suggested that the same might be true for receding angles.

In accordance with Patankar’s criterion for designing a super-hydrophobic surface, it is confirmed that a forest of slender pillars is the most stable water-repellent texture. This same topography exhibited superhydrophilicity, confirming the ambivalence of topography-enhanced

wetting/dewetting. It is also suggested that nano-pits can support stable Cassie drops only if the diameter is large compared to the spacing.

Having verified the design criterion, the hypothetical angle of the epicuticular wax crystalloids of the Lotus leaf was calculated. The results support the suggestion (Patankar, 2004a) that the sub-micrometric structures of the Lotus leaf play a main role in its water-repellent behaviour.

The PCL nano-pits exhibited a Cassie-Baxter behaviour, despite the contact angle on PCL being $\theta_Y=77^\circ < 90^\circ$. These results, besides proving that air-trapping can occur on such “hydrophilic” surfaces, are in agreement with previous work (Abdelsalam, 2005, Herminghaus, 2000) and strongly support the consideration that the hydrophobic/hydrophilic boundary contact angle is not 90° , but rather between 62° and 90° (Hayashi, 2002, Vogler, 1998).

3 The DLVO force between a micro-sphere and regular sub-micrometric patterns: a Surface Element Integration study.

The rapid improvement of fabrication techniques has allowed the patterning of regular surface features at the nano-scale, the physical and biocompatible properties of which are raising great interest at the moment (Martines, 2005, Riedel, 2001, Dalby, 2004, Gallagher, 2002). As a further characterisation, Surface Element Integration was used to simulate the DLVO interaction of a 10 μm silica sphere with a nanopatterned silica plate in a 1:1 aqueous electrolyte solution. Both surface protrusions (nano-pillars) and depressions (nano-pits) were considered: the height, diameter and shape of the asperities were varied to show the influence of their geometric parameters on the plate-sphere DLVO interaction.

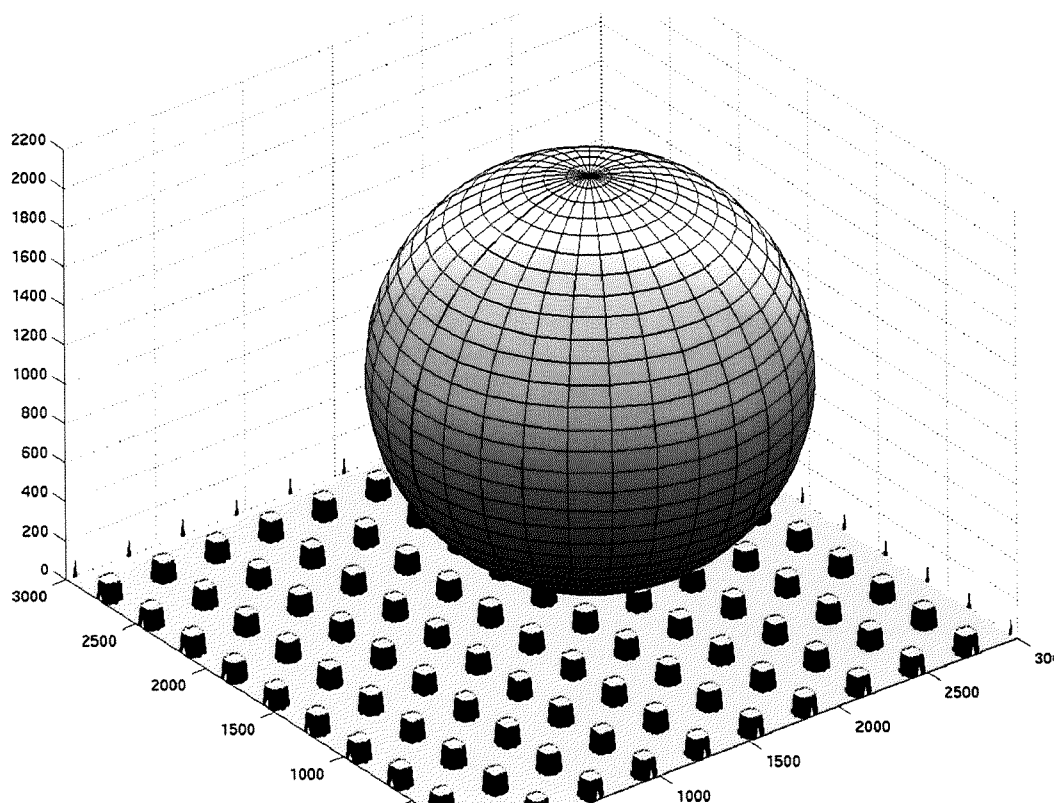


Figure 23. A Matlab reconstruction of a 2 μm sphere approaching an orthogonal array of nano-cylinders. Units on the axis are in nm.

3.1 Introduction

Traditionally, inter-particle forces have been described by the DLVO (Derjaguin-Landau-Verwey-Overbeek) theory, (Verwey, 1948) in which the total interaction energy between two surfaces is calculated as the sum of the electrostatic double layer and van der Waals interactions. The original DLVO theory assumed that the interacting surfaces were ideal, i.e. molecularly smooth. For most of real surfaces, there appears to be a discrepancy between predictions based on the DLVO theory and particle-surface force measurements; such departure between theory and experiments has been ascribed to surface roughness (Ducker, 1991, Suresh, 1997, Walz, 1998, Toikka, 1996) and non-DLVO forces (Horn, 1989, Chapel, 1994, Grabbe, 1993, Meagher, 1992, Israelachvili, 1982) amongst others.

Studies on the coagulation (Kihira, 1992) and deposition of particles on collector surfaces (Hull, 1969) concluded that the observed results could not be explained by the classic DLVO theory; Elimelech & O'Melia (Elimelech, 1990) postulated that the higher deposition rates of colloidal particles on spherical solid collectors (packed bed) could be due to surface roughness. AFM force-distance curves on rough membranes ("colloid-probe" technique (Ducker, 1991) showed that the energy barriers (see 3.2.4) were lower than the corresponding barrier for a smooth membrane (Drechsler, 2004, Hoek, 2003), and that this reduction was correlated to the size of the surface-features, rather than to their periodicity (Hoek, 2003); Bowen *et al.* (Bowen, 2002) showed that the magnitude of the double-layer repulsion on a rough membrane was greatly reduced on the protruding peaks, although adhesion was much stronger in the depressions. It was also suggested that the interaction between particles was not determined by their radii of curvature, but rather by the radii of curvature of their surface asperities (Elimelech, 1990, Snoswell, 2005).

Extensive work has been done to model the effect of surface roughness on colloidal forces (Bhattacharjee, 1997, Czarniecki, 1980, Herman, 1991, Sparnaay, 1983, Sun, 2001, Van Bree, 1974, Suresh, 1996). In particular, Suresh *et al.* (Suresh, 1996, Suresh, 1997) calculated the interaction energy in aqueous electrolyte of a rough spherical probe approaching a flat plate at constant potential. In order to do so, they first modelled a rough plate by superimposing hemispherical asperities (of radius up to 40 nm) onto an ideal flat plate. Then they applied the Derjaguin approximation (Derjaguin, 1934) (see 3.2.5) to the case of a rough plate facing a smooth plate, thus obtaining the interaction energy between a rough sphere and a flat plate (although the same procedure yields the energy of a smooth sphere on a rough plate). They observed that the roughness decreased the energy barrier and the depth of the secondary minimum (defined in 3.2.4), and pushed the latter to larger separation distances. They also found that the size of the asperities had a greater impact on the interaction energy than their density at low surface coverage (< 4%). One of the limitations of this model, besides its dependence on the Derjaguin approximation, is that

the reliability of the prediction decreases inversely with asperity size. Thus, for hemispherical protrusions of order 30 nm the surface covered by asperities must be less than 10%, and calculations involving protrusions of order 100 nm would be nonsensical. Besides, the model cannot be applied to the case of concave asperities (i.e. surface depressions).

A common problem of many models is their dependence on the Derjaguin approximation (Derjaguin, 1934) to calculate the energy between a spherical probe and a plate, because this approximation is not valid at small separation distances or for highly curved surfaces, and it cannot be applied to concave topographies. Models like the Surface Element Integration (SEI) (Bhattacharjee, 1997) or the model of Sun *et al.* (Sun, 2001) on the other hand allow to approximate the interaction between interfaces with an arbitrary surface topology. The SEI in particular, consists of a straightforward analytical method to calculate interaction energies between two surfaces at constant potential; SEI was proven to be in closer agreement than the Derjaguin approximation with exact finite-element solutions of the sphere-plate interaction (Bhattacharjee, 1997), and with experimental measurements (Todd, 2004).

In this work, the SEI technique was applied to simulate the DLVO interaction energy between a 10 μm silica sphere and regular silica nanotopographies of varying shape and dimensions, in a 1:1 aqueous electrolyte solution. The height, diameter and shape of the asperities were varied to show the influence of these geometric parameters on the potential energy of interaction. By using this simplified model system, the influence of nano-fabricated surface features on the DLVO interaction energy was simulated as it could be measured by the “colloid-probe” technique. Unlike in earlier work (Herman, 1991, Suresh, 1996), concave (or hollow) surface topography was successfully modelled (“*nano-pits*”). My simulation confirms previous predictions (Suresh, 1996) that protruding surface topography/roughness (“*nano-pillars*”) should lower the energy barrier and the depth of the secondary minima, although no dramatic shift in the position of the wells was observed. The changes in energy barrier and secondary well induced by the nano-pits were less striking than the ones induced by the nano-pillars. The lower energy barriers would yield much larger particle deposition rates than predicted by the DLVO theory for particles on smooth surfaces, in qualitative agreement with experimental observations (Elimelech, 1990).

3.2 Theoretical background

This chapter contains a brief overview of inter-particle interactions; all information has been extracted from J. Israelachvili, *Intermolecular and Surface forces*, 2nd ed., Academic Press, 1991 (Israelachvili, 1991), unless otherwise specified by the appropriate citations.

The interaction potential $W(D)$ between two particles separated by a distance D is also called *potential energy of mean force* (in solvent medium), *free energy* or *available energy*. Eq 13 formulates the relation between the inter-particle force F and its corresponding potential energy W , as a function of the separation distance D (Figure 24):

$$F(D) = -\frac{dW(D)}{dD} \quad (13)$$

The *thermal energy* (kT) is an indicator of the strength of the interaction: if $W(D)$ is higher than kT , it will “win out” against the disorganising effects of the thermal energy, and the particles will adhere to the surface. The potential energy of interaction between particles also depends on the size (radius R) of the particle, thus the interaction energy can be much stronger than kT even at separations D above 100 nm.

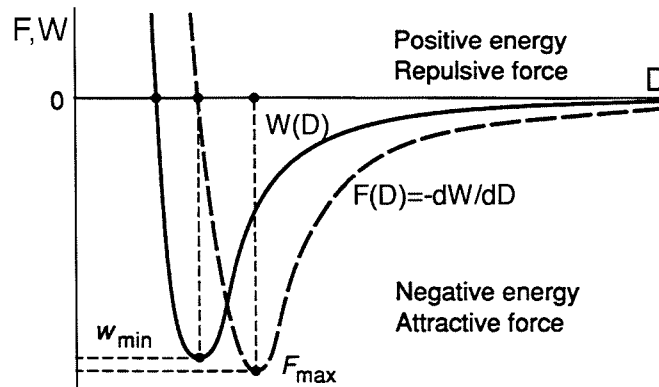


Figure 24. Schematic plot of the relation between the potential energy of interaction (W) and the force (F) experienced by the particles, as a function of their separation distance D . Image modified from J. Israelachvili, *Intermolecular and Surface forces*, 2nd ed., Academic Press, 1991.

The interaction of “soft” particles (like biological cells) with a surface depends on the interplay between interparticle and intraparticle forces (because they can deform). Since this chapter only deals with the interaction of a solid microsphere with a structured plate, the following paragraphs will briefly introduce the interparticle forces between non-deformable bodies. In electrolyte solutions, the total interaction between any two surfaces is composed of various forces of different origin. The Van der Waals (3.2.1) and the electric double layer (3.2.2) interactions yield, when superimposed, the so-called DLVO interaction (3.2.4). The DLVO theory has many

limitations (Ninham, 1999), due to the interplay with other forces that are commonly referred to as “non-DLVO” interactions (3.2.6). The contribution of these forces to the total interaction between surfaces is briefly introduced in the following paragraphs.

3.2.1 The van der Waals force

The *dispersion* force, like the gravitational force, acts between all atoms and molecules. Dispersion forces make up one third and perhaps most important contribution to the total *van der Waals forces*, the two others being the dipole-dipole and the dipole-induced dipole interactions. The van der Waals forces play a central role in the intermolecular interactions, because they are always present, unlike the electrostatic and H-bonding forces; generally, the van der Waals force is attractive. Figure 25 shows the van der Waals interaction laws (“Hamaker expressions”) for some common geometries, given in terms of the Hamaker constant A (Hamaker, 1937). For two particles (1 and 2) interacting through medium 3, the approximate expression for the non-retarded Hamaker constant based on the Lifshitz theory is shown in eq 14:

$$A \approx \frac{3}{4} kT \left(\frac{\varepsilon_1 - \varepsilon_3}{\varepsilon_1 + \varepsilon_3} \right) \left(\frac{\varepsilon_2 - \varepsilon_3}{\varepsilon_2 + \varepsilon_3} \right) + \frac{3h\nu_e}{8\sqrt{2}} \frac{(n_1^2 - n_3^2)(n_2^2 - n_3^2)}{\sqrt{(n_1^2 + n_3^2)(n_2^2 + n_3^2)} \left[\sqrt{(n_1^2 + n_3^2)} + \sqrt{(n_2^2 + n_3^2)} \right]} \quad (14)$$

where ε_1 , ε_2 and ε_3 are the static dielectric constants of the three media, n the refractive index of the media in the visible, ν_e the main electronic absorption frequency in the visible and h Planck’s constant. The first term in the above equation ($A_{v=0}$) gives the “zero-frequency” contribution of the van der Waals interaction, while the second term ($A_{v>0}$) gives the dispersion energy contribution: the former includes the dipolar contributions, the latter the London energy contribution. With increasing separation distance the dispersion energy contribution ($A_{v>0}$) between two surfaces begins to decay faster than predicted by eq 14: this is called the *retardation effect*. The van der Waals forces can be long-range, and the retardation effects should be taken into account; for this reason, there is no simple equation to describe the van der Waals force at all separation distances. To complicate things further, the zero-frequency term is screened by free electrolyte ions, therefore the Hamaker constant decreases with growing ion concentration.

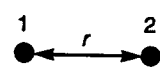
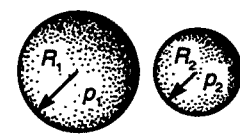
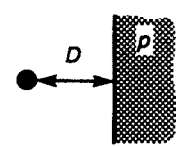
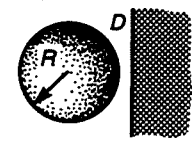
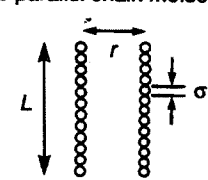
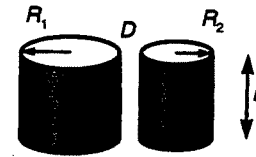
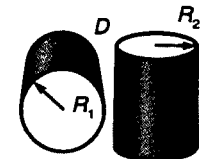
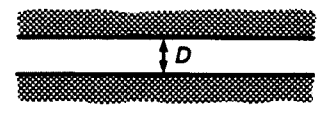
<p>Two atoms</p>  <p>$w = -C/r^6$</p>	<p>Two spheres</p>  <p>$W = \frac{-A}{6D} \frac{R_1 R_2}{(R_1 + R_2)}$</p>
<p>Atom-surface</p>  <p>$w = -\pi C p / 6D^3$</p>	<p>Sphere-surface</p>  <p>$W = -AR/6D$</p>
<p>Two parallel chain molecules</p>  <p>$W = -3\pi CL/8\sigma^2 r^5$</p>	<p>Two cylinders</p>  <p>$W = \frac{AL}{12\sqrt{2} D^{3/2}} \left(\frac{R_1 R_2}{R_1 + R_2} \right)^{1/2}$</p>
<p>Two crossed cylinders</p>  <p>$W = -A\sqrt{R_1 R_2} / 6D$</p>	<p>Two surfaces</p>  <p>$W = -A/12\pi D^2$ per unit area</p>

Figure 25. Non-retarded van der Waals interaction free energies between bodies of different geometries calculated on the basis of Hamaker summation method. The interaction energy (W) can be expressed as the Hamaker constant (A) times a geometric term describing the interacting surfaces. Image from J. Israelachvili, *Intermolecular and Surface forces*, 2nd ed., Academic Press, 1991.

3.2.2 The electric double-layer force

The electric double layer force between charged surfaces decays roughly exponentially and is repulsive if the charge on the interacting surfaces has the same sign. Its strength is governed by the electrical potential of the surfaces, its range by the ionic strength of the electrolyte solution.

A surface in a liquid can be charged by ionization or dissociation of surface groups (e.g. $-\text{COOH} \rightarrow \text{COO}^- + \text{H}^+$), and/or by adsorption (binding) of ions from the solution onto a previously uncharged surface. The surface charge is balanced by an atmosphere of *counterions*, some transiently bound to the surface (within the *Stern layer*, see below), some diffuse in rapid thermal motion close to the surface (*diffuse electric double layer*). The widely accepted model for the

electrochemical double-layer according to Gouy, Chapman, Stern and Grahame is schematically shown in Figure 26. The Stern layer is further assumed to be composed by two planes where immobile counterions (outer Helmholtz plane) and immobile coions (inner Helmholtz plane) are adsorbed (Werner, 1998).

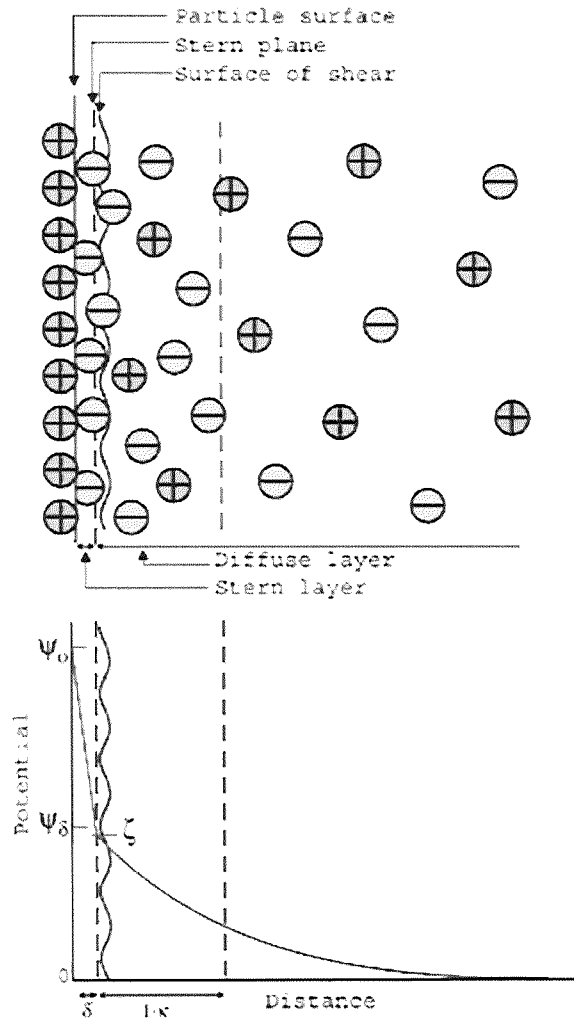


Figure 26. Schematic representation of the electric double-layer, which is composed of the Stern layer (at a distance δ from the surface wall) and the diffuse layer (of thickness $1/\kappa$). The surface potential is ψ_0 , while the Stern layer has potential ψ_δ . The zeta-potential ζ at the plane of shear is also shown. Image downloaded on 01/10/2005 from www.bic.com/WhatisZetaPotential.html.

The electric double-layer force can be calculated theoretically as a solution of the *Poisson-Boltzmann* (PB) equation (eq 15), which is the fundamental equation describing the counterion distribution in the diffuse layer between two plane charged surfaces in solution:

$$\frac{d^2\psi}{dx^2} = -\frac{ze\rho}{\epsilon\epsilon_0} = -\left(\frac{ze\rho_0}{\epsilon\epsilon_0}\right)e^{-\frac{ze\psi}{kT}} \quad (15)$$

where z is the valency of the ions, e the electronic charge, ϵ the dielectric permittivity of the medium, ϵ_0 the dielectric permittivity of vacuum, ρ_0 the number density of ions at the midplane between plates, k the Boltzmann constant and T the temperature. When solved, the PB equation

gives the potential ψ , the electric field $E = \delta\psi/\delta x$ and the counterion density ρ at any point x in the gap. To solve the PB equation, certain boundary conditions have to be assumed, e.g. constant potential or constant charge distribution of the surfaces. The relation between the surface charge σ and the surface potential ψ_0 is given by the *Grahame equation* for the case of a mixed NaCl + CaCl₂ electrolyte:

$$\sigma = \sqrt{8\epsilon\epsilon_0 kT} \sinh\left(\frac{e\psi_0}{2kT}\right) \sqrt{[Na^+]_{\infty} + [Ca^{2+}]_{\infty} (2 + e^{-e\psi_0/kT})} \quad (16)$$

In most cases neither the surface charge nor the surface potential remains constant as the solution conditions change: if specific ions from the solution bind to the ionizable sites of the surface (*potential determining ions*), both ψ_0 and σ will vary as the salt concentration and/or pH are changed. For low surface potentials ($\psi_0 < 25$ mV), the Grahame equation reduces to:

$$\sigma = \epsilon\epsilon_0 \kappa \psi_0 \quad (17)$$

where $1/\kappa$ is the *Debye length*, i.e. the “thickness” of the diffuse electric double-layer given by eq 18:

$$\kappa = \sqrt{\sum_i \rho_{xi} e^2 z_i^2 / \epsilon\epsilon_0 kT} \quad (18)$$

Typical values of the Debye length in a 1:1 electrolyte are: $\kappa^{-1} \approx 10$ nm at 1 mM and $\kappa^{-1} \approx 1$ nm at 100 mM. The magnitude of the Debye length depends solely on the properties of the liquid, and not on the surface properties as is the case for the surface charge and potential.

The *contact value theorem* (eq 19) defines the pressure (force) P between two surfaces at separation distance D , as a function of the ionic concentration at the surface ρ_s :

$$P(D) = kT[\rho_s(D) - \rho_s(\infty)] \quad (19)$$

By using the Poisson-Boltzmann equation to calculate the ionic distribution between two surfaces, and incorporating it in the contact value theorem, it is possible to obtain the double-layer potential energy (W_{EDL}) per unit area between two planar surfaces:

$$W_{EDL}(D) = \frac{64kT\rho_{\infty}}{\kappa} \tanh^2\left(\frac{ze\psi_0}{4kT}\right) e^{-\kappa D} \quad (20)$$

where ρ_{∞} is the concentration of ions in the bulk and D the separation distance of the two plates. It can be noted that the double layer interaction between surfaces decays exponentially with distance, with a characteristic decay length (the Debye length $1/\kappa$). The above equation is known as the *weak*

overlap approximation for the interaction between two similar surfaces at constant potential ψ_0 . At low surface potentials ($\psi_0 < 25$ mV), the above equation simplifies to the following:

$$W_{EDL}(D) \approx 2\varepsilon\varepsilon_0\kappa\psi_0^2 e^{-\kappa D} = 2\sigma^2 e^{-\kappa D} / \kappa\varepsilon\varepsilon_0 \quad \text{per unit area} \quad (21)$$

where σ and ψ_0 are related by eq 17. However, both eq 20 and eq 21 are accurate only for surface separations beyond about one Debye length. Hogg *et al.* (Hogg, 1966) obtained an analytical expression for the double-layer interaction energy per unit area between two flat plates at constant (but different) surface potential (eq 22). This is an exact analytical solution of the linearised PB equation that is valid for small surface potentials:

$$W_{EDL}(D) = \frac{\varepsilon_r \varepsilon_0 \kappa}{2} (\psi_{01}^2 + \psi_{02}^2) \left(1 - \coth(\kappa D) + \frac{2\psi_{01}\psi_{02}}{(\psi_{01}^2 + \psi_{02}^2)} \operatorname{cosech}(\kappa D) \right) \quad (22)$$

where ψ_{01} and ψ_{02} are the surface potentials of the two flat surfaces representing the materials of the sphere and the flat plate, ε_0 is the dielectric permittivity of vacuum, ε is the dielectric constant of the solvent and κ is the inverse Debye length.

3.2.3 Surface potential and ζ -potential

In order to calculate the electric double-layer repulsion, proper values of the surface potentials are required. The surface potentials can be represented by the potential ψ_δ at the boundary between the Stern and the diffuse layer (Figure 26). The electrokinetic potential ζ (which is the potential at the hydrodynamic solid/liquid boundary, i.e. at the shear plane) is usually considered a good first approximation of ψ_δ , and it can be measured directly (Hunter, 2002, Werner, 1998). Although ζ is perhaps not identical to ψ_δ (Johnson, 1995, Attard, 2000), it is felt that ζ will resemble ψ_δ much more than ψ_0 , which would mean that the hydrodynamic shear plane corresponds more or less exactly to the first layer of adsorbed ions. However, the place of the shear plane is by no means self-evident, and considerable deviations between ζ and ψ_δ occur for nonideal solid surfaces, e.g., due to roughness, porosity, or the presence of hairy layers.

3.2.4 The DLVO theory

The total DLVO interaction between any two surfaces must take into account the van der Waals and the electric double layer forces: by superimposing them, the total potential energy of interaction between two bodies is obtained. The DLVO interaction energy per unit area between two infinite planar surfaces is obtained by summing the van der Waals and the double-layer interactions (eq 23):

$$W_{plane}(h) = W_{VDW}(h) + W_{EDL}(h) \quad (23)$$

As a first approximation, the van der Waals potential is considered insensitive to electrolyte concentrations and pH, so it is assumed to be fixed. When $D \rightarrow 0$, the van der Waals energy dominates because it is a power-law, whereas the double layer interaction energy remains finite or rises more slowly. Depending on the electrolyte concentration, the surface charge density or potential, different cases can occur under the combined action of the two forces. In the case of highly charged surfaces in electrolyte solution there is a strong long-range repulsion that peaks at some distance (1-4 nm), usually at the *energy barrier*, followed by a significant *secondary minimum* or *well* as shown in Figure 27. The potential energy minimum at adhesive contact is known as the *primary minimum* for a colloidal system, and if the energy barrier is too high to be overcome, the particles sit in the weak secondary minimum or they remain totally dispersed.

The main factor bringing two surfaces into adhesive contact is the decreasing of the surface charge or potential (by screening or binding) by increasing the salt concentration. However, if the surface has a high potential, even after adding electrolyte to the solution, the surfaces can still adhere in a secondary minimum.

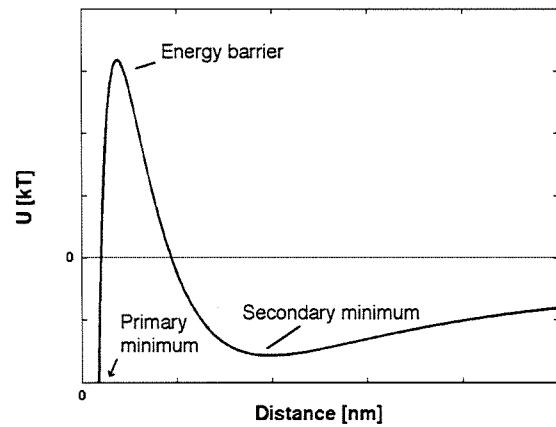


Figure 27. Schematic of a DLVO curve.

3.2.5 The Derjaguin approximation

It is convenient to relate the interaction force $F(D)$ between two curved surfaces to the interaction free energy $W(D)$ between two planar surfaces. The *Derjaguin approximation* (Derjaguin, 1934) (DA, eq 24) gives the van der Waals force between two spheres of radii R_1 and R_2 in terms of the energy per unit area of two flat surfaces at the same distance D , assuming $R_1 \gg D$ and $R_2 \gg D$:

$$F(D)_{\text{sphere-sphere}} \approx 2\pi \left(\frac{R_1 R_2}{R_1 + R_2} \right) W(D)_{\text{plane-plane}} \quad (24)$$

If $R_2 \gg R_1$, we obtain the limiting case of a sphere near a planar surface:

$$F(D)_{\text{sphere}} = 2\pi R W(D)_{\text{planes}} \quad (25)$$

This relation is valid for any type of force law, assuming that the radius of curvature of the two bodies is much bigger than their separation distance ($R \gg D$). Subsequently, it is possible to obtain the free energy of interaction between a sphere and a plate by applying eq 13:

$$W(D)_{sphere} = 2\pi R \int_D^{\infty} F(D)_{sphere} \quad (26)$$

3.2.6 Other non-DLVO forces

When two surfaces approach closer than a few nanometers, continuum theories of attractive van der Waals and repulsive double-layer forces often fail to describe their interaction. This is either because these theories break down at small separations or because other non-DLVO forces come into play. *Solvation forces* can be oscillatory, monotonically attractive or monotonically repulsive (Israelachvili, 1996). In aqueous systems, the monotonically repulsive solvation force that rises between hydrophilic surfaces is called (*repulsive*) *hydration* or *structural* force; this is due to the surface-induced changes in the structure and density of adjacent water and it has been simulated by Grunze and co-workers via Monte Carlo technique (Hayashi, 2002, Pertsin, 2000). Correspondingly, hydrophobic surfaces in water experience an additional attractive (hydration) force which can be very long-range (*hydrophobic force*) (Israelachvili, 1982). *Steric forces* result from the approaching of two surfaces that are dynamically rough, i.e. with no sharp, well-defined boundaries, as is the case with polymeric or amphiphilic surfaces.

3.3 Surface Element Integration (SEI)

The SEI technique (Bhattacharjee, 1997) calculates the total DLVO interaction energy between two bodies as the sum of the energies between differential projected surface elements. In simple terms, the surfaces are discretised in small elements, and the area of each element is projected on the XY plane parallel to the surface. The projected elements that are facing each other (on the two surfaces) are treated as parallel facing planes, and their interaction energy is calculated. By integrating over the whole surface of the particle, the energies of all pairs of elements are summed, and the total interaction energy between bodies is obtained. The integration procedure is applied to the exact geometry of the interacting surfaces: therefore, in the case of a sphere interacting with a plane, the interaction energy between the plane and the half sphere that is facing away from the plate is also considered. Unlike the DA, the SEI can be used for any surface shape (convex and concave) of any radius of curvature. From now on the case of a spherical particle approaching a (rough) surface will be considered.

The basic governing equation of SEI is shown in eq 27.

$$W(D) = \iint_{particle} W_{plane}(h) dA \quad (27)$$

where $W(D)$ is the total interaction energy between the particle and the surface, D is the distance of closest approach between the particle and the surface (as defined in Figure 31), $W_{plane}(h)$ is the

interaction free energy per unit area between two infinite planar surfaces separated by a distance h , and dA is a projected differential surface area of the particle. The surface integral in eq 27 is evaluated only over the area directly under the sphere, for both faces of the sphere (Figure 28). This means that during the computation of the interaction energy between a sphere and a structured surface, only those asperities within the projected area of the sphere are considered.

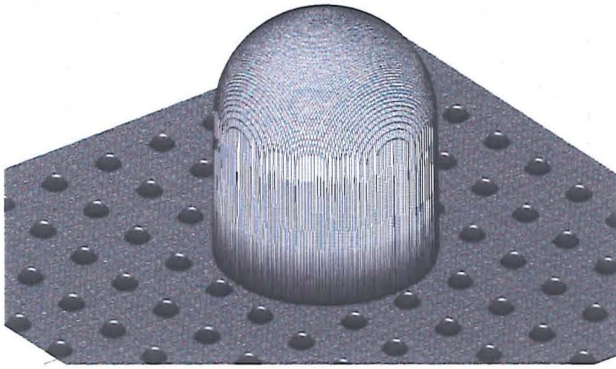


Figure 28. Schematic of a sphere interacting with a rough surface. The SEI considers only the interaction between facing elements on the sphere and the surface, thus the integral is evaluated over the area directly under the sphere, for both hemispheres (facing the surface, and facing away from it).

$W_{plane}(h)$ represents the DLVO interaction between each pair of facing surface elements, which are considered as infinite parallel plates (eq 28) (Bhattacharjee, 1997):

$$W_{plane}(h) = W_{VDW}(h) + W_{EDL}(h) \quad (28)$$

Where $W_{VDW}(h)$ is the van der Waals energy, and $W_{EDL}(h)$ is the double-layer energy. Several expressions are available to formulate these energies: in this work, the non-retarded Hamaker's integration approach was used to calculate the van der Waals interaction (eq 29) (Hamaker, 1937):

$$W_{VDW}(h) = -\frac{A}{12\pi h^2} \quad (29)$$

where A is the Hamaker constant of the interacting media. The expression of Hogg *et al.* (Hogg, 1966) (eq 22) for two planes at constant potential was used to calculate the double-layer interaction $W_{EDL}(h)$. By substituting eq 29 and eq 22 in eq 28, and finally into eq 27, the total interaction energy $W(D)$ between the spherical particle and the surface is obtained. If the surface is not flat, but rough or patterned, the differential energies between facing surface elements varies with their distance h , and this is reflected in the final sum (eq 27) which yields the overall energy of interaction between the particle and the surface.

3.4 Modelling

All calculations were carried out in Matlab 6.5 (Mathworks Natick, MA) on a Mac OSX (1.6 GHz). Surfaces with orthogonal arrays of asperities were generated as meshes of 100 nm^2 Cartesian elements over an area of $12 \text{ }\mu\text{m} \times 12 \text{ }\mu\text{m}$. The size of the elements was chosen as a compromise between precision and computing time; a mesh of 100 nm^2 elements would yield ca. 10 elements on the top of the asperities. Three types of asperities were considered: cylindrical holes (“pits”, Figure 29), cylindrical protrusions (“cylindrical pillars”, Figure 29), and cylindrical protrusions ending with a hemispherical top (“hemispherical pillars”, Figure 29). The centre-to-centre distance l between asperities was fixed at 300 nm, while their diameter d and height h were varied between 20-200 nm and between 20-150 nm, respectively. Table 6 shows the different patterns with their dimensions and nomenclature. The dimensions were chosen to be representative of the nanostructures used for contact angle measurements and cell culture in this work and by other authors (Curtis, 2001, Dalby, 2004, Gallagher, 2002, Suresh, 1997).

	20d20h	100d150h	150d75h	150d150h	150d150h-vall	200d150h
Diameter (nm)	20	100	150	150	150	200
Height/Depth (nm)	20	150	75	150	150	150
Aspect ratio	1	1.5	0.5	1	1	0.75
Pitch (nm)	300	300	300	300	300	300
Sphere position	“centred”	“centred”	“centred”	“centred”	“valley”	“centred”

Table 6. Simulated nanopatterns: nomenclature, dimensions and corresponding sphere axis position.

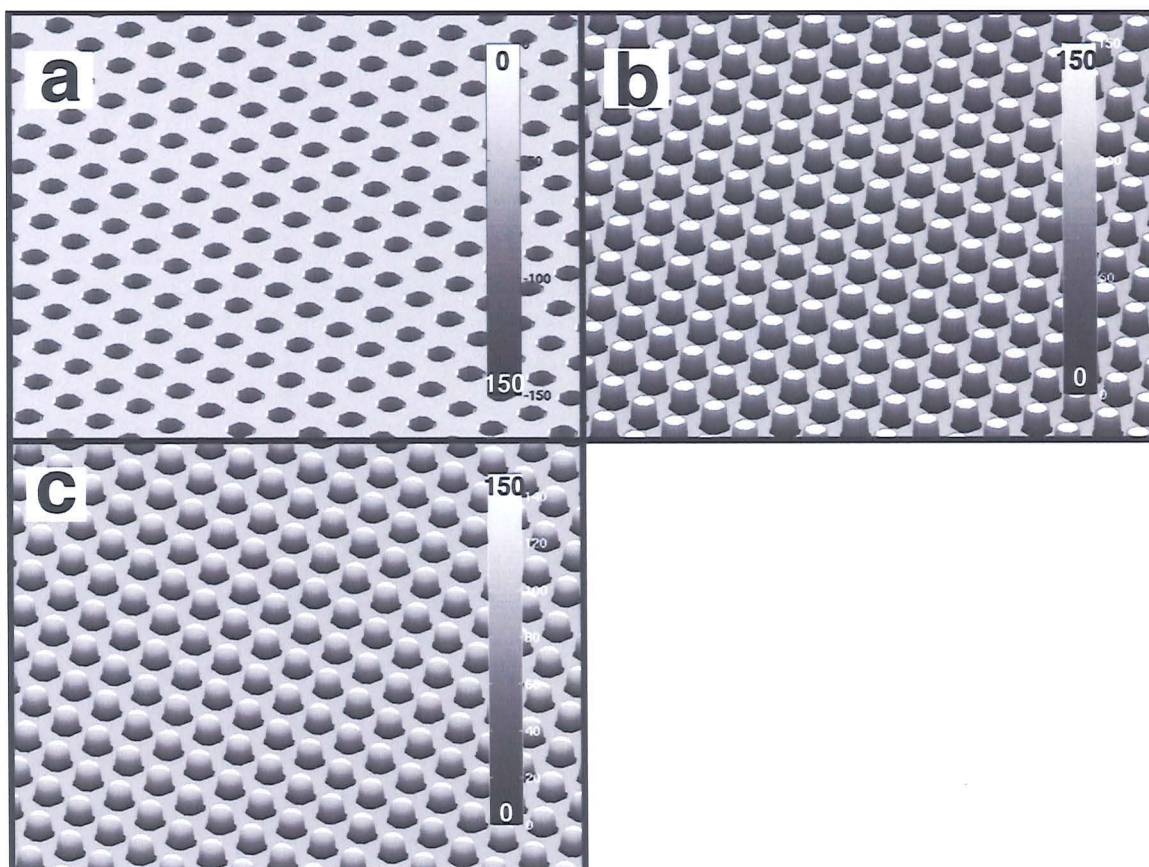


Figure 29. Matlab reconstructions of nanopatterned surfaces of diameter 150 nm, depth/height 150 nm, spacing 300 nm. a) Cylindrical nano-pits. b) Cylindrical nano-pillars. c) Hemispherical nano-pillars.

The diameter of the sphere was 10 μm . The centre of the sphere was placed on the axis of symmetry of the asperities (“centred”) or at the intersection of the planes of symmetry running through the axis of the asperities (“valley”), as shown in Figure 30. Table 6 details the position of the sphere attributed to the different nanopatterns.

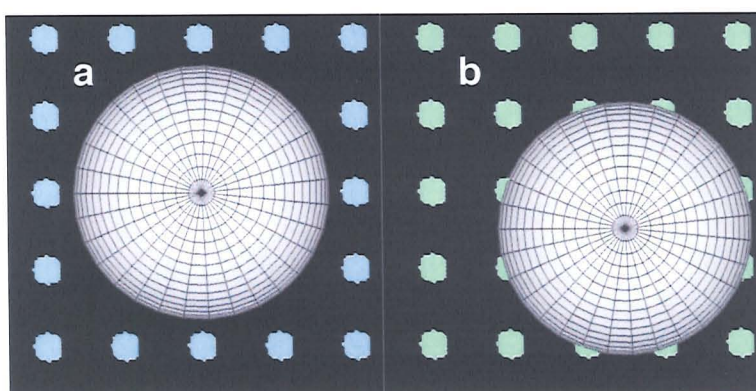


Figure 30. Position of the sphere axis on the plane of the surface. a) “centred”; b) “valley”.

The distance D between the nanopatterns and the sphere varied from 0 to 120 nm, in the following manner: on the nano-pillars, the first 2 nm were divided in 0.1 nm steps, the following 5 nm in 0.25 nm steps, then the interaction from 8 to 120 nm was calculated in 1 nm steps; on the nano-pits and the flat control, the first 8 nm were divided in 0.2 nm, then the interaction from 8 to 120 nm was

calculated in 1 nm steps. The different steps ensured that the desired accuracy was achieved around the energy barrier, while minimising computing time. The distance of closest approach $D=0$ (Figure 31) between the sphere and the surface was set to be at the “hard-wall contact”, rather than at the mean-plane or bottom plane of the surface, to avoid instances where portions of the sphere would overlap with a volume of space occupied by protruding asperities. Hence, on the topographies specified in Table 7, at $D=0$ the sphere is not in contact with the surface, and the curves are shifted by a finite distance from the “hard-wall contact”.

<i>Pits</i>					<i>Pill. Cyl</i>	<i>Pill. Hem.</i>
20d20h	100d150h	150d75h	150d150hh	200d150h	150d150h-vall	150d150h-vall
0.005	0.125	0.281	0.281	0.5	0.281	1.1

Table 7. Shift (nm) in separation distance of the curves computed for the topographies that are not in contact with the microsphere at $D=0$.

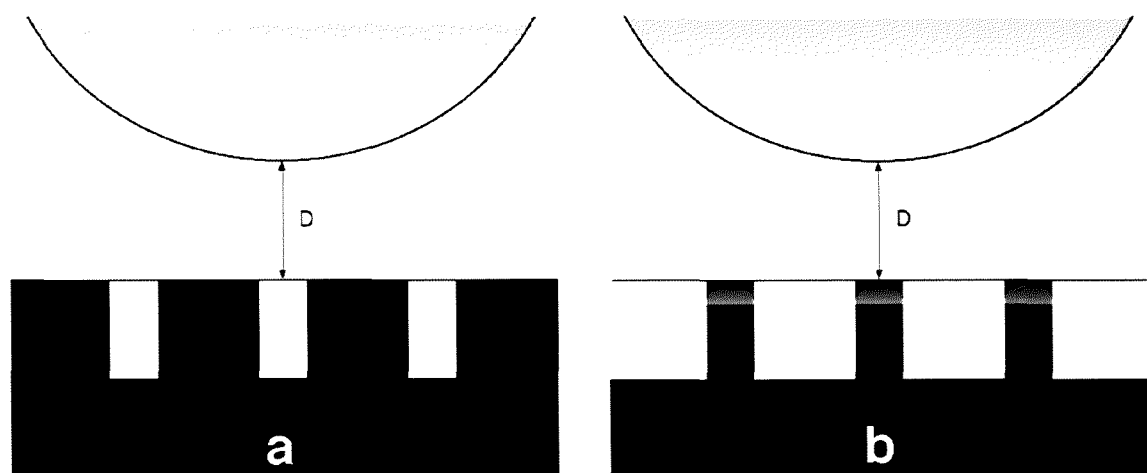


Figure 31. a) Distance from the flat control and the nano-pits. b) Distance from the nano-pillars (cylindrical and hemispherical).

The simulated physical parameters were chosen to correspond to a symmetrical SiO_2 -water- SiO_2 system, in a 1:1 aqueous electrolyte solution (e.g. NaCl); hence, the non-retarded Hamaker constant A was 0.8×10^{-20} J (Ducker, 1992). Retardation effects of the van der Waals attraction have not been accounted for in this work. The electrolyte concentrations were chosen to be 1 mM and 100 mM: the latter is of particular interest because it is close to physiological conditions (ca. 145 mM). At these molarities the literature reports different values of the ζ potentials and fitted diffuse layer potentials $\psi_{\text{D-ft}}$ of silica in 1:1 electrolyte (Bowen, 2000, Chapel, 1994, Considine, 2001, Ducker, 1992, Horn, 1989, Janusz, 2003). This is because the surface potentials of silica are extremely sensitive to a number of factors such as the measuring technique, the method of preparation, the

prehistory of measurement, pH, electrolyte concentration and surface roughness (Considine, 2001, Grabbe, 1993, Hartley, 1997, Vigil, 1994). Therefore, the values of $\zeta = -50$ mV at 1 mM and $\zeta = -25$ mV at 100 mM in 1:1 electrolyte were chosen, which fall in the middle-range of the data reported in the literature.

Figure 32 shows the range of the plane-plane interaction between two flat 100 nm^2 elements, which correspond to the mesh elements used in the SEI simulation; the van der Waals attraction and the double layer repulsion at 1 mM and 100 mM in 1:1 aqueous electrolyte solution are shown. The expression used for the double layer interaction is the one from Hogg *et al.* (Hogg, 1966) (eq 10): strictly, this expression is valid for constant and small surface potentials $\psi < 25$ mV, however the authors showed that it was applicable with potentials up to 100 mV (although in that case the values at short distances are of little significance).

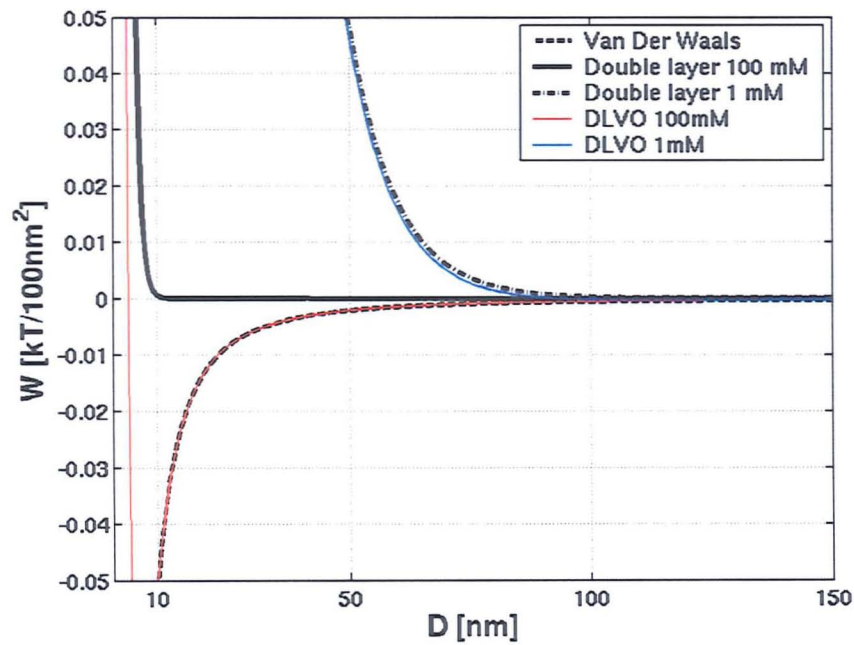


Figure 32. DLVO interaction between two flat 100 nm^2 elements facing each other $A_H = 0.8 \times 10^{-20} \text{ J}$; at 1 mM, $\psi_S = \psi_M = -50$ mV; at 100 mM, $\psi_S = \psi_M = -25$ mV in a 1:1 electrolyte.

3.5 Results

All the results concerning the separation distances (and consequently the energies) are subject to a degree of uncertainty that depends on the discretisation of the distance. For clarity, the interaction between the $10 \text{ }\mu\text{m}$ sphere and the small asperities 20d20h (pits, cylindrical pillars and hemispherical pillars) is described separately in 3.5.3.

3.5.1 Flat control: SEI and DA

Since the DA is valid in the case of a 10 μm sphere approaching a flat surface, the interaction energy between a sphere and a smooth flat plate was calculated by DA and by SEI: the results are plotted in Figure 33a-c. Table 8 summarizes the magnitude and position of the secondary wells and energy barriers on the flat control as calculated by SEI and DA. The SEI predicts a lower energy barrier and a shallower secondary minimum than the DA, at both 1 mM and 100 mM (Figure 33a-c); since the order of magnitude of the energy barrier is of thousands of kT , the two models can be considered to be in agreement. Besides, the position of the secondary minima predicted by the two approaches are very consistent (Table 8).

	1 mM		100 mM	
	SEI D=X \pm 0.2 nm	DA D=X \pm 0.01 nm	SEI D=X \pm 0.2 nm	DA D=X \pm 0.01 nm
Energy Barrier	W=15400 D=1.2	W=15442 D=1.12	W=390.6 D=1	W=395.97 D=0.93
Secondary Well	W=-14.456 D=92	W=-15.753 D=91.94	W=-299.77 D=4	W=-302.28 D=4.09

Table 8. Magnitude (W) and separation distance (D) of the energy barrier and secondary minimum of the potential energy of interaction between a 10 μm sphere and a flat plate, calculated by Surface Element Integration (SEI) and Derjaguin Approximation (DA). $A_H=0.8 \times 10^{-20}\text{J}$; at 1 mM, $\psi_S=\psi_M=-50\text{ mV}$; at 100 mM, $\psi_S=\psi_M=-25\text{ mV}$ in a 1:1 electrolyte.

3.5.2 Nano-pits and nano-pillars: SEI

The interaction energies between a 10 μm sphere and the nanopatterns of different dimensions were calculated by SEI and compared to the interaction energy with the flat control. The results for *nano-pits* are plotted in Figure 33d-f: they show that the magnitude of the energy on the flat control and the nano-pits is similar at both 1 mM and 100 mM. The potential energy in case of *cylindrical and hemispherical nano-pillars* is plotted in Figure 34a-c and Figure 34d-e, respectively. Both cylindrical and hemispherical nano-pillars reduce the energy barriers significantly, at both 1 mM and 100 mM. This effect is more pronounced with hemispherical rather than cylindrical pillars, particularly at 100 mM, where the interaction with hemispherical pillars is entirely in the attractive region. Table 9 and Table 10 summarise the magnitude and position of the energy barriers and secondary wells of all topographies at both molarities.

At 1 mM the energy barrier is increasingly lowered from flat to pits, to cylindrical pillars and finally to hemispherical pillars. For a fixed asperity height/depth (150 nm), at the ‘‘centred’’ configuration, the dependence of the energy barrier on the diameter of the asperities inverted on

pits and pillars: on pits the energy barrier decreases inversely with the diameter, while on both cylindrical and hemispherical pillars the lowest energy barrier is found with the smallest diameter. All three topographies made the secondary wells shallower than on the flat control; this effect is more pronounced on pillars than on pits. Again, the trend is opposite on pits and pillars, since on pits the largest diameter has the shallowest well, while on the pillars this relation is inverted.

At 100 mM, the energy barrier is increasingly lowered from pits to flat, to cylindrical pillars and finally to hemispherical pillars: unlike at 1 mM, now the energy barriers on the pits are higher than on the flat; for a fixed height (150 nm), at the “centred” configuration, the dependence of the energy barrier on the diameter of the asperities is the same for pits and cylindrical pillars, showing an increase in energy barrier with an increase in diameter. However, the dependence of the secondary wells on the diameter is opposite on pits and pillars, like at 1 mM: on pits, the largest diameter yields the shallowest minimum, while on pillars the same topography has the deepest well. On hemispherical pillars the curves are now entirely in the attractive region.

The *position of the secondary wells* on the nano-pits at both molarities is within 1 nm from the value on the flat control, and mainly shifted to closer distances (for the topographies specified in Table 7, due to the definition of $D=0$ the fixed shift has to be added to the position of the secondary well). Similarly, the secondary minima of both cylindrical and hemispherical pillars (Figure 34b and e, respectively) are generally shifted to closer distances (more so on the hemispherical than on the cylindrical pillars), but with differences of up to 10 nm (20d20h). On hemispherical pillars 20d20h and 150d150h-vall, the wells disappear and the curves tend to the primary minimum. The *difference between “valley” and “centred”* sphere on 150d150h is significant only on pillars at 100 mM: on the “valley” between cylindrical pillars the interaction is mainly attractive and the energy barrier is much shallower than on the centred configuration; on the “valley” between hemispherical pillars the energy barrier disappears, and the curve tends to the primary minimum. Decreasing the *height/depth* of the asperities from 150 nm to 75 nm makes the energy more attractive at both molarities; this is more visible at the secondary minima, but is true for the energy barriers too.

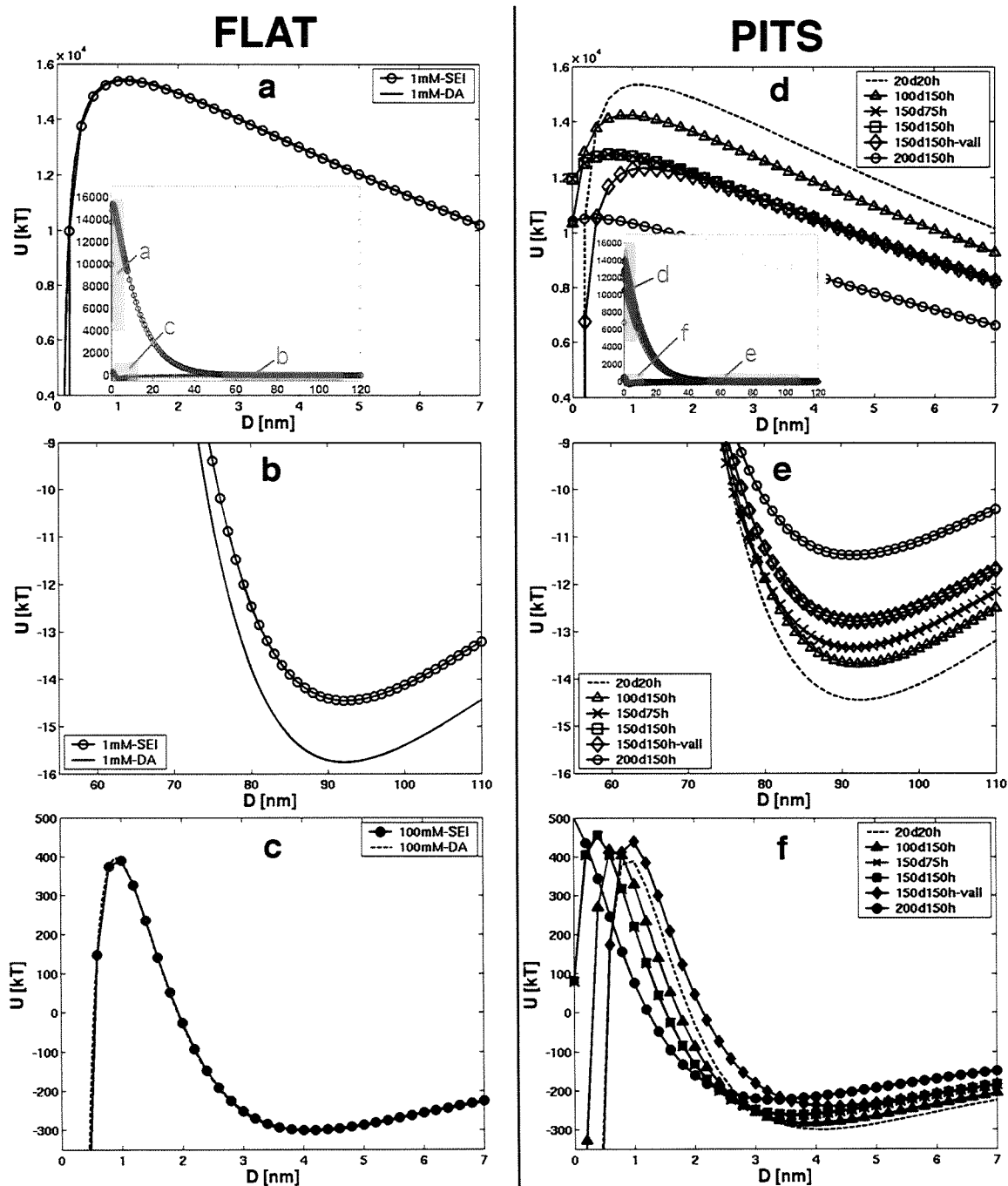


Figure 33. a-c) Potential energy of interaction between a $10\ \mu\text{m}$ sphere and a flat surface: a) Energy barrier at 1 mM (the insert shows the full range of the curve); b) Secondary well at 1 mM; c) Interaction energy at 100 mM. d-f) Potential energy of interaction between a $10\ \mu\text{m}$ sphere and nano-pits of different dimensions: d) Energy barrier at 1 mM (the insert shows the full range of the curve); e) Secondary well at 1 mM; f) Interaction energy at 100 mM. $A_H=0.8\times 10^{-20}\text{J}$; at 1 mM, $\psi_S=\psi_M=-50\text{ mV}$; at 100 mM, $\psi_S=\psi_M=-25\text{ mV}$ in a 1:1 electrolyte.

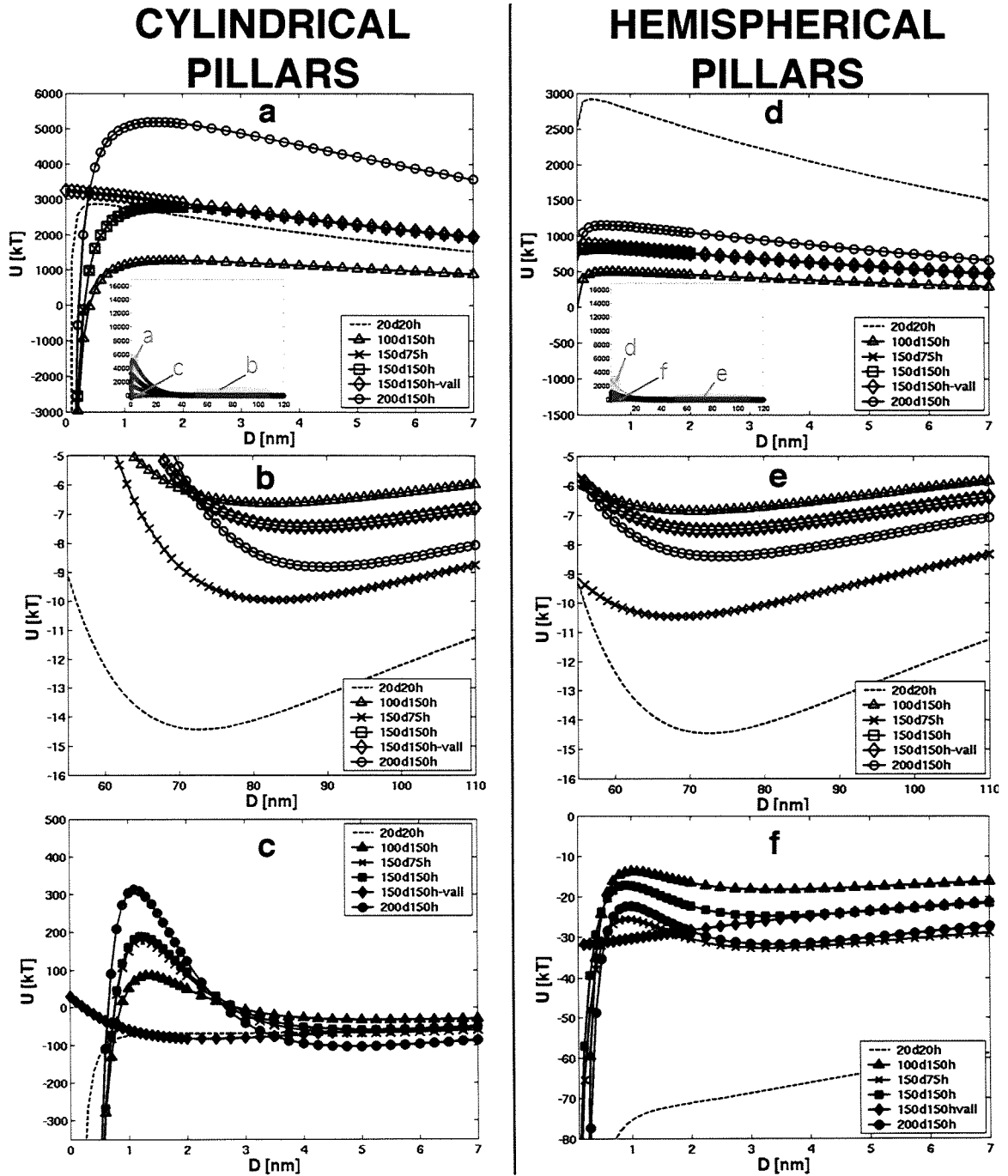


Figure 34. a-c) Potential energy of interaction between a $10\ \mu\text{m}$ sphere and cylindrical nano-pillars of different dimensions: a) Energy barrier at 1 mM (the insert shows the full range of the curve); b) Secondary well at 1 mM; c) Interaction energy at 100 mM. d-f) Potential energy of interaction between a $10\ \mu\text{m}$ sphere and hemispherical nano-pillars: d) Energy barrier at 1 mM (the insert shows the full range of the curve); e) Secondary well at 1 mM; f) Interaction energy at 100 mM. $A_H=0.8\times 10^{-20}\text{J}$; at 1 mM, $\psi_S=\psi_M=-50\ \text{mV}$; at 100 mM, $\psi_S=\psi_M=-25\ \text{mV}$ in a 1:1 electrolyte.

	1 mM			100 mM		
	Pits	Pill. Cyl.	Pill. Hem.	Pits	Pill. Cyl.	Pill. Hem.
	D=X±0.2 nm	D=X±0.1 nm	D=X±0.1 nm	D=X±0.2 nm	D=X±0.1 nm	D=X±0.1 nm
20d20h	W=15352.53 D=1.2	W=2874.469 D=0.5	W=2922.998 D=0.3	W=389.07 D=1	W=- D=-	W=- D=-
100d150h	W=14230.274 D=1	W=1278.231 D=1.9	W=500.526 D=0.7	W=417.82 D=0.6	W=87.015 D=1.3	W=- D=-
150d75h	W=12833.361 D=0.6	W=2786.880 D=1.7	W=833.236 D=0.5	W=455.9 D=0.4	W=180.43 D=1.2	W=- D=-
150d150h	W=12833.295 D=0.6	W=2787.803 D=1.7	W=833.382 D=0.5	W=457.91 D=0.4	W=188.79 D=1.2	W=- D=-
150d150h-vall	W=12346.005 D=1.2	W=3242.976 D=0	W=906.202 D=0	W=440.04 D=1	W=30.634 D=0	W=- D=
200d150h	W=10525.631 D=0.4	W=5201.876 D=1.5	W=1157.162 D=0.6	W=502.97 D=0	W=314.36 D=1.1	W=- D=-

Table 9. Magnitude (W [kT]) and separation distance (D [nm]) of the energy barriers of the potential energy of interaction between a 10 μm sphere and a nanopatterned plate, calculated by Surface Element Integration (SEI). $A_H=0.8\times 10^{-20}\text{J}$; at 1 mM, $\psi_S=\psi_M=-50\text{ mV}$; at 100 mM, $\psi_S=\psi_M=-25\text{ mV}$ in a 1:1 electrolyte. The shading highlights the topographies with fixed height $h=150\text{ nm}$.

	1 mM			100 mM		
	Pits D=X±1 nm	Pill. Cyl. D=X±1 nm	Pill. Hem. D=X±1 nm	Pits D=X±0.2 nm	Pill. Cyl. D=X±0.25 nm	Pill. Hem. D=X±0.25 nm
20d20h	W=-14.449 D=92	W=-14.422 D=73	W=-14.443 D=72	W=-299.24 D=4	W=-68.229 D=2.5	W=- D=-
100d150h	W=-13.677 D=92	W=-6.6135 D=82	W=-6.6743 D=81	W=-282.51 D=3.8	W=-31.797 D=5.25	W=-18.187 D=3.5
150d75h	W=-13.335 D=91	W=-9.9511 D=83	W=-10.007 D=81	W=-262.64 D=3.6	W=-66.351 D=5	W=-32.724 D=3.25
150d150h	W=-12.782 D=92	W=-7.4289 D=87	W=-7.381 D=81	W=-260.76 D=3.6	W=-58.595 D=5	W=-24.705 D=3.5
150d150h-vall	W=-12.782 D=92	W=-7.429 D=87	W=-7.3811 D=81	W=-239.18 D=4.2	W=-82.486 D=2.25	W=- D=-
200d150h	W=-11.382 D=91	W=-8.7917 D=90	W=-8.2672 D=81	W=-221.73 D=3.4	W=-102.46 D=4.75	W=-31.763 D=3.25

Table 10. Magnitude (W [kT]) and separation distance (D [nm]) of the secondary minima of the potential energy of interaction between a 10 μm sphere and a nanopatterned plate, calculated by Surface Element Integration (SEI). $A_H=0.8 \times 10^{-20}$ J; at 1 mM, $\psi_S=\psi_M=-50$ mV; at 100 mM, $\psi_S=\psi_M=-25$ mV in a 1:1 electrolyte. The shading highlights the topographies with fixed height $h=150$ nm.

3.5.3 Small asperities 20d20h. SEI and Suresh's model.

Of all the nano-pits, 20d20h yielded the smallest difference in energy barrier and secondary minimum with the flat control at both molarities. On the other hand, at 1 mM both cylindrical and hemispherical pillars 20d20h reduced the energy barrier significantly compared to the flat control, and with similar magnitude (see Table 9), while yielding small effects on the secondary minimum compared to the other asperities. At 100 mM, the 20d20h nano-pillars had a dramatic effect on the potential energy, which became always attractive.

Asperities of this shape and dimensions have been treated previously by Suresh *et al.* (Suresh, 1996) as a model of surface roughness: although in their simulation the roughness is on the sphere rather than on the plate, their formulas can also be applied to the case of a smooth sphere on a rough plate. Therefore, the non-retarded interaction energy of 20d20h hemispherical pillars was calculated and used for a comparison between SEI and Suresh's method at both 1 mM (Figure 35), and at 100 mM (Figure 36). For the case of 20d20h hemispheres, Suresh's model predicts a higher energy barrier and a deeper secondary minimum than the SEI. This is mainly because Suresh's model is based on the DA which, as already seen in Figure 33b, predicts deeper secondary minima than SEI. By taking this into account, the results yielded by SEI and Suresh's model can be considered to be in good agreement.

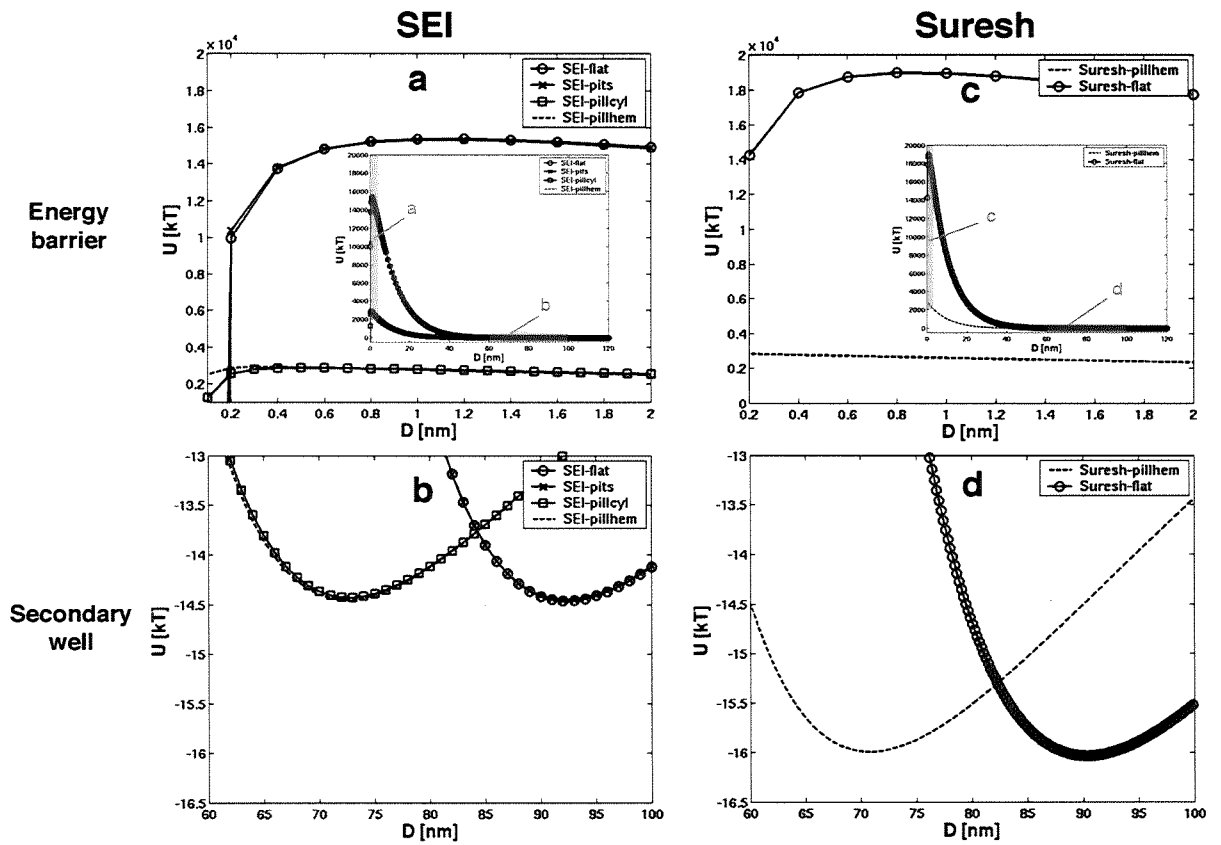


Figure 35. DLVO interaction between the sphere and the smallest asperities (20d20h) at 1 mM. Comparison between SEI and Suresh's results. $A_H=0.8 \times 10^{-20}$ J; at 1 mM, $\psi_S=\psi_M=-50$ mV; at 100 mM, $\psi_S=\psi_M=-25$ mV in a 1:1 electrolyte.

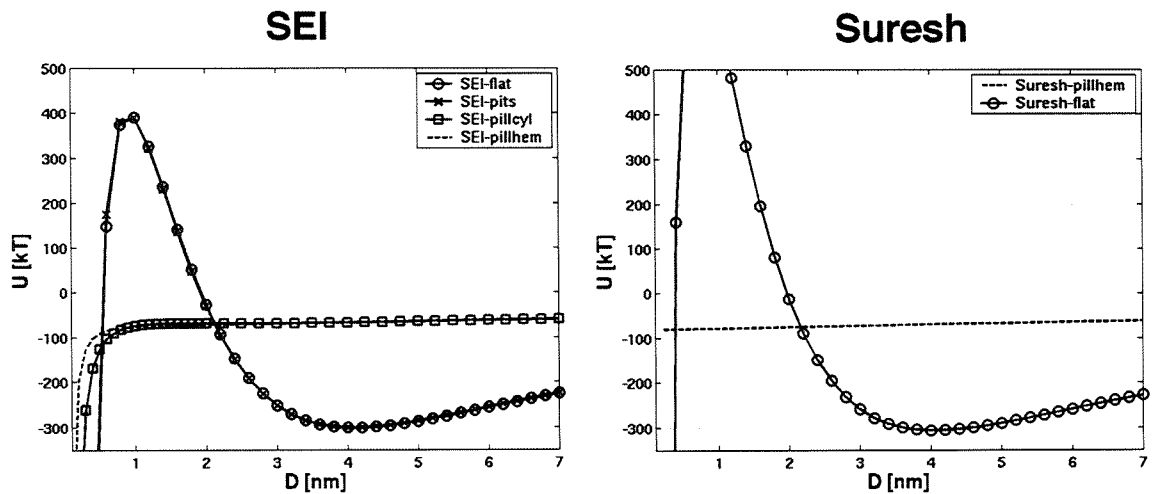


Figure 36. DLVO interaction between the sphere and the smallest asperities (20d20h) at 100 mM. Comparison between SEI and Suresh's results. $A_H=0.8 \times 10^{-20}$ J; at 1 mM, $\psi_S=\psi_M=-50$ mV; at 100 mM, $\psi_S=\psi_M=-25$ mV in a 1:1 electrolyte.

3.6 Discussion

Overall, the energy difference between the pits and the flat control is much less pronounced than the difference between pillars and the flat control: the pillars reduced the energy barrier considerably. In particular, if their top is hemispherical the pillars appear to favour adhesion at the primary minimum by greatly reducing the energy barrier at both molarities.

On *150-nm-high cylindrical pillars* the double-layer repulsion is dominated by the flat top of the pillars, because the double-layer repulsion between elements from the bottom surface decays before 150 nm (Figure 32): hence, decreasing the *diameter* (or rather, increasing the aspect ratio h/d) of cylindrical pillars at 1 mM will result in lower energy barriers. In the case of *150-nm-high hemispherical pillars*, the further lowering of the energy barriers can be explained by the decreasing of the double-layer interaction between surfaces that curve away from each other, so that for equivalent pillar height, the energy barrier of a 10 μm sphere with hemispherical nanopillars will be lower than on cylindrical nano-pillars. This suggestion has already been put forward by Elimelech & O'Melia (Elimelech, 1990), who also postulated that an increase in the radius of curvature in the protrusions leads to an increase in energy barrier. For this reason, it would be interesting to model protrusions with cusped and conical tops. Increasing the diameter of the *150-nm-deep nano-pits* at 1 mM results in lower energy barriers as well, although their order of magnitude is the same as on the flat control. However, at 100 mM the energy barriers on the nanopits are higher than on the flat control, and here the highest barrier corresponds to the largest diameter. Therefore, in contrast to what can be seen at 1 mM, it appears that at 100 mM a pitted nanotopography would reduce the likelihood of adhesion of a 10 μm sphere. This is very interesting, since it can be connected to previous reports of AFM force-distance measurements of the interaction between ZnS particles: Toikka *et al.* (Toikka, 1996) showed that in 20 mM aqueous electrolyte the roughness seemed to decrease the influence of the van der Waals attraction, which became undetectable; on the other hand, they showed that the roughness on the particles was made not only by crystallites (size 50 nm), but by cracks and pores. This seems to support the prediction that at high molarity, a hollow surface topography causes the interparticle interaction to become more repulsive. Lowering the *height/depth* of the 150-nm-diameter asperities (pits and pillars), from 150 nm to 75 nm at 1 mM, makes the interaction energy more attractive. This is probably due to the the van der Waals attraction by the bottom surface (on both pits and pillars), the intensity of which increases inversely with asperity height/depth (because the particle can get closer to the bottom surface). Hoek *et al.* (Hoek, 2003) observed that particles on a rough surface in 10 mM 1:1 aqueous electrolyte were attracted and repelled more strongly by the peaks, rather than by the "valleys"; nevertheless, they suggested that if the asperities are comparable in dimensions to the probe particle, this may be funneled towards adhesion in the low-energy "valley" regions of the surface. Even though the dimensions of the probe used in this SEI simulation are big compared to

the topography, my calculations predict that at 100 mM, a 10 μm sphere approaching the “valley” between hemispherical pillars 150d150h would be attracted towards adhesion at the primary minimum. The same would happen on the smaller roughness 20d20h. From these results, no conclusion can be drawn regarding the influence of the sphere position on the strength of adhesion with a nanopatterned surface; however, particle adhesion on a rough surface is expected to be stronger on the “valleys” between asperities (Bowen, 2000, Gotzinger, 2004).

At 100 mM, the 20d20h nano-pits yield little energy difference with the flat control. Inversely, the 20d20h nano-pillars make most of the surface inaccessible to the sphere at distances where the repulsion becomes steep, so that the attraction dominates, yielding a purely attractive energy that would drive the sphere towards adhesion at the primary minimum. The tops of the pillars provide a very small repulsion, even smaller when their radius of curvature decreases. The influence of hemispherical protrusions of these dimensions on the interaction energy between a rough sphere and a plate has been modelled by Suresh *et al.* (Suresh, 1996) As shown in Figure 35-Figure 36, my results are consistent with Suresh’s previous simulations, where they found that hemispherical protrusions decrease the energy barriers and the depth of the secondary minima. However, their statement that the secondary minima are pushed to further distances cannot be generalised: when Suresh’s model was applied to my simulated conditions, and when the origin of the curves was chosen according to Figure 31, the results from the two methods are coherent and no significant minima shift is visible. Suresh’s predicted energy barriers are higher than calculated by SEI, however the latter should be more accurate at short distances because it is neither based on the DA, nor on the weak overlap approximation for the double-layer potential (eq 8), unlike Suresh’s calculations which for those reasons are valid at large separation distances only.

In conclusion, it appears that for these submicrometric patterns, the variation of asperity diameter is the most influential parameter upon the energy of interaction with a microsphere. However, the scale of the topography is also an important factor, as demonstrated by the potential energy of the smallest asperities 20d20h with the sphere. Another determining parameter is the shape of the topography, since the calculations demonstrate that the radius of curvature of the tops of the pillars have a dramatic effect on the height of the energy barriers. Although retardation effects and non-DLVO forces have not been taken into account in this work, these results provide some understanding in the effect of nanopatterning of a silica plate on its interfacial energy of interaction with a microsphere. Since the dimensions of the patterns are of utmost importance, this work should be followed up by a methodical investigation of the influence of shape and aspect ratio of protruding asperities on the interaction energy with spheres of different diameters, for different dimensions and scales of the topography starting from orders of 10 nm into the micron range. This should include the study of the effect of ionic strength on the energy barrier between a pitted surface and colloids of different sizes, for it could be of interest in the field of fouling prevention.

3.7 Conclusion

So far most attempts at modelling the DLVO interaction between rough surfaces has considered protruding asperities, mainly because the different models were based on the Derjaguin approximation. The SEI allows the modelling of hollow topography, and to my knowledge this is the first consistent attempt to model the potential energy of interaction between a sphere and a surface with depressions (pits) of different dimensions.

The present SEI simulations are coherent with previous calculations and experimental observations that protruding roughness (nano-pillars) decreases the energy barrier and the depth of the secondary minima of the interaction energy: it follows that a nano-pillared surface will greatly enhance the adhesion of particles onto it, even more so when the tops of the pillars are hemispherical rather than flat. The changes induced by the nano-pits were much less significant: generally, while the secondary minima are only slightly affected by changes between pitted and pillared topography, the energy barrier is strikingly decreased when the asperities are protruding rather than hollow. Interestingly though, the nano-pits at 100 mM were predicted to increase the energy barrier against adhesive contact, which can be related to previous experimental observations (Toikka, 1996), and could have useful implications in the context of fouling prevention.

The geometrical characteristics of the pattern are important: with the dimensions used in my simulation, the height variation yielded a small difference in energy, whereas the changes in diameter were a determining factor. The position of the sphere axis had a strong importance on nano-pillars at 100 mM: a sphere approaching a pillared surface on the “valleys” between protrusions would be attracted towards the primary minimum.

Future work should clearly involve the verification of this model by AFM colloid-probe measurements on nano-structured silicon plates.

4 Cell reaction to nano-pillars

In this chapter, the behaviour of human fibroblasts, mouse endothelial cells and rat osteoblasts on PCL nano-pillars was investigated. It is shown how the nano-pillars inhibited the proliferation of human fibroblasts, while favouring the formation of a close-packed monolayer of endothelial cells. A possible synergistic role for air-trapping and surface area reduction at the interface is discussed.

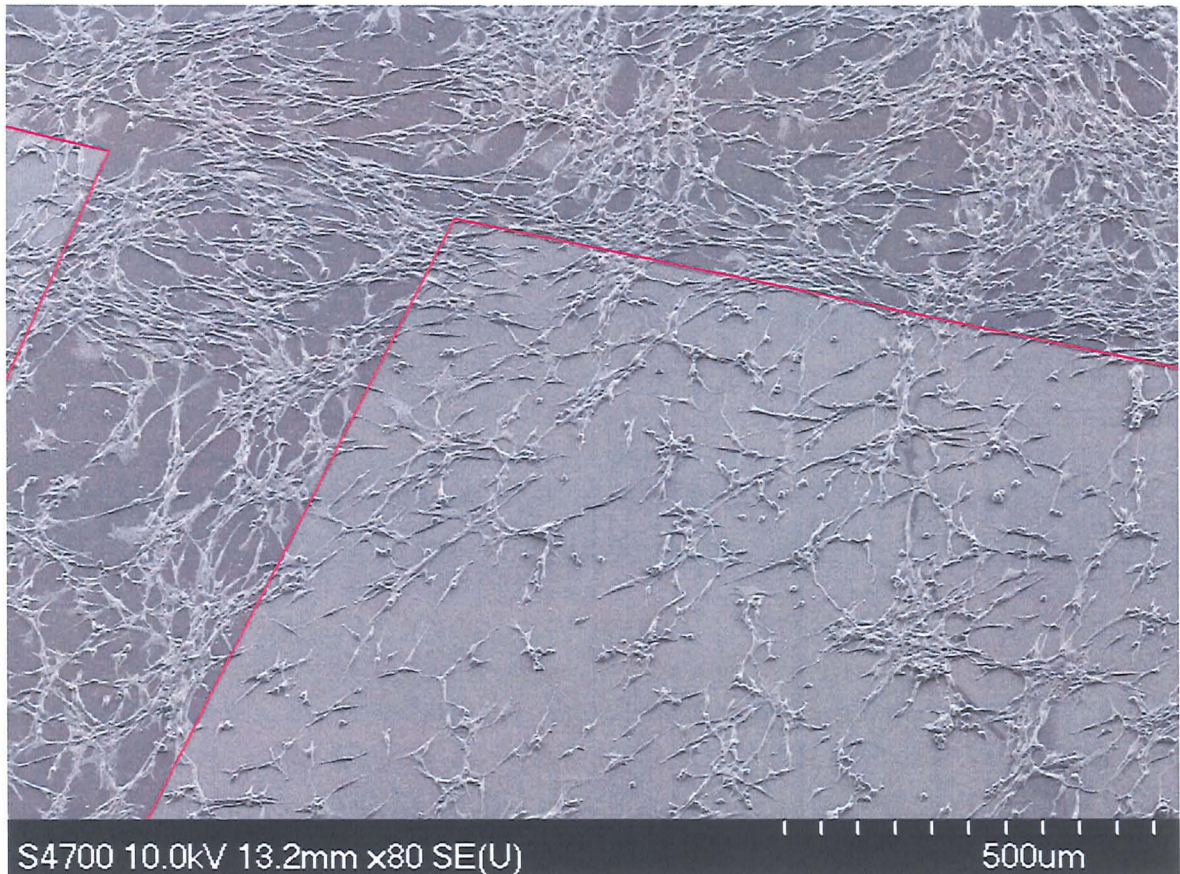


Figure 37. SEM micrograph of BHK21 cells on squares of irregular nano-pillars (lighter areas within the red lines) after 96 h. The cells can be seen to be more confluent outside the nano-patterns. The image corresponds to the results discussed in Part II (4.7.3).

4.1 Introduction

Cell adhesion on nanopatterned surfaces has raised great interest in recent years. Nano-structures (i.e. surface topographies with features of dimensions 0.001-1 μm) are much smaller than cells normally measuring 5-40 μm . Understanding why and how the behaviour of cells is modified by such patterns has great potential for both clinical applications and fundamental biology. Nature seems to make extensive use of nano-structured surfaces to achieve specific functions, such as reduction of bio-fouling (Baum, 2001), structural colour (Gu, 2003), water-repellency (Barthloot, 1997), mechanical stability (Watson, 2004), and tissue scaffolding (Goodman, 1996). Goodman *et al.* (Goodman, 1996) replicated the sub-endothelial matrix of the arteries of some mammalian species; they showed that the matrix has a complex topography at the micro- and nano- scale, and that endothelial cells cultured on these patterns not only spread faster, but at confluence also more closely resembled the cells as they appear *in vivo* (less spread, more rounded and thicker).

It is known that surface roughness has a marked effect on cell culture. Recently, two studies by Wieland *et al.* (Wieland, 2002, Wieland, 2005) investigated the influence of various surface treatments on the roughness of titanium (Ti) dental and orthopedic implants, showing that at constant surface chemistry, human fibroblasts and rat osteoblasts had increasingly thicker cell bodies on surfaces with increasing roughness (rms 0.08-7.64 μm). Since the cells in the same study were also proven to have constant volume, it can be inferred that their spreading area decreased with increasing roughness. Also, in the same paper the osteoblasts were seen to form more focal adhesions on the smoothest surface, a finding also supported by Meredith *et al.* (Meredith, 2005). Turner *et al.* (Turner, 1997) cultured astrocytes on RIE-fabricated nano-columnar structures ("silicon grass", diameter ca. 57 nm, height ca. 230 nm, surface density 137 μm^{-2}), and wet-etched surfaces (depression width 100-250 nm, average peak-to-valley distance 115 nm, surface density 27 μm^{-2}) on neighbouring micrometric stripes. They showed that immortalized cells grew better on the wet-etched stripes, while the primary astrocytes preferred the silicon grass.

Curtis *et al.* (Curtis, 2001) studied the reaction of rat epitenon fibroblasts⁴ on a square lattice of EBL-fabricated silicon nano-pillars (diameter 50 nm, spacing 300 nm); the number of cells on the nanopattern was significantly smaller than on the control. Gallagher *et al.* (Gallagher, 2002) embossed silicon nano-pillars in poly- ϵ -caprolactone, thus obtaining nano-pits (diameter 216 nm, height 100 nm, pitch 300 nm). By coating the substrates with Poly-L-Lysine and culturing rat epitenon fibroblasts on coated and uncoated samples, they concluded that surface chemistry did not

⁴ a fibroblastic cell line extracted from the Epitenon sheath that surrounds the flexor tendon of Sprague-Dawley rats.

override the effect of topography: the cells on the nanopattern always had smaller focal adhesions and smaller spreading area. Later in his thesis (Gallagher, 2003), Gallagher reported that the epitenon cells on PCL, polyurethane and poly-carbonate nano-pits selectively migrated outside the nanopatterned area, and did not proliferate on it. He also observed faster cell locomotion and the formation of cell clusters on the nano-pits, and claimed that these phenomena were neither polymer-dependent nor cell-dependent, having observed it with mouse macrophages, MDCK, HGTFN endothelial cells and rat epitenon cells. Dalby *et al.* (Dalby, 2002a, Dalby, 2002b) and Riehle *et al.* (Riehle, 2003) studied the effect of 13-nm-high polymer-demixed nanoislands on, respectively, human endothelial cells, human fibroblasts and rat calvaria bone cells. It was shown that the nano-islands increased both endothelial and fibroblast spreading; furthermore, since in fibroblasts cell spreading is a *conditio sine qua non* for proliferation (Meredith, 1993), the up-regulation of the genes required for cell proliferation confirmed the morphological observations. No significant change in the behaviour of bone cells was detected; this was because the surface chemistry of the nano-islands did not support bone cell growth. Dalby *et al.* (Dalby, 2004) also cultured human fibroblasts on nano-columns (diameter 100 nm, height 160 nm, spacing \approx 230 nm), showing that after 3 h the number of cells on the flat control and on the nanopattern was not significantly different, even though the cells were significantly more spread on the former. They also observed that for cells on the nano-columns, the Actin cytoskeleton was less organised, and the focal adhesions were smaller and very faint compared to the ones on the flat control. Furthermore, TEM imaging revealed that the cell membrane did not form adhesive contacts with the bottom surface between nano-columns. This last observation has recently been revisited by Curtis *et al.* (Curtis, 2005) who showed that the cell membrane could bend between nano-pillars. However their study did not prove the formation of cell adhesions with the bottom surface.

The observed reactions of cells to nanotopography, especially pits and pillars, has raised several questions concerning the nature of these interactions, since the sizes of the surface features are at least 2 orders of magnitude smaller than the cells. Mechanical restriction is not a possibility at this scale (while it is at the micro-scale); current hypotheses include a change in protein adsorption or conformation due to the surface patterns, or simply a reduction in the surface area available for focal contact formation, assuming that, as Dalby observed (Dalby, 2004), the cells do not adhere to the bottom surface. Very few studies have been concerned with the investigation of protein adsorption and conformation on nano-structured surfaces. Webster *et al.* (Webster, 2000) showed that nanophase ceramics adsorbed significantly greater quantities of vitronectin, which in turn enhanced osteoblast adhesion. On the same substrates fibroblast adhesion decreased and endothelial adhesion was similar to the flat control. However, the authors did not seek information regarding the conformation and bio-activity of the proteins. Riedel *et al.* (Riedel, 2001) fabricated germanium nanopyramids ($60 \times 60 \text{ nm}^2 \times 15 \text{ nm}$) and adsorbed γ -globulin (160 kD) on these

substrates; they observed that while more protein was adsorbed on a higher density of nano-pyramids, protein activity decreased, along with the viability of cultured monocytes U937; yet, the study did not yield information regarding the conformation of the protein. Denis *et al.* (Denis, 2002) observed that the amount of collagen on a nanotextured substrate and on the flat control was the same, but that the supramolecular organisation was inhibited. However, the size of collagen fibrils (up to 600 nm) was much bigger than the nanotopography (75 nm), thus the underlying dotlike protrusions could have been concealed by the protein.

The role of focal contacts in cell adhesion and signalling has already been outlined in the main introduction. This raises questions with regard to the minimum surface area required by the cells to form adhesion sites. Massia *et al.* (Massia, 1991) cultured human fibroblasts on RGD-coated substrates (covalently attached) and concluded that a minimum peptide-to-peptide spacing of 440 nm and of 140 nm is necessary for cell spreading and for focal contact formation, respectively. However, Maheshwari *et al.* (Maheshwari, 2000) proved that nano-scale clustering of the ligands significantly reduced the average ligand density required to support cell migration. In fact, non-clustered Integrin ligands support cell attachment but not full spreading. They suggested that there exists a minimum size and number of Integrin clusters required in order to achieve significant values of cell adhesion and migration. In a more recent study, Arnold *et al.* (Arnold, 2004) have been able to control the position of single RGD peptides by arranging them in hexagonal close-packed templates tunable between 28-120 nm. By varying their spacing, they saw that a peptide separation >73 nm limited cell adhesion and spreading, and they attributed the phenomenon to restricted ligand clustering. In conclusion, the formation of adequate focal adhesions to support cell spreading is linked to the size and ligand density of the adhesion sites. Thus, assuming that the cells adhere only to the top of some nanotopographies (Dalby, 2004), the nanopatterning of biomaterials could reduce the area available for adhesion formation, resulting in decreased cell attachment, spreading and inhibited proliferation.

Finally, recent evidence shows that nanopatterned materials with contact angle in the range 65° - 90° can trap air in their surface asperities (see 2.5.4, and Abdelsalam *et al.* (Abdelsalam, 2005)). The presence of air-bubbles on the surface could hinder the adsorption of proteins on the surface (Wu, 2005), and/or influence the molecular mechanisms that underlie cell adhesion.

This work was aimed at elucidating by which mechanisms different types of mammalian cells (human fibroblasts, mouse endothelial cells, rat osteoblasts and baby hamster kidney cells) react to nanopatterns. In Part I of this study, cell reaction to regular nano-pillars (diameter 170 nm, height 131 nm) was investigated. By molding PCL against a nanopitted hydrophobic master, a large number of samples could be replicated. After analysing cell coverage, morphology and focal contact formation of the three cell types on the nanopatterned PCL replicas, the samples were gold-

coated and the study proceeded with comparing the influence of the two equally patterned materials on fibroblasts. The influence of protein-coating on the surface coverage of fibroblasts and endothelial cells is also shown. The second part of the study (Part II) shows a set of limited but interesting results obtained by culturing cells on irregular nano-pillars, which were fabricated by replicating PCL on a hydrophilic pitted master.

Part I. Cells on regular nano-pillars

4.2 Materials and Methods. I.

4.2.1 Fabrication of the nanopatterns

4.2.1.1 Fabrication and replication

In Chapter 1, it was explained how after measuring the contact angle on the nanopatterned silicon masters, these dies were replicated in poly- ϵ -caprolactone (PCL) by “thumb-embossing” (2.2.3). These same PCL replicas are used in this chapter for cell adhesion experiments. Briefly, nanopatterns of different morphology and dimensions (nano-pits and nano-pillars) were fabricated in silicon wafers, and made hydrophobic by octadecyltrichlorosilane (OTS) coating. PCL sheets were embossed onto them by melting the polymer on the master at 85°C, and then manually pressing a glass-slide on it. The nomenclature of the nanopatterns in this chapter will be the same defined in Chapter 1 (page 28). All the silicon masters were fabricated by Dr K. Seunarine.

However in this study, only the pillared PCL H90-r replicas were used for the cell culture: the reason for this choice is clear from Figure 40 and is discussed in 4.3. Therefore, throughout this chapter I will refer to this pattern only, unless otherwise specified.

For time-lapse video microscopy only, the nano-pillars H90-r were replicated in poly-carbonate (PC), because the samples needed to be transparent for filming. The embossing procedure is the same as for PCL, except that the melting temperature is 140°C, hence the glass slide was pressed with a pair of forceps; the polymer was air-cooled after embossing.

The diameter of the H90-r pillars were measured with ImageJ (Rasband, 1997-2005) from SEM images. Their height was measured by Atomic Force Microscopy in tapping mode (Nanoscope III, Digital Instruments).

4.2.1.2 Sterilisation

After embossing, the PCL samples were sterilised by immersing them in 70% ethanol (BDH). Then they were rinsed in copious amounts of RO water and finally stored in RO water at 4°C for up to 7 days. Alternatively, both sides of the samples were sterilised by exposing them to the collimated light of a mercury vapour arc lamp (100 W) for 5 min at a distance of 30 cm. Prior to cell seeding, the samples were rinsed in HEPES Saline.

4.2.1.3 Protein coating and gold coating

Fibronectin coating. The sterilised samples were incubated overnight in 10 μ g/ml of a Fibronectin solution (0.1% from human plasma, Sigma, 440-500 KDa) in PBS at 4°C, then washed twice with PBS, and rinsed with HEPES saline prior to cell seeding.

Poly-L-Lysine (PLL) coating. The sterilised samples were incubated for 1 h in 100 µg/ml solution in water (0.01%, Sigma, 150-300 KDa) at room temperature, then washed twice with sterile RO water, and rinsed with HEPES saline prior to seeding. For visualisation of the coating by fluorescence microscopy, FITC-labelled Poly-L-Lysine (Sigma, 30-70 KDa) was used.

Gold-palladium (AuPd) coating. The samples were sputter-coated with 10 nm of gold-palladium in a sputter coater (Emscope, Ashford, UK). Immediately after coating the samples were immersed and kept in RO water, to avoid contact with atmospheric contaminants. Thus their hydrophilicity was preserved.

4.2.2 Cell culture

Three different types of cells were cultured on the nanopattern: 1) Infinity™ telomerase immortalized primary human fibroblasts (hTERT-BJ1, Clonetechnologies Laboratories Inc, USA), 2) Mouse SV129 brain endothelioma (b.End3, ECACC) and 3) Rat calvaria bone cells from primary culture. Details of media and solutions can be found in Chapter 8.

4.2.2.1 Passage of hTERT and B.End3

The cells were expanded in 25 cm² tissue culture flasks (Corning Incorporated, USA) at 37°C with a 5% CO₂ atmosphere until confluence, with medium changes every three days. Before reaching confluence, the flasks were washed twice with HEPES Saline (to rinse away the medium), then twice with versene (to break the cell-cell junctions). The flasks were then incubated in 5 ml of 0.01% (v/w) trypsin (Gibco) in versene until the cells appeared rounded, in order to detach them from the flasks. Once the cells detached, 5 ml of DMEM complete growth medium were added to neutralize trypsin activity. The suspension was transferred into a centrifuge tube (Sterilin, UK) and centrifuged for 5 min at 1500 rpm. The resultant pellet was resuspended in 1 ml of culture medium with a hypodermic needle (1.2X40, BD Microlance 3, Ireland) for cell counting (Improved Neubauer haemocytometer, BS.748, Hawksley). The cell suspension was then diluted and split into three 25 cm² tissue culture flasks for further expansion or used for experimental purposes.

4.2.2.2 Primary culture of bone cells

Rat calvaria bone cells were isolated by Anne Macintosh from the bony calvariae of 4 neonatal rats (1-5 days p.n.) by serial digestion (agitated for 20 min at 37°C) with collagenase type I (1 mg/ml) in DMEM/Hams F10 mixture (1:1). After sedimentation the cells were seeded into flasks and fed every 3rd day with DMEM (10% calf serum) supplemented with 0.003 mg/ml ascorbic acid. After reaching confluence, the cells were isolated by trypsinisation and seeded at the desired density onto the substrates.

4.2.2.3 Cell seeding

4.2.2.3.1 hTERT and B.End3

For seeding on the PCL samples, the cells were resuspended in DMEM at a density of $1-1.5 \times 10^4$ cells/ml, and 4 ml of suspension were placed on each sample, yielding a total of $4-6 \times 10^4$ cells per sample. For each time point or assay, 2 samples were seeded in a 6-well plate.

4.2.2.3.2 Bone cells

For seeding on the PCL samples, the cells were resuspended in DMEM at a density of $1-1.5 \times 10^4$ cells/ml, and 4 ml of suspension were added into each well, yielding a total of $4-6 \times 10^4$ cells per well. For each time point or assay, 2 samples were seeded in a 6-well plate.

4.2.2.4 Fixation

To fix the cells, the samples were rinsed with PBS at 37°C, incubated for 15 min in 4% formaldehyde/PBS (with 2% Sucrose) at 37°C, and stored in PBS at 4°C.

4.2.3 Cell staining and Imaging

The cells could be visualized by ordinary phase-contrast microscopy, but it was desirable to stain the whole cell body for cell morphology analysis. The cell cytoskeleton is transparent in standard light and electron microscope preparations, and is therefore “invisible”. By immunofluorescence staining it was possible to attach fluorescently-labeled antibodies to specific molecules, thus revealing the desired cell component. The cell surface could be seen by Scanning Electron Microscopy.

4.2.3.1 Cell body staining

In order to visualize the whole cells for cell counts, cell area and surface coverage analysis, the fixed cells were stained with Coomassie Blue solution for 15 min, then rinsed in PBS until the excess dye was washed away; the cells were then counted under a Zeiss Axiovert 25 at X5 magnification. A camera (Scion Corporation) transmitted the images to a PC. Images of the microscope field were captured with Visicapture 1.1 (Scion Corporation). Images of the whole replicas after Coomassie staining were acquired with a Nikon D1 camera (objective AF Nikkor, 35-70 mm).

4.2.3.2 Time-lapse video microscopy

HTERT cells were cultured on PLL-coated poly-carbonate replicas (5×10^4 cells in 4 ml DMEM), and filmed with a time-lapse video recorder (Panasonic) by capturing 1 frame/min for 96 h under a Zeiss Axiovert 25 in phase contrast. The movies were digitized with a MacOSX.

4.2.3.3 Immunofluorescence: Actin/Vinculin Staining

The cells were stained simultaneously for F-Actin using fluorescent Phalloidin and for Vinculin using antibodies. After fixation, the cell membrane was permeabilised by washing with PBS and a permeabilising buffer for 5 min at 4°C; permeabilisation was blocked by adding 1% BSA/PBS for 5 min at 37°C. After removing the BSA, 200 µl of primary anti-Vinculin/Phalloidin solution (see Note below) were added on each sample, and incubated for 1 h at 37°C. The cells were washed in 0.5% Tween 20/PBS a few times, then the secondary antibody (Alexa –588 donkey anti-mouse, stock 1:100 in BLK, Molecular Probes) was added. The samples were washed in 0.5% Tween 20 a few times, then mounted on a glass slide in a mounting medium that contained DAPI, a fluorescent nuclear stain. After a few minutes for the nuclear stain to work, the cells could be viewed by fluorescence microscopy (Zeiss Axiovert 200M at X40 magnification).

[Note: *Preparation of the anti-Vinculin/Phalloidin solution.* First, the anti-Vinculin solution is prepared (1:150 in 1% BSA/PBS, Hvin1 monoclonal anti-human raised in mouse (IgG1), Sigma). Then, 10 µl oregon-green Phalloidin solution (1:50, Molecular Probes, Oregon) is added to 1 ml of anti-Vinculin solution].

4.2.3.4 Immunofluorescence: Actin/Fibronectin Staining

The cells were stained simultaneously for F-Actin using fluorescent Phalloidin and for Fibronectin using antibodies. After fixation, the cell membrane was permeabilised by washing with PBS and a permeabilising buffer (see 4.2.3.1) for 5 min at 4°C; permeabilisation was ended and unspecific binding sites blocked by adding 1% BSA/PBS for 5 min at 37°C. After removing the BSA, 200 µl of primary anti-Fibronectin/Phalloidin solution (see Note below) were added on each sample, and incubated for 1 h at 37°C. The cells were washed in 0.5% Tween 20/PBS a few times, then the secondary antibody (1:50 biotinylated anti-rabbit, Sigma) was added and the sample again incubated for 1 h at 37°C. The samples were washed in 0.5% Tween 20 a few times, then incubated in fluorescein-conjugated Streptavidin (1:50) for 30 min at 4°C. Finally, the samples were washed in 0.5% Tween 20 a few times, and mounted on a glass slide as described above. Samples were viewed by fluorescence microscopy (Zeiss Axiovert 200M) at X40 magnification.

[Note: *Preparation of the anti-Fibronectin/Phalloidin solution.* First, the anti-Fibronectin solution is prepared (1:100 in 1% BSA/PBS, rabbit anti-human Fibronectin polyclonal, Chemicon International). Then, 10 µl oregon-green Phalloidin (1:50, Molecular Probes, Oregon) is added to 1 ml of anti-Fibronectin solution].

4.2.3.5 Proliferation assay

BrdU (5-bromo-2-oxymethyluridine, CalBiochem) is a Thymidine analogue taken up by cells when they enter the S-phase, which is the phase of the cell cycle where DNA is replicated before mitosis,

indicating that the cells are proliferating. In order to allow direct visualisation of the proliferating hTERT, the cells were cultured for 72 h in DMEM, then incubated in BrdU-supplemented DMEM (see Note below) for 3 h. Afterward the cells were fixed as described in 4.2.2.4. After fixation, the cells were immunostained as in 4.2.3.1, except that the primary antibody in this case is anti-BrdU(1:100, 200 μ l/sample, Amersham Biosciences). After being mounted on a glass slide in DAPI-containing medium, the samples were viewed by fluorescence microscopy (Zeiss Axiovert 200M at X10 magnification).

[Note: Preparation of the BrdU-supplemented DMEM. A 1 mM stock solution of BrdU in HEPES Saline is prepared by dissolving 0.015 g of BrdU in 1 ml DMSO, then adding 49 ml of HEPES Saline. Subsequently, a 10 μ M solution of BrdU in DMEM is made up by adding 100 μ l of the BrdU/HEPES stock solution in 50 ml of DMEM. The medium was filter-sterilised prior to incubating with the cells].

4.2.3.6 Scanning Electron Microscopy

Prior to SEM imaging, the samples were processed by Margaret Mullin. The samples were fixed in 1.5% Gluteraldehyde (Sigma) in 0.1 M sodium cacodylate (Agar, UK) overnight at 4°C. After being washed in 0.1 M sodium cacodylate buffer, the cells were incubated in 1% Osmium Tetroxide in sodium cacodylate for 1 h at room temperature, and finally stored in sodium cacodylate buffer.

Before freeze-drying, the samples were rinsed in RO water. They were plunge-frozen into (33% pentane) / (66% propane) at -180°C, then freeze-dried overnight at -80°C at 10^{-6} bar (Balzers Freeze Drying Device FDU 001 with Turbo Pump). The next day the samples were warmed up at +20°C/h until their temperature reached 30°C. The samples were removed from the freeze-drier and sputter-coated with 20 nm of gold-palladium (Emscope, Ashford, UK), then imaged with a Hitachi S4700 at 10 kV.

4.2.4 Data analysis

4.2.4.1 From Coomassie-staining

To assess cell spreading, elongation and surface coverage, at least 20 images covering 1274×959 μ m² were acquired on each Coomassie-stained sample, of which at least 10 images of cells on the nanopatterned area, and at least 10 on the surrounding flat area.

Individual cells were counted on each image up to the 24 h time-point and their area and aspect ratio measured (ImagePro-Plus, 5.0.1.1.1, Media Cybernetics) on the patterned area (“pillars”) and on the surrounding flat area (“flat” control). Subsequently, the values from the 10 images were averaged to obtain the average cell number per unit area, cell area and aspect ratio, on the “Flat”

control and on the “Pillars” of each sample. In order to measure the surface coverage, Coomassie images were thresholded in ImageJ (Rasband, 1997-2005) and the average surface coverage was calculated as the average ratio of thresholded pixels over the total number of pixels per image, and averaged over all images (from “Pillars” and from “Flat”). The aspect ratio was calculated by ImagePro-Plus as the ratio of major and minor axis of the cell.

Since each time point was tested in duplicate, it was necessary to verify the significance of averaging values from equivalent groups of the two samples (e.g. average cell area on “pillars” 1 and average cell area on “pillars” 2). Since all the values were positively skewed, they were normalized by a \log_{10} . Then, unpaired *t*-Test (two-tailed assuming unequal variance) was used to compare equivalent groups of values and non-equivalent groups of values (e.g. number of cells on “flat” 1 and number of cells on “pillars” 1) from the two samples at the same time-point. Results of $p < 0.05$ were considered significant. The test confirmed that the difference between equivalent groups (e.g. flat1-flat2) was not significant, while it was significant between non-equivalent groups (e.g. flat1-pillars1, flat1-pillars2); hence, the equivalent values from the two samples could be averaged.

The cells started forming contacts after the 24 h time-point. This is known to alter individual cell behaviour (Curtis, 1962). For this reason, it was not meaningful to analyse individual cell areas and morphology after this point. Thus, only the surface coverage was measured for the 48 h to 96 h time-points.

4.2.4.2 From Vinculin staining

For each surface the number of Vinculin-containing cell-substrate adhesions (but not their area) was counted using immunofluorescent images of at least 20 cells. The number of adhesions in each cell was divided by the cell area in order to obtain the densities of adhesions; these values were averaged to yield the average number of adhesions per cell-unit-area on each surface. It should be noted that the counts included focal complexes, focal adhesions/contacts and fibrillar adhesions, since they all contain Vinculin.

4.2.4.3 From the proliferation assay

In order to analyse cell proliferation, at least 20 pictures per surface were captured of the BrdU/DAPI-stained samples. Subsequently, the total number of nuclei (DAPI stain) and the number of BrdU-stained nuclei (proliferating cells) on each image were counted (ImagePro-Plus, 5.0.1.1.1, Media Cybernetics). The total percentage of proliferating cells was obtained by summing over the values of all the pictures.

4.3 Initial results: why pillars and not pits

Figure 40 shows the SEM profiles of the nanofabricated masters (top row) and the SEM images of the corresponding PCL nanopatterns (middle row). In order to test which nanopattern had an evident effect on cell adhesion, PCL replicas were embossed from all the silicon masters. The replicas consisted of a 1 cm² nanopatterned square in the middle of the sample, surrounded by a flat area. The diameters of the nano-pits and nano-pillars is shown in Table 2, page 29. After sterilisation, hTERT cells were seeded on these patterns (1.5×10^4 cells/sample) for 96 h, then they were fixed and Coomassie-stained.

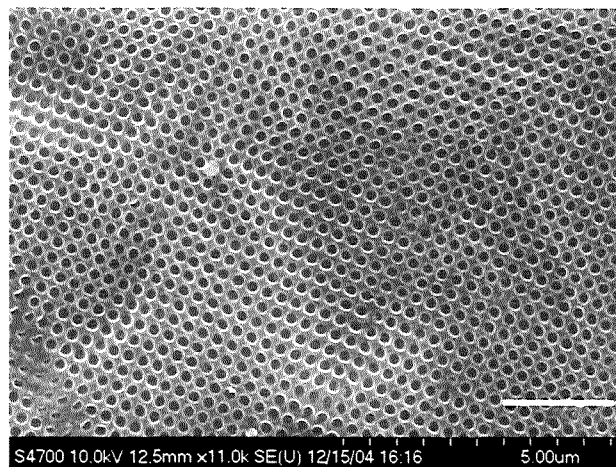


Figure 38. SEM image of the PCL nano-pits used by Gallagher *et al.* (Gallagher, 2003) this nanopattern was shown to inhibit cell attachment. The diameter of the pits (216 ± 10 nm) was measured by ImageJ (Rasband, 1997-2005) from this picture. Bar: 2 μ m.

It is obvious from Figure 40 that both nano-pillared replicas (H83-r and H90-r) had the similar effect of strongly reducing cell coverage at confluence, while the cell culture on the nano-pitted patterns (P21-r, P13-r and P12-r) resembled the one on the flat sample. Only on P21-r a very light reduction in cell coverage could be seen. This seems at first in contradiction with previous results (Gallagher, 2002, Casey, 1997), which showed that cell adhesion was significantly reduced by nano-pits. However on analysing by SEM a PCL sample embossed with the pattern used by Gallagher (Gallagher, 2003) it became evident that this difference could be due to the much larger diameter of the pits he used (216 ± 10 nm, Figure 38). This point will be discussed further in 4.5. It should also be noted that the experiment was repeated with both ethanol- and UV-sterilised replicas, with the same results.

Because H90-r and H83-r elicited the most obvious and therefore immediately interesting cell reaction, the results of cell counts, morphology, area and surface coverage of hTERT on sample H83-r (Figure 39) and sample H90-r (Figure 47) were gathered. Figure 39 shows these results for sample H83-r. Initially (1 h) there were significantly more cells on the pillared area than on the surrounding flat area. This is due to the seeding process, which often results in an increased number of cells in the middle of a large sample, due to user-induced and vibration-induced whirling of the medium in the Petri dish. The number of cells did not differ significantly from flat to pillared areas over 12 h, but from 6 h the area of the cells on the nano-pillars started to decrease, and this contributed to decreasing the surface coverage on the nano-pillars at 12 h. The cells on the

pillars also became more elongated from 6 h, and this was thought to be due to cell alignment to the stitching errors on the nanopillared area. The results on H83-r are very consistent with the parallel ones that were obtained on sample H90-r, which will be systematically presented throughout Part I of this chapter. Time restriction imposed a choice between H83-r and H90-r (diameter 196 ± 11 and 170 ± 14 , respectively), and the latter was chosen in order to carry on with a more thorough study. The reason for this choice is that H90-r consists of smaller nano-pillars, and an interesting question is how small a nanopattern can still affect cell behaviour. Hence, H90-r will be the only substratum used in Part I of this chapter, and all the results obtained on this pattern are presented next.

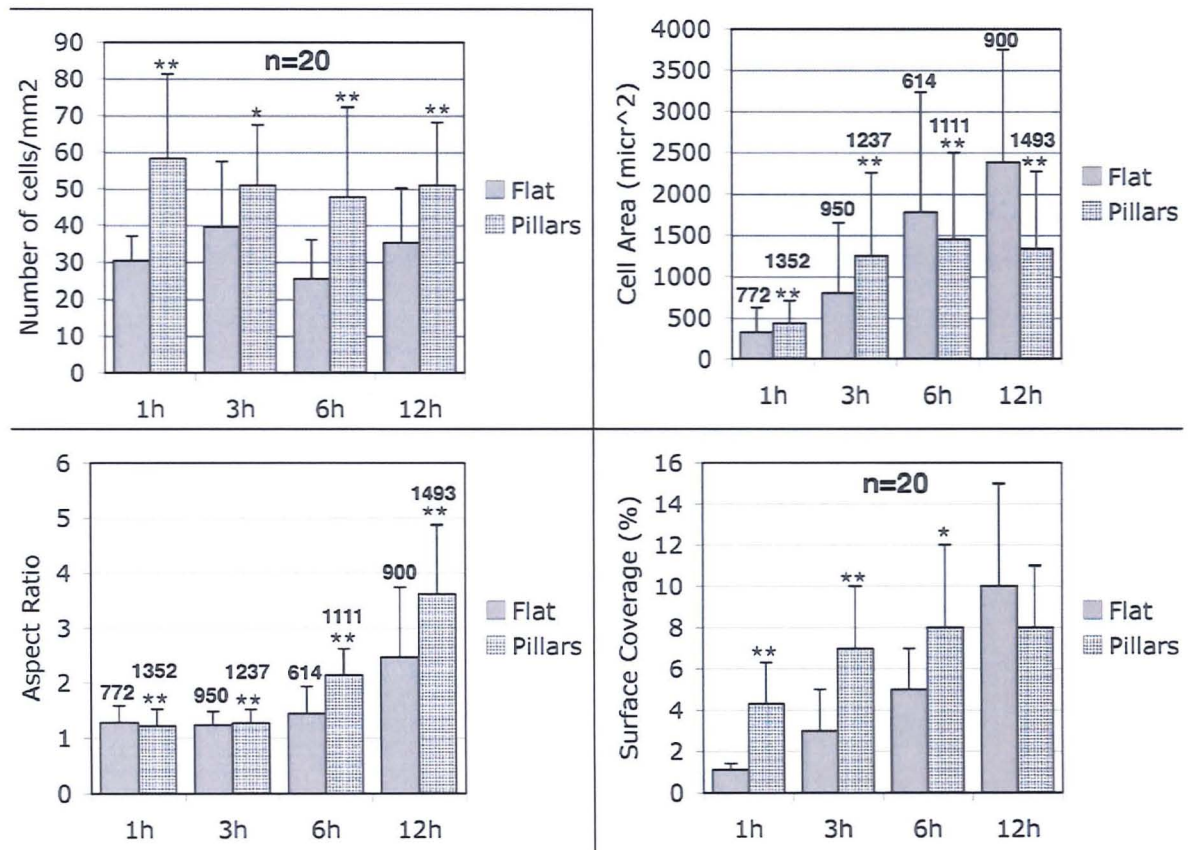


Figure 39. Average cell counts, cell area, aspect ratio and surface coverage of hTERT cells on nanopillared PCL (H83-r), fixed at different time points (up to 12 h) and stained with Coomassie Blue. Results are the mean \pm standard deviation. The total number of averaged values (n) is indicated above the error bars. * $p < 0.05$, ** $p < 0.01$ from unpaired t -Test (two-tailed assuming unequal variance). Over this period of time, the number of cells was always significantly higher on the nano-pillars. However their area started to decrease after 6 h, which contributed to the surface coverage reduction at 12 h. The aspect ratio data suggests that the cells aligned to the stitching errors on the patterned area.

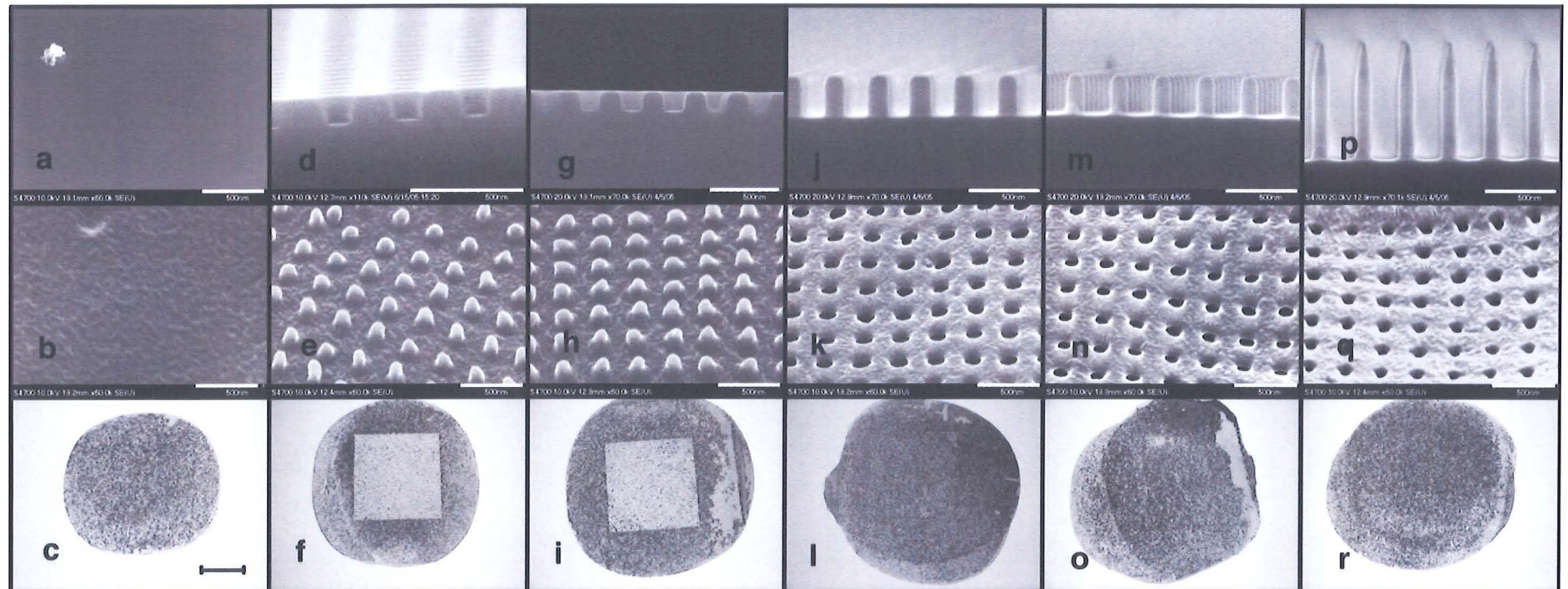


Figure 40. Top row: SEM profiles of the nanopatterned masters. Middle row: SEM images of the PCL replicas. Bottom row: Nikon pictures of the hTERT culture after Coomassie staining (1.5×10^4 cells/sample, fixed at 96 h), where dark areas indicate the presence of cells. a-c) flat PCL control; d-f) H90-r; g-i) H83-r; j-l) P21-r; m-o) P13-r; p-r) P12-r. The flat PCL was replicated from an OTS-coated flat silicon wafer. The “craters” on the PCL replica might be imprints of some OTS clumps. White scale bars (top and middle row): 500 nm. Black scale bar (bottom row): 5 mm.

4.4 Results. I.

4.4.1 Samples

4.4.1.1 Fabrication and replication

Figure 41 shows SEM micrographs of both the silicon master (a), PCL replica (b) and PC replica (c,d) of the H90 nanopattern. The PC replica were more regular than the PCL replica, probably because the polymer is stiffer. The pillars had base diameter 170 ± 14 nm, and height 131 ± 13 nm. The diameter was measured at the base of the pillars; the top diameter would be smaller. The AFM height measurement (Figure 42) was taken after ca. 200 PCL replicas were embossed.

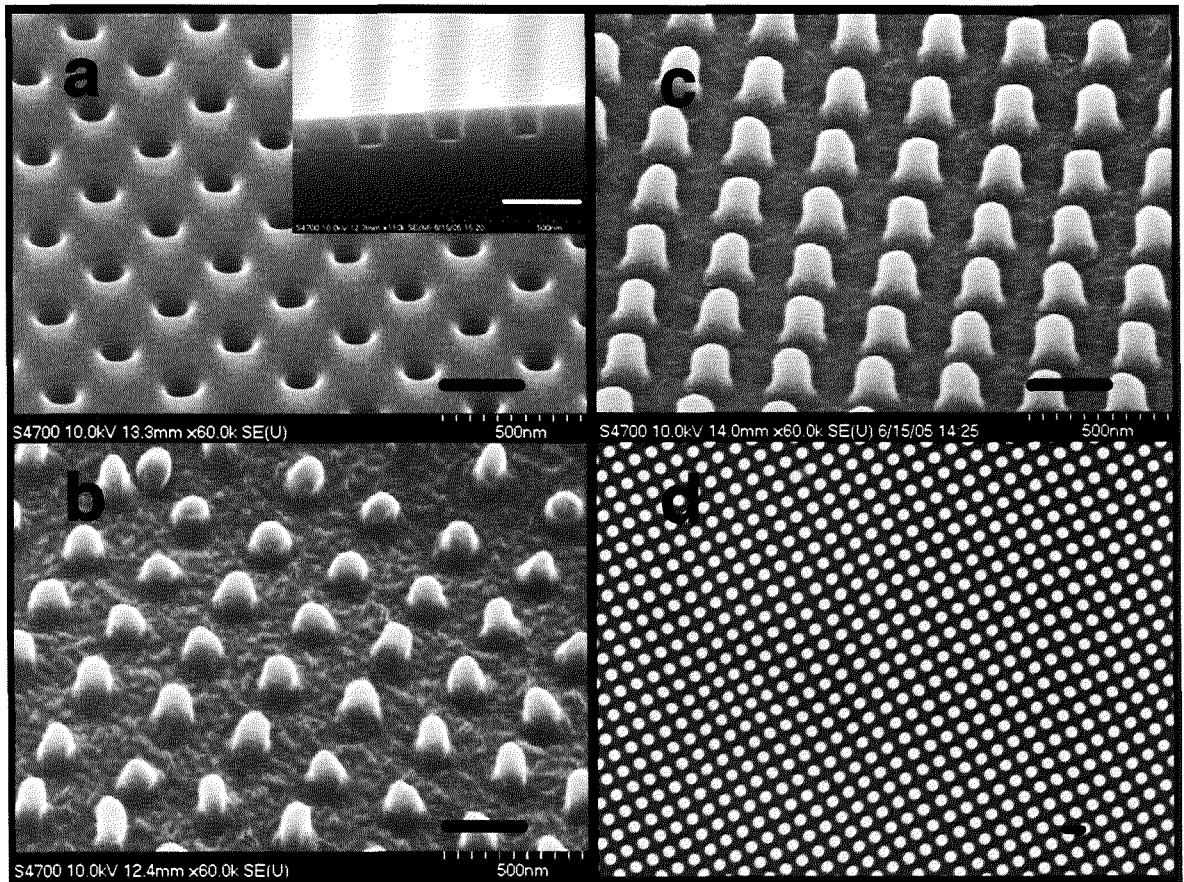


Figure 41. SEM micrographs of a) H90 silicon master, the insert shows its profile; b) H90-r (PCL replica of H90); c-d) PC replica of H90. Bars: 300 nm.

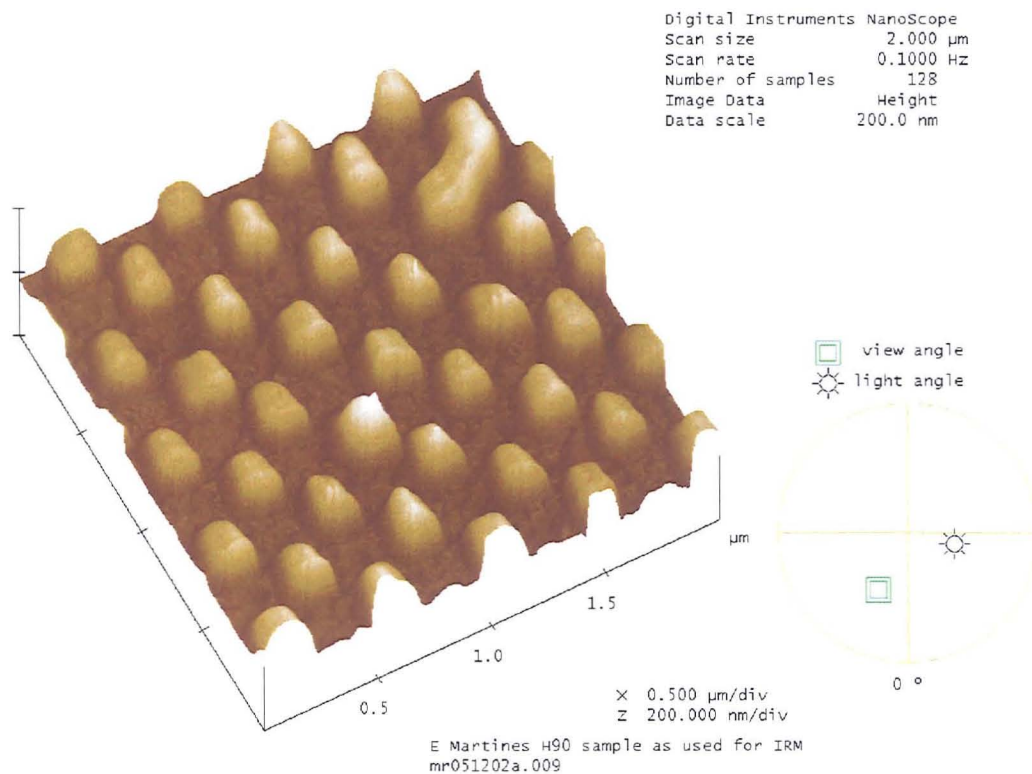


Figure 42. AFM reconstruction of the H90-r PCL pillars.

AFM scans ($10 \mu\text{m} \times 10 \mu\text{m}$) of the “flat” area surrounding the nano-pillars revealed an rms roughness of 5.3 nm (Figure 43).

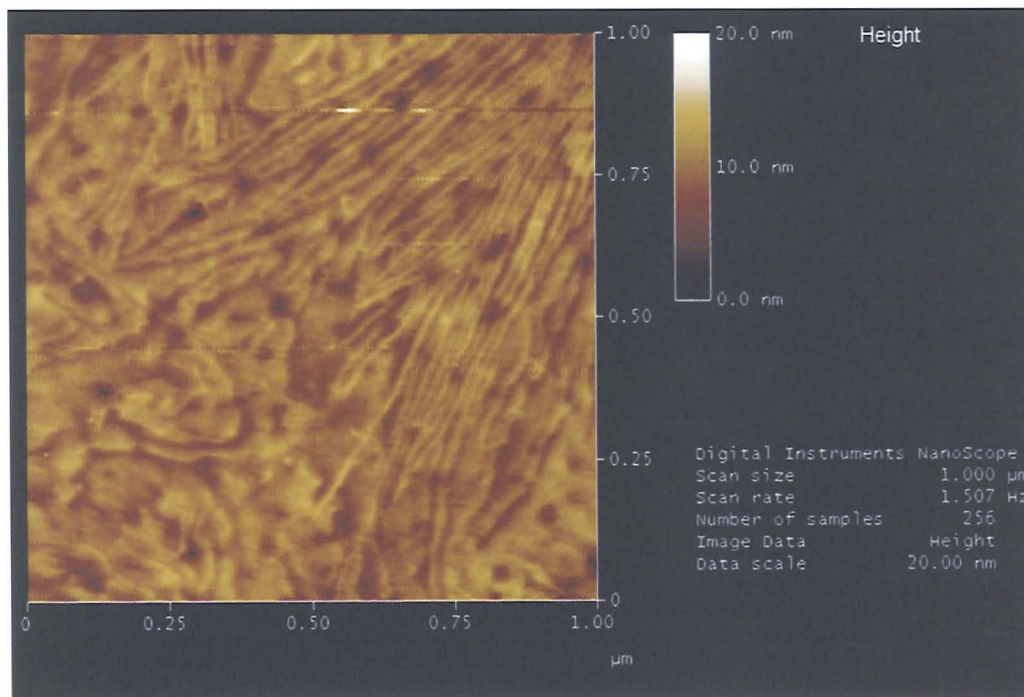


Figure 43. AFM image of “flat” PCL.

4.4.1.2 Fibronectin coating

Figure 44 shows the immunofluorescent staining of a Fibronectin-coated flat PCL substrate. The coating is not perfectly uniform, with sparse clusters; however, it appears that the protein covers most, if not all, the surface. Likewise, Figure 45 shows a Fibronectin-coated nanopillared PCL sample; the coating seems even less uniform, with more clusters. The presence of clusters could be due to polymerisation of the protein in the solution.

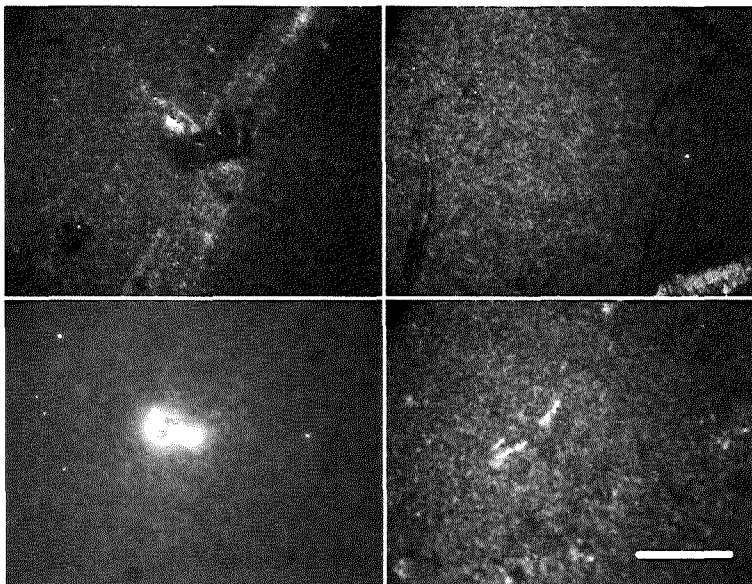


Figure 44. Immunofluorescence-stained Fibronectin-coated flat PCL. The four pictures belong to different flat areas around the nano-pillared square. Bar: 50 μm .

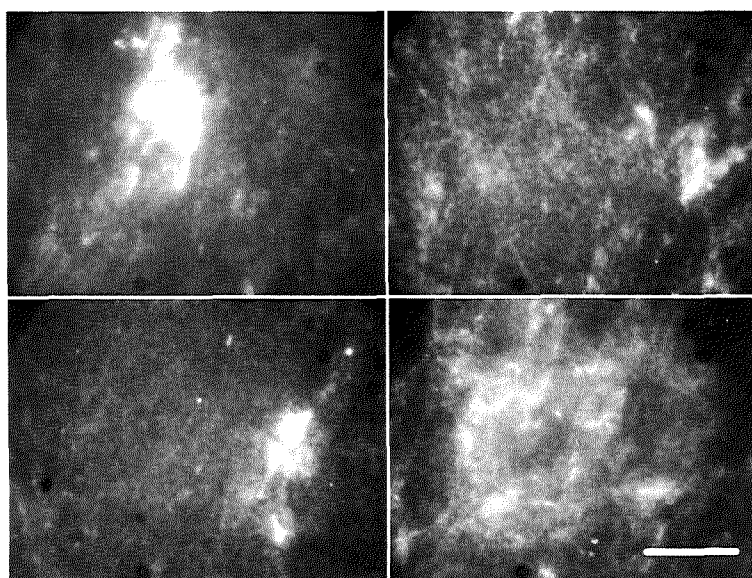


Figure 45. Immunofluorescence-stained Fibronectin-coated nanopillared PCL. The four pictures belong to different areas of the nano-pillared square. Bar: 50 μm .

4.4.1.3 Poly-L-Lysine coating

Imaging the Poly-L-Lysine coating was more difficult. Nonetheless, it was concluded from the fluorescent images that the molecule was present on the surface.

4.4.2 Cell counts, morphology and surface coverage

Initially, the three cell types were cultured on uncoated PCL H90-r replicas, and their reaction to the nanopatterns was revealed by cell body staining with Coomassie blue.

4.4.2.1 hTERT

Figure 47 shows the results of the average cell density, average cell area, average aspect ratio and average surface coverage of hTERT on both flat and nanopillared areas (“Flat” and “Pillars”) of sample H90-r. Up to 12 h, more cells can be found on the pillars, probably because the seeding procedure can yield a higher cell concentration in the middle of the pattern. This indicates that this surface should not be called “non-adhesive”, since the cells adhere equally well on both surfaces, if not better to the nano-pillars. The number of cells on Flat and Pillars does not follow any trend up to 24 h, possibly because the cells did not enter the cell cycle until then. However, from 6 h the cell area is significantly smaller on the “Pillars” than on the “Flat”. The aspect ratio of the cells on the nano-pillars seems to increase with time, but at 24 h there is no difference with the flat. Perhaps the most interesting result is in the surface coverage: on the flat PCL, the cell coverage increases exponentially with time, consequently to normal proliferation; on the nano-pillars though, from 24 h the coverage is significantly less than on the flat, and the difference at 96 h is striking (Figure 50). This supports the hypothesis that the cells entered the cycle at ca. 24 h, and that more cells did so on the flat area than on the pillars.

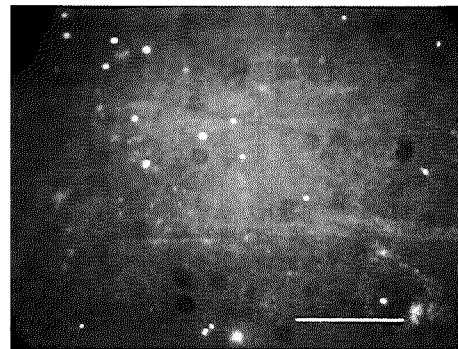


Figure 46. FITC-conjugated PLL coating on nanopillared PCL. Bar: 50 μm .

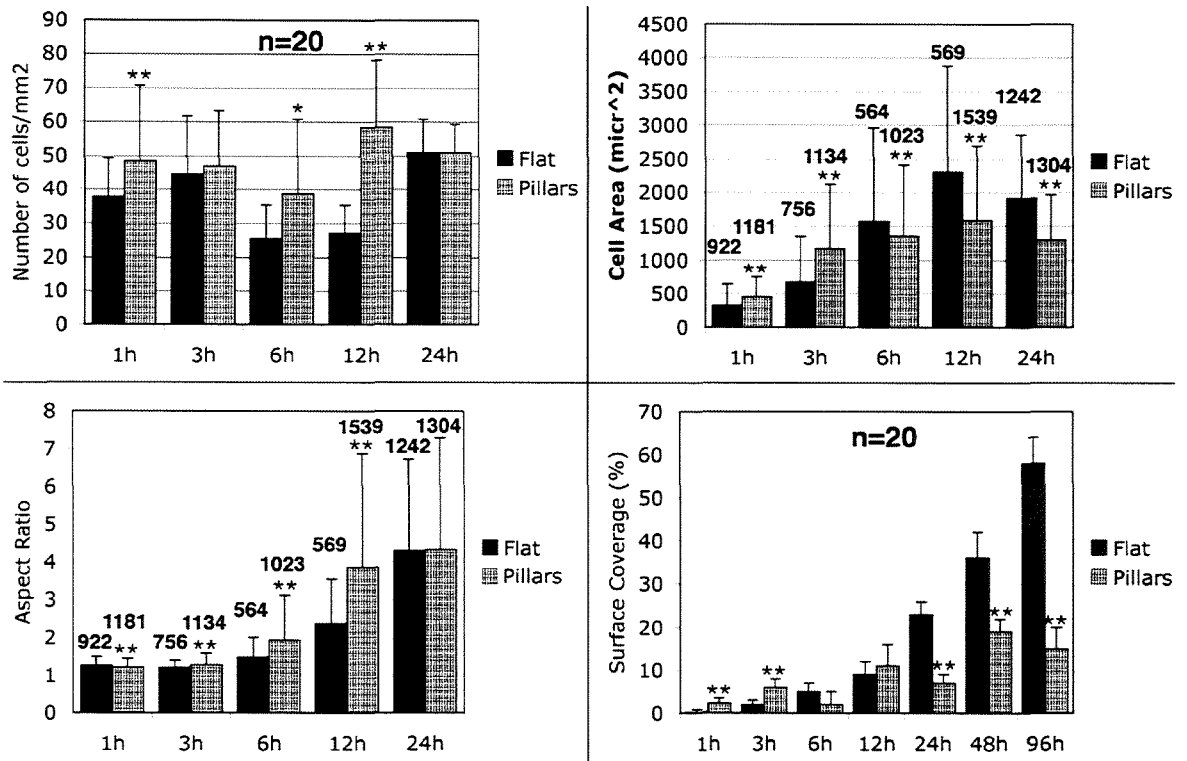


Figure 47. Average cell counts, cell area, aspect ratio and surface coverage of hTERT cells on nanopillared PCL (H90-r), fixed at different time points and stained with Coomassie Blue. Results are the mean \pm standard deviation. The total number of averaged values (n) is indicated above the error bars. * $p < 0.05$, ** $p < 0.01$ from unpaired t -test (two-tailed assuming unequal variance).

These results were corroborated by the direct observation of bright-field microscope images of the cells (Figure 48, Figure 49), and overview pictures of the whole samples (Figure 50). Both show that after 96 h, there are many more cells on the flat area than on the nano-pillars. Figure 48 shows how the initial spreading at 3 h is similar on the flat and the pillars. However, at 96 h there are many more cells on the flat area, and they are more spread than on the pillars. Besides, as shown in Figure 49c, the cells on the nano-pillars tend to aggregate in clusters. Figure 49 makes the previous description more evident, and also shows cell alignment along the edges of the nanopattern.

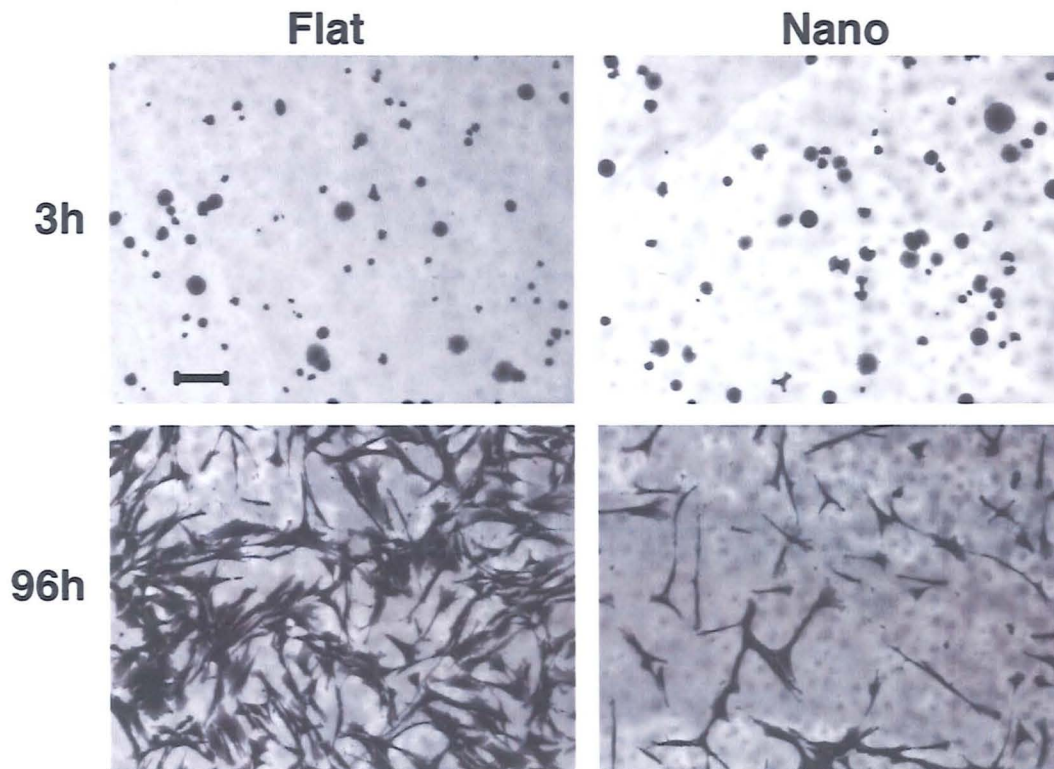


Figure 48. hTERT cells on H90-r PCL at 3 h and 96 h. The initial spreading and number of cells on flat and pillared areas are similar. However, at 96 h the cells are more spread and more confluent on the flat area surrounding the pillars. Scale bar: 100 μm .

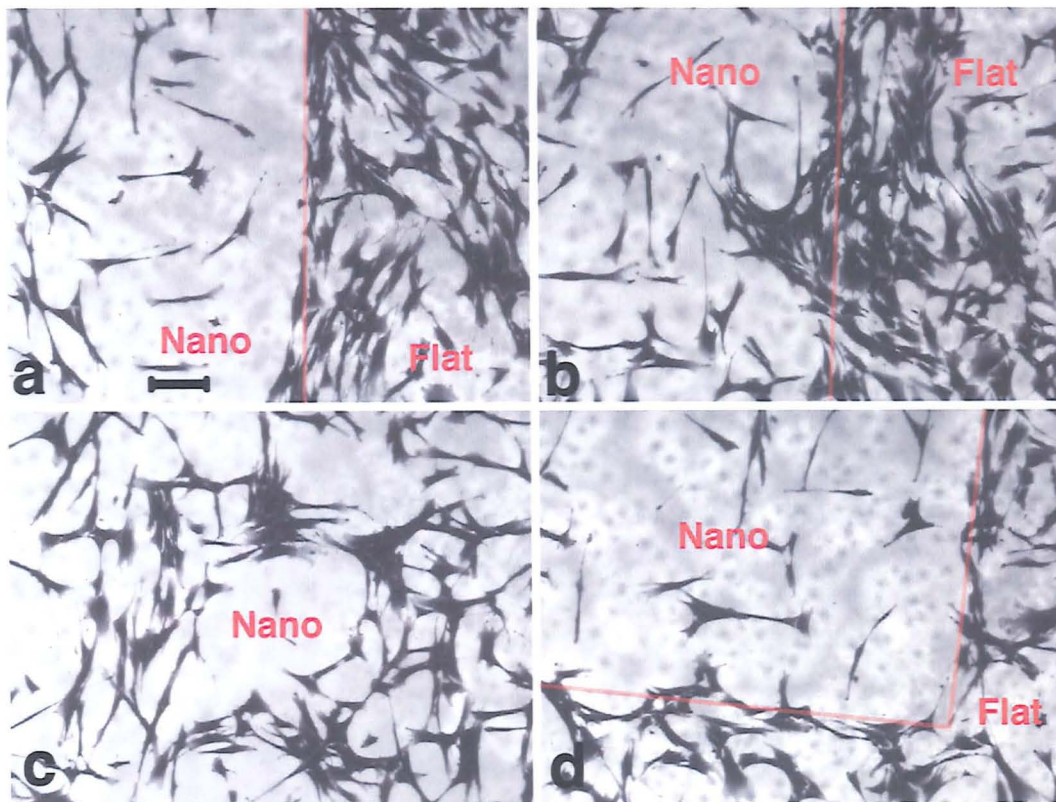


Figure 49. hTERT cells at 96 h on PCL H90-r. The edge-effect at the boundaries between patterned and flat areas is visible: the cells align to the edges. The formation of cell clusters on the nano-pillars is shown in c). Scale bar: 100 μm .

Figure 50 shows that at 96 h the surface coverage of the cells (blue area) is much higher on the area surrounding the nano-pillars.

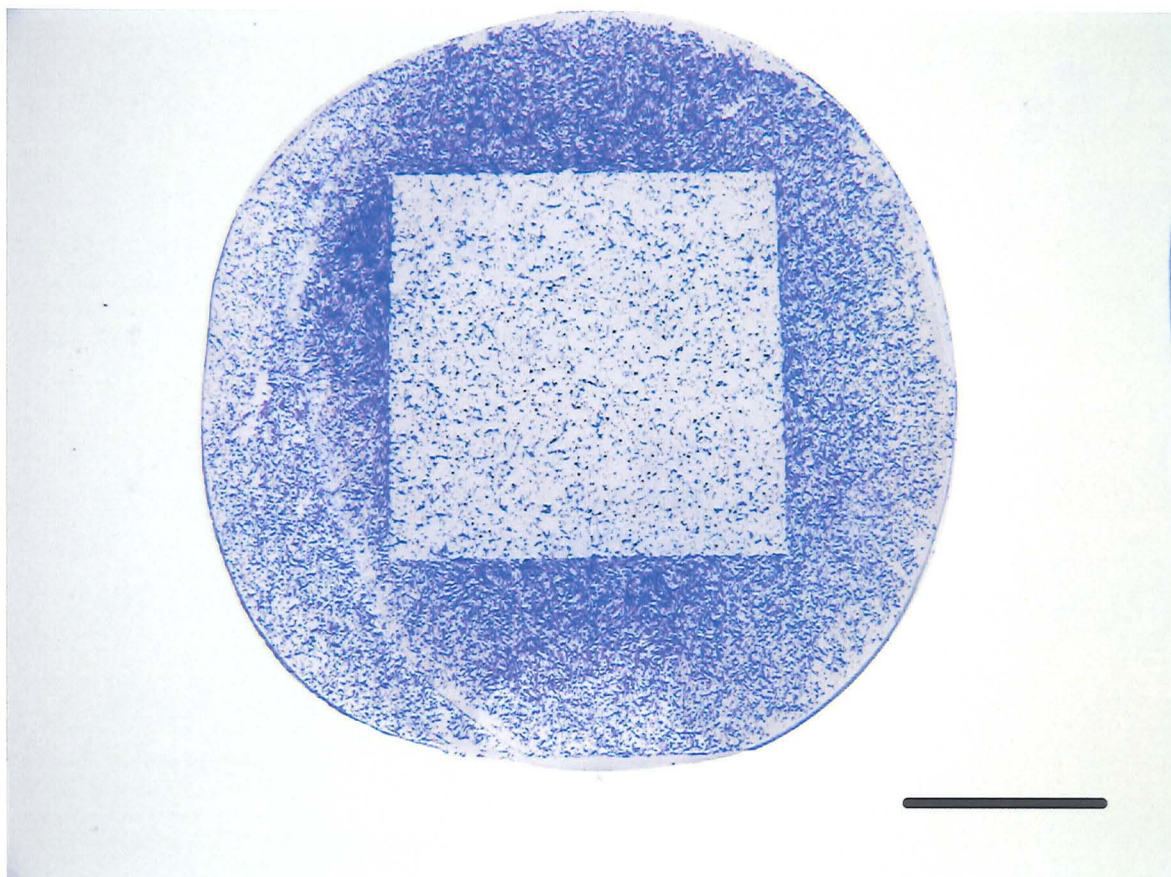


Figure 50. Overview picture of Coomassie-stained hTERT cells on an H90-r PCL sample after 96 h. The blue colour indicates the presence of cells. It is evident that cells on the area surrounding the nano-pillars (1 cm² pattern in the middle) are more confluent. Bar: 5 mm.

4.4.2.2 B.End3

Figure 51 shows the results of the average cell density, average cell area and average surface coverage of B.End3 on both flat and nanopillared areas (“Flat” and “Pillars”) of sample H90-r. Initially, the number of cells on the pillars is higher than on the flat, and so it is at 12 h. Also, up to 12 h the cell area on the pillars is always smaller than on the flat. The cell coverage increases exponentially with time on both flat and pillared PCL, but from 48 h the coverage on the nano-pillars was significantly higher than on the flat. This suggested either an increase of cell proliferation on the pillars, or an increase in spreading area.

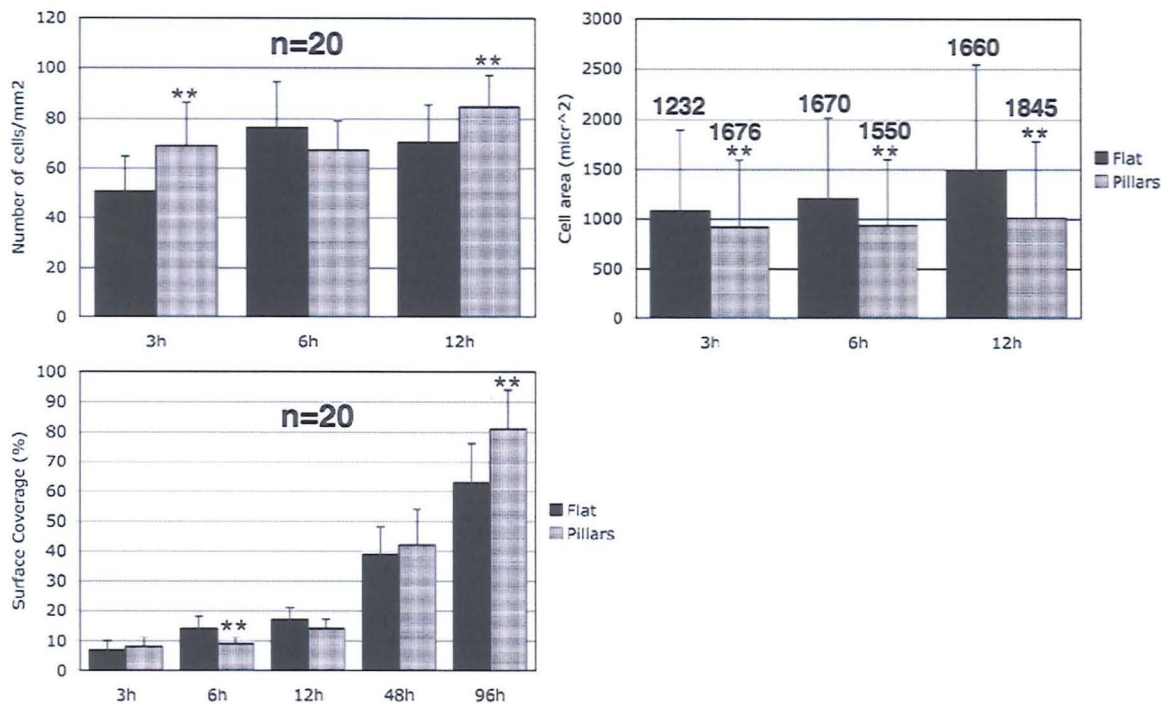


Figure 51. Average cell density, cell area, aspect ratio and surface coverage of B.End3 on flat and nanopillared PCL (H90-r), fixed at different time points and stained with Coomassie Blue. Results are the mean \pm standard deviation. The total number of averaged values (n) is indicated above the error bars. * p <0.05, ** p <0.01 unpaired t -test (two-tailed assuming unequal variance).

The direct observation of bright-field microscope images of Coomassie-stained cells (Figure 52, Figure 53) showed that the cells at confluence seemed more spread on the nano-pillars than on the surrounding flat area. In fact on the pillars the cells seemed to form a packed monolayer, whereas there were always visible gaps between cells on the flat substrate. Figure 52 shows the appearance of cells on the nano-pillars and on flat control at 3 h and 96 h: at 3 h the cells spread more uniformly on the flat surface, while they assume a stellate shape on the nano-pillars. At 96 h, this tendency seems to reverse, and the cells are more rounded and spread on the pillars rather than on the flat. On the nano-pillars they seem to form a cobble-stone pattern that is more resemblant of their morphology *in vivo*. Figure 53 illustrates an area with a border between the nano-pillars and flat: the difference in cell spreading and surface coverage on the two surfaces is self-evident. It should be noted that the presence of “giant cells” visible in all images is endemic in endothelial cell populations. The overview pictures of the whole samples after 96 h are consistent with the previous observations, by showing a more uniform but less dense cell layer on the nanopatterned square (light blue patch in Figure 54).

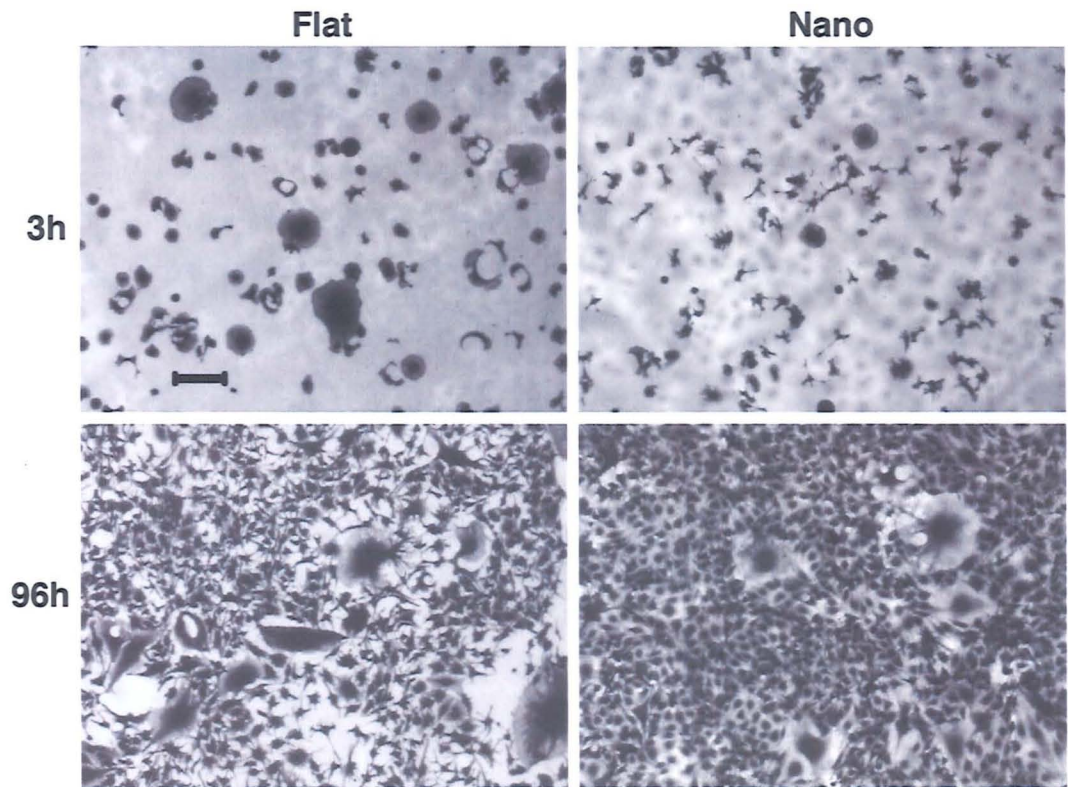


Figure 52. B.End3 cells on H90-r PCL at 3 h and 96 h. At 3 h, the initial number of cells on flat and pillared areas was similar, but the cells seemed to spread more uniformly on the flat control. However, at 96 h the cells were more spread and more confluent on the nano-pillars than on the flat surrounding area. Note the presence of “giant” cells. Scale bar: 100 μm .

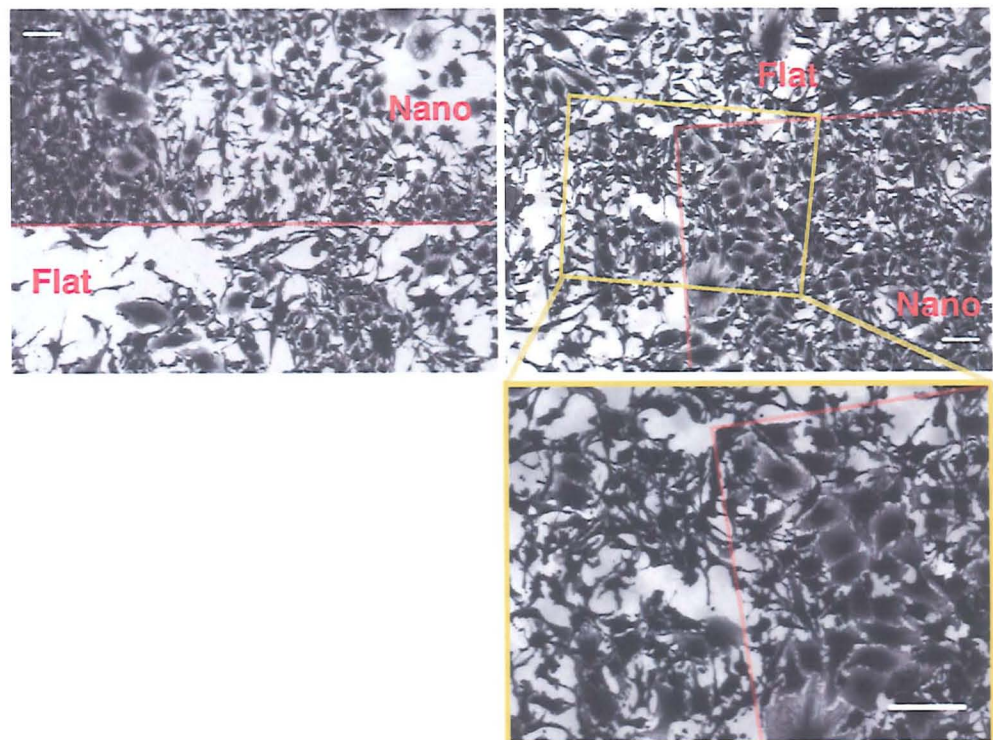


Figure 53. B.End3 cells on H90-r PCL at 96 h. The cells align to the edges, and have a different appearance on the nano-pillared and flat areas. Bars: 100 μm .

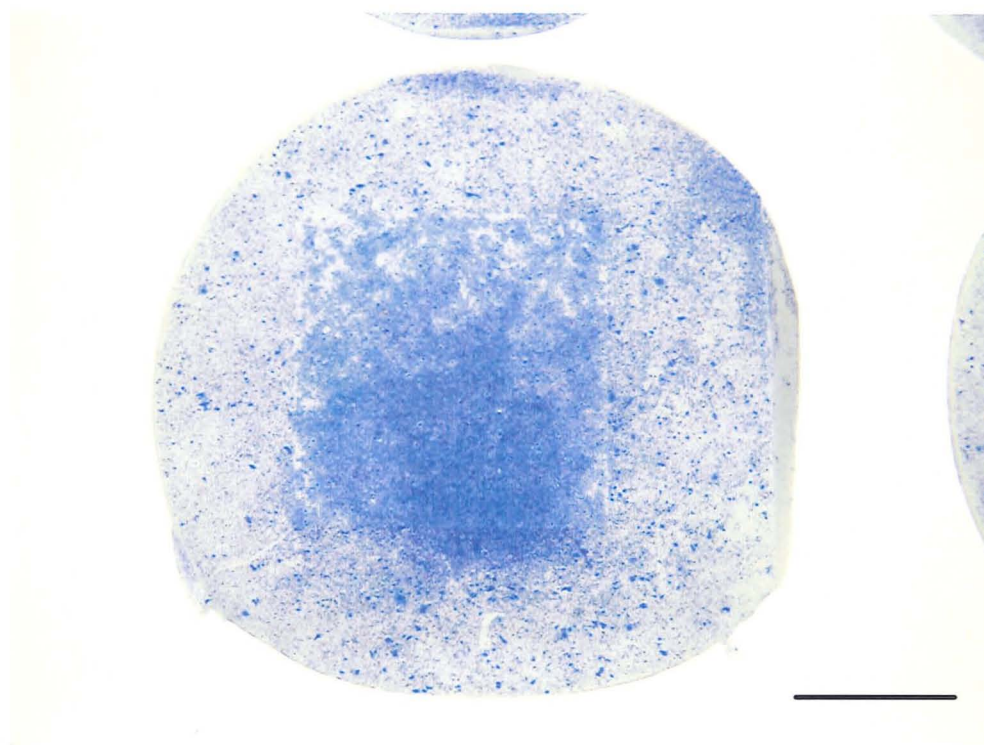


Figure 54. Overview picture of Coomassie-stained B.End3 cells on an H90-r PCL sample after 96 h. The blue colour indicates the presence of cells. It is evident that the surface coverage of cells on the nano-pillared area (1 cm² pattern in the middle) is much higher than on the surrounding flat area. Besides, the shade of blue at the lower edge can be seen to change from the pattern to the flat: this is consistent with the presence of a less thick layer on the patterned area. Bar: 5 mm.

4.4.2.3 Bone cells

Figure 55 shows the results of the average cell density, average cell area and average surface coverage of rat calvaria bone cells on both flat and nanopillared areas (“Flat” and “Pillars”) of sample H90-r. The average number of cells on flat and pillars did not show any significant trend up to 24 h. However, from 6 h the cell area on the pillars was significantly smaller than on the flat. Again, the surface coverage on the nano-pillars increased less than on the flat. It can be noted that, unlike with B.End3 and hTERT, the surface coverage on the flat area does not show the expected exponential increase with time. This is probably due to the fact that primary osteoblasts are more sensitive than the other two cell lines to the amount of nutrients in the growth medium, and unless fed before 72 h, the cells will stop proliferating and start dying. However, the comparison between flat and pillars at each time point is self-consistent.

These results are corroborated by the direct observation of bright-field microscope images of the cells (Figure 56), and overview pictures of the whole non-coated samples at 72 h (Figure 57). At confluence, on the non-coated sample there are more cells on the flat area than on the nano-pillars.

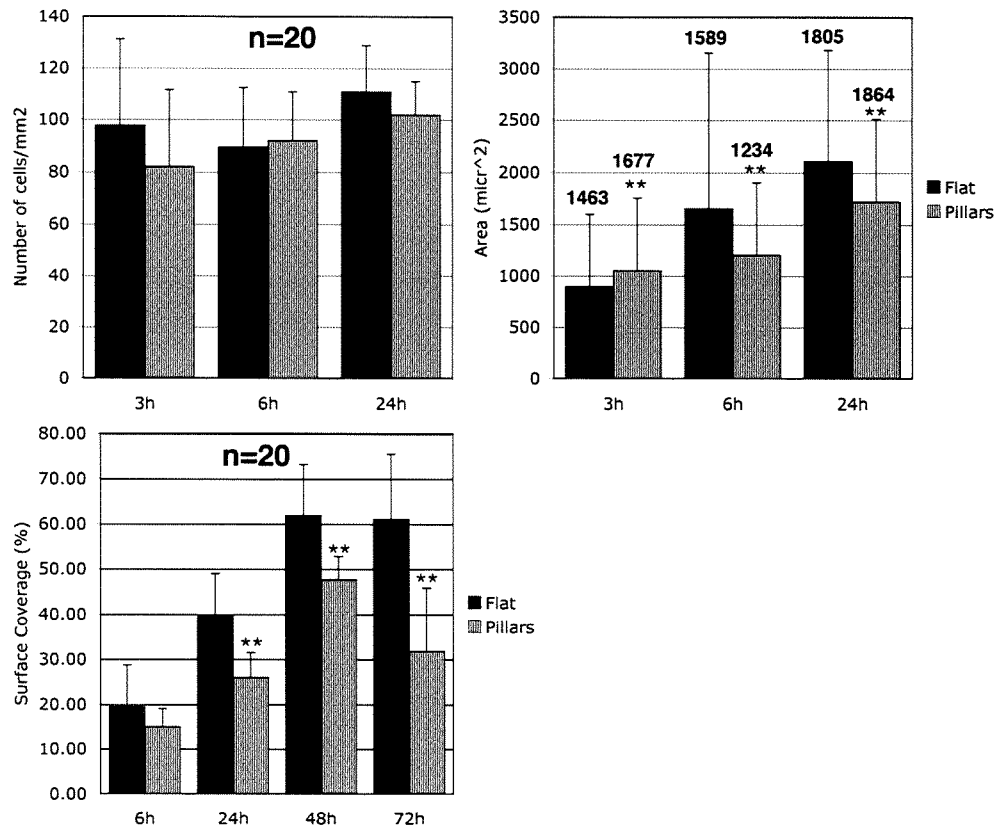


Figure 55. Average cell density, cell area, aspect ratio and surface coverage of rat calvaria osteoblasts on flat and nanopillared PCL (H90-r), fixed at different time points and stained with Coomassie Blue. Results are the mean±standard deviation. The total number of averaged values (n) is indicated above the error bars. * $p < 0.05$, ** $p < 0.01$ unpaired t -test (two-tailed assuming unequal variance).

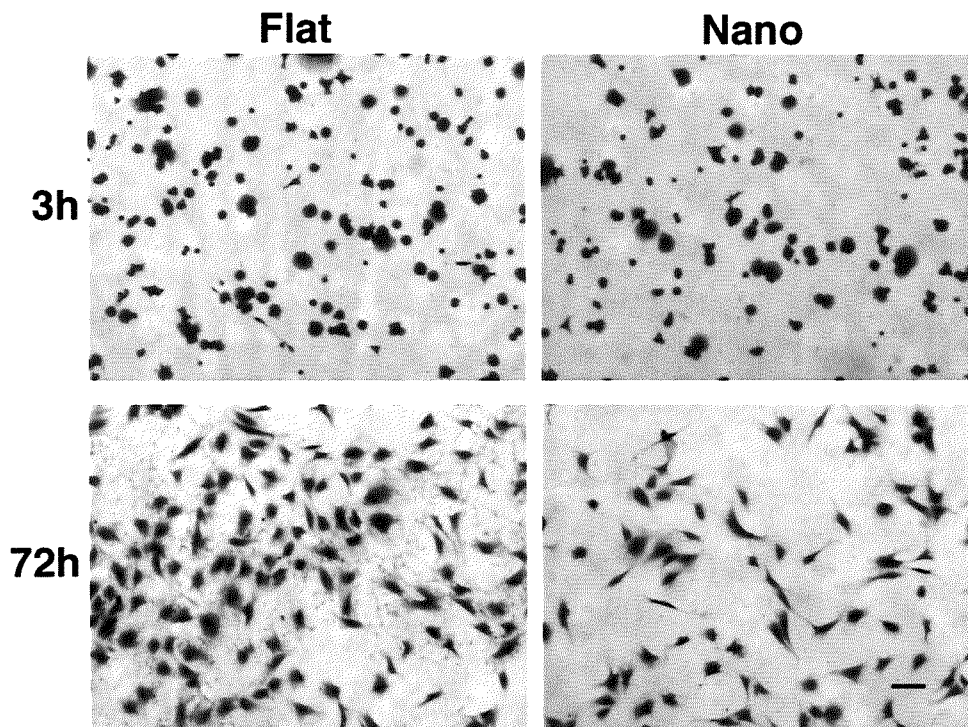


Figure 56. Rat calvaria bone cells on H90-r PCL at 3 h and 72 h. The initial spreading and number of cells on flat and pillared areas are similar. However, at 72 h the cells are more spread and more confluent on the flat area surrounding the pillars. Scale bar: 100 μ m.

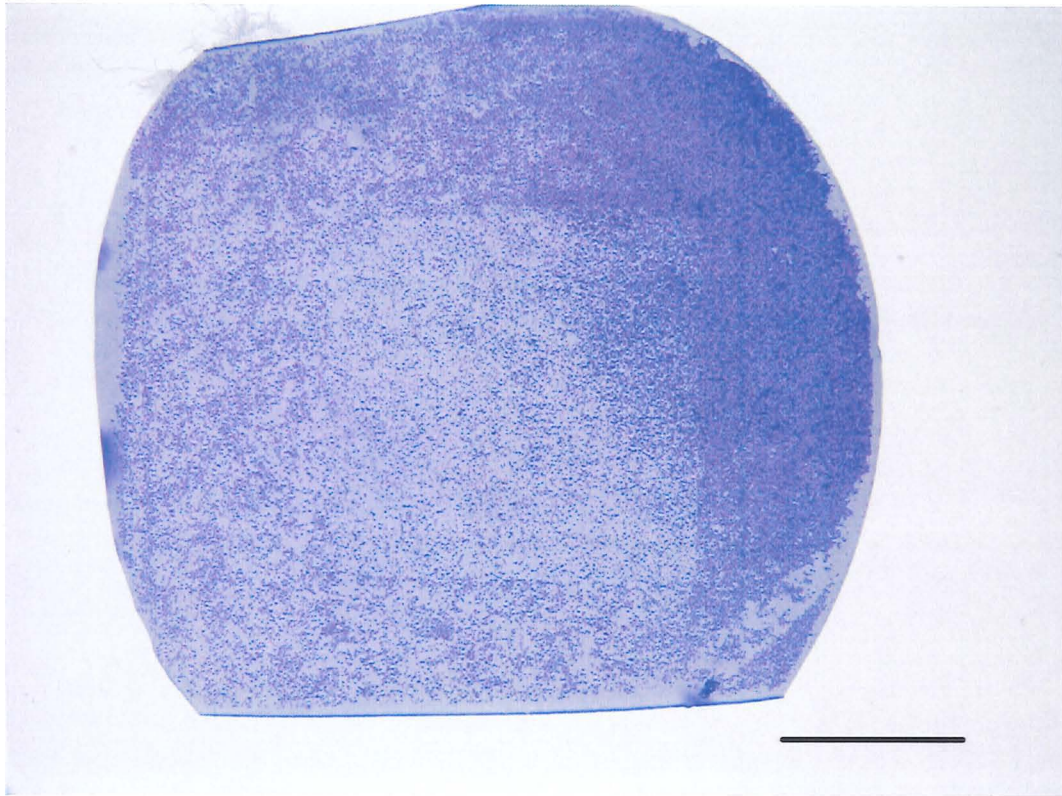


Figure 57. Overview picture of Coomassie-stained bone cells on an H90-r PCL sample after 72 h. The blue colour indicates the presence of cells. It is evident that there are many more cells on the area surrounding the nano-pillars (1 cm² pattern in the middle). Bar: 5 mm.

4.4.3 Actin/Vinculin staining

In order to investigate the formation of focal adhesions on the nano-pillars, the three cell types were cultured on uncoated PCL H90-r replicas, and immunostained for Actin and Vinculin.

4.4.3.1 hTERT

Figure 58 shows the Vinculin staining of hTERT cells on flat and nano-pillared H90-r samples. It is apparent that the cells on the nano-pillars were smaller than on the flat control where mature focal contacts were visible (dashed clusters near the edges). Mature focal contacts were less visible in the cells on the nano-pillars, where the Vinculin was more diffuse and less organised. The Actin stress fibres are visible on the flat control, but not on the nano-pillars.

4.4.3.2 B.End3

Figure 59 shows the Vinculin staining of b.End3 cells on flat and nano-pillared H90-r samples: there was no visible difference in the Vinculin arrangement on flat and pillars. In fact, the stain showed that the cells formed focal adhesions on both patterned and flat areas, even though the cells seemed to be more spread on the pillared area. The Actin stain did not work for this cell type.

4.4.3.3 Bone cells

Figure 60 shows the Vinculin staining of rat calvaria bone cells on flat and nano-pillared H90-r PCL samples. The cells on the nano-pillars seemed smaller than on the flat control. Focal

adhesions were more visible on the flat control than on the pillared areas, where some Vinculin clusters were present only at the edge of the cells.

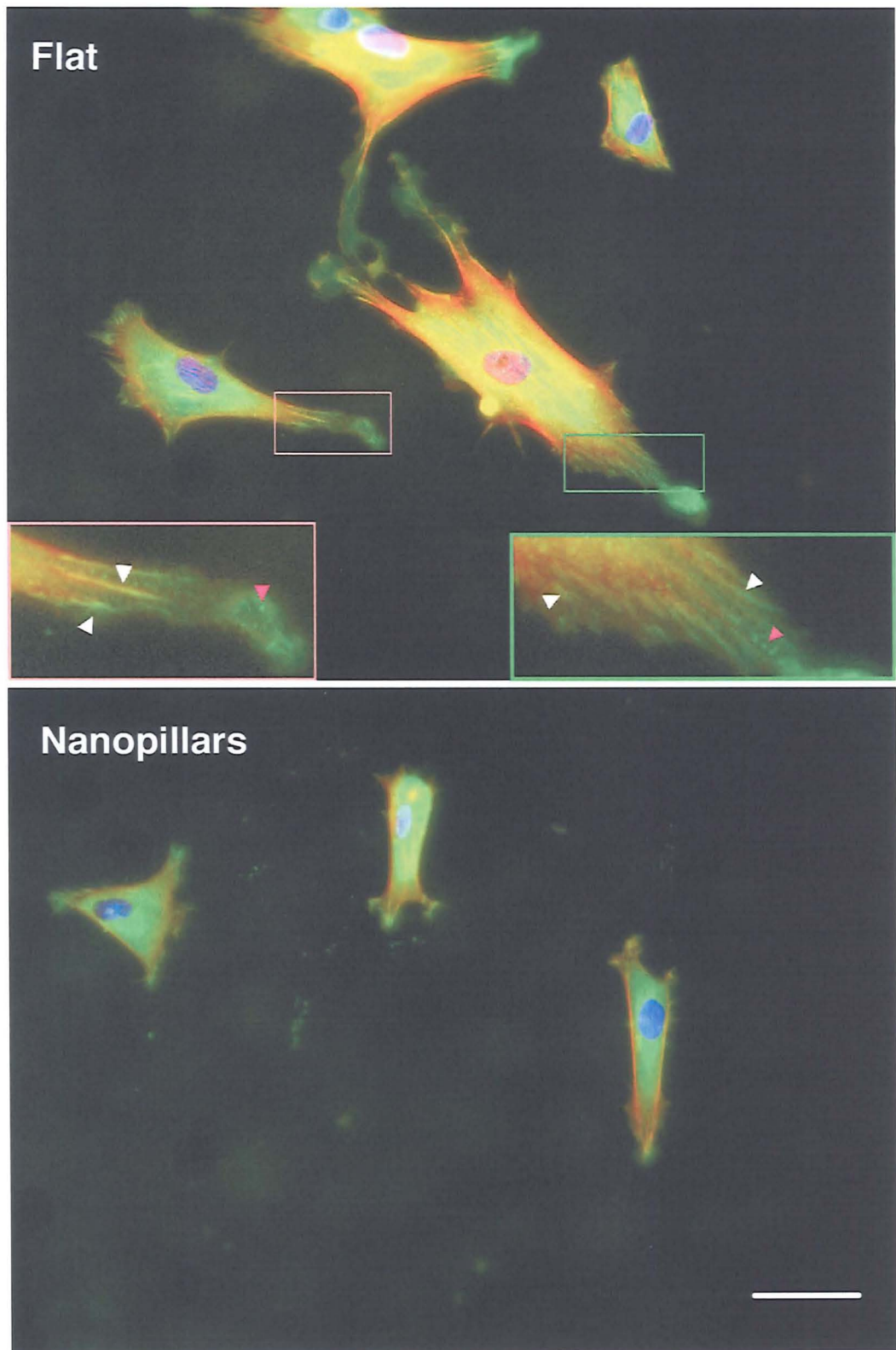


Figure 58. Vinculin staining of hTERT cells after 24 h on flat and nano-pillared uncoated PCL (H90-r). Green Vinculin, red Actin, blue nucleus. White arrows indicate mature focal adhesions, pink arrows nascent focal complexes. Bar: 50 μm .

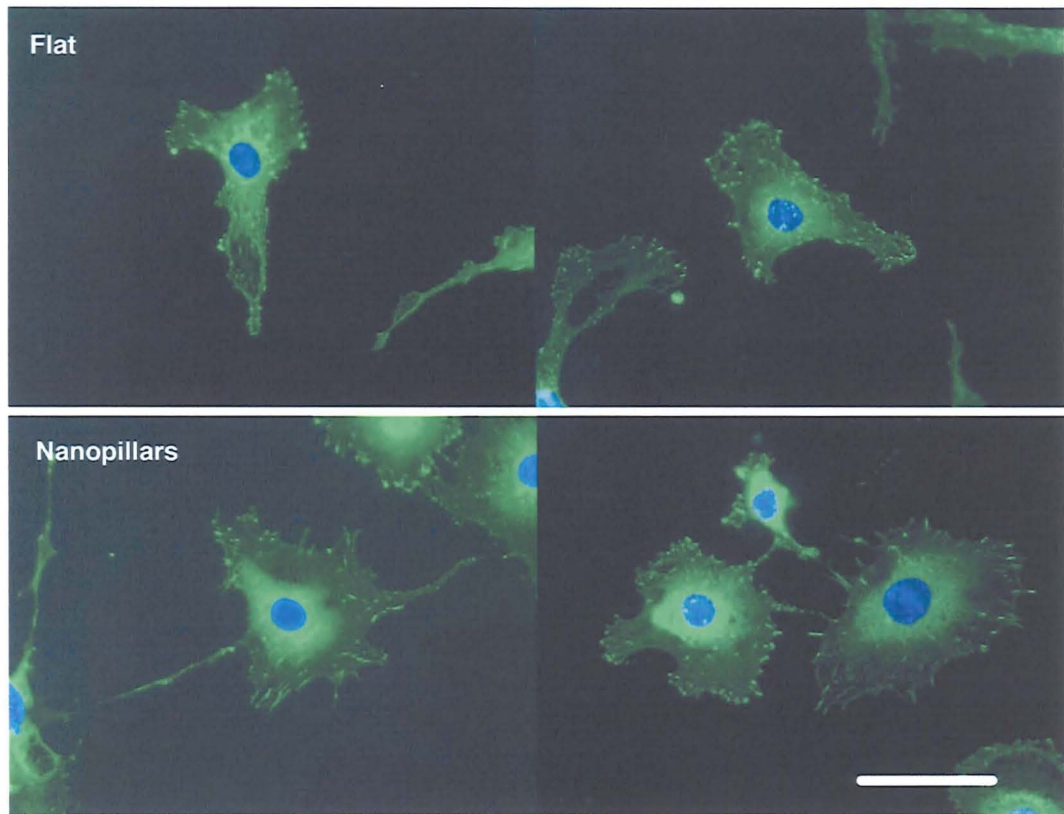


Figure 59. Vinculin staining of B.END3 cells after 24 h on flat and nano-pillared H90-r replica. Green Vinculin, blue nucleus. Bar: 50 μ m.

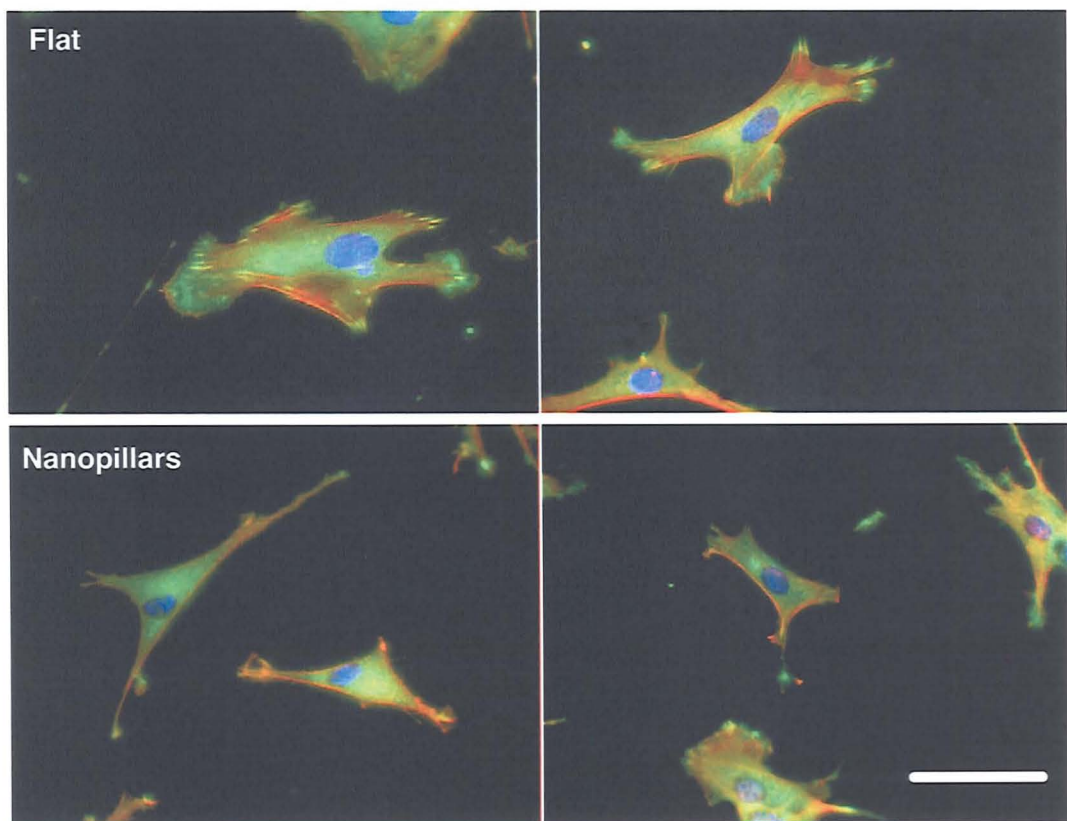


Figure 60. Vinculin staining of rat calvaria bone cells after 24 h on flat and nano-pillared PCL (H90-r). Green Vinculin, red Actin, blue nucleus. Bar: 50 μ m.

4.4.4 Protein coating

4.4.4.1 hTERT

In order to test the effect of surface chemistry on the nano-pillars-induced cell reaction, the PCL was protein-coated, and hTERT cells were seeded and fixed after 96 h. The results (Figure 61) showed that the PLL retained the effect of the nano-pillars to a lesser, but significant, extent, while the Fibronectin masked the visible effect of the nanostructure. Figure 62 shows the corresponding Overview pictures of the whole samples.

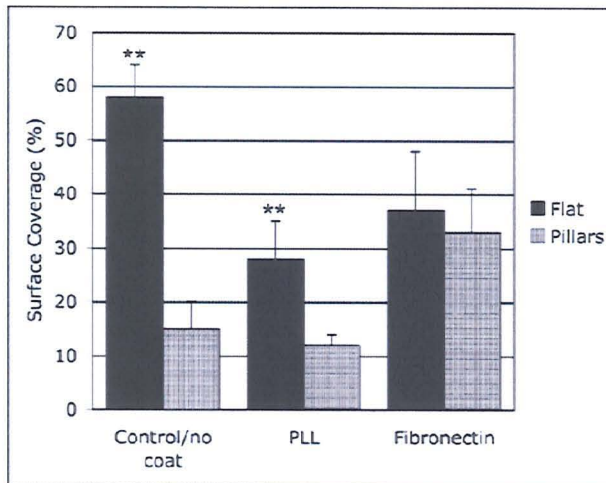


Figure 61. hTERT cells fixed after 96 h, Coomassie stained on differently coated samples: Fibronectin, Poly-L-Lysine (PLL) and non-coated control. Results are the mean \pm standard deviation ($n=20$). * $p < 0.05$, ** $p < 0.01$ unpaired t -test (two-tailed assuming unequal variance).

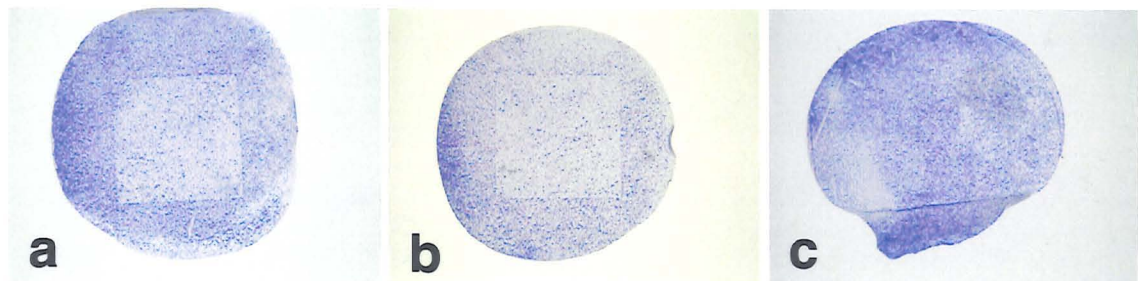


Figure 62. Overview picture of Coomassie-stained hTERT cells on H90-r PCL sample after 96 h. a) Non-coated control; b) PLL; c) Fibronectin. The blue colour indicates the presence of cells. While there is an apparent difference in surface coverage on both non-coated and PLL-coated samples, this visible difference disappears on the Fibronectin-coated replica. Bar: 5 mm.

Since the Fibronectin coating suppressed the influence of the nano-pillars, the organisation of Fibronectin on both Fibronectin-coated and non-coated H90-r was investigated by immunofluorescence. Figure 63 shows the Fibronectin/Actin staining of hTERT cells on flat and nano-pillared non-coated H90-r samples. On both surfaces, only the Fibronectin produced by the cells was visible, right underneath them, corresponding to the location of focal adhesions; the Fibronectin clusters were more defined on the flat control rather than on the pillars, where they were smaller and mostly located at the edges of the cell. On the other hand, when the samples were Fibronectin-coated (Figure 64), Fibronectin trails were visible around the cells, denoting that the cells had rearranged the protein during their attachment and migration (Avnur, 1981), but no apparent difference could be seen between pillared and flat areas.

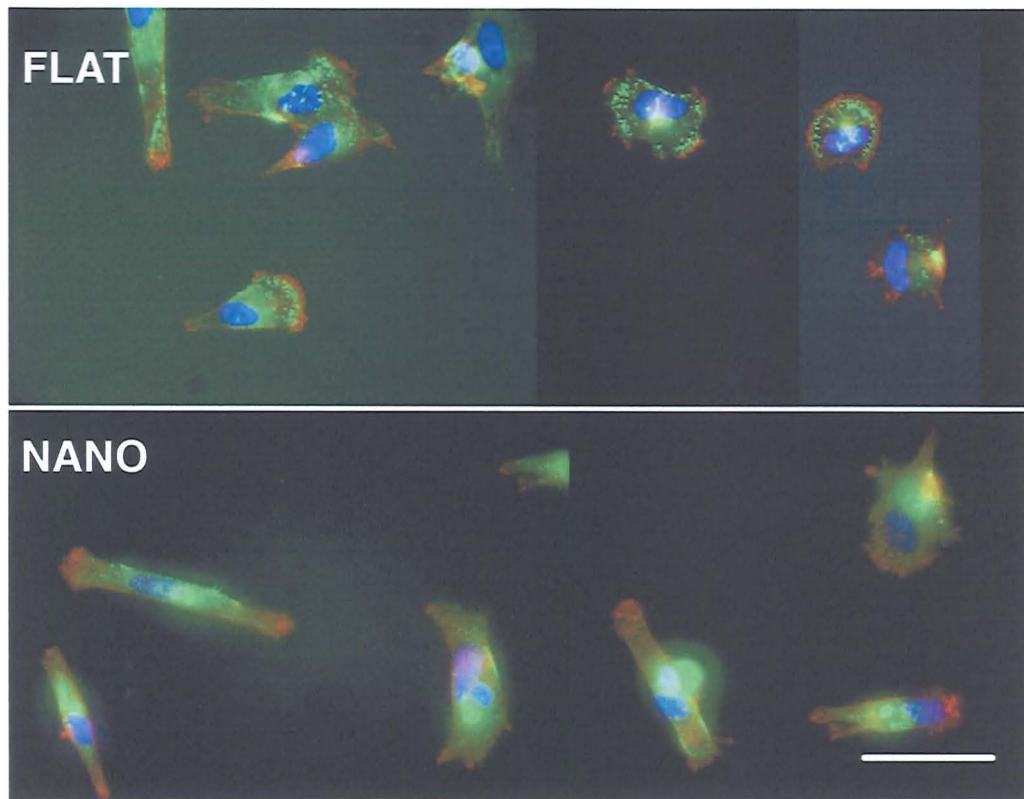


Figure 63. Actin/Fibronectin staining of hTERT cells after 24 h on flat and nano-pillared PCL on a non-coated H90-r replica. Red Actin, green Fibronectin, blue nucleus. The Actin staining (red) is shown at low contrast, only to outline the cell body. Bar: 50 μm .

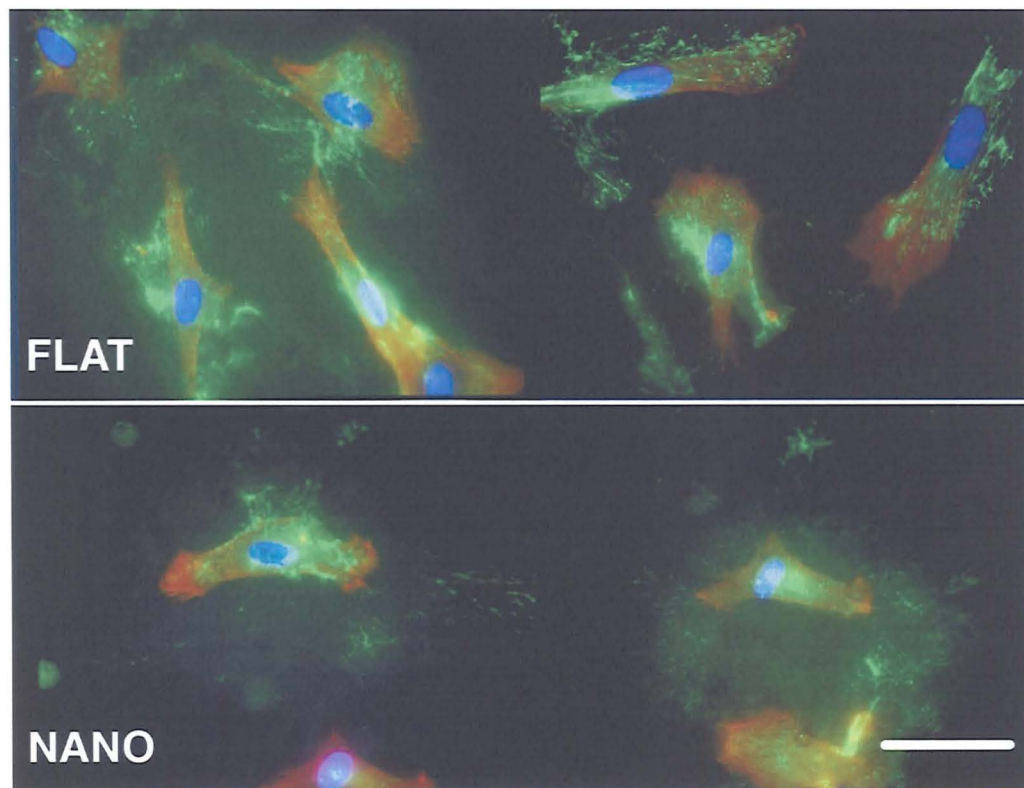


Figure 64. Actin/Fibronectin staining of hTERT cells after 24 h on flat and nano-pillared PCL on a Fibronectin-coated H90-r replica. Red Actin, green Fibronectin, blue nucleus. The Actin staining (red) is shown at low contrast, only to outline the cell body. Bar: 50 μm .

4.4.4.2 Bone cells

Because the Fibronectin-coated PCL replicas yielded the stronger difference with the uncoated samples in terms of hTERT surface coverage, the same experiment was repeated with bone cells. The results show suppression of the effect of the nano-pillars, resulting in uniform surface coverage, analogously to what seen with the hTERT. The surface coverage at 96 h on the Fibronectin-coated sample is shown separately: when compared to the uncoated sample, the coating significantly hinders the effect of the underlying nanopattern.

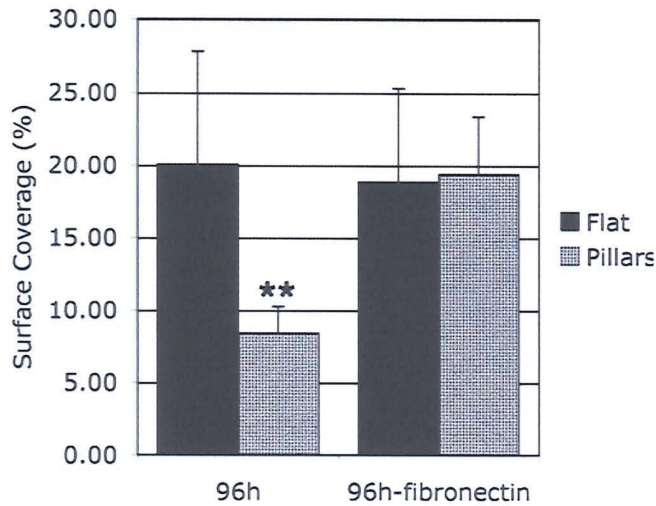


Figure 65. HTERT cells fixed after 96 h, Coomassie stained on Fibronectin-coated samples and non-coated control. Results are the mean±standard deviation ($n=20$). * $p<0.05$, ** $p<0.01$ unpaired t -test (two-tailed assuming unequal variance).

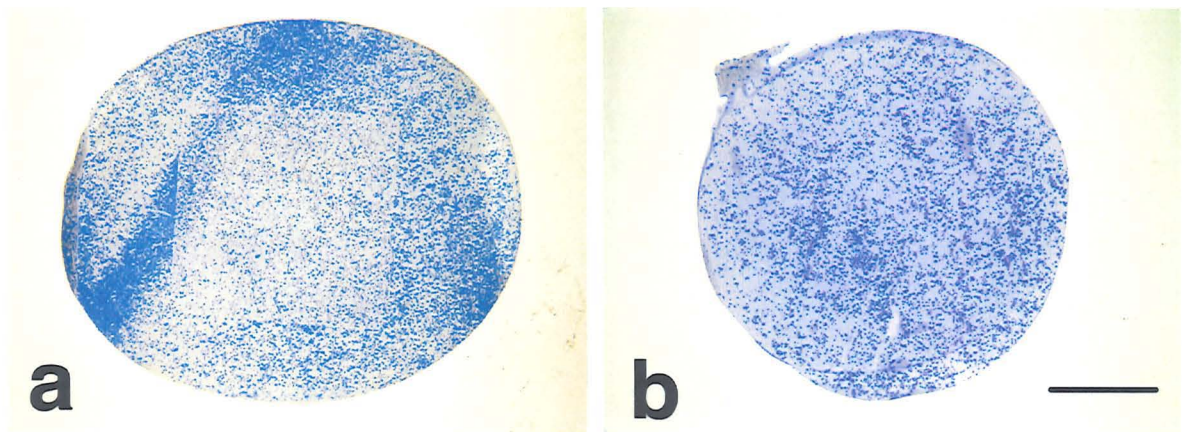


Figure 66. Overview picture of Coomassie-stained rat calvaria bone cells on H90-r samples after 96 h (with no media replacement). a) Non-coated control; b) Fibronectin-coated sample. The blue colour indicates the presence of cells. While there is an apparent difference in surface coverage on the non-coated sample, this difference disappears on the Fibronectin-coated replica. Bar: 5mm.

4.4.4.3 B.End3

Finally, B.End3 cells were also cultured on Fibronectin-coated PCL replicas. The Fibronectin coating yielded an ambiguous result, since a difference in the appearance of cell coverage is visible in one of the samples (Figure 67c), but not in the other (b). Unfortunately, this study could not be quantitatively analysed. However, an immunofluorescent stain could be observed (Figure 68), showing that there seems to be more Fibronectin fibrils on the flat PCL rather than on the pillars.

Endothelial cells are much less motile than hTERT fibroblasts, and this explains why the Fibronectin rearrangement in this case is less marked.

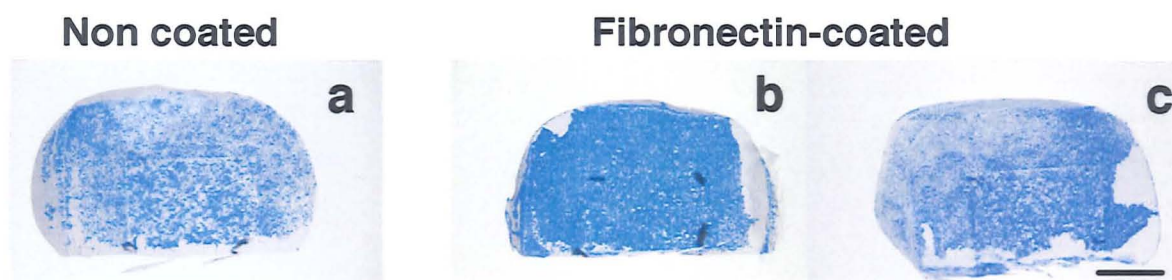


Figure 67. Overview picture of Coomassie-stained B.End3 cells on an uncoated and a Fibronectin-coated H90-r PCL sample after 96 h. The blue colour indicates the presence of cells. The effect of the Fibronectin coating is not evident, although in picture b) it seems to suppress any difference between the cells on the flat and the nano-pillared area. Bar: 5 mm.

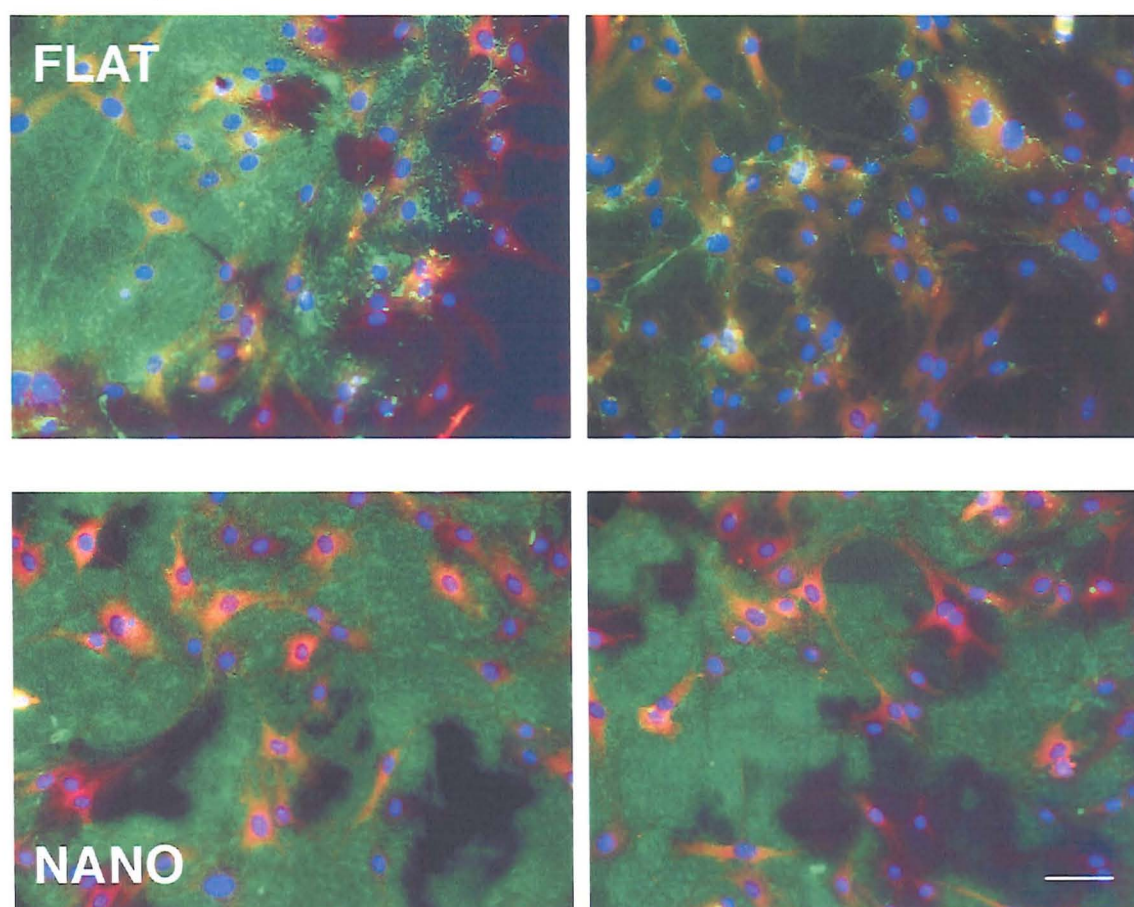


Figure 68. Vinculin/Fibronectin staining of B.End3 cells after 24 h on flat and nano-pillared PCL on a Fibronectin-coated H90-r replica. Red Vinculin, green Fibronectin, blue nucleus. The Vinculin staining (red) is shown at low contrast, only to outline the cell body. Bar: 50 μ m.

4.4.5 Further work on hTERT

Time restrictions imposed to carry on the investigation with only one cell type. The reaction of hTERT to the non-coated PCL nano-pillars was much more dramatic than the reaction of the two other cell types. For this reason, the rest of the investigation was continued with hTERT only.

4.4.5.1 SEM

Figure 69 shows SEM images of hTERT cells on the flat area (top row) and the nanopillared area (bottom row) of the uncoated H90-r. The samples were tilted at 45° to show the area underneath the cells. Unfortunately, some cell cracking from processing is unavoidable. The ringed areas on the cells on the flat control correspond to the nuclei. On the nanopattern, the cells can be seen to probe the surface with filopodia, and seem to be “pulling” on the pillars. However, the last phenomenon could be due to shrinkage of the cell during dehydration.

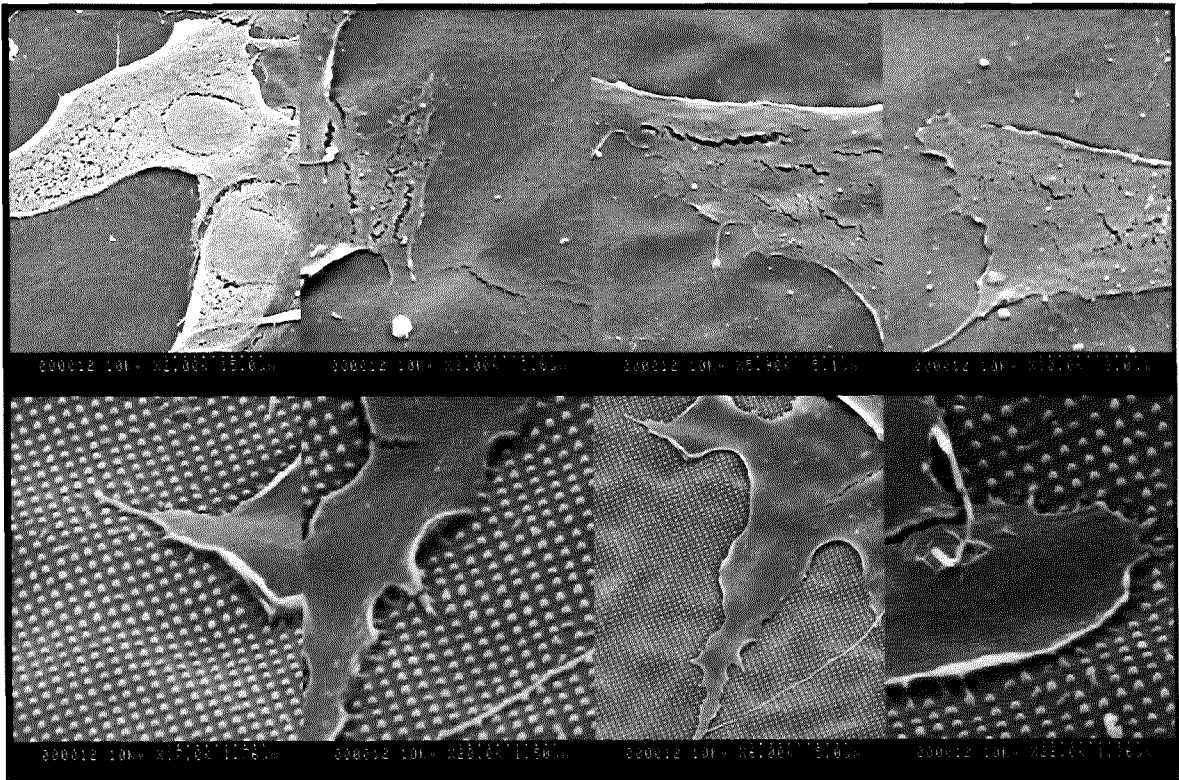


Figure 69. SEM micrographs of hTERT at 24 h on H90-r replicas. All images were taken at 45° tilt.

4.4.5.2 Time-lapse video recording

Time-lapse recording of hTERT cells at the flat/pillars boundary (movie available on the attached CD-ROM) showed that the cells on the nano-pillars are much less spread than on the flat substrate, and they tend to aggregate with other cells to form cell clusters, which indicates that they try to avoid contact with the surface. It is interesting to note that at 11 h there are more cells on the nano-pillars than on the flat area, meaning that initially the cells adhere equally well everywhere, if not better to the nanopatterned area (Figure 70). Note that the material used in this experiment (only

was not PCL, but PLL-coated polycarbonate. The cells migrated in both directions across the nanopattern.

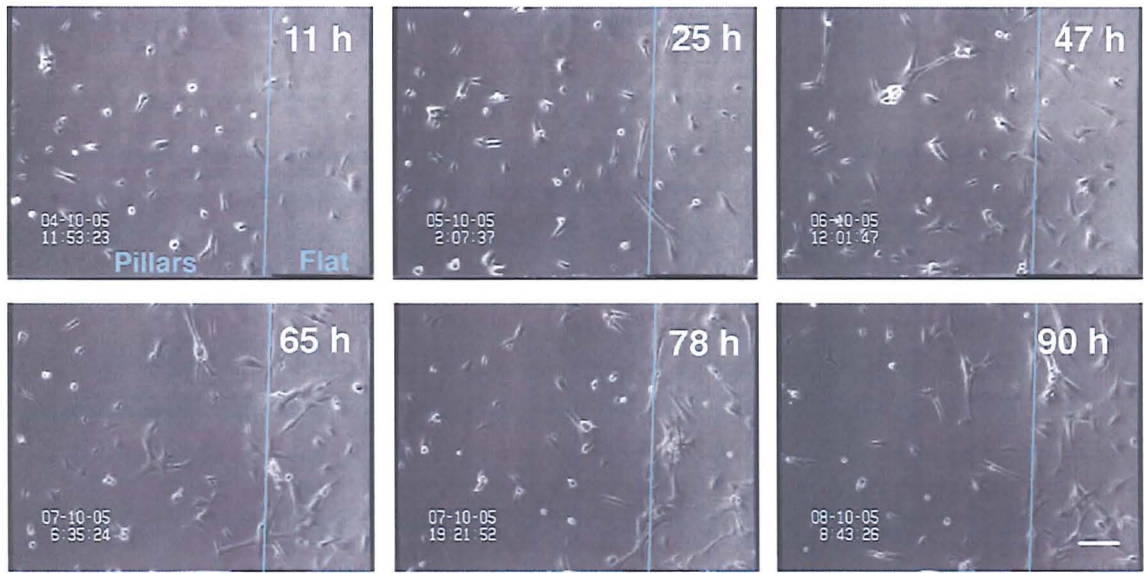


Figure 70. Still frames extracted from the time-lapse movie of hTERT cells on H90-r sample (PLL-coated poly-carbonate). Bar 200 μm .

4.4.5.3 Gold-coating: surface coverage and Vinculin staining

All the results described so far suggested that the cells did not proliferate on the PCL nanopillars. In order to test if this effect was due to the presence of air pockets between the nanopatterns, the replicas were sputter-coated with 10 nm gold-palladium (AuPd), and hTERT cells were seeded and fixed after 96 h. By sputter coating with a very hydrophilic material such as AuPd, it could be assumed that no air-trapping would happen at the surface. The results of surface coverage

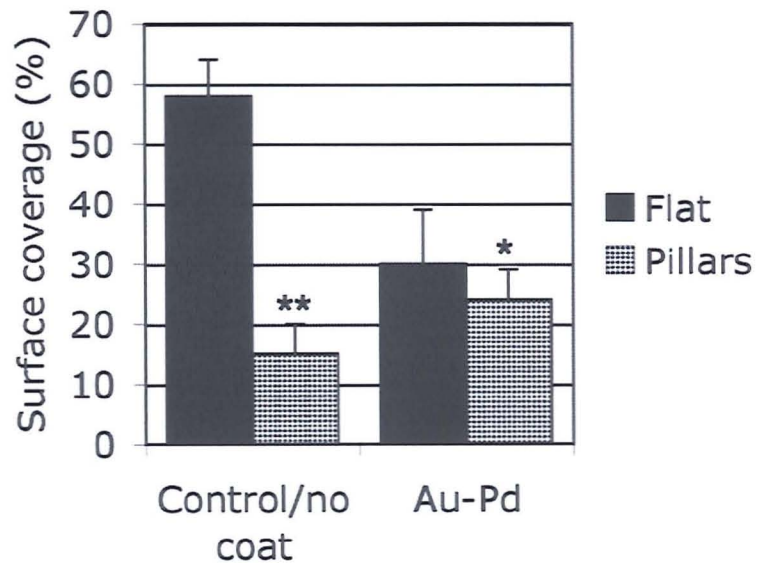


Figure 71. HTERT cells fixed after 96 h, Coomassie stained on AuPd-coated replicas and non-coated control. Results are the mean \pm standard deviation ($n=20$). * $p<0.05$, ** $p<0.01$ unpaired t -test (two-tailed assuming unequal variance).

analysis (Figure 71) showed that the gold-coating retained the effect of the nano-pillars yielding a small, but significant, difference. Figure 72 shows the corresponding overview picture of the whole

sample. Although the patterned square was still visible, the cells did clearly grow more on the AuPd-coated pillars.

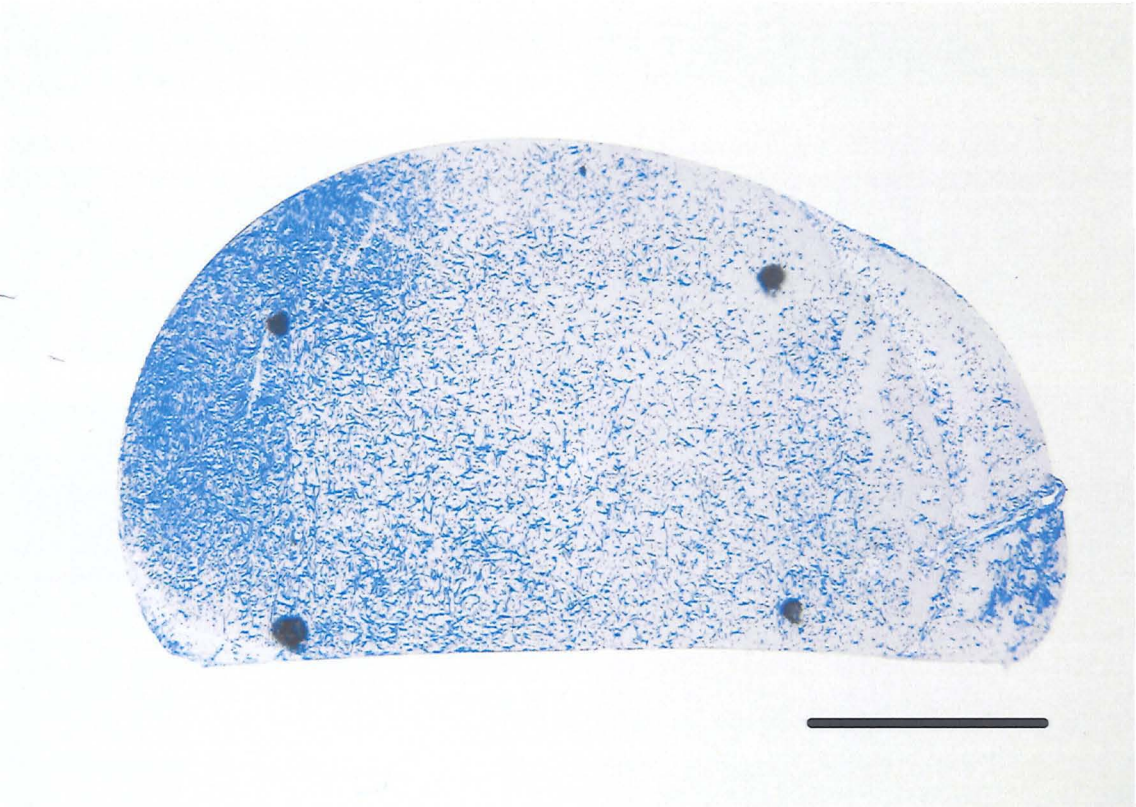


Figure 72. Overview picture of Coomassie-stained hTERT cells on AuPd-coated H90-r PCL sample after 96 h. The blue colour indicates the presence of cells. The patterned square (1 cm^2 pattern in the middle) is visible, although the difference is not very strong. Bar: 5 mm.

In order to compare the focal adhesion formation on the AuPd-coated pillars as a possible reason for the difference with the uncoated pattern, the cells on the AuPd-coated samples were immunostained for Vinculin. A difference in focal adhesion size was still visible on the gold-coated flat and nano-pillared areas (Figure 73). However, the difference was less obvious than on the uncoated replicas, and the cells seemed to form mature focal adhesions on the AuPd nano-pillars as well, as indicated by the size of the Vinculin patches close to the surface.

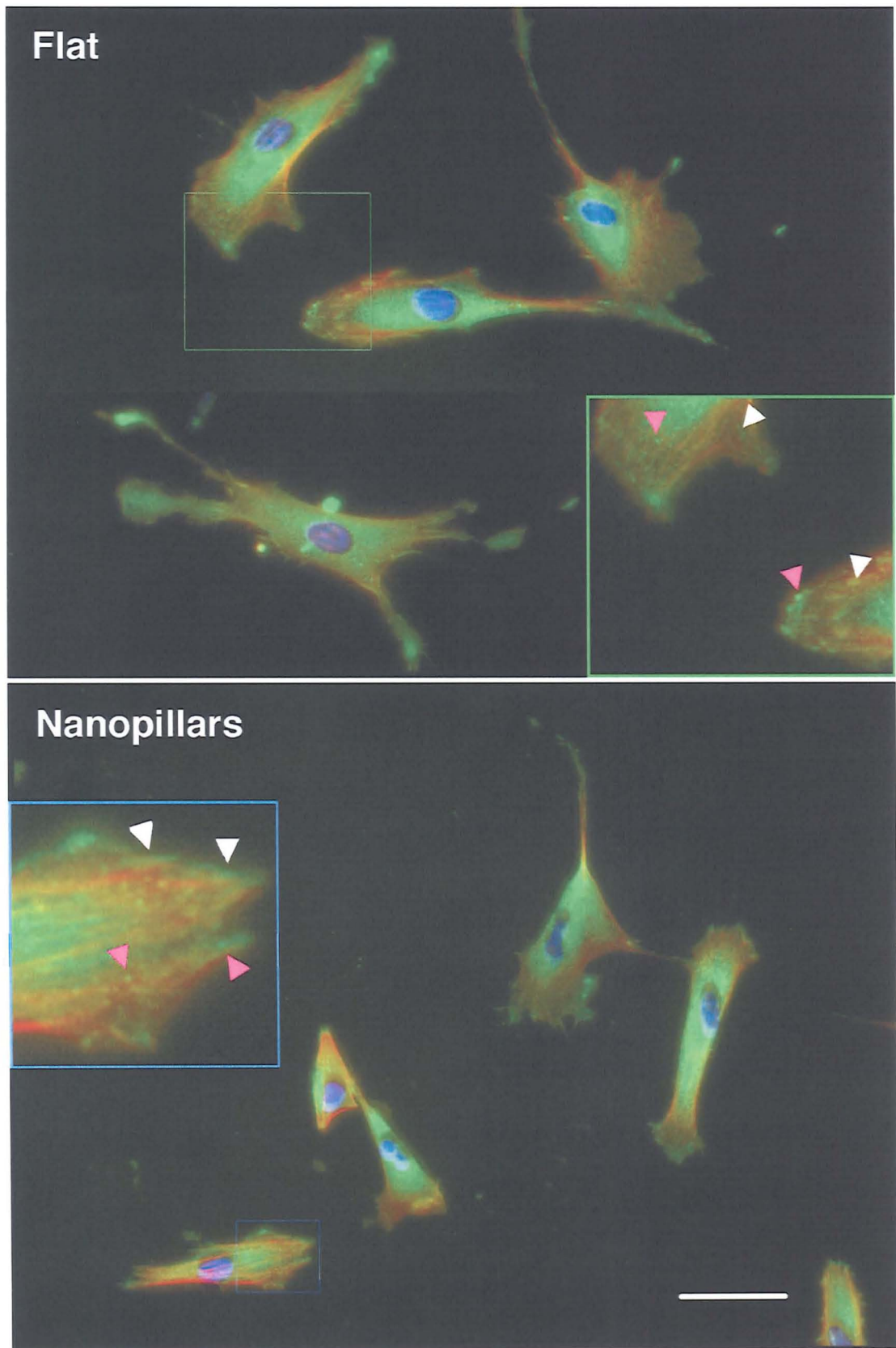


Figure 73. Vinculin staining of hTERT cells after 24 h on gold-coated flat and nano-pillared PCL (H90-r). Green Vinculin, red Actin, blue nucleus. White arrows indicate mature focal adhesions, pink arrows nascent focal complexes. Bar: 50 μm .

A quantitative comparison of focal adhesion formation on the AuPd-coated and non-coated nanopillars was done by counting the Vinculin-containing adhesion sites. These would include nascent focal complexes, mature focal adhesions and fibrillar adhesions. Figure 74 shows the counts of the average number of adhesions per unit area in hTERT cells, cultured on uncoated and gold-coated H90-r PCL substrata. The *p*-values of the *t*-tests comparing the adhesion densities on the samples (Table 11) reveal that the average number of adhesions between different topographies (flat and pillars) of the same chemistry is not significantly different, while it is significantly different between any topographies of different chemistry. Therefore, the surface chemistry seems to override the effects of topography with respect to the number of Vinculin-containing adhesions/unit area.

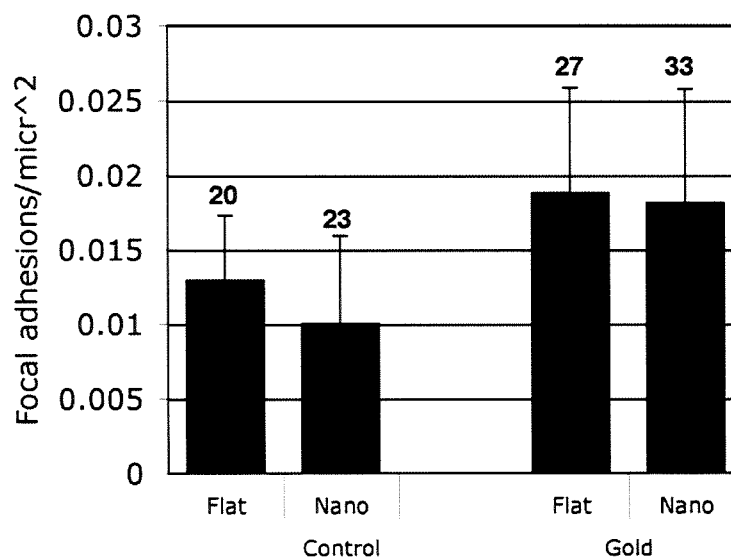


Figure 74. Number of Vinculin-containing adhesions per μm^2 in hTERT cells cultured on uncoated control and AuPd-coated samples for 24 h. Results are mean \pm standard deviation. The total number of averaged values (*n*) is indicated above the error bars.

	AuPd_flat		
Uncoated_flat	**	Uncoated_flat	
AuPd_pillars	-	**	AuPd_pillars
Uncoated_pillars	**	-	**

Table 11. *p*-values from unpaired *t*-test (two-tailed assuming unequal variance) applied to the focal adhesion densities in Figure 74. Values of $p < 0.05$ are considered significant. (**) $p < 0.01$, (*) $p < 0.05$, (-) $p > 0.05$.

4.4.5.4 Proliferation assay: non-coated and gold-coated PCL replicas

The surface coverage results and the time-lapse movie of hTERT cells on the uncoated PCL pillars suggested that the reason for the decreased cell coverage could be inhibited proliferation. Thus, this possibility was investigated directly by immunostaining the cells for BrdU. The results of the proliferation assay (Table 12) confirmed the hypothesis. On the uncoated PCL replica, the cells were proliferating on the flat control, while they did not do so on the nanopillared area, or at least much less. On the gold-coated sample, the cells were equally proliferating on flat and pillared areas. Figure 75 shows examples of the fluorescent pictures from which the proliferating nucleae were identified.

	Uncoated PCL		Gold-coated PCL	
	<i>Flat</i>	<i>Pillars</i>	<i>Flat</i>	<i>Pillars</i>
Proliferating cells (%)	45 ^a	16 (**) ^b	18 ^c	20 (-) ^d

Table 12. Percentage of proliferating cells on flat and nano-pillared areas of uncoated and gold-coated PCL. Results are mean±standard deviation. (**) $p < 0.01$; (-) $p > 0.05$. (ⁿ) is the number of values: (^a) 21, (^b) 21, (^c) 22, (^d) 22.

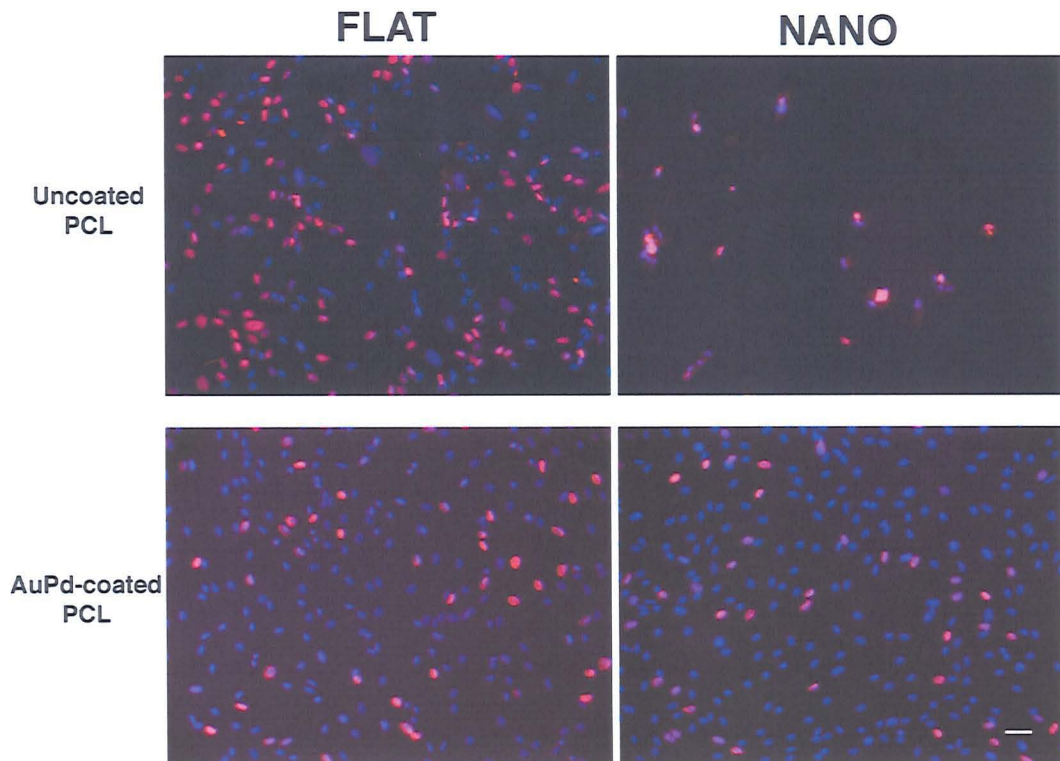


Figure 75. Proliferation assay on hTERT cells after 72 h on uncoated and AuPd-coated flat and nano-pillared PCL (H90-r). Red: BrdU-stained nucleae, blue: nuclear DNA. Bar: 50 μm .

4.5 Discussion. I.

4.5.1 Fabrication

By imaging the sample height after ca. 200 replicas, it was verified that the replication was reliable. The dimensions of pillars on the replicas ($d=170$ nm, $h=131$ nm) seem very big compared to the dimensions of the master ($d=105$ nm, $h=116$ nm). The discrepancy is explainable for the diameter: in the case of the master die, the diameter was SEM-measured at the bottom of the pits to be 105 nm, while in the replicated pillars the diameter was measured at the base (170 nm): however, the base diameter of the pillars is actually replicated from the top-opening of the master nano-pits, which is ca. 200 nm. The discrepancy in height is more surprising, since the replicated pillars were higher than the depth of the master pits; this could be due to a plastic elongation of the pillars during demolding. Finally, two notes on the nomenclature used throughout this chapter: first of all, the control surface is called “Flat”, but actually it has a roughness ($rms=5.3$ nm) that is very visible in Figure 40b and in Figure 43. Therefore, the term “flat” here is to be intended as relative to the more substantial roughness of the nanopattern. Secondly, even the term “regular” nano-pillars used to describe the protrusions of sample H90-r is to be intended as relative, by comparison with the more disordered protrusions that will be discussed in Part II of this chapter. However, regularity is found in the centre-to-centre distance of the pillars.

4.5.2 Cell culture

4.5.2.1 Non-coated PCL replicas

When cultured on the nano-pillars, time-lapse recording of the hTERT fibroblasts showed that the cells on the pattern are smaller and very motile. This phenomenon had already been observed with epitenon fibroblasts by J. Gallagher (Gallagher, 2003), who measured a higher cell motility on nano-pits, and the formation of cell clusters. Gallagher claimed to have observed selective migration of cells towards the planar surface; however, this was not apparent from my data. So why were there significantly less cells on the nano-pillars at 96 h? Unless the cells selectively migrated outside the pattern, the only other explanation that could justify their dramatically reduced number at 96 h, is the lack of cell proliferation on the nano-pillars. Thus, both the high motility of the cells on the pattern and the inhibited proliferation ensured that at 96 h the surface coverage on the nanopattern was significantly lower than on the surrounding flat area. The reduction of proliferation on the uncoated PCL H90-r nano-pillars was definitely confirmed by BrdU staining of the cells. However, the cells did initially adhere to the surface after they sedimented from the suspension: for this reason, with respect to fibroblasts these surfaces should be called “proliferation-inhibiting” rather than “non-adhesive”.

A possible reason for reduced fibroblast proliferation can be found in their spreading area, which in turn is linked to the formation of focal adhesions. Mature focal adhesions are a necessary

requirement for the cells to proliferate (Meredith, 1993). Small focal complexes are thought to be precursors of focal adhesions; if they are not allowed to “mature”, the cells cannot spread fully, hence they will be able to migrate but not to proliferate. Differences in spreading area of hTERT on randomly-arranged nano-columns had already been noticed by Dalby *et al.* (Dalby, 2004), who also noticed a non-significant difference in initial cell number (which confirms the initial adhesion of cells everywhere) and a significant difference in spreading area. Consistently with the latter measurements, both Dalby *et al.* (Dalby, 2004) and J. Gallagher (Gallagher, 2003) reported that fibroblastic cells were able to form mature focal contacts on the flat area, while on the nanopattern they only formed small focal complexes.

Cell area analysis on these uncoated H90-r PCL samples confirmed that hTERT cells spread less on the nanopillared surface than on the flat area. The average number of Vinculin-containing adhesions per unit area was not significantly different between flat and pillars, however the main determining factor in cell spreading is the adhesion size and types, rather than their density. Assuming that the cells do not form adhesions with the lower surface between the nano-pillars, it could be that the tops of the nano-pillars do not provide adequate adhesion sites for the cells to form mature focal adhesions, hence to spread and proliferate. The top area of the pillars could be too small, and their spacing too large, especially since they are not perfectly cylindrical. It has been shown (Arnold, 2004, Maheshwari, 2000) that the clustering of RGD peptides on surfaces can determine cell adhesion and motility. In particular, a separation >73 nm between Integrin molecules resulted in limited cell attachment and spreading (Arnold, 2004), and it was suggested that there exists a minimum threshold cluster size for cells to adhere (Maheshwari, 2000). Therefore, further investigation is required to determine which type of adhesion is prevailing, and if on the nano-pillars the cells form a smaller number of mature adhesions. This can be achieved by analysing the area or length distribution of the Vinculin-containing adhesions, in order to differentiate between focal complexes and focal contacts, while the fibrillar adhesions would be revealed by immunostaining for Tensin.

The hypothesis that the cells adhere only to the top surface of the nanopattern seems likely, since this has been previously observed by TEM imaging of hTERT on nano-columns (Dalby, 2004). At focal adhesions, the distance between the cell membrane and the substrate is 10-15 nm (Izzard, 1976), thus unless the ECM can bridge the gap between asperities (which probably happens when the pattern is coated with Fibronectin, hence the shielding of any visible cell response to the pillars in that case), on asperities of dimensions of 100s nm focal contacts can only be formed on top of the pillars, or between nano-pits.

Therefore, the ultimate reason why the cells might not form mature focal contacts could be a reduction of available surface area. This hypothesis could reconcile the discrepancies with the

preliminary results (4.3) obtained on nano-pits, on which the cell surface coverage showed little or no difference if compared with the flat control. In the preliminary results, only the nano-pits with the largest diameter (P21-r) started to show a slight surface coverage reduction. In his thesis, Gallagher (Gallagher, 2003) cultured rat fibroblasts on nano-pits, and obtained similar results to these obtained on H90-r nano-pillars with human fibroblasts. In fact, the diameter of the nano-pits used by Gallagher was much wider (216 nm), resulting in an important reduction of the surface area directly available for adhesions (from 100% to 59%). Table 16 illustrates the surface reduction corresponding to different nanotopographies. Assuming that the cells can adhere only to the top of the surface, it is easy to understand why nano-pillars and nano-pits can have the same inhibiting effect on the formation of focal contacts, and why the regularity of the nano-pillars is not an important factor, as long as the geometry of the nanopattern does not allow the cell to adhere to most of the surface. This hypothesis could be verified by culturing cells on nanopatterns, protruding and hollow, whose surface area is purposely varied.

	H90-r (Figure 40i)	Gallagher (Figure 38)	P21-r (Figure 40k)	P13-r (Figure 40n)	P12-r (Figure 40q)
Diameter_	170 nm_	216 nm_	147 nm_	118 nm_	88 nm_
topography	pillars	pits	pits	pits	pits
Available top surface (%)	25	59	81	88	93

Table 13. Surface area available for focal contact formation on different nanopatterns (assuming cylindrical flat-topped pits and pillars).

The B.End3 endothelial cells had an opposite reaction than hTERT: even though the B.End3 initially spread less on the pillared surface, at 96 h the surface coverage of cells on the nanopattern was much higher than on the surrounding flat area. This seemed due to an increase in cell area, rather than to an increased number of cells on the pillars. In fact, on the nano-pillars the cells appeared to form a continuous monolayer. This surprising behaviour was corroborated by the immunofluorescent stain, which showed that the cells formed focal contacts on both flat and pillared surfaces. Similar results have been obtained by Dalby *et al.* (Dalby, 2002b), who observed an increased spreading area of human endothelial cells on 18-nm-high random nanoislands at 72 h. Since Goodman *et al.* (Goodman, 1996) showed that the subendothelial matrix is highly textured at the micro- and nano-scale, and that bovine endothelial cells assume a more *in vivo*-like appearance on nano-textured replicas, it seems that an appropriately textured substrate could be more suitable for the culture of endothelial cells. In conclusion, the reaction of B.End3 to the nano-pillars was more subtle than with the hTERT, and was not investigated as extensively. A thorough study of the reaction of endothelial cells to nano-pillared surface could provide new insights on the effect of

surface texture on cell adhesions, and possibly lead to the development of selective implant surfaces that would favour the adhesion of a desired cell type whilst inhibiting or rather reducing the probability of continuous adhesion of others.

A third cell type, rat calvaria bone cells, was also used. Unlike hTERT and B.End3, these were primary cells, thus their behaviour could be more indicative of the cell behaviour of this specific cell type. However, a disadvantage of a primary culture is that it is probably more heterogeneous than the cell lines. The bone cells had a reaction very similar to the one of hTERT, but less dramatic: at 96 h the surface coverage on the pillars was significantly less than on the flat surface, and the area of the cells on the pillars was smaller. A difference in focal adhesions could be detected: more mature focal contacts are visible on the flat surface rather than on the pillars, where the Vinculin looks less clustered. These results supported the hypothesis that the inability to form mature focal adhesions is the key to understand the reaction of some cell types to nano-pillars.

4.5.2.2 Protein-coated PCL

In order to investigate if a different surface chemistry could influence the proliferation-inhibiting effect of nanotopography on hTERT, the PCL replicas were coated either with PLL or Fibronectin, and the cell cultures were observed at confluence (96 h). The present data supports the observations by Gallagher (Gallagher, 2003), that the PLL coating did not diminish the effect of the nanopattern on cell behaviour. The hTERT coverage on the flat was still significantly higher than on the nanopatterned surface. On the other hand, the reaction of hTERT and bone cells to Fibronectin-coated replicas was very different from the PLL. The Fibronectin inhibited any effect of the nanopattern on cell coverage, since there was no difference in surface coverage between the nanopillared and flat area at 96 h. The immunofluorescent staining of Fibronectin-coated samples showed that the fibroblasts rearranged the Fibronectin on both the surfaces as expected (Pompe, 2005). A possible explanation of the difference between these two coatings is that the PLL molecules (150-300 KDa) did not significantly modify the surface topography, while the size of human Fibronectin (440-500 KDa or 5 nm diameter/ 55 nm length before dimerisation) might enable the molecules (and the fibrils that are formed by the cells) to simply hide the underlying nanopattern by bridging the gaps between pillars. This in turn seems to support the idea that nanopattern-induced surface area reduction is the main cause of decreased hTERT proliferation.

4.5.2.3 Gold-coated PCL

Another possible explanation of the effect of nanotopography on hTERT cells could be the formation of air pockets between nano-asperities. In Chapter 1 it was shown by contact angle measurements that air-trapping can occur on nano-pitted PCL surfaces. Unfortunately, it was not possible to measure the contact angles on H90-r PCL replicas, therefore it was necessary to resort to an indirect investigation. By coating the nanopattern with a very hydrophilic material such as

gold ($\theta \approx 30^\circ - 40^\circ$) (Churaev, 1995), it can be assumed that no air trapping could possibly occur; simple visual inspection of the substrates indicated a completely wettable surface (even though the actual contact angles were not measured).

Table 14 and Table 15 summarize the differences that were found between the hTERT cells on uncoated and gold-coated PCL at 96 h. Overall, the gold coating has the effect of hampering the differences induced by the nanotopography. When the PCL nano-pillars were gold-coated, their proliferation-inhibiting effect vanished, although the surface coverage difference was still significant. On the other hand, the density of focal adhesions was irrespective of the topography, while it was significantly different on the two chemistries (p-values in Table 11). However, while the cells are generally expected to attach more efficiently on hydrophilic surfaces such as gold (Vogler, 1998), the present results show that after 5 days the cells were more confluent on the hydrophobic PCL. This could be due to a different ECM secretion of the cells on the two different chemistries, following initial attachment.

These results do not disprove the suggestion that the proliferation of hTERT could be inhibited by the presence of air pockets between nano-pillars. This would justify the strong surface coverage reduction on uncoated PCL, and it would imply that on gold nano-pillars the cells can proliferate because there is no air. If this was the case, the fact that the surface coverage is still significantly different on gold-coated flat and nanopillared surface could be explained with an accelerated speed of migration on the pattern. This could be due to a modified adhesiveness of the substrate (Palacek, 1997) as a result of surface area reduction, and would result in an increased probability of finding the cells outside the nanopatterned area. Finally, it should be noted that the initial results of cell coverage were the same on ethanol-sterilised and UV-sterilised PCL replicas, and that both procedures would counteract the occurrence of air-trapping. In summary, this interpretation advocates a synergistic effect due to air-trapping and surface area reduction.

	Uncoated PCL		Gold-coated PCL	
	<i>Flat</i>	<i>Nano</i>	<i>Flat</i>	<i>Nano</i>
Surface coverage of cells (%)	58	15 (**)	30	24 (*)
Focal adhesions (μm^{-2})	0.004	0.003 (-)	0.0058	0.0056 (-)
Proliferating cells (%)	45	16 (**)	18	20 (-)

Table 14. Summary of HTERT analyses at 96 h. The p-values refer to the corresponding flat control. (**)
 $p < 0.01$. (*) $p < 0.05$. (-) $p > 0.05$.

	AuPd_flat	Uncoated_flat	AuPd_pillars	Uncoated_pillars
AuPd_flat		**	-	-
Uncoated_flat	**		**	**
AuPd_pillars	*	**		-
Uncoated_pillars	**	**	**	

Table 15. p-values from unpaired *t*-test (two-tailed assuming unequal variance) applied to the surface coverages and proliferating cell counts in Table 14. Grey: surface coverage. White: proliferation assay. (**)
 $p < 0.01$, (*) $p < 0.05$, (-) $p > 0.05$.

Future work should involve TEM imaging to confirm the adhesion of cells to the top of the nanopatterns, and the distribution analysis of focal adhesion sizes/types. The possible presence of air bubbles at the cell-substrate interface is a very important issue that should definitely be investigated further. Ideally, it would be very interesting to fabricate surfaces of identical topography and chemistry, but with controllable presence or absence of air-pockets. This would give information on the possible effect of air bubbles at the cell-biomaterial interface. A more straightforward but equally interesting study should involve the fabrication of nano-pillars with specifically chosen dimensions (diameter, height, centre-to-centre spacing) in order to prove the dependence of hTERT proliferation and speed of migration on the surface area available for focal contact formation. Finally, given the strongly different behaviour shown by fibroblasts and endothelial cells, the two cell types from the same species should be co-cultured. The study of cell behaviour in such mixed culture could help develop a “cell type-selective” surface.

Part II. Cells on arrays of irregular nano-pillars: preliminary comparison with regular pillars.

This section contains a set of preliminary results of cell culture on arrays of irregular nano-pillars of varying dimensions. It is shown that a systematic investigation of the effect of pillar size on cell behaviour is a necessity for the future.

4.6 Materials and Methods. II.

4.6.1 Fabrication and preparation of the replicas

Arrays of nano-pits of decreasing diameters (5X5 arrays of 2 mm² patterned squares) were fabricated in silicon wafers by the same procedure described in 2.2.1, page 23. All the masters were fabricated by Dr K. Seunarine. The diameters of the master nano-pits were measured with ImageJ (Rasband, 1997-2005) from SEM images. The silicon masters were not hydrophobised. Poly- ϵ -caprolactone (PCL) sheets were embossed on these substrata by melting the polymer on the pattern at 85°C and then pressing a glass-slide on it (“thumb-embossing”, see 4.2.1.1). After embossing and prior to cell seeding, the PCL replicas were sterilised by immersing them in 70% ethanol (BDH). Then they were rinsed in copious amounts of RO water and finally stored in Hepes Saline at 4°C. The dimensions of the replicated nano-pillars were not measured.

4.6.2 Cell culture

hTERT and B.End3 cells were cultured as detailed in 4.2.2. Another type of fibroblastic cells was also used: Baby Syrian Hamster Kidney cells (BHK 21 CL 13 (IZS), ECACC); these cells were passaged as described in 4.2.2. The growth medium was DMEM for hTERT and B.End3, and ECT for BHK21.

4.6.2.1 Cell seeding, fixation and staining

For seeding on the PCL replicas, the cells were resuspended in growth medium at a density of 1-1.5×10⁴ cells/ml, and 4 ml of suspension were placed on each sample, yielding a total of 4-6×10⁴ cells per sample. The cells were fixed at 3 h, 24 h and 72 h. Each time point was repeated 3 times. To fix the cells, the samples were rinsed with PBS at 37°C, incubated for 15 min in 4% formaldehyde/PBS at 37°C, and stored in PBS. The cells were then stained with Coomassie Blue for 15 min, and finally rinsed in PBS.

4.6.2.2 Imaging

Images of the whole replicas after Coomassie staining were acquired with a Nikon D1 camera (objective AF Nikkor, 35-70 mm). The cells were also observed under a Zeiss Axiovert 25 at X5

magnification. A camera (Scion Corporation) transmitted the images to a PC: images of the microscope field were captured with Visicapture (Scion Corporation).

4.6.2.3 Surface coverage analysis

Only the surface coverage of the hTERT cells was measured, because a 2 mm² area was too small to obtain significant statistics about individual cells (for e.g. cell numbers or areas). The surface coverage was calculated as the ratio of black pixels/total pixels in the thresholded Nikon images (ImageJ)(Rasband, 1997-2005). The values from equivalent squares on the three samples were averaged, and an average value for the “flat” control was obtained by averaging all the non-patterned areas together. This is schematically represented in Figure 78, which also shows the nomenclature used to designate the different squares.

4.7 Results. II.

4.7.1 Fabrication

Figure 76 shows the SEM images of the silicon master consisting of an array of nano-pits, with diameters ranging from 68 to 188 nm (Table 16). SEM pictures of the embossed PCL replicas revealed an array of irregular but ordered nano-pillars (Figure 77). The replicate of the smallest pits (diameter 68 nm) were not detected under the SEM, so they were not considered for the cell surface coverage analysis. For clarity, the position of the images of the replicas (shown in Figure 77) parallel the arrangement of the images of their corresponding “source” nano-pits on the master (Figure 76), i.e. the pillars in Figure 77a are embossed from the pits in Figure 76A, etc. In reality, the replicated nano-pillars will have a mirror-like arrangement as illustrated in Figure 78. The nano-pillars had a rather elongated, stretched shape and they tended to collapse on the surface.

L 167 ±4	M 167 ±3	N 173 ±4	O 178 ±4	P 188 ±5
K 165 ±4	J 158 ±3	I 156 ±4	H 150 ±4	G 142 ±3
B 107 ±4	C 113 ±4	D 116 ±5	E 131 ±3	F 140 ±4
A 97 ±5	68 ±7			

Table 16. Diameters of the nano-pits on the different squares of the silicon master, corresponding to the images in Figure 76.

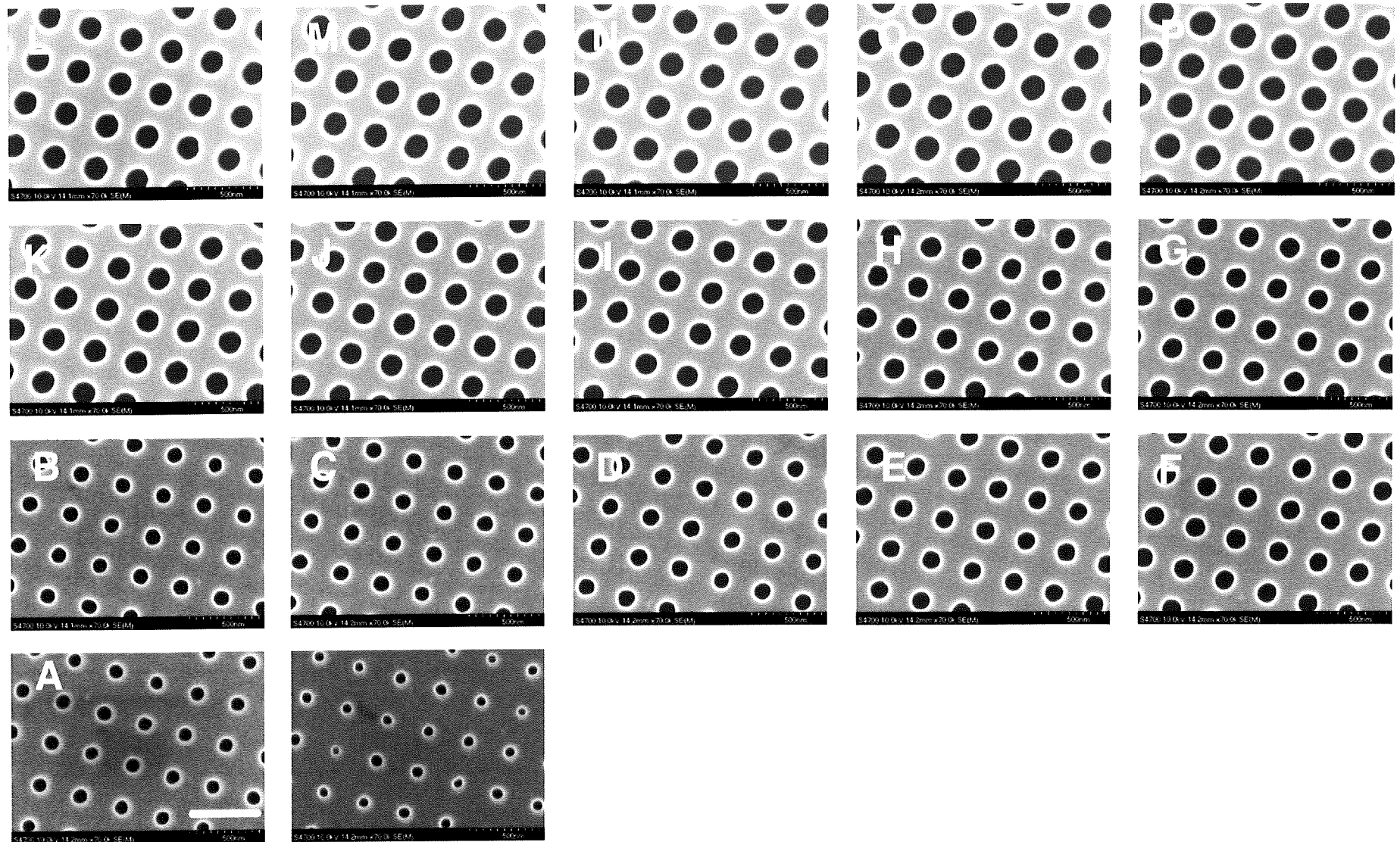


Figure 76. SEM images of the nano-pits that are patterned on each square of the array. The position in this image corresponds to the position of the square on the master. Scale: 500 nm.

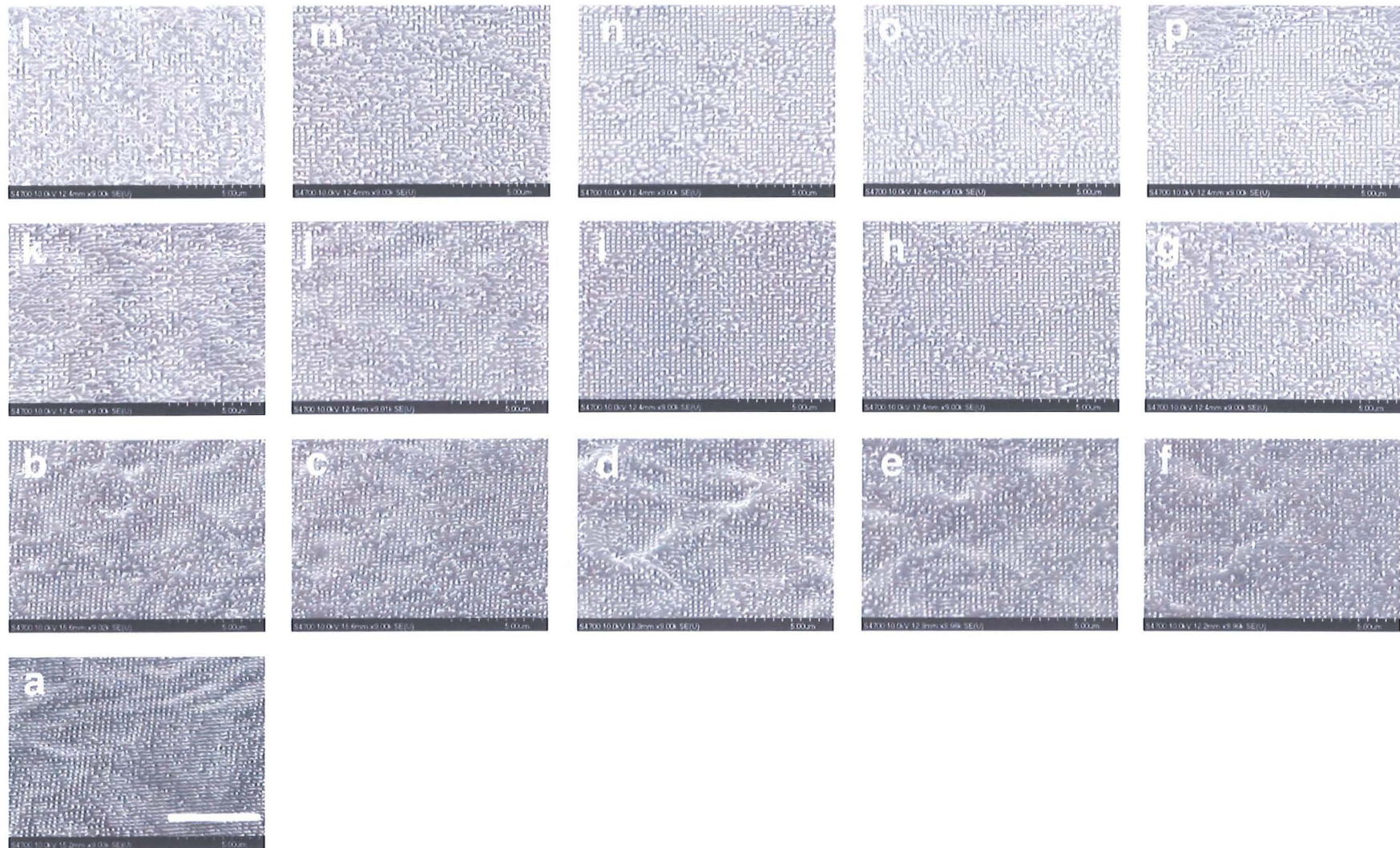


Figure 77. SEM images of the PCL nanopillared replicas: each image shows the nano-pillars in each square of the array. The position of the patterns in this image corresponds to the position of the corresponding nano-pits on the silicon master in Figure 76. In reality, after embossing the nano-pillars will have a mirror-like arrangement compared to the master, as illustrated in Figure 78. Scale: 5 μm .

4.7.2 Cell culture: hTERT

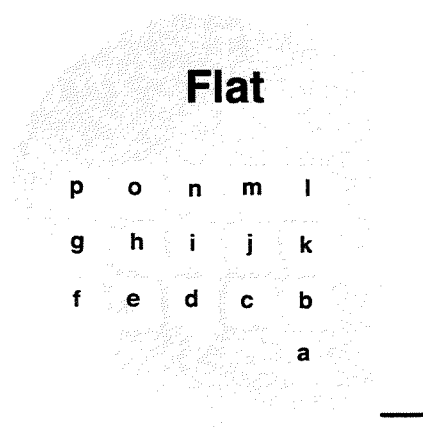


Figure 78. Schematic representation of a PCL replica, and the nomenclature associated with each nanopatterned square. (a) corresponds to the smallest pillars, (p) to the biggest ones. The diameter increases in a raster-scan manner. All the area outside the square is considered to be the “Flat” control. Bar: 2 mm.

Figure 79 shows the results of surface coverage measurements of hTERT after 3 h, 24 h and 72 h. The surface coverage was measured from the images in Figure 80, which shows the overview pictures of the PCL arrays seeded with hTERT and Coomassie-stained. At 3 h the coverage was rather independent from the location on the sample. The dependence of the cell coverage on pillar diameter did not show a clear trend, which could be also due to the underlying non-uniformity of cell density over the surface. At 24 h, the coverage decreased from flat to square “a”, then it seemed constant, except for “f”. At 72 h, the coverage seemed to decrease steadily until square “d”, then it appeared to remain constant except “k” and “l”). There were some denser areas, due to the occasional non-uniformity of the initial cell culture.

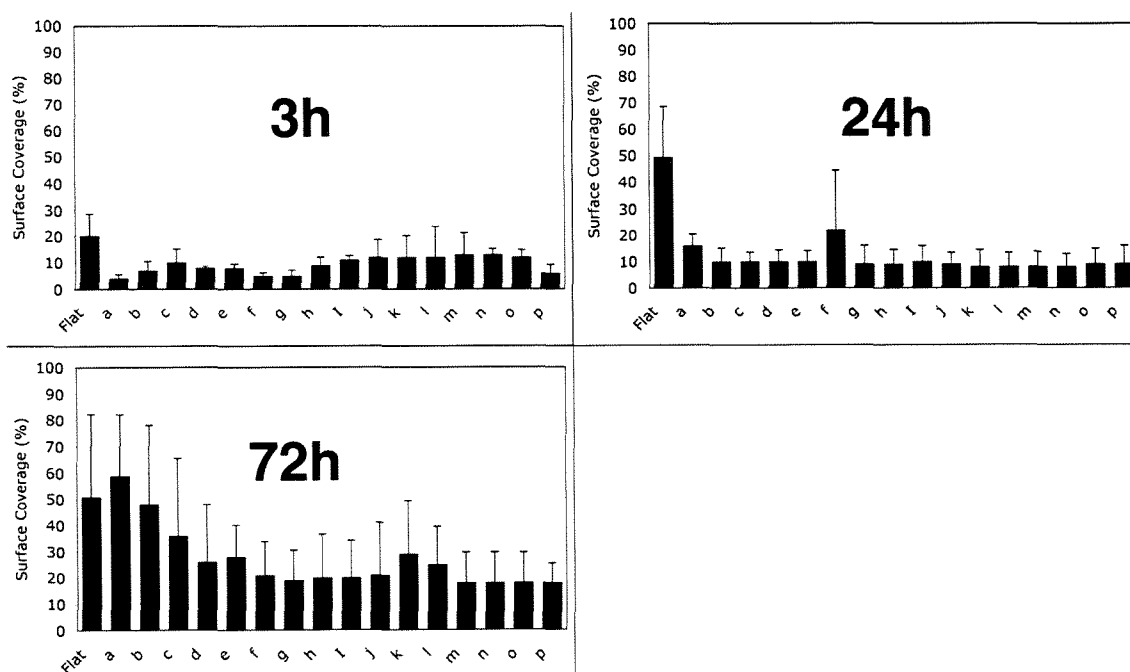


Figure 79. Surface coverage of hTERT cells on the different nanopatterned squares as function of time. At 3 h the coverage was rather independent from the location. At 24 h the coverage looked constant after square “a”, at 72h it seemed constant after square “d”. Results are mean±standard deviation, $n=3$.

Figure 81 is a montage of several microscope images (Zeiss Axiovert 25, X5 magnification), showing the area between nano-pillared squares (p, o, g, h): it can be seen that the “flat” stripes between nanopatterns were covered with cells, while on the patterns the cells were very sparse, and sometimes clustered.

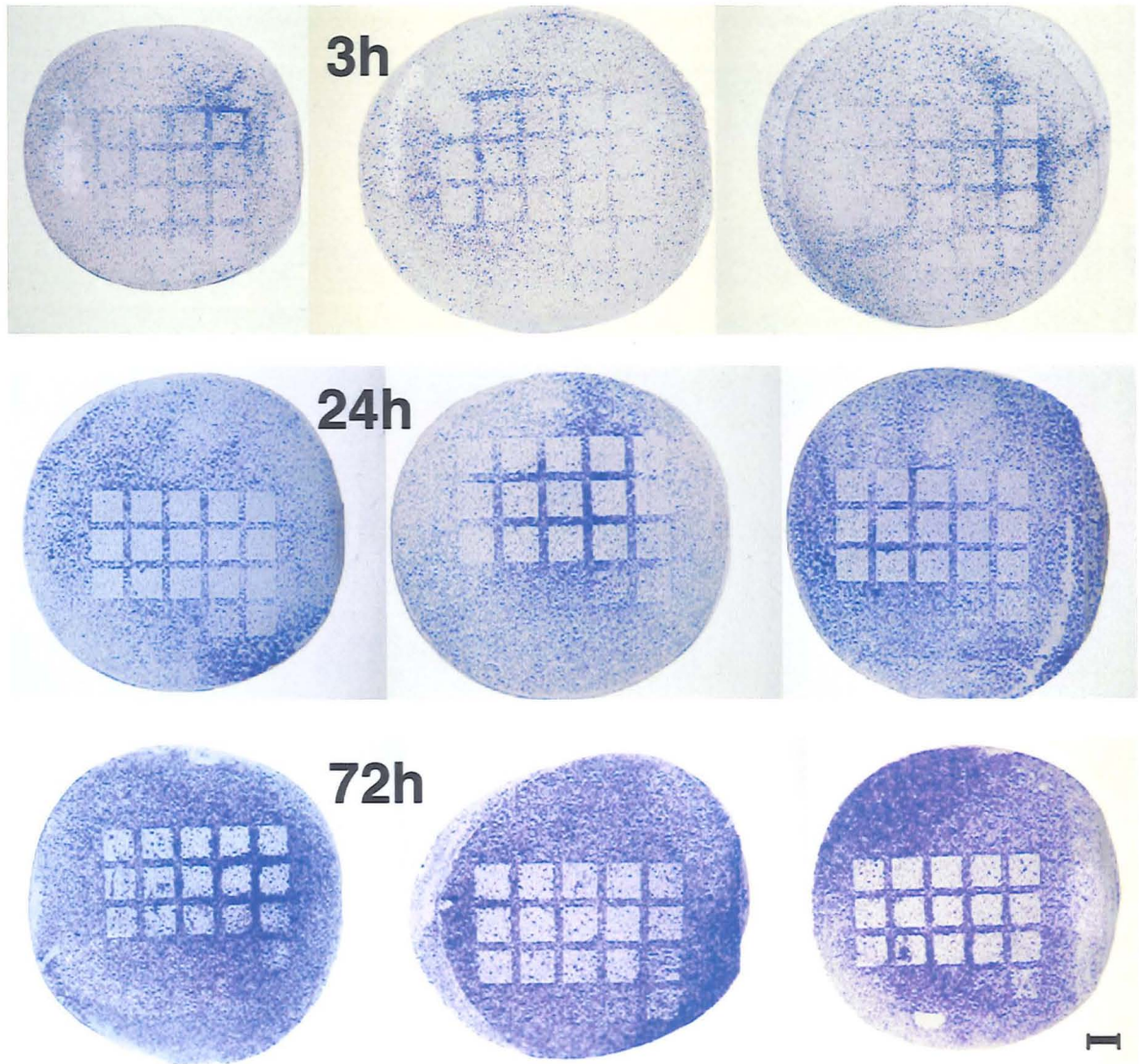


Figure 80. Overview pictures of hTERT culture after cell fixation at different time points. Blue colour indicates the presence of cells. Bar: 2 mm.

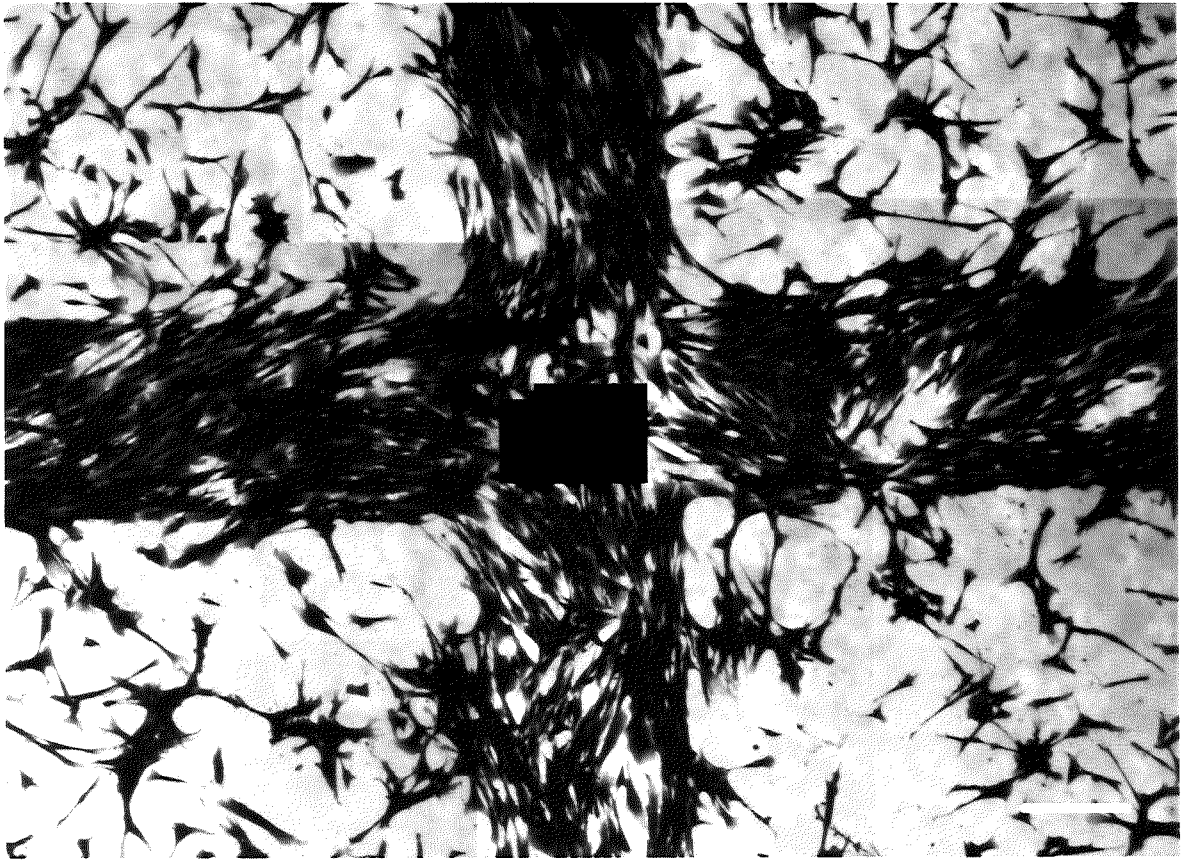


Figure 81. Montage of bright-field images of Coomassie-stained hTERT cells at 96h. The image shows the corner between four nano-pillared squares (p, o, g, h). It can be seen that the “flat” stripes between nanopatterns are covered with cells, while on the patterns the cells are very sparse or clustered. Bar: 0.5 mm.

4.7.3 Cell culture: B.End3

Figure 82 shows the overview pictures of the PCL replicas seeded with B.End3 and Coomassie-stained at 3 h, 24 h, and 72 h. Figure 83 is a montage of several microscope images (Zeiss, X5 magnification), showing the area between nano-pillared squares (p, o, g, h). Unlike hTERT, the endothelial cells did not seem to be less confluent on the pattern: instead, they formed a monolayer of spread cells which were much more uniform than the cells on the non-patterned area (which were denser and arranged less orderly).

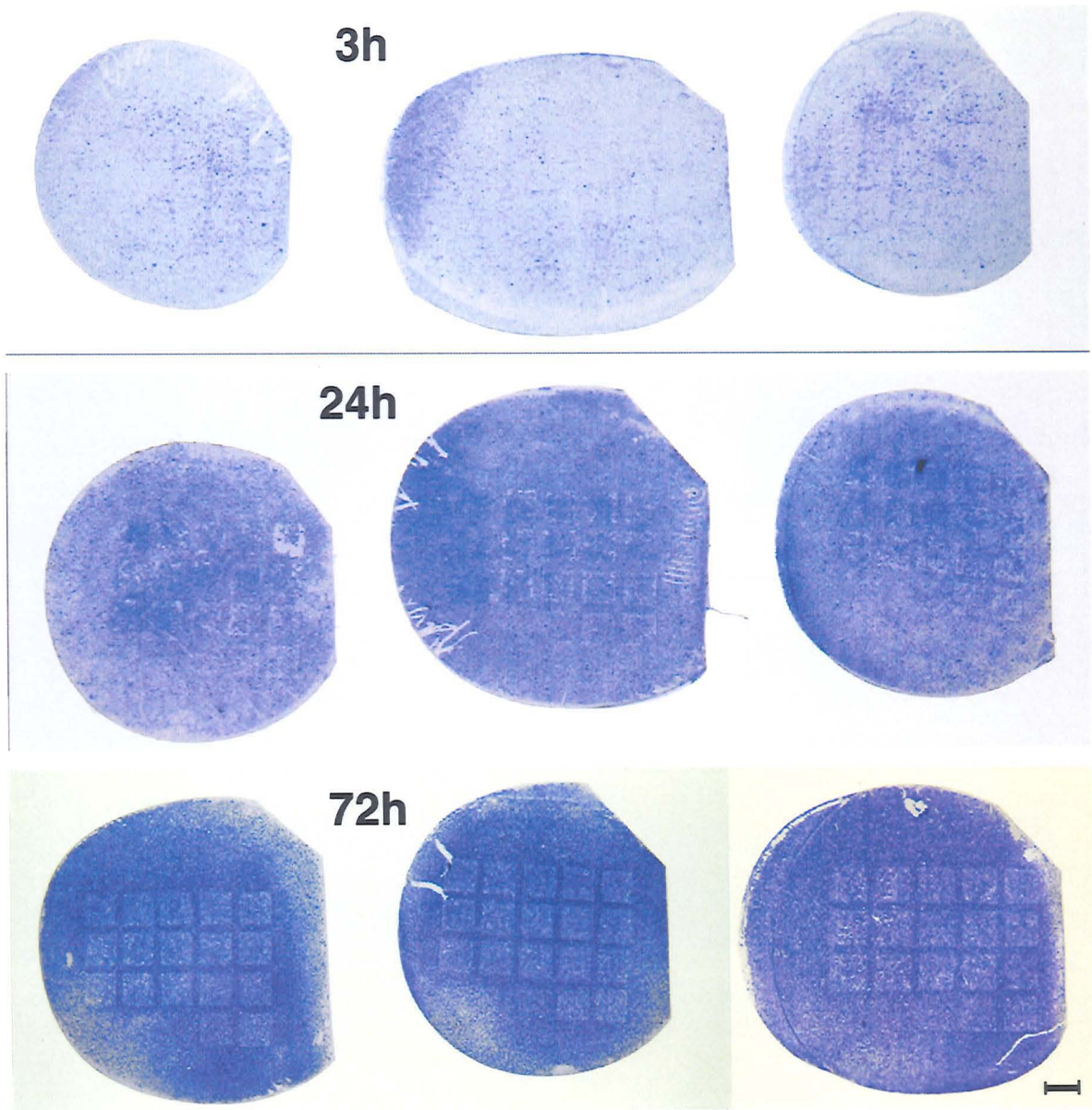


Figure 82. Overview pictures of B.End3 culture after cell fixation at different time points. Blue colour indicates the presence of cells. Bar: 2 mm.

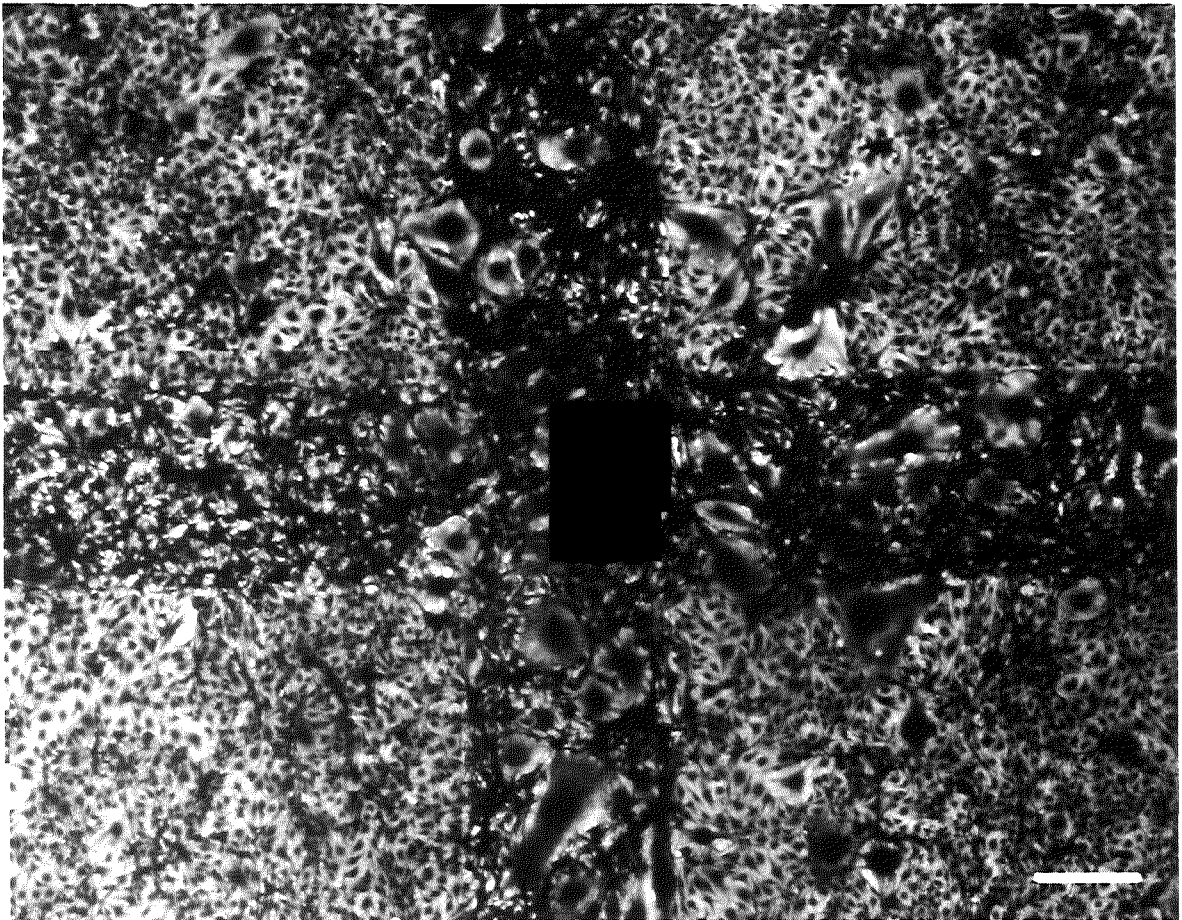


Figure 83. Montage of bright-field images of Coomassie-stained B.End3 cells at 96h. The image shows the corner between nano-pillared squares (p, o, g, h). The cells on the “flat” stripes between nanopatterns are much more packed than the cells on the patterns, which seem to form a uniform monolayer. Note the presence of giant cells, particularly on the flat stripes. Bar: 0.5 mm.

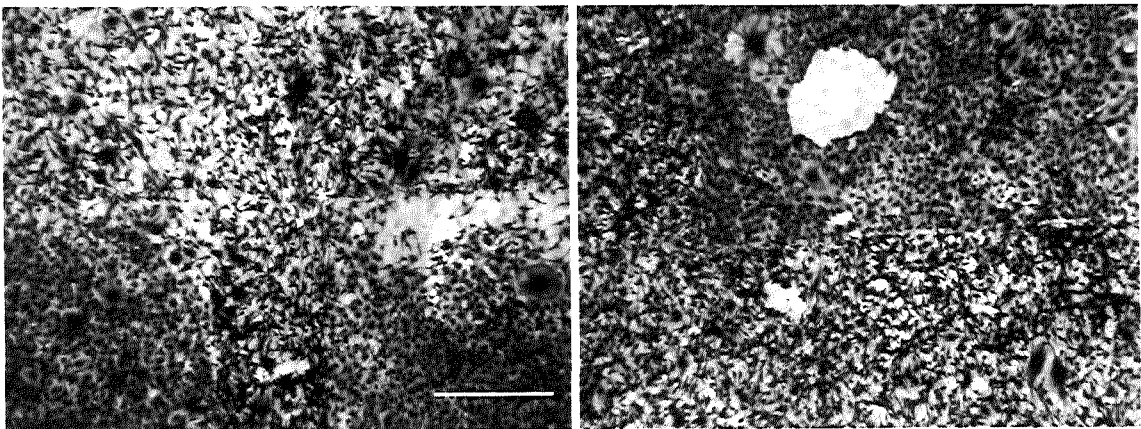


Figure 84. Bright-field images of Coomassie-stained B.End3 cells at 96h. The image shows the corners between nano-pillared squares. The cells on the patterned squares seem to form a uniform monolayer. This makes the pattern boundary self-evident. Bar: 0.5 mm.

4.7.4 Cell culture: BHK21

Figure 85 shows the overview pictures of the PCL replicas seeded with hTERT and Coomassie-stained at 3h, 24h, and 72h. Figure 86 is a montage of several microscope images (Zeiss Axiovert 25, X5 magnification), showing the area between nano-pillared squares (p, o, g, h the “flat” stripes

between nanopatterns were covered with cells, while on the patterns the cells were very sparse, and sometimes clustered. These images are similar to the ones obtained with hTERT.

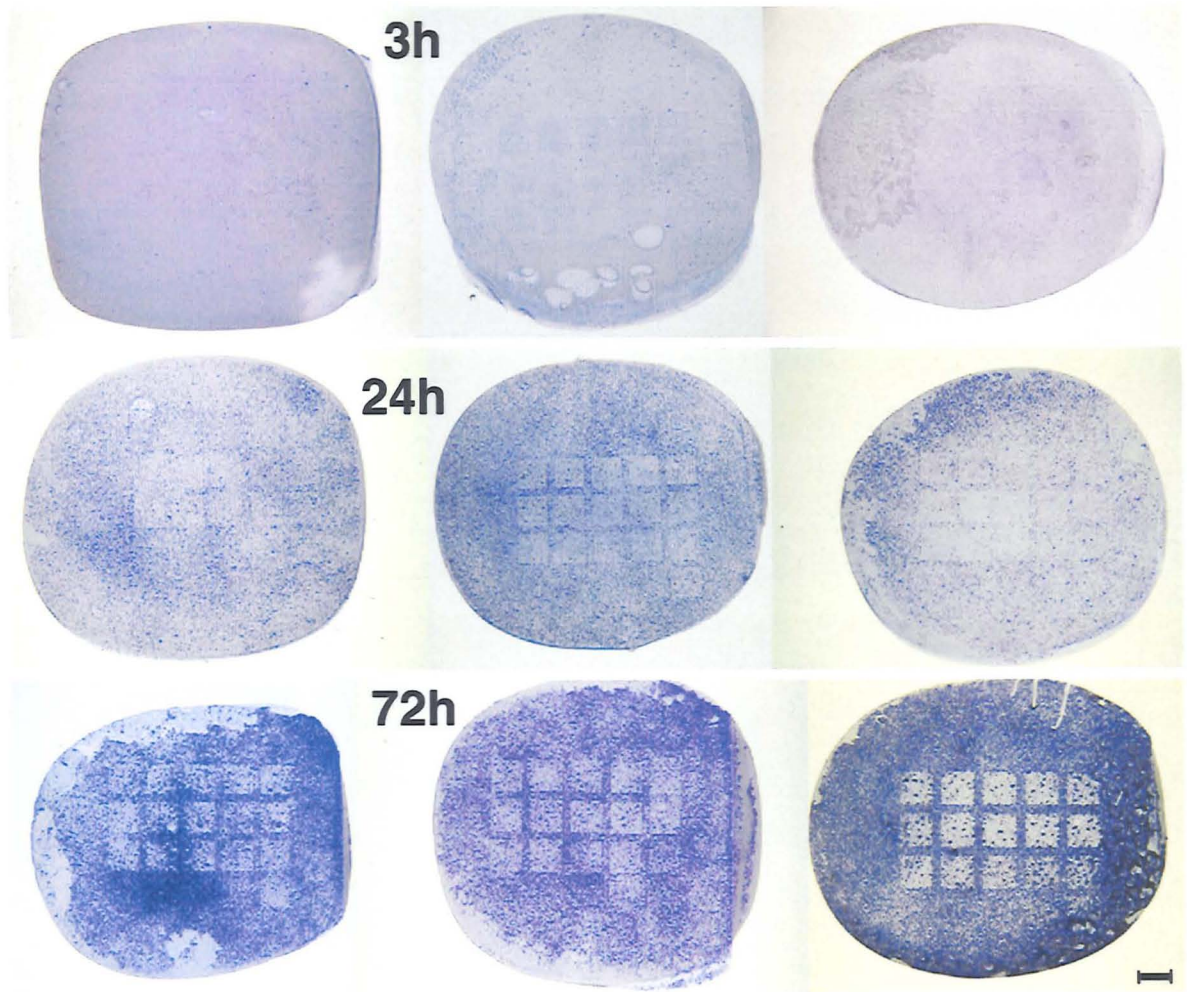


Figure 85. Overview pictures of BHK21 culture after cell fixation at different time points. Blue colour indicates the presence of cells. Bar: 2 mm.

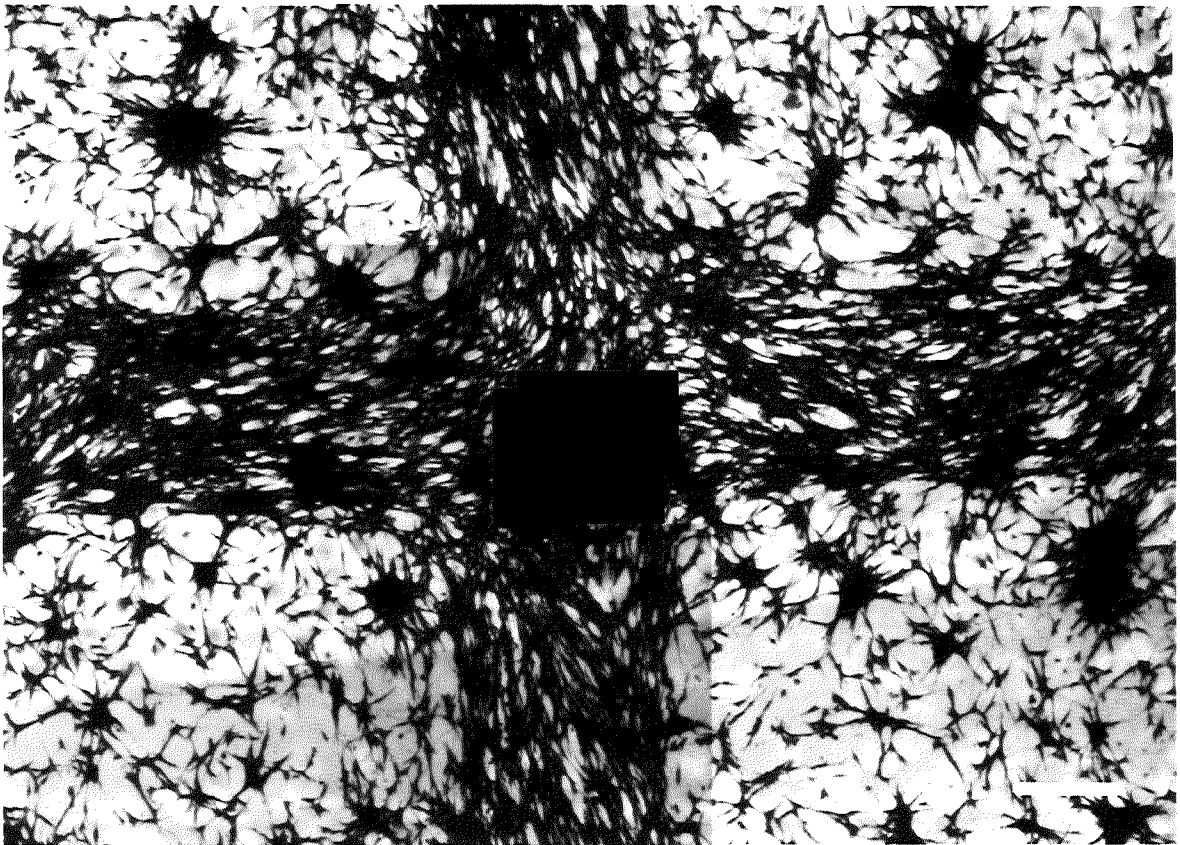


Figure 86. Montage of bright-field images of Coomassie-stained BHK21 cells at 96h. The image shows the corner between four nano-pillared squares (p, o, g, h). It can be seen that the “flat” stripes between nanopatterns are covered with cells, while on the patterns the cells are more sparse, or clustered. Bar: 0.5 mm.

4.7.5 Cell culture: comparison between regular and irregular nanopatterns.

HTERT and B.End3

As a final crosscheck, hTERT cells and b.End3 cells were cultured at the same time on both the regular H90-r nano-pillars used in Part I, and on the 5X5 array of irregular nano-pillars used in Part II. The cells were fixed at 72 h and Coomassie-stained. The overview pictures of the hTERT cultures and B.End3 cultures are shown in Figure 87 and

Figure 88, respectively. The cell surface coverage was very similar on both regular and irregular nano-pillars: the surface coverage of hTERT was much lower on the pillars than on the flat areas, while the B.End3 formed patches of monolayer-like sheets (light-blue areas) on the nanopatterns.

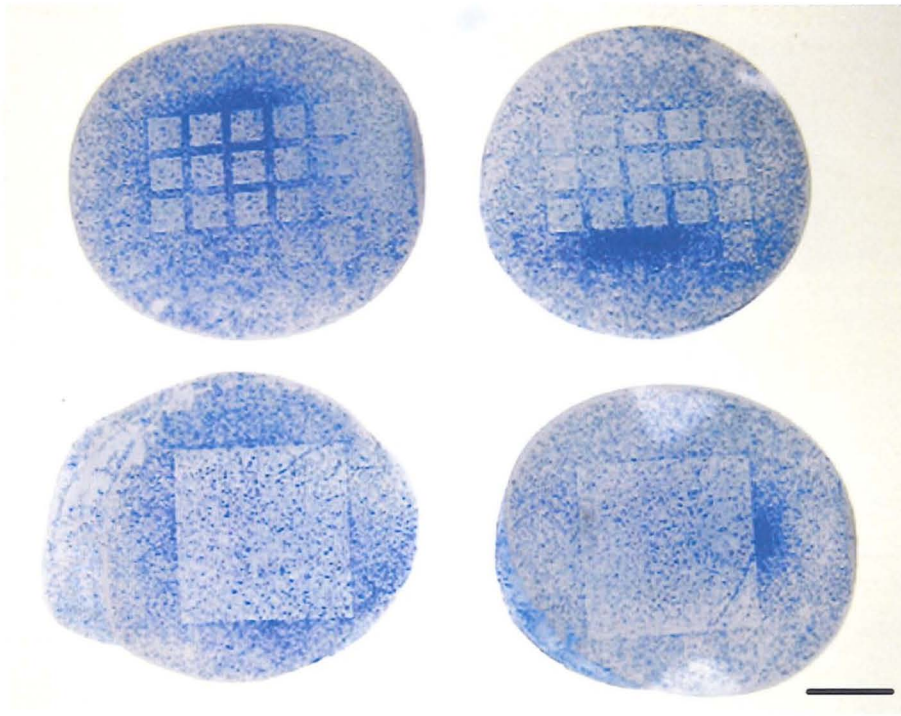


Figure 87. Overview pictures of hTERT cells on PCL with nanopatterned areas, Coomassie-stained at 72 h, on irregular (top row) and regular "H90-r" (bottom row) PCL replicas. The surface coverage appearance is very similar on all samples. Bar: 5 mm.

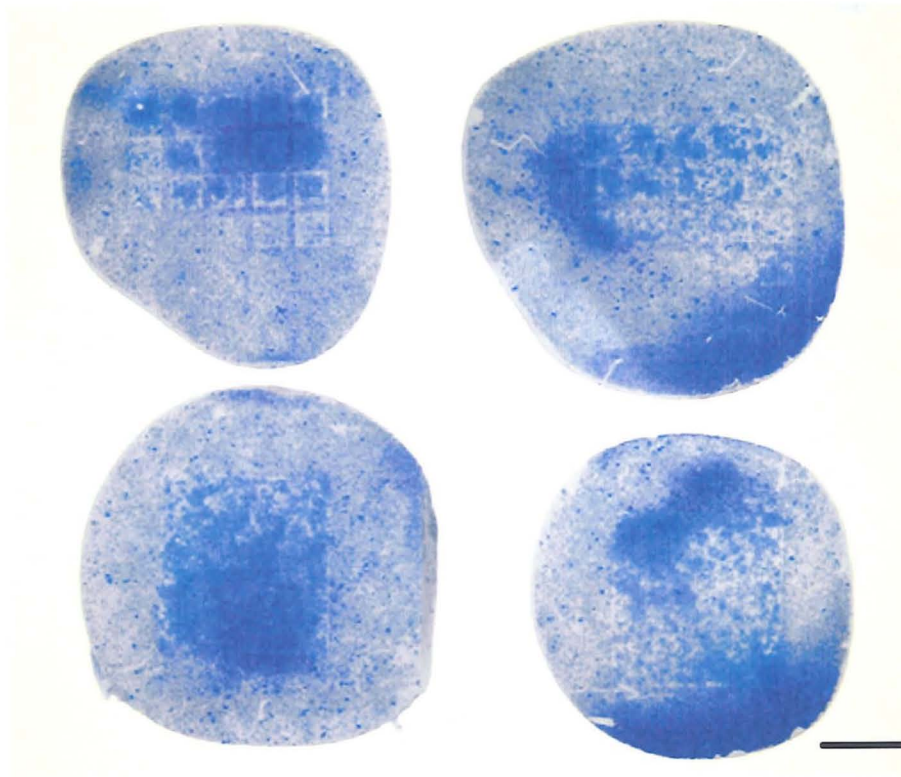


Figure 88. Overview pictures of B.End3 cells on PCL with nanopatterned areas, Coomassie-stained at 72 h, on irregular (top row) and regular "H90-r" (bottom row) PCL replicas. The surface coverage appearance is very similar: the light-blue patches indicated the presence of a monolayer. Bar: 5 mm.

4.8 Discussion II. Regular or irregular nanopatterns?

Unlike the nano-pillars in Part I, which were embossed from a hydrophobic master, the arrays of irregular nano-pillars in Part II were embossed from an untreated silicon master (i.e. hydrophilic): the resulting PCL pillars were more elongated, and of a stretched shape that tended to collapse on the surface. This could very well be due to a stronger adhesion between the polymer and the master stamp, which resulted in extension of the pillars during demolding.

From the second part of this chapter, it appears that the surface coverage of both fibroblastic cell lines used herein (hTERT and BHK21) on irregular nano-pillars is very low. However, the dependence of the cell coverage on pillar diameter does not show a clear trend. At 72 h, the coverage seems to decrease steadily until square “d”, then it appears to remain constant. Since the initial surface coverage is non-zero all over the sample, the different surface coverage at 72 h can be explained either by cell migration outside the nanopatterned squares, by apoptosis (cell death) on the nano-pillars, or by reduced or inhibited cell proliferation on the pillars. On the other hand, the endothelial cells B.End3 seem more spread on the pillars, and look as if arranged in a monolayer. As already suggested in the previous Discussion, it might be that a textured pattern is more reminiscent to the natural extra-cellular matrix of endothelial cells. Hence, the increased confluence.

These results are consistent with Wieland *et al.*'s previous observations of human fibroblasts (Wieland, 2002) and rat osteoblasts (Wieland, 2005) cultured on Ti substrates of increasing surface roughness: they determined that while the cell volume remained constant, cell thickness increased with substrate roughness, which leads to the conclusion that the cells were also less spread. Because cell spreading is a pre-requisite for fibroblasts to proliferate, proliferation could have been inhibited on their Ti substrates. Thus, even though the reasons for less surface coverage on these irregular nano-pillars was not investigated, it is likely that it relies on the inhibition of proliferation, rather than on selective cell migration outside the pattern. This would be coherent with the results from Part I. Besides, if the cells are assumed to form adhesions only with the top surface, the surface coverages would suggest that there is a threshold pillar size below which the cells can form adhesions with the bottom surface. Finally, a role for air-trapping cannot be excluded even on the irregular nano-pillars.

4.9 Conclusion

The results of cell culture on regular and irregular nano-pillars were very consistent, indicating that nano-pillars of order of 100 nm can inhibit the proliferation of fibroblastic cells, while favouring the spreading and the formation of a confluent monolayer of endothelial cells. It can be concluded that the cells are not as sensitive to the regularity of the asperities, as to their average size and centre-to-centre distance. The results of hTERT coverage on irregular nano-pillars confirm that a systematic variation of asperity size and spacing is a necessary future step to follow up this investigation.

All the results are consistent with the hypothesis that the availability of surface sites for ligand clustering is at the origin of fibroblast behaviour. Therefore, it is postulated that the main reason behind the lack of proliferation of hTERT cells on PCL nano-pillars is the inability of fibroblasts to form mature focal adhesions. It seems reasonable to assume that the cells will adhere to the top of the asperities. Therefore, in the light of previous studies on nano-pits (Gallagher, 2003) and nano-pillars (Dalby, 2004), it is suggested herein that the main mechanism responsible for the suppression of focal adhesion formation is the reduction in surface area due to the nanopatterns. However, there might also be a role for air-trapping between nano-pillars or inside nano-pits. When the PCL nano-pillars were gold-coated, the proliferation-inhibiting effect of the nano-pillars disappeared.

Endothelial cells were not only able to form focal adhesions, but also formed a confluent and cobble-stone-looking monolayer on the nano-pillars. Differential cell responses were also observed by Turner *et al.* (Turner, 1997) and Clark *et al.* (Clark, 1991), as discussed in 4.1. This cell-type dependent, differential effect on cell adhesion makes these nano-pillars most interesting for the possible development of “cell-selective” surfaces.

5 Cell flow on nano-pits

Rat Epitenon cells have been shown to react strongly to nanotopography in static culture (Gallagher, 2002): when cultured on PCL nano-pits, their proliferation was strongly inhibited, and their migration rate highly increased. Therefore, it seemed interesting to investigate the behaviour of these cells on nano-pits when the forces acting on the cells were different. In this chapter, a parallel-plate flow chamber was designed and built, and a suspension of Rat Epitenon cells was made to flow over a nano-pitted sample of poly-methyl-methacrylate. In order to establish a baseline, the initial cell adhesion on the nano-pits and the flat control was quantified and compared.

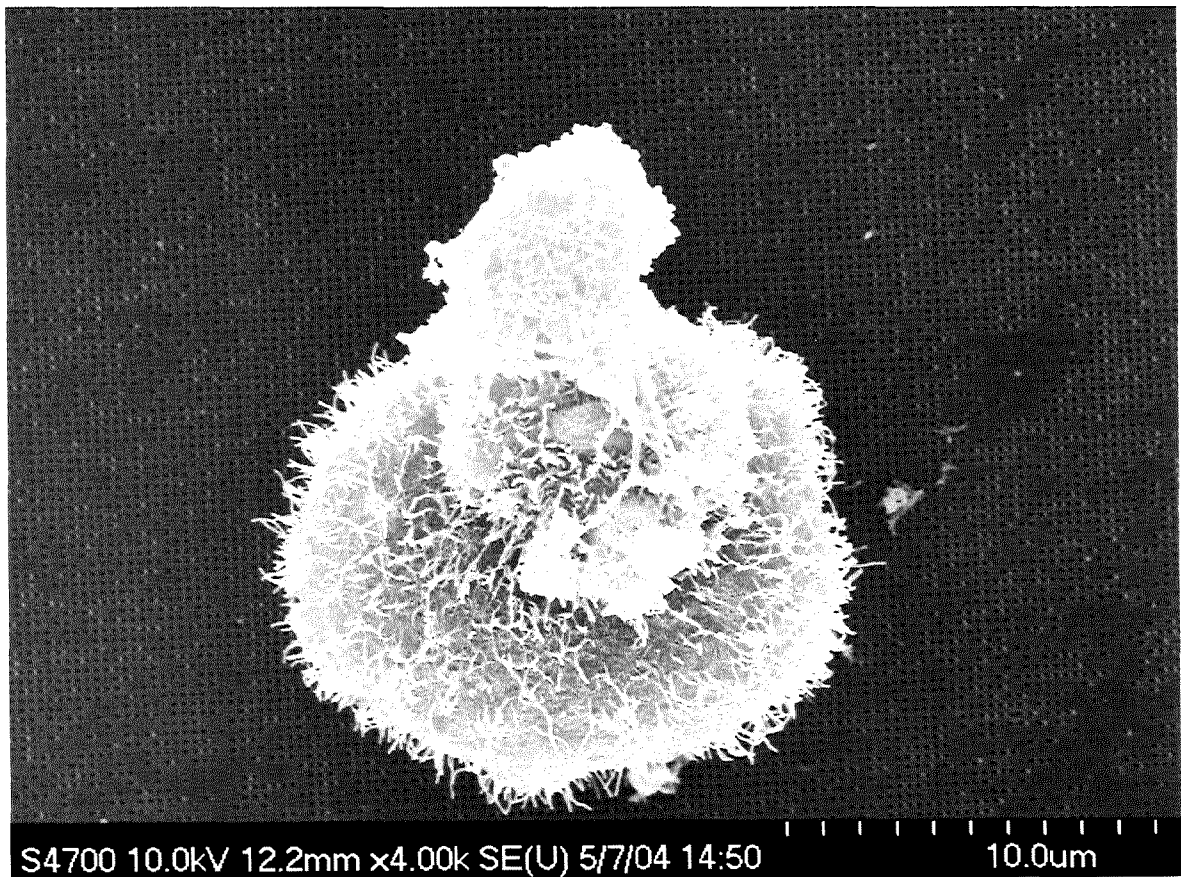


Figure 89. Epitenon cell on nano-pitted PMMA after 24 h in static culture.

5.1 Introduction

Cell adhesion under flow conditions has a very important role in many physiological functions, e.g. in the immune and developmental system. In the living body many cells are always surrounded or transported by actively moving fluids (e.g. blood cells, lymphatic and endothelial cells in the circulatory system). Making cells flow over a substrate can change their adhesion process, binding strength and morphology if compared with a static culture (Bongrand, 1994, Doroszewski, 1977, Stavridi, 2003, Van Kooten, 1992). Not only it is, perhaps, physiologically correct to culture cells in a flow, but it allows the investigation of phenomena, like the rolling motion of leukocytes (Tissot, 1992) or the migration of granulocytes (Doroszewski, 1988), whose mechanisms are still poorly understood. A number of flow chambers have been developed through the years, including parallel-plate flow chambers and stagnation-point flow chambers, which have been used to study, among others, cell adhesion, bacterial adhesion, microsphere deposition and receptor-ligand bonds (Dvorak, 1971, Pierres, 1996, Poyton, 1970, Spring, 1978, Van Kooten, 1992, Yang, 1999).

Gallagher *et al.* (Gallagher, 2002) claimed that 60-150 nm diameter pits on a 300 nm pitch in poly- ϵ -caprolactone had a marked effect in reducing epitenon cell adhesion in static cultures. Their work was carried out in static conditions, where Brownian motion, gravity and perhaps convection are the main forces acting on cells.

The aim of this work was to compare epitenon cell adhesion on nano-pits from a sedimenting suspension (Gallagher, 2002) to cell adhesion from a flowing suspension, where the main acting forces were hydrodynamic. For this purpose a parallel-plate flow chamber was built, where the cells could flow steadily over poly-methyl-methacrylate nano-pits (diameter 90 nm, height 100 nm and pitch 300 nm). This system allowed real-time and unobtrusive observation of flowing cells. Cell adhesion on the nano-pits was quantified after 1 hour, in order to determine if the nanotopography had an influence in the initial formation of cell-substrate bonds.

5.2 Materials and Methods

5.2.1 Fabrication of the nanopatterns

The fabrication of nanopatterns in PMMA was done in three steps (Gadegaard, 2003b), as shown in Figure 90. First the pattern was written in the resist layer by electron beam lithography (Figure 90a), then the nanopatterned resist was used as a template for electroplating a nickel shim (Figure 90b), and finally the PMMA samples were embossed in the shim (Figure 90c).

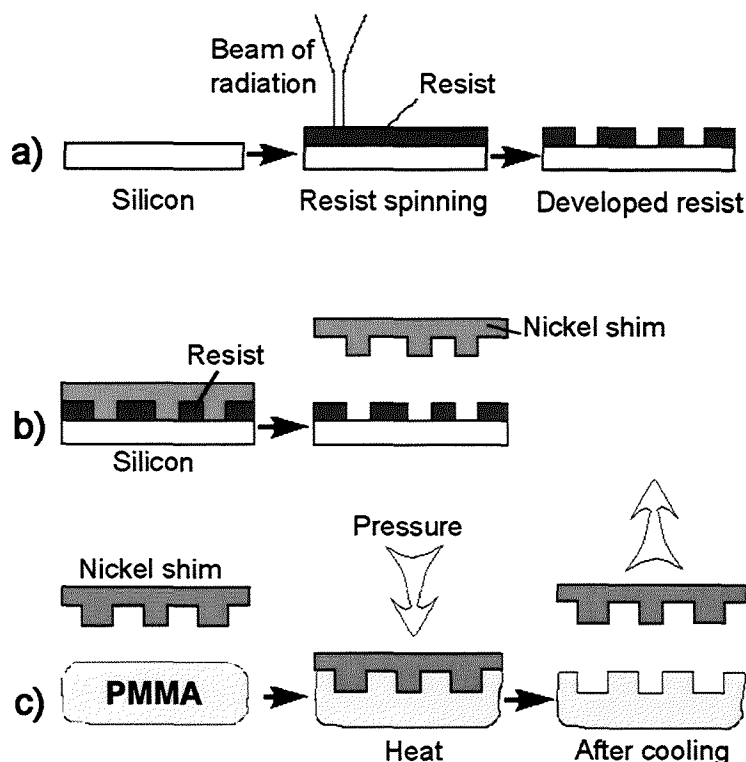


Figure 90. Schematic representation of the fabrication of nano-pits in PMMA. a) Electron beam patterning and development of the template in the resist; b) Electroplating of the nickel shim; c) Replication of the nickel shim in polymer (PMMA).

5.2.1.1 Resist template

A silicon sample (70 mm × 30 mm) was cut from a silicon wafer and spin-coated with 40%ZEP520A at 5 krpm (100 nm thick coating), then baked at 180°C for 1 hour. The sample was then exposed in the e-beam writer (Leica EBPG5-HR) and developed in *o*-xylene for 60 s (Figure 90a). Finally, the template was rinsed in RO water and blow-dried in N₂. This master resist template had of a square area (15x15 mm²) in the middle, which carried a nano-pitted pattern (pits of diameter 120 nm, depth 100 nm and spacing 300 nm). The template was fabricated by Keiran McGhee.

5.2.1.2 Nickel shim

A nickel shim had to be embossed in the polymer instead of a silicon template, because the latter could have been damaged by the embossing: for this reason, a shim was created after the master die by electroplating (Figure 90b); thus, the shim was the mold which carried the negative image of the nanopatterned resist template, i.e. nano-pillars of diameter 113±6 nm (as measured with ImageJ (Rasband, 1997-2005) from the SEM image seen in Figure 94b), depth 100 nm and spacing 300 nm. John Pedersen kindly performed all electroplating at SDC Denmark A/S under standard industrial conditions. Masters were mounted with UV adhesive on glass plates with a diameter of 160 mm used for CD and DVD manufacturing. A thin (50-100 nm) seeding layer was deposited on

the glass plate and masters by either sputter coating with a nickel vanadium alloy or by evaporation of nickel. The seeding layer acted as electrode in the subsequent electroplating, where nickel ions in a nickel sulfamate (290 g/l) solution were reduced on the seeding layer, and deposited. The process was stopped when the total thickness of the shim, had reached 200-285 μm . The temperature of the bath was kept at $52\pm 1^\circ\text{C}$ and pH 3.8-4.0. Boric acid was added (50-60 g/l) as pH buffer. The electroplating process was executed with a current density of 21 A/dm^2 in DC mode (Gadegaard, 2003a).

5.2.1.3 Polymeric replicas

Poly-methyl-methacrylate (PMMA, GoodFellow UK, 1 mm thickness) was chosen because of its biocompatibility and physical properties (transparent, suitable melting temperature $> 60^\circ\text{C}$). Rectangular samples (60 mm \times 20 mm) were cut from the PMMA sheets. In the Nanoimprinter (Obducat, Sweden), the PMMA was embossed into the nickel shim (temperature 180°C at 15 bars for 300 s), as shown in Figure 90c, then it was cooled to 50°C by a flow of nitrogen gas and demolded. As a result, a square nano-pitted pattern ($15\times 15 \text{ mm}^2$) was embossed in the middle of the PMMA replicas. The nano-pits on the PMMA had a diameter of $90\pm 7 \text{ nm}$ (as measured with ImageJ (Rasband, 1997-2005) from the SEM image seen in Figure 94b), depth 100 nm and spacing 300 nm; these samples were used as the bottom wall of the flow chambers, on which the cells were observed.

The embossed PMMA substrates were sputter coated with AuPd (Emscope, Ashford, UK)), then examined by a Hitachi S800 Scanning Electron Microscope at a voltage of 10 keV.

5.2.2 Fabrication of the flow chamber

The flow chamber (Figure 91) was designed to achieve a laminar flow (see 5.6 for details of the calculations). The embossed PMMA substrates were sonicated in ethanol (Analar) for 1 min and in RO water for 2 min, then further rinsed in RO water twice, and blow-dried.

The internal shape of the chamber was cut in a sample of thermoplastic polymer (50 mm \times 15 mm, thickness=170 μm , Nescofilm, Bando Chemical Ind. Ltd, Japan) around a metal master (custom-made in the IBLS Mechanical Workshop), in order to create a waterproof gasket for the flow chamber. Two circular holes (of diameter 2.5 mm, spaced 39 mm) were micromachined into ordinary glass slides (25 mm \times 75 mm, BDH) in the Electronics and Electrical Engineering Mechanical Workshop. These holes provided the inlet and outlet of the flow. The modified glass slides were cleaned by sonicating them for 10 min in each of the following: Opticlear, acetone, isopropanol and RO water, and finally blow-dried with N_2 .

The parallel-plate flow chamber (Figure 91) was constructed by clamping the thermoplastic gasket between the modified glass slide and the patterned PMMA substrate using glass coverslips (0.15 mm thick) as spacers. The whole system was then incubated at 50°C for 12 h; the heat melted the gasket, thus sealing the chamber. The spacers kept the height of the chamber at 0.15 mm. The chambers for the flat controls were built by using a non-embossed PMMA sheet instead of a patterned one.

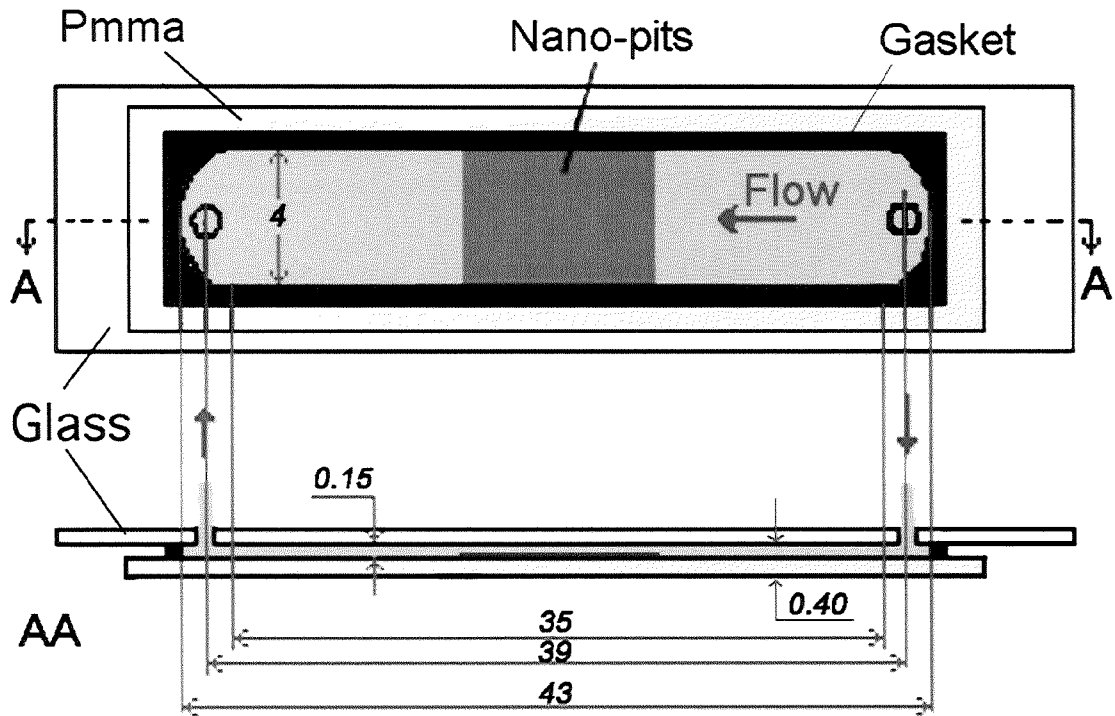


Figure 91. Dimensions and structure of the parallel-plate flow chamber.

5.2.3 Flow apparatus

A schema of the flow apparatus can be seen in Figure 92.

The flow chamber (Figure 93c) was inserted in a flow cell. The flow cell (custom-made by the IBLS Mechanical Workshop, see Figure 93b) consisted of a hollow transparent parallelepiped which contained the internal pipes that led the flow to the inlet of the chamber; similar pipes conveyed the outflow. A hollow metal plate was connected to the transparent block by four screws. When the chamber was placed against the corresponding inlet/outlet of flow, the screws were tightened manually, thus fixing the chamber in the cell. The PVC pipes (of bore diameter 0.5 mm, Altec, Alton Hants, UK) were connected to the extremities of the internal pipes of the flow cell.

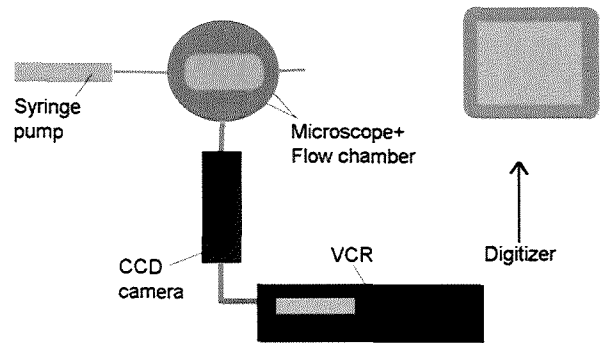


Figure 92. Schematic representation of the flow apparatus.

A 5 ml syringe (BD Plastipak, Spain) containing 3 ml of cell suspension generated the flow from the syringe-pump (Figure 93a), kept at a constant flow rate of $0.13 \mu\text{l/s}$. The flow reached the flow cell through the pipes, then the chamber through the first circular inlet. The chamber was observed under an inverted microscope (Leitz Diavert). A CCD camera (Panasonic VW-BL600) captured bright-field images with a 2.5X objective, which were recorded on a Panasonic AG-6720A videorecorder, and shown on a monitor. Table 17 shows the experimental flow conditions used for this study.

Dimensions of the chamber (L×b×2h)	$35 \times 4 \times 0.15 \text{ mm}^3$
μ_{HECT} (viscosity)	$0.7734 \times 10^{-3} \text{ N-s/m}^2$
ρ_{HECT} (density)	1.012 g/ml
γ (shear rate)	9 s^{-1}
Re (Reynolds n.)	0.03
L (entrance length)	$0.2 \mu\text{m}$

Table 17. Characteristics of the flow generated by a 5 ml syringe at the slowest pump speed ($1.32 \times 10^{-3} \text{ mm/s}$). These values were calculated as detailed in 5.6.

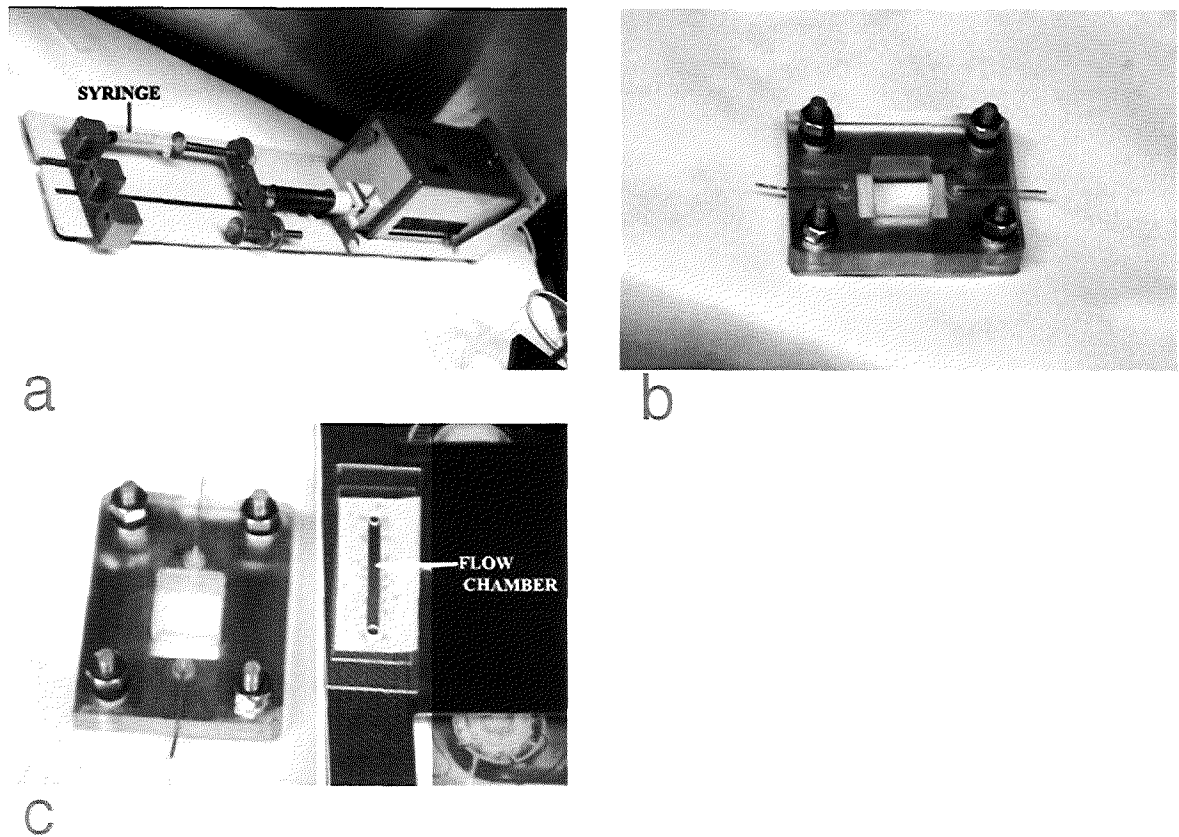


Figure 93. Images of the components of the flow apparatus. a) Syringe pump. b) Flow cell. c) Flow chamber (next to the flow cell). For comparison, the flow chamber is 3 cm wide.

5.2.3.1 Syringe pump

A translational syringe pump (CFP, England) generated the flow (Figure 93a). The translational velocities of the pump, V_{syr} , can be seen in Table 18, with the associated flow rate Q . The flow rate depends on the diameter of the syringe (the diameter of a 5 ml syringe is $\phi=11.12$ mm, as measured by a micrometer) and on the translational velocity of the pump.

V_{syr} (mm/s)	1.3×10^{-3}	2.65×10^{-3}	5.29×10^{-3}	0.01	0.02	0.04
Q (mm ³ /s)	0.13	0.26	0.51	1.03	2.06	4.11

Table 18. Speed of pump and syringe flow rate for a 5 ml syringe.

5.2.3.2 Flow experiment: Modus Operandi

Details of media and solutions can be found in Chapter 8. The flow chamber was inserted in the flow cell; in order to clean the chamber and pre-adsorb adhesive proteins on the PMMA, the chamber was first washed with a flow of 70% ethanol for 10 min, then of Millipore RO water for 10 min; afterwards, it was conditioned with a flow of HECT growth medium for 10 min. The flow of suspended Epitenon cells (10^6 cells/ml) in HECT medium was continued for 1 h, then the chamber was rinsed with 4% formal saline for 15 minutes. The formal saline fixed the cells that had adhered to the substrate, while washing off the others. When no free flowing cells were visible,

images were acquired for cell counting. All experiments were carried out at 37°C. New PVC pipes and a new flow chamber were used at each experiment. Every change of flowing media implied that a syringe containing the next liquid replaced the previous one.

5.2.4 Cell culture

Rat epitenon fibroblasts were cultured from laboratory stocks (described by Wojciak *et al.* (Wojciak-Stothard, 1995a)) in HECT complete medium. Epitenon cells were cultured in 25 cm² tissue culture flasks (Corning Incorporated, USA), and their growth medium was replaced every two-three days. The medium was filter-sterilised through a 0.2 µm microfilter (Minisart, Sartorius, Germany).

5.2.4.1 Passage and cell suspension

The cells were passaged as already described in the previous chapter (page 77). After detaching the cells from the tissue culture flasks, a cell suspension was made for further expansion or to be used for experimental purposes: in the latter case, 3 ml of a 10⁶ cells/ml suspension were prepared and inserted into a 5 ml syringe.

5.2.4.2 Fixation

When fixing a cell culture in flow, the cells were directly rinsed with a flow of formal saline at 37°C for 15 min: hence, the cells that were not attached were removed by the flow of formalin, which fixed the adhered cells at the same time (this was observed on the monitor, which showed that no flowing cells were visible within 10 min from the beginning of the formalin flow). When the flow was stopped, the cells were imaged.

5.2.4.3 Imaging and analysis

Between 11 and 24 frames per experiment were acquired within a 15x4 mm² area (the visible patterned area) on four controls and six pitted substrates. The images were digitised with NIH Image (National Institute of Health, USA) at 12.5 frames/sec, and the adhering cells were counted.

Unpaired *t*-test (two-tailed, assuming unequal variances) was used to compare the statistical significance of cell adhesion on the pitted substrates against the flat control.

5.3 Results

5.3.1 Nanopatterned replicas

Embossing in the Nanoimprinter was found to be a suitable technique to obtain transparent, evenly thin sheets of PMMA for the assembling of the flow chamber. Scanning Electron Microscopy showed that the nanopatterns were successfully embossed, reproducing the topography of the resist (Figure 94).

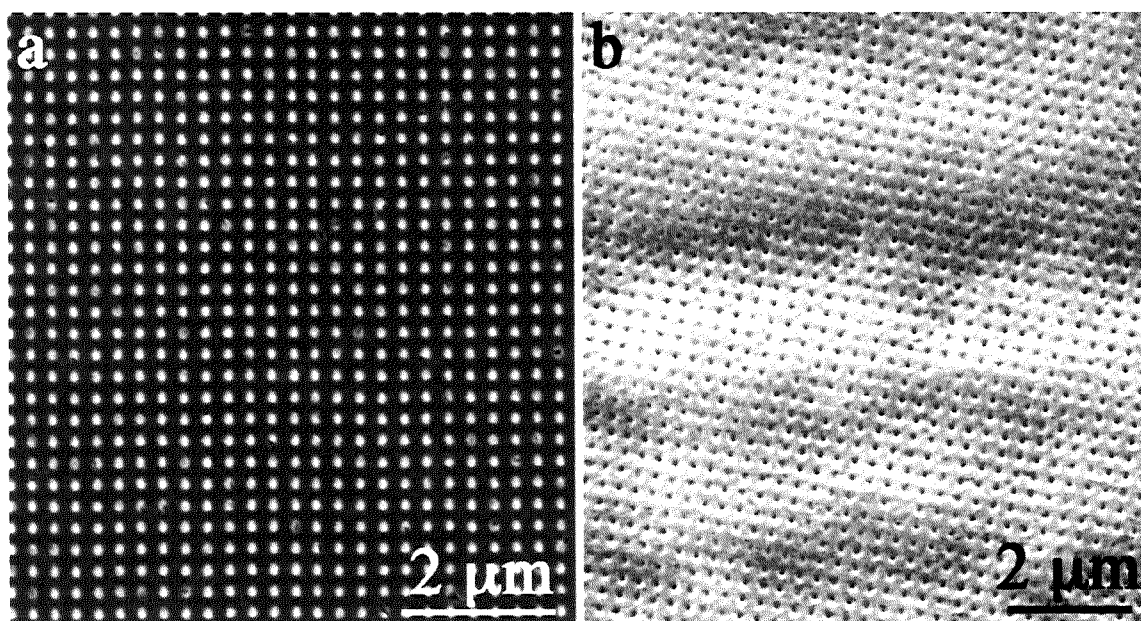


Figure 94. Scanning electron micrographs of a) the nickel shim (pillar diameter= 113 ± 6 nm) and b) the corresponding PMMA replica (pits diameter= 90 ± 7 nm). The ondulation in the polymer was induced by the SEM.

5.3.2 Flow chamber and flow apparatus

A flow chamber was designed, which allowed real-time, unobtrusive imaging of cells flowing over a symmetrical nanopatterned substrate. The small height of the chamber made sure that the flow was laminar and steady over the nano-pits. Visual inspection confirmed that the streamlines were parallel (unlike in turbulent flow). The cells could be imaged during the flow (see Movie in attached CD) and after fixation (Figure 95).

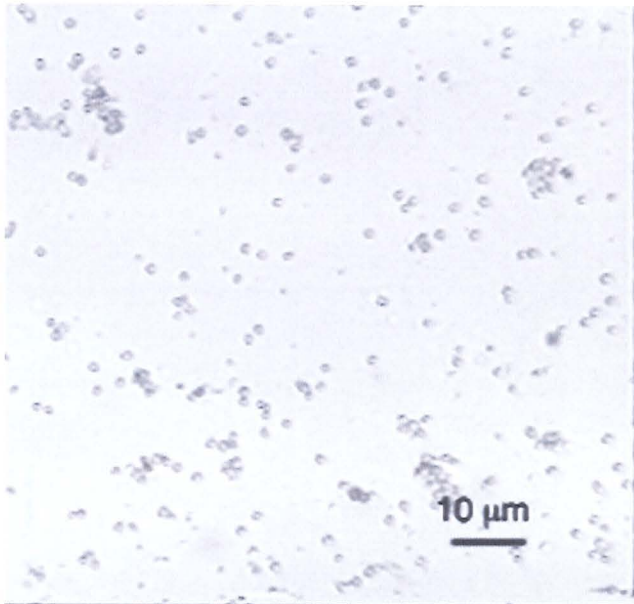


Figure 95. Microscope frame at 2.5X magnification, showing Epitenon cells fixed on a nanopitted PMMA surface after 1 h flow. The cells were counted and the total number was averaged with analogous counts on the remaining nano-pitted area. Note the presence of cell clusters.

5.3.3 Cell adhesion

Figure 96 shows the results of initial cell adhesion on the nano-pits. Epitenon cells adhered significantly less to the nano-pits than to the flat controls. Rolling motion and short-time arrests of the cells closest to the surface were observed, as reported by Pierres *et al.* (Pierres, 1996) Several cell clusters could be observed.

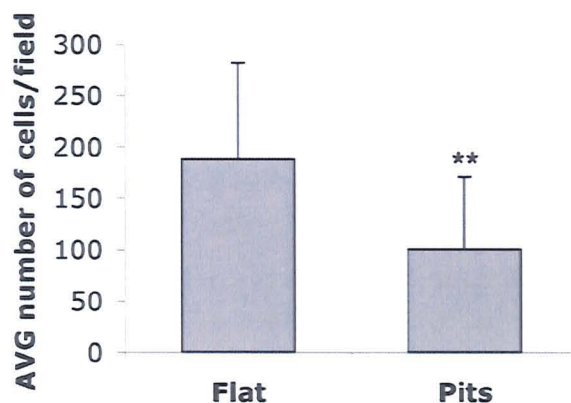


Figure 96. Number of cells per frame on the flat control on the nano-pitted PMMA after 1 h flow. Results are mean \pm standard deviation. (**) $p < 0.01$ from unpaired t-test. $n = 72$ (Flat) and $n = 97$ (Pits).

5.4 Discussion

5.4.1 Flow apparatus

The flow chamber ensured a steady laminar flow at $\gamma = 9 \text{ s}^{-1}$ because of its small height, thus allowing real-time and non-invasive imaging of flowing and rolling cells. PMMA proved to be the best material for this application, because it was transparent, its melting temperature was higher than the one required to seal the flow chamber, and the polymer would be demolded at 50-60°C, which was the lowest cooling temperature reached by the Nanoimprinter. The last reason ruled out

the use of PCL, since thumb-embossing would not have provided transparent sheets of even thickness.

The syringe pump did not give rise to reservoir effects (unlike peristaltic pumps), which meant that the velocity of flow was constant at all times. However, even though the flow could have been kept for up to 14 h at a flow rate of 28 s^{-1} , the cells sedimented inside the syringe, which meant that after approximately 1 h, only growth medium was flowing into the chamber.

Running the experiment proved to be a difficult task. The chamber was very fragile, and changing the syringes with the different media was an extremely delicate operation, since the syringes had to be disconnected from the pipes. This could cause the infiltration of air bubbles, which would and did compromise several experiments.

The next step in improving this set up would involve the fabrication of a flow cell and chamber where only the nanopatterned polymer is replaced at each experiment, instead of the whole chamber. Also, a pumping system based on valves, rather than on syringe replacement, could be designed: this would allow the changing of liquid media without disconnecting the pipes, ensuring sterility at all times.

5.4.2 Initial cell adhesion

The wall shear rate of this flow chamber ($\gamma_{\text{wall}}=9 \text{ s}^{-1}$) is much lower than in any physiological condition (see 5.6.4): hence the velocity profile is much less parabolic, meaning that the flowing cells undergo less torque than *in vivo*, which should make their adhesion more likely. Instead, Figure 96 shows that the PMMA nano-pits significantly reduced initial cell adhesion. This could be due to a reduction in surface area available for the first cell-substrate contact: since the nano-pits reduced the surface area by 20%, the formation of initial bonds would occur less frequently. Alternatively, the nanopits might increase the slippage of the medium at the surface (Cottin-Bizonne C., 2003). In this case, reduced surface friction would make cell adhesion less probable.

Cell clusters formed on both patterned and flat surfaces (Figure 95), suggesting that cells adhere more easily to other cells rather than to the substrate, or simply that an adhered cell constitutes an obstacle for a flowing one, thus starting the nucleation of clusters. In the latter case, it is possible that a region of micro-turbulence is created behind an adhered cell, and that this in turn favours cell adhesion. Alternatively, the clusters might form in the suspension, or in the regions of turbulence in the flow path.

As Gallagher *et al.* (Gallagher, 2002) proved that some nano-pitted surfaces prevent or reduce static Epitenon cell adhesion *in vitro*, the purpose of the present study was to investigate cell adhesion on the same nano-pits, but under dynamic conditions, which is a more physiological-resembling

situation than the static culture. However, for the reasons explained in the previous paragraph, PMMA had to be used instead of PCL, and only the initial cell adhesion was quantified.

From the present results it would appear that, consistently with Gallagher's claims, irrespective of the chemistry (PMMA/PCL) a nano-pitted topography effectively reduces cell adhesion on a substrate. However, and unfortunately, later experiments showed that the Epitenon cells from our laboratory stocks had probably been over-passaged, causing the cells to stop spreading and proliferating in static culture. Also, successive static cultures of both Epitenon and h-TERT cells indicated that both PMMA and PCL nano-pits of diameter 90 ± 7 had no effect at all on cell adhesion and proliferation in static culture. In order to explain the discrepancy with Gallagher's results, SEM images of the samples used in their study were taken, revealing the different size of the nano-pits used for their cell culture (216 ± 10 as measured with ImageJ (Rasband, 1997-2005) from Figure 97). As it is visible in Figure 97, the surface area reduction of the PCL nano-pits used in Gallagher's work (41%) is double the one yielded by the PMMA nano-pits used for my flow chamber (20%).

For all the aforementioned reasons, the meaningfulness of these results is questionable, and this study was suspended to better investigate cell adhesion on nanopatterns in static culture. This led to the results already shown in Chapter 4.

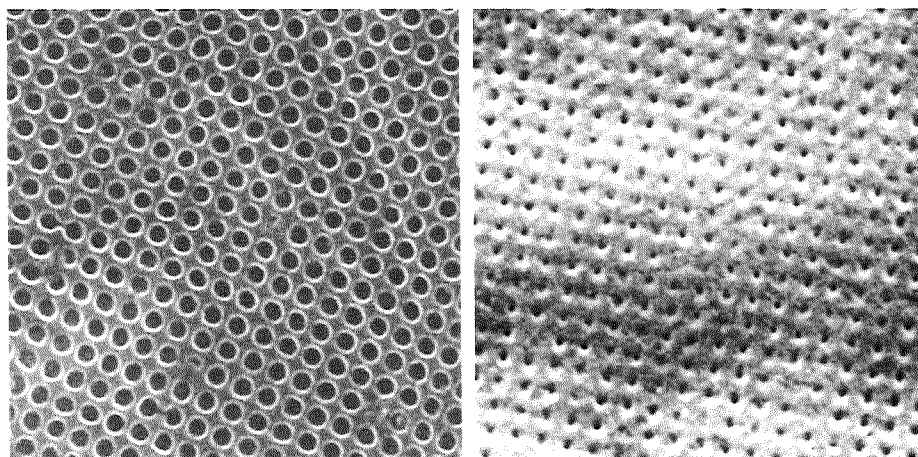


Figure 97. Left: $5\ \mu\text{m} \times 5\ \mu\text{m}$ area showing the nano-pits used by J. Gallagher (Gallagher, 2003) (diameter = 216 ± 10 nm). Right $5\ \mu\text{m} \times 5\ \mu\text{m}$ area from Figure 94b, showing the PMMA nano-pits used in this work (diameter = 90 ± 7 nm). The centre-to-centre spacing between pits is 300 nm in both figures.

In conclusion, regardless of the problems encountered during my study, it can be said that this method should be used to develop and test nanopatterned surfaces that could coat prosthetic devices, especially the ones in contact with the circulatory system. In fact, not only it has been shown in Chapter 4 that PCL nano-pillars induce a different reaction in fibroblasts and endothelial cells, but also it is clear that these flow experiments should be carried on with cell types that are relevant to physiological flow. Therefore, it would be extremely interesting to culture a monolayer

of endothelial cells on nano-pillars, and then observe the behaviour of endothelial cells when subjected to a flow of medium at physiological blood shears ($>100 \text{ s}^{-1}$) (Hoeks, 1995). Afterwards, the adhesion of blood cells (e.g. platelets, monocytes) to such endothelial monolayer from a flowing suspension should be investigated.

5.5 Conclusion

A parallel-plate flow chamber was built, which proved to be an interesting way of observing and analysing the behaviour of flowing and rolling cells over nanopatterns. It ensured that the flow was laminar at all times, and that the surface of interest was always within the depth of field of the microscope, which entails the use of thin, parallel sheets of transparent nanoembossed materials. The initial adhesion of Epitenon cells on nano-pitted PMMA was significantly lower than on the flat control. This could have been due to a reduction in surface area available for the first cell-substrate contact, or to increased fluid slippage on the nano-pits.

5.6 Appendix: fluid dynamics

There are a very few known cases for which the equations of viscous flow can be solved without approximation: one of them is the flow of an incompressible fluid between two parallel infinite plates (Munson, 1990). For this geometry the fluid particles move in the x direction parallel to the plates, and there is no velocity in the y and z direction (Figure 98). In the case of steady flow, the Navier-Stokes equations are easily solved and, if the two plates are fixed, the velocity distribution becomes:

$$u_x = \frac{1}{2\mu} \left(\frac{\partial p}{\partial x} \right) (y^2 - h^2) \quad (30)$$

where μ is the dynamic viscosity of the fluid, p is the hydrodynamic pressure and h is the half height of the chamber.

Figure 98 shows that the velocity profile u_x between the two fixed plates is parabolic (Figure 98), i.e. the flow is laminar (characterized by the "slipping motion of layers of fluid over other layers" (Prandtl, 1952)). In case of rectangular ducts, such as the flow chamber in this project, the equations cannot be so easily be solved, and the solution is more complex (Langlois, 1964). Because of two pair of sidewalls, the velocity profile is a paraboloid. However, in the present flow chamber the width b is 23 times greater than the height h , so that the two slides have been considered as two infinite (wide) parallel plates. The flow is also assumed to be steady and incompressible, and the fluid Newtonian. For this model, three parameters have been calculated (summarised in Table 17): a) the Reynolds number Re ; b) the entrance length l_e ; and c) the wall shear rate $\dot{\gamma}_{wall}$.

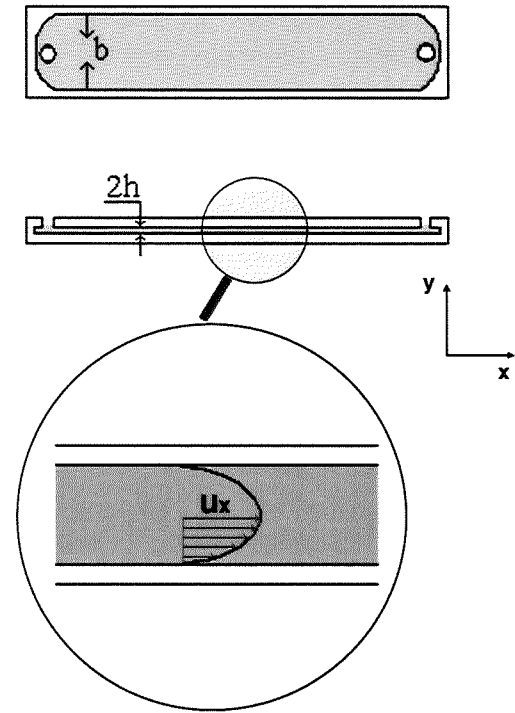


Figure 98. Velocity profile of the laminar flow in a parallel-plate flow chamber

5.6.1 Reynolds number

A way to predict if the flow is going to be laminar or not is to calculate the dimensionless Reynolds number (Re), which is the ratio between the inertial forces and the viscous forces due to the flow (eq 31). If $Re \ll 1$, the viscous forces are predominant, thus the flow will be laminar:

$$Re = \frac{\rho V D}{\mu} \quad (31)$$

where ρ is the density of the fluid, V is the mean velocity of the flow, h is half the height of the chamber, b is the width of the chamber and D is the hydraulic diameter for rectangular pipes (Munson, 1990) (eq 32):

$$D = \frac{4bh}{b + 2h} \quad (32)$$

The *dynamic viscosity* μ of the suspension can be calculated according to Happel and Brenner (Happel, 1965), and in the case of our dilute system it can be approximated to the viscosity of the HECT medium, which has been measured with a 27942 ASTM-IP Ostwald viscometer. At 37°C, $\rho_{HECT}=1.012$ g/ml and $\mu_{HECT}=0.7734 \times 10^{-3}$ N-s/m². Calculations of the Reynolds number for this flow chamber showed that the viscous effects are predominant ($Re=0.02$), which is not surprising due to the small height of the chamber.

5.6.2 Entrance length

When the flow is entering the chamber, it needs a certain length before it becomes fully developed, i.e. before the velocity profile becomes parabolic. This is the so-called entrance length l_e . Different correlations have been accepted to calculate the entrance length (Munson, 1990, Prandtl, 1952); for this chamber, the expression from Munson *et al.* (Munson, 1990) has been used, where D is the hydraulic diameter:

$$l_e = 0.065 Re D \quad (33)$$

The turbulent effects due to the geometry have not been considered which means that the entrance length is longer than calculated. The flow pattern represents a sharp-edged "source and sink" configuration (Prandtl, 1952), which will give rise to turbulence near the inlet and outlet. However, the distance between the inlet and the centre of the chamber is 19.5 mm, which is 10^4 times bigger than the calculated entrance length ($l_e = 0.6$ μ m): it seems therefore reasonable to assume that the flow in the middle is fully developed.

5.6.3 Wall shear rate

The most commonly cited haemodynamic factor implicated in cell adhesion defects, disease initiation and ligand-receptor bond dissociation is the wall shear stress τ_{wall} , while the wall shear rate γ_{wall} ($=\tau_{wall}/\mu$) seems to affect bond formation (Chen, 2001). The shear rate γ quantifies the speed of deformation of a flowing fluid, and it is inversely proportional to the viscosity μ . The wall shear rate is calculated from the velocity distribution in a Newtonian fluid flowing between two wide, parallel plates (Munson, 1990):

$$\gamma_{wall} = \frac{3Q}{2bh^2} \quad (34)$$

where b is the width of the chamber, h is the half height and Q is flow rate (eq 35):

$$Q = \pi \frac{\phi_{syr}^2}{4} V_{syr} \quad (35)$$

where ϕ_{syr} is the diameter of the syringe and V_{syr} is the translational velocity of the syringe.

In this flow chamber, at $Q=0.13 \text{ mm}^3/\text{s}$, $\gamma_{wall} = 9 \text{ s}^{-1}$.

5.6.4 Wall shear rate of blood in vessels

For a comparison with blood flow, the radial velocity V_z of a steady, laminar flow in a circular tube (Poiseuille's flow, eq 36) was considered:

$$V_z = \frac{1}{4\mu} \frac{\partial P}{\partial z} (r^2 - R^2) \quad (36)$$

where z is the position along the axis of the tube, r is the radial distance from the axis and R is the radius of the tube. The associated shear rate is formulated in eq 37:

$$\gamma = -\frac{\partial V}{\partial r} = 1 \frac{1}{4\mu} \frac{\partial P}{\partial z} 2r \quad (37)$$

The mean velocity V is related to the radial velocity V_z by eq 38:

$$V_z = V \left[1 - \left(\frac{r}{R} \right)^2 \right] \quad (38)$$

By replacing eq 38 into eq 36 and 37, the wall shear rate in a tube γ_{wall} was finally obtained:

$$\gamma = \frac{2Vr}{R^2} \quad \Rightarrow \quad \gamma_{wall}(r=R) = \frac{2V}{R} \quad (39)$$

Values of the mean velocity of blood and the radius of the vessels were found in Tortora & Grabowski (Tortora, 2000), and substituted in eq 39 to calculate the wall shear rates. In the aorta, $V \approx 40 \text{ cm/s}$ and the cross-sectional area, $\pi R^2 \approx 3\text{-}5 \text{ cm}^2$. It follows $R_{aorta} \approx 0.98\text{-}1.26 \text{ cm}$, thus $\gamma_{wall-aorta} \approx 82\text{-}63 \text{ s}^{-1}$. In the capillaries, $V \approx 0.1 \text{ cm/s}$, and the total cross-sectional area is $4500\text{-}6000 \text{ cm}^2$. The average diameter of the capillaries is $R_{capill} = 8 \text{ }\mu\text{m}$ (<http://www.nanomedicine.com/NMI/8.2.1.2.htm>), thus $\gamma_{wall-capill} \approx 250 \text{ s}^{-1}$.

6 Final discussion

Despite the increasing amount of literature on the effects of nano-topographies on cell behaviour (Casey, 1997, Clark, 1991, Curtis, 1964, Curtis, 1998a, Dalby, 2002b, Dalby, 2004, Flemming, 1999, Gallagher, 2002, Goodman, 1996, Stavridi, 2003, Turner, 1997, Wieland, 2005, Wilkinson, 2001, Wojciak-Stothard, 1996), the origin of the vast and disparate set of reported phenomena is still unknown also because the wide range of materials and shapes used in previous experimental reports makes it difficult to classify the different.

One possible explanation for some of the observed phenomena, such as reduced spreading and low proliferation, is that nano-scale patterning could cause or enhance the formation of air pockets on the surface. This would shield protein adsorption on the substrate (Wu, 2005), and would generally reduce the area available for cells to form focal contacts. The cells might attach to the proteins absorbed at the air-medium interface (Lu, 1999), but a vapour cavity would not provide the mechanical resistance required for focal adhesion development (Pelham, 1997).

In 1994, Parker *et al.* (Parker, 1994) proposed that the long-ranged hydrophobic attraction (10-100 nm) is due to preexisting bubbles that bridge the two approaching surfaces. There is increasing evidence of the formation of nano-bubbles (or more precisely, nano-cavities) on hydrophobic surfaces (Ishida N., 2000, Tyrrell, 2001). In particular, Attard and co-workers (Tyrrell, 2001) imaged a close-packed network of “nano-bubbles” of height 20-30 nm and radii of curvature of the order of 100 nm, literally covering a hydrophobic surface. However, the presence of such a network is controversial (Mao, 2004). The occurrence of nano-bubbles on hydrophobic surfaces has been suspected to influence colloidal stability (Snoswell, 2003) and cavitation probability (Bunkin, 1997), and it was suggested that it is increased by submicrometric roughness (Ryan, 1998). The existence and stability of nanobubbles is hard to reconcile with conventional thermodynamics. Such small cavities should rapidly dissolve because of their high internal pressure; from the Laplace equation [$P_{int}-P_{ext}=2\gamma/r$, where P_{int} is the pressure from the concave side of the bubble, P_{ext} the pressure from its convex side, γ is the surface tension and r the radius of the bubble], the internal pressure of a 50-nm-radius air bubble in water would be 30 atm, and 140 atm in a 10-nm-radius bubble, with $\gamma_{(25^{\circ}\text{C})}=72.75$ mN/m. Nevertheless, Tyrrel *et al.* (Tyrrell, 2001) noticed by AFM imaging that the bubbles were not spherical, but rather flattened on the surface, which suggested a lower internal pressure. Besides, the bubbles seemed stable for 10-20 min. They explained the phenomenon by air supersaturation of the water, possibly due to e.g. heating by the AFM laser or entrainment of bubbles during solution exchange.

In Chapter 1, the contact angles of water on nano-topographies of well-defined dimensions and surface chemistry were measured, and the results confirmed that not only air-trapping can occur

between hydrophobic ($\theta_Y=113^\circ$) nano-asperities, but also that air pockets were formed in PCL ($\theta_Y=77^\circ$) nano-pits, which is a common biomaterial used for cell culture. It was shown that the low-rate advancing angles of water will depend on the geometric parameters of the nano-topography, which in turn determines the occurrence of air-trapping. In both the hydrophobic and the hydrophilic case, the contact angles on nanotopographies were proven to be predictable by analytical models, that so far had only been proven reliable to model the wetting of micro-topographies. These results are revealing, not only in view of potential applications (Blossey, 2003, Grunze, 1999), and as a long-overdue answer to the question of air-trapping by surface roughness, but also because they could serve to provide an explanation to the phenomenon of nanotopography-induced cell behaviour.

The presence of air pockets inside the PCL nano-pits was shown indirectly as the Cassie-Baxter model provided the best fit to the measured advancing angles of water at room temperature. However, the cells in Chapter 4 were cultured in growth medium on nano-pillars at 37°C . Even assuming that the PCL nano-pillars can trap air in water, not only will the temperature and viscosity of the growth medium affect the contact angle, but also the medium contains 10% serum and trace amounts of non-ionic surfactants (Tween-20, Triton X 100), both of which will favour the spreading of the liquid inside the nano-topography. Also, it has been shown in Chapter 1 how external pressure can force the water inside the surface textures, and how on certain nanotopographies (P21) very little energy was needed to effect the transition. When pouring a cell suspension on the substrate, the velocity and the height at which the suspension is pipetted out are not controlled, and this can add variability to the results, by inducing transitions from air-trapping to asperity-filling. Therefore, while air-trapping is an interesting hypothesis that needs further investigation, caution must be heeded when extending interpretations from low-rate advancing angles of water to cell behaviour on similar surfaces.

Due to the slip-stick behaviour of water droplets during contact angle measurements and mainly because of shortage of time, it was not possible to establish directly if the very same nano-pillars used for cell culture induced air-trapping in water. However, coating the nano-pillars with gold-palladium, which is highly hydrophilic, masked the “proliferation-inhibiting” effect that the PCL nano-pillars had on human fibroblasts. This could be due to several factors, one of them being the unlikely occurrence of air-trapping on a hydrophilic surface. In that case, the different surface coverage on gold flat and nano-pillared areas could be explained by the increased motility of fibroblasts due to reduced surface area available for focal contact formation. The occurrence of air-trapping could also be an explanation for the decreased initial adhesion of rat epitenon fibroblasts in flow. The latter in particular could be linked to the decreased surface friction that is expected on

air-trapping roughness (Cottin-Bizonne C., 2003). By increasing the interfacial slippage, the PMMA nano-pits might make initial cell adhesion in flow more unlikely.

If, on the other hand, we assume that there is no air-trapping at the surface, the question that raises is how focal adhesions can form on and between protrusions. Previous TEM evidence (Dalby, 2004) suggests that the cells adhere only to the top of the pillars. However, in a recent article Curtis *et al.* (Curtis, 2005) showed that the cell membrane can bend between nano-pillars. Even though the TEM image shown in their paper does not provide information about the formation of adhesions, it is clear that this question needs further investigation. Therefore, a possible hypothesis is that the observed reduced number of mature focal contacts should be due primarily to the reduced surface area available for focal contact formation, irrespective of the presence of air bubbles between asperities. This could help explain the observation that cells generally grow on nano-pits, unless their diameter is very large (Gallagher, 2002). Moreover, another reason for decreased surface coverage of human fibroblasts on the nanopillars could be a higher migration rate on the pattern (Gallagher, 2003). This effect should be mediated by the formation of nascent focal complexes, which would provide sufficient attachment to ensure migration, but would not mature into focal adhesions, which are necessary for fibroblast spreading and proliferation.

Nevertheless, an increased migration alone does not explain why the difference between pillars and flat is much more evident on the uncoated PCL replicas, and barely visible on the gold-coated replicas. Assuming no air-trapping, it could be argued that the difference in cell coverage in the overview picture (Figure 72) of the gold-coated replicas is actually visible only at the edges of the pattern. This would be consistent with increased migration rates and subsequent higher probability of finding the cells outside the patterned area, given that the cells were proven to proliferate on the gold-coated pillars. However, the difference in coverage between nano-pillars and flat on the uncoated replicas was too striking and too uniform to be attributable to increased migration rates only. Besides, the cells on the pillars were shown not to proliferate. Therefore, in the end, a likely interpretation advocates for a synergistic effect of the uncoated PCL pillars in increasing the migration rates of the fibroblasts and inhibiting their proliferation rate probably by air-trapping, since this could efficiently ensure a reduction in available surface area. On the gold-coated pillars, the formation of mature focal contacts seemed possible, and the proliferation was not inhibited, therefore it might be that without air pockets the cells can form attachments even between pillars.

The possible presence of air-bubbles at the surface would also affect the interfacial force experienced by a sedimenting cell or an approaching particle. This possibility has not been considered in Chapter 3, where the DLVO interaction between a microsphere and a nano-patterned plate was simulated. The question of the effect of nano-patterning on the interfacial forces between regular nano-pits and 2 μm carboxylated spheres was raised by Curtis *et al.* (Curtis, 2001)

Therefore, it seemed recommendable to investigate theoretically the DLVO interaction between a microsphere and a nano-patterned silica plate. Surface Energy Integration showed that the energy barriers towards particle adhesion predicted by the DLVO theory should be dramatically decreased by nano-pillars, in agreement with previous suggestions and observations. This model relies on several simplifying assumptions and does not include short-range forces. Nevertheless, this characterisation is interesting, since the influence of surface roughness on colloidal forces is still the object of research, and this model could prove very useful for future AFM colloid-probe measurements of sphere-nanopattern interactions. A particular advantage of the SEI technique is that hollow depressions can be modelled just as reliably as the surface protrusions, which have been the only topography considered by most modelling attempts so far. Besides, surfaces of arbitrary topology can be used, as long as mathematically representable. Thus, it is hoped that these calculations will be validated by experimental evidence. If this will be the case, it would be interesting to model the interaction between nanotopographies and spheres with dimensions, refractive index and surface charge similar to a rounded cell. Afterwards, similar nanotopographies could be fabricated, and their effect on cell sedimentation and initial adhesion monitored. Hence, the understanding of intermolecular forces between a sphere and a nanopattern might help to shed some light on the forces experienced by the cells when sedimenting on a nanotopography.

Future work

Having established the reliability of the Cassie-Baxter and Wenzel equations at the nano-scale, it would be very interesting to investigate the behaviour of water droplets at the hydrophobic/hydrophilic boundary, and to define this boundary in terms of the occurrence of air-trapping in the asperities. For that purpose, not only it will be necessary to fabricate polymeric patterns of defined and regular geometries (cylinders, hemispherical-top cylinders, spheres), but the accurate determination of their dimensions will be a pre-requisite for the reliable interpretation of dynamic contact angle measurements.

The verification of the SEI model presented in Chapter 3 should be done by AFM force-distance measurements.

In order to comprehend the effect of PCL nanopillars on fibroblast proliferation, two principal questions are left open: the first concerns the existence of nano-bubbles between PCL nanopillars, the second the likelihood of focal contact formation between nanopillars of order of 100 nm.

The question regarding the occurrence of air-trapping at nano-patterned biocompatible surfaces, and its effect on cell culture *in vitro* should definitely be investigated further. To do so, regular nano-pillared polymeric surfaces should be fabricated and their topography accurately characterised. Secondly, the contact angle of growth medium at 37°C should be measured on these

substrata, in order to investigate the presence of air pockets. It would also be interesting to repeat the measurements with degassed medium. Once determined if a surface traps air or not, and especially in the second case, TEM investigations and immunofluorescence would be needed to elucidate the question of cell attachment to the bottom area between protrusions. During the cell culture, it should be made sure that the cell suspension is poured on the substrates in a manner resembling of the contact angle measurement, i.e. at similar velocity and height, to ensure comparability with the contact angle measurement.

In order to determine if surface area reduction is the main cause for reduced fibroblast proliferation, the experiment described above should be repeated for nano-pitted and nano-pillared surfaces of different spacings and aspect ratios. In this context, the determination of the adhesion type distribution should define if the cells can form as many mature focal adhesions on the pillars as on the flat. This would also be linked to the migration of cells. Since it is suggested here that a reason for decreased surface coverage could be the increased speed of migration on the nano-patterns, a quantitative analysis of fibroblast locomotion should be done. Subsequently, the percentage of nascent focal complexes and mature adhesions on the nanopillars should be determined and compared to the control.

The increased spreading of mouse endothelial cells on the same nano-pillars that inhibited human fibroblast proliferation was extremely interesting. This work should be followed by a more extensive investigation of this type of cell culture. If the present observations that nano-pillared surfaces can favour the formation of a monolayer of endothelial cells was to be unambiguously established, this finding could have exciting implications for the field of tissue engineered vascular implants (Niklason, 1999, Richter, 2005). Such work should be followed by the culture of endothelial cells in a flow system that incorporates a nano-pillared surface. Another interesting experiment should involve the co-culture of human fibroblasts and endothelial cells on nano-pillars, since this could lead to the development of cell-selective surfaces.

7 Conclusion

The wetting of hydrophobic and hydrophilic nanotopographies is predictable by analytical laws, which relate the low-rate advancing angles to the geometric parameters of the nanopatterns and to the advancing angle on a flat surface of the same chemistry.

Air-trapping occurs between hydrophobic nano-topographies of appropriate geometric parameters. However, air-trapping can “unexpectedly” occur on hydrophilic (contact angle $<90^\circ$) nano-structured surfaces as well. This suggests that the hydrophobic/hydrophilic boundary is before 90° .

Surface Element Integration simulations predict that the energy barrier toward particle deposition (10 μm SiO_2 sphere approaching a SiO_2 nano-patterned plate, in 1 and 100 mM of 1:1 aqueous electrolyte) should be dramatically decreased by the presence of surface asperities, and that the energy barrier decreases with the radius of curvature of the asperities, in agreement with previous suggestions.

The proliferation of human fibroblasts on PCL replicas is drastically reduced when the cells are cultured on nano-pillars. This phenomenon disappears when the pillars are gold-coated. Possible explanations include air-trapping between uncoated PCL nano-pillars and a (possibly related) reduction of surface area available for the formation of mature focal adhesions; the latter, in turn, would increase the speed of migration and inhibit the proliferation of the fibroblasts.

While human fibroblasts did not proliferate, on the PCL nano-pillars mouse endothelial cells formed a cobble-stone pattern suggestive of a close-packed monolayer, which is more resemblant of their morphology *in vivo*. This differential effect of nano-pillars on cell behaviour evokes the possibility of creating cell-selective surfaces.

8 Appendix. Solutions

This section contains the recipes of the different solutions, in alphabetical order.

Antibiotics mix. 144 mM Glutamine (Gibco), 11.9 μ M Amphoterin (Gibco), 1950 U/ml Penicillin/Streptomycin (Gibco), 7 ml 7.5% Bicarbonate (Gibco).

1% BSA/PBS. 1 g BSA (bovine serum albumin, Gibco) into 100 ml PBS. Store frozen.

Coomassie Blue Stain. 225 ml methanol, (BDH) 50 ml glacial acetic acid (BDH), filled to 500 ml RO water. Add 1.25 g Coomassie Brilliant Blue (BDH,UK).

DMEM. 71% Dulbecco's Modified Eagle's medium (Sigma, UK), 17% Medium 199 (Sigma), 9% foetal calf serum (Life Technologies, UK), 1.6% 200 mM L-glutamine (Life Technologies) and 0.9% 100 mM sodium pyruvate (Life Technologies).

Eagles water. 134 ml of Millipore™ Reverse Osmosis (MilliQ RO) purified water, autoclaved and stored at 4°C.

ECT. 180 ml Eagles water, 16 ml BHK21X10 (Biowest), 20 ml Calf serum (Gibco), 5 ml Antibiotics mix, 20 ml Tryptose phosphate broth (Sigma), 1 ml 7.5 % Sodium Bicarbonate (Gibco).

Formal Saline (made to 1 l RO water). 8 g NaCl, 0.2 g KCl, 1.15 g Na₂HPO₄, 0.2 g KH₂PO₄, 100 ml 40% formaldehyde (Sigma), pH adjusted to 7.2, add 2 g sucrose.

HamsF10. 500 ml HamsF10 (Biowest), 15 ml foetal calf serum (Gibco), 12.5 ml antibiotics mix, 2.5 ml 7.5% Sodium Bicarbonate (Gibco), 5 ml ITS (Insulin, Transferrin, Selenite solution, Gibco).

HECT. 180 ml HEPES water, 16 ml BHK21X10 (Biowest), 20 ml Calf serum (Gibco), 5 ml Antibiotics mix, 20 ml Tryptose phosphate broth (Sigma), 1 ml 7.5 % Sodium Bicarbonate (Gibco).

Hepes Saline buffer. 8 NaCl, 0.4 KCl, 1 D-glucose(Fisher), 2.38 HEPES ((N-2 hydroxyethyl piperazine-N' 2 ethane sulphonic acid, BDH), 0.1 Phenol-Red Sodium salt (Sigma), 1 l RO water, pH adjusted to 7.5.

HEPES water. 1 litre RO water supplemented with 5.25 g HEPES, pH-adjusted (with NaOH) to pH7.5 and stored at 4°C.

Permeabilising buffer. 10.3 g sucrose, 0.292 g NaCl, 0.06 g MgCl₂-6H₂O, 0.476 g Hepes in 100 ml PBS. Adjust pH to 7.2, then add 0.5 ml Triton X.

Phosphate buffered saline (PBS) X10 (made to 1 l RO water). 11.5 g/l Na₂HPO₄ (BDH), 2 g KH₂PO₄ (BDH), 80 g/l NaCl (BDH), 2 g/l KCl (BDH). adjust to Ph7.4

0.5% Tween/PBS. 0.5 ml Tween 20 into 100 ml PBS.

Versene buffer. 8 g NaCl, 0.4 g KCl, 1 g D-glucose, 2.38 g HEPES, 0.1 g Phenol-Red, 0.2 g EDTA (Di Sodium salt, Sigma), 1 litre RO water, pH adjusted to 7.5.

9 Bibliography

- ABDELSALAM, M. E., BARTLETT, P.N., KELF, T., BAUMBERG, J. (2005) Wetting of regularly structured gold surfaces. *Langmuir*, 21, 1753-1757.
- ARNOLD, M., CAVALCANTI-ADAM E.A., GLASS R., BLUMMEL J., ECK W., KANTLEHNER M., KESSLER J., SPATZ J.P. (2004) Activation of integrin function by nanopatterned adhesive interfaces. *ChemPhysChem*, 5, 383-388.
- ASHTON, J. (1921) A revision of the Australian Cicadidae. Part I. *Proc. Roy. Soc. Vict.*, 33, 87-107.
- ATTARD, P., ANTELM, D., LARSON, I. (2000) Comparison of the zeta potential with the diffuse layer potential from charge titration. *Langmuir*, 16, 1542-1552.
- AVNUR, Z., GEIGER, B. (1981) The removal of extracellular Fibronectin from areas of cell-substrate contact. *Cell*, 25, 121-132.
- BARTHLOOT, W., NEINHUIS, C. (1997) Purity of the sacred lotus, or escape from contamination in biological surfaces. *Planta*, 202, 1-8.
- BAUM, C., MEYER, W., STELZER, R., FLEISHER, L.G., SIEBERS, D. (2001) Average nanorough skin surface of the pilot whale (*Globicephala melas*, Delphinidae): considerations on the self-cleaning abilities based on nanoroughness. *Marine Biology Online*.
- BHATTACHARJEE, S., ELIMELECH, M. (1997) Surface Element Integration: A Novel Technique for Evaluation of DLVO Interaction between a Particle and a Flat Plate. *J. Coll. Int. Sci.*, 193, 273-285.
- BICO, J., MARZOLIN, C., QUERE D. (1999) Pearl drops. *Europhys. Lett.*, 47, 220-226.
- BICO, J., THIELE, U., QUERE, D. (2002) Wetting of textured surfaces. *Coll. Surf. A*, 206, 41-46.
- BICO, J., TORDEUX C., QUERE D. (2001) Rough wetting. *Europhys. Lett.*, 55, 214-220.
- BLOSSEY, R. (2003) Self-cleaning surfaces-virtual realities. *Nature Materials*, 2, 301-306.
- BOHN, H. F., FEDERLE, W. (2004) Insect aquaplaning: Nephentes pitcher plants capture prey with their peristome, a fully wettable water-lubricated anisotropic surface. *PNAS*, 101, 14138-14143.
- BONGRAND, P. (1995) Adhesion of cells. IN LIPOWSKY, R., SACKMANN, E. (Ed.) *Handbook of biological physics*. Elsevier Science B.V.
- BONGRAND, P., CLAESSON PM, CURTIS ASG (EDS) (1994) *Studying cell adhesion*, Berlin Heidelberg, Springer-Verlag.
- BOWEN, W. R., DONEVA, T.A. (2000) Atomic force microscopy studies of membranes: effect of surface roughness on double-layer interactions and particle adhesion. *J. Coll. Int. Sci.*, 229, 544-549.
- BOWEN, W. R., DONEVA, T.A., STOTON, J.A. (2002) The use of atomic force microscopy to quantify membrane surface electrical properties. *Colloids and Surfaces A; Physicochemical and Engineering Aspects*, 201, 73-83.
- BRUNETTE, D. M. (1986a) Fibroblasts on micromachined substrata orient hierarchically to grooves of different dimensions. *Exp. Cell Res.*, 164, 11-26.

- BRUNETTE, D. M. (1986b) Spreading and orientation of epithelial cells on grooved substrata. *Exp. Cell Res.*, 167, 203-217.
- BUNKIN, N. F., KISELEVA, O.A., LOBEYEV, A.V., MOVCHAN, T.G., NINHAM, B.W., VINOGRADOVA, O.I. (1997) Effect of salts and dissolved gas on optical cavitation near hydrophobic and hydrophilic surfaces. *Langmuir*, 13, 3024-3028.
- BURTON, Z., BHUSHAN, B. (2005) *Nano Letters*, 5, 1607-1613.
- CASEY, B. G., MONAGHAN, W., WILKINSON, C.D.W. (1997) Embossing nanoscale features and environments. *Microelec. Eng.*, 35, 393-396.
- CASSIE, A. B. D., BAXTER, S. (1944) Wettability of porous surfaces. *Trans. Farad. Soc.*, 40, 546.
- CASTNER, D. G., RATNER, B.D. (2002) Biomedical surface science: Foundations to frontiers. *Surf Sci*, 500, 28-60.
- CHAPEL, J. P. (1994) Electrolyte species dependent hydration forces between silica surfaces. *Langmuir*.
- CHEHROUDI, B., BRUNETTE, D.M. (1995) Effects of surface topography on cell behaviour. IN DONALD, D., WISE L, ALTOBELLI DE, YASZENSKI MJ, GRESSER JD, SCHWARTZ ER (Ed.) *Encyclopedic handbook of biomaterials and bioengineering. Part S: Materials*. New York, Marcel Dekker.
- CHEHROUDI, B., BRUNETTE, D.M. (2002) Subcutaneous microfabricated surfaces inhibit epithelial recession and promote long-term survival of percutaneous implants. *Biomaterials*, 23, 229-237.
- CHEHROUDI, B., GOULD, T.R., BRUNETTE D.M. (1988) Effects of a grooved epoxy substratum on epithelial cell behaviour in vitro and in vivo. *J. Biomed. Mat. Res.*, 22, 459-473.
- CHEHROUDI, B., MCDONNELL, D., BRUNETTE, D.M. (1997) The effects of micromachined surfaces on the formation of bonelike tissue on subcutaneous implants as assessed by radiography and computer image processing. *J. Biomed. Mat. Res.*, 34, 279-290.
- CHEN, S., SPRINGER T.A. (2001) Selectin receptor-ligand bonds: Formation limited by shear rate and dissociation governed by the Bell model. *PNAS*, 98.
- CHEN, W., FADEEV, A.Y., HSIEH, M.C., ONER, D., YOUNGBLOOD, J., MCCARTHY, T.J. (1999) Ultrahydrophobic and ultralyophobic surfaces: some comments and examples. *Langmuir*, 15, 3395-3399.
- CHENG, Y., RODAK, D.E. (2005) Is the lotus leaf superhydrophobic? *Appl. Phys. Lett.*, 86, 144101.
- CHURAEV, N. V. (1995) Contact angles and surface forces. *Adv. Coll. Interf. Sc.*, 58, 87-118.
- CLARK, P., CONNOLLY P, CURTIS ASG, DOW JAT, WILKINSON CDW (1991) Cell guidance by ultrafine topography in vitro. *J. Cell Sci.*, 99, 73-77.
- CLARK, P., CONNOLLY, P., CURTIS, ASG., DOW, JAT., WILKINSON, CDW. (1987) Topographical control of cell behaviour I: Simple step cues. *Development*, 99, 439-448.
- CLARK, P., CONNOLLY, P., CURTIS, ASG., DOW, JAT., WILKINSON, CDW. (1990) Topographical control of cell behaviour II: Multiple grooved substrata. *Development*, 108, 635-644.

- CONSIDINE, R., DRUMMOND CJ (2001) Surface roughness and surface force measurement: a comparison of electrostatic potentials derived from atomic force microscopy and electrophoretic mobility measurements. *Langmuir*, 17, 777-7783.
- COTTIN-BIZONNE C., B. J. L., BOCQUET L., CHARLAIX E. (2003) Low-friction flows of liquid at nanopatterned interfaces. *Nature Materials*, 2, 237-240.
- CURTIS, A. S. G. (1962) Cell contact and adhesion. *Biol. Rev.*, 37, 82-129.
- CURTIS, A. S. G., CASEY B., GALLAGHER J.O., PASQUI, D., WOOD., M.A., WILKINSON, C.D.W. (2001) Substratum nanotopography and the adhesion of biological cells. Are symmetry or regularity of nanotopography important? *Biophys Chem*, 94, 275-283.
- CURTIS, A. S. G., DALBY, M.J., GADEGAARD, N. (2005) Nanoimprinting onto cells. *J. R. Soc. Interface*, online.
- CURTIS, A. S. G., VARDE, M. (1964) Control of cell behaviour: topological factors. *J. Nat. Cancer Inst.*, 33, 15-26.
- CURTIS, A. S. G., WILKINSON, C.D.W. (1997) Topographical control of cells. *Biomaterials*, 18, 1573-1583.
- CURTIS, A. S. G., WILKINSON, C.D.W. (1998a) Reactions of cells to topography. *J. Biomater. Sci. Polymer Edn.*, 9, 1313-1329.
- CURTIS, A. S. G., WILKINSON, C.D.W. (1998b) Topographical control of cell migration. IN SOLL, D., WESSELS D (Ed.) *Motion Analysis of Living Cells*. New York, Wiley-Liss.
- CZARNECKI, J., DABROS, T. (1980) Attenuation of the van der Waals attraction energy in the particle/semi-infinite medium system due to the roughness of the particle surface. *J. Coll. Int. Sci.*, 78, 25-30.
- DALBY, M., YARWOOD SJ, RIEHLE MO, JOHNSTONE HJH, AFFROSSMAN S, CURTIS ASG (2002a) Increasing fibroblast response to materials using nanotopography: morphological and genetic measurements of cell response to 13-nm-high polymer demixed islands. *Exp Cell Res*, 276, 1-9.
- DALBY, M. J. (2005) Topographically induced direct cell mechanotransduction. *Med. Eng. Phys.*, 27, 730-742.
- DALBY, M. J., RIEHLE, M.O., AFFROSSMAN, S., CURTIS, A.S.G. (2002b) In vitro reaction of endothelial cells to polymer demixed nanotopography. *Biomaterials*, 23, 2945-2954.
- DALBY, M. J., RIEHLE, M.O., SUTHERLAND, D.S., AGHELI, H., CURTIS, A.S.G. (2004) Fibroblast response to a controlled nanoenvironment produced by colloidal lithography. *J Biomed Mater Res*, 69, 314-322.
- DANEN, E. H. J., SONNENBERG, A. (2003) Integrins in regulation of tissue development and function. *J. Pathol.*, 201, 632-641.
- DECKER, E. L., GAROFF, S. (1996) Using vibrational noise to probe energy barriers producing contact angle hysteresis. *Langmuir*, 12, 2100-2110.
- DEMALI, K. A., WENNERBERG K., BURRIDGE, K. (2003) Integrin signaling to the actin cytoskeleton. *Curr. Op. Cell. Biol.*, 15, 572-582.

- DENIS, F. A., HANARP, P., SUTHERLAND, D.S., GOLD, J., MUSTIN, C., ROUXHET, P.G., DUFRENE, Y.F. (2002) Protein adsorption on model surfaces with controlled nanotopography and chemistry. *Langmuir*, 18, 819-828.
- DERJAGUIN, B. V. (1934) *Kolloid Z.*, 69, 155-164.
- DOROSZEWSKI, J., KIWALA A. (1988) Adhesion and locomotion of granulocytes under flow conditions. *J. Cell Sci.*, 90, 335-340.
- DOROSZEWSKI, J., SKIERSKI, J., PRZADKA, L. (1977) Interaction of neoplastic cells with glass surface under flow conditions. *Exp. Cell. Res.*, 104, 335-343.
- DRECHSLER, A., PETONG, N., ZHANG, J., KWOK, D.Y., GRUNDKE, K. (2004) Force measurements between Teflon AF and colloidal silica particles in electrolyte solutions. *Coll. Surf. A*, 250, 357-366.
- DUCKER, W. A., SENDEN, T.J., PASHLEY, R.M. (1991) Direct measurement of colloidal forces using an atomic force microscope. *Nature*, 353, 239-241.
- DUCKER, W. A., SENDEN, T.J., PASHLEY, R.M. (1992) Measurement of forces in liquids using a force microscope. *Langmuir*, 8, 1831-1836.
- DUNN, G. A., BROWN, A.F. (1986) Alignment of fibroblasts on grooved surfaces described by a simple geometric transformation. *J. Cell Sci.*, 83, 313-340.
- DUNN, G. A., HEATH, J.P. (1976) A new hypothesis of contact guidance in tissue cells. *Exp. Cell Res.*, 101, 1-14.
- DVORAK, J., STOTLER W (1971) A controlled-environment culture system for high resolution light microscopy. *Exp Cell Res*, 68, 144-148.
- ELIMELECH, M., O'MELIA, C.R. (1990) Effect of particle size on collision efficiency in the deposition of Brownian particles with electrostatic energy barriers. *Langmuir*, 6, 1153-1163.
- FLEMMING, R. G., MURPHY, C.J., ABRAMS, G.A., GOODMAN, S.L., NEALEY, P.F. (1999) Effects of synthetic micro- and nano-structured surfaces on cell behaviour. *Biomaterials*, 20, 573-588.
- FURSTNER, R., BARTHLOTT, W., NEINHUIS, C., WALZEL, P. (2005) Wetting and self-cleaning properties of artificial superhydrophobic surfaces. *Langmuir*, 21, 956-961.
- GADEGAARD, N., MOSLER, S., LARSEN, N.B. (2003a) Biomimetic polymer nanostructures by injection molding. *Macromol. Mater. Eng.*, 288, 76-83.
- GADEGAARD, N., THOMS S., MACINTYRE D.S., MCGHEE K., GALLAGHER J.O., CASEY B., WILKINSON C.D.W. (2003b) Arrays of nano-dots for cellular engineering. *Microelec. Eng.*, 67-68, 162-168.
- GALLAGHER, J. O. (2003) Interactions of cells with nanotopography. PhD Thesis. Infection and Immunity, IBL. University of Glasgow.
- GALLAGHER, J. O., MCGHEE, K.F., WILKINSON, C.D.W., RIEHLE, M.O. (2002) Interaction of animal cells with ordered nanotopography. *IEEE Transactions on Nanobioscience*, 1, 24-28.
- GARCIA, A. J., VEGA, M.D., BOETTIGER, D. (1999) Modulation of cell proliferation and differentiation through substrate-dependent changes in fibronectin conformation. *Mol. Biol. Cell*, 10, 785-798.

- GEIGER, B., BERSHADSKY, A., PANKOV, R., YAMADA, K.M. (2001) Transmembrane extracellular matrix-cytoskeleton crosstalk. *Nature*, 2, 793-804.
- GIANCOTTI, F. G., TARONE, G. (2003) Positional control of cell fate through joint integrin/receptor protein kinase signaling. *Annu. Rev. Cell Dev. Bio.*, 19, 173-206.
- GILLESPIE, P. G., WALKER, R.G. (2001) Molecular basis of mechanosensory transduction. *Nature*, 413, 194-202.
- GLEICHE, M., CHI, L.F., FUCHS, H. (2000) Nanoscopic channel lattices with controlled anisotropic wetting. *Nature*, 403, 173-175.
- GOODMAN, S. L., SIMS, P.A., ALBRECHT, R.M. (1996) Three-dimensional extracellular matrix textured biomaterials. *Biomaterials*, 17, 2087-2095.
- GOTZINGER, M., PEUKERT, W. (2004) Particle adhesion force distributions on rough surfaces. *Langmuir*, 20, 5298-5303.
- GRABBE, A., HORN, R.G. (1993) Double-layer and hydration forces measured between silica sheets subjected to various surface treatments. *J. Coll. Int. Sci.*, 157, 375-383.
- GRUNZE, M. (1999) Driven Liquids. *Science*, 283, 41-45.
- GU, Z., UETSUKA, H., TAKAHASHI, K., NAKAJIMA, R., ONISHI, H., UJISHIMA, A., SATO, O. (2003) Structural color and the Lotus effect. *Angew. Chem. Int. Ed.*, 42, 894-897.
- GUMBINER, B. M. (1996) Cell adhesion: the molecular basis of tissue architecture and morphogenesis. *Cell*, 84, 345-357.
- HAMAKER, H. C. (1937) The London-Van Der Waals attraction between spherical particles. *Physica*, 10, 1058-1072.
- HAPPEL, J., BRENNER H (1965) *Low Reynolds Number Hydrodynamics*, New York, Prentice-Hall, Inc.
- HARRISON, R. G. (1910) On the stereotropism of embryonic cells. *J Exp Zool*, 10.
- HARTLEY, P. G., LARSON, I., SCALES, P.J. (1997) Electrokinetic and direct force measurements between silica and mica surfaces in dilute electrolyte solutions. *Langmuir*, 13, 2207-2214.
- HAYASHI, T., PERTSIN, A.J., GRUNZE, M (2002) Grand canonical Monte Carlo simulation of hydration forces between nonorienting and orienting structureless walls. *J. Chem. Phys.*, 117, 6271-6280.
- HE, B., LEE, J., PATANKAR, N.A. (2004) Contact angle hysteresis on rough hydrophobic surfaces. *Coll. Surf. A*, 248, 101-104.
- HERMAN, M. C., PAPADOPOULOS, K.D. (1991) A method for modeling the interactions of parallel flat plate systems with surface features. *J. Coll. Int. Sci.*, 142, 331-342.
- HERMINGHAUS, S. (2000) Roughness-induced non-wetting. *Europhys. Lett.*, 52, 165.
- HERRWERTH, S., ECK, W., REINHARDT, S., GRUNZE, M. (2003) Factors that determine the protein resistance of oligoether self-assembled monolayers- internal hydrophilicity, terminal hydrophilicity, and lateral packing density. *J. Am. Chem. Soc.*, 125, 9359-9366.
- HOEK, E. M. V., BHATTACHARJEE, S., ELIMELECH, M. (2003) Effect of membrane surface roughness on colloid-membrane DLVO interactions. *Langmuir*, 19, 4836-4847.

- HOEKS, A. P. G., SAMIJO, S.K., BRANDS, P.J., RENEMAN, R.S. (1995) Noninvasive determination of shear-rate distribution across the arterial lumen. *Hypertension*, 26, 26-33.
- HOGG, R., HEALY, T.W., FUERSTENAU, D.W. (1966) Mutual coagulation of colloidal dispersions. *Trans. Faraday Soc.*, 62, 1638-1651.
- HOLLOWAY, P. J. (1969) The effects of superficial wax on leaf wettability. *Ann. Appl. Biol.*, 63, 145-153.
- HORN, R. G., SMITH, D.T., HALLER, W. (1989) Surface forces and viscosity of water measured between silica sheets. *Chem. Phys. Lett.*, 162, 404-408.
- HULL, M., KITCHNER, J.A. (1969) Interaction of spherical colloidal particles with planar surfaces. *Trans. Faraday Soc.*, 65.
- HUNTER, R. (2002) The significance of stagnant layer conduction in electrokinetics. *Adv. Coll. Int. Sc.*, 100-102, 153-167.
- HYNES, R. O. (2002) Integrins: bidirectional, allosteric signaling machines. *Cell*, 110, 673-687.
- ISHIDA N., I., T., MIYAHARA, M., HIGASHITANI, K. (2000) Nano bubbles on a hydrophobic surface in water observed by tapping-mode atomic force microscopy. *Langmuir*, 16, 6377-6380.
- ISRAELACHVILI, J., PASHLEY, R. (1982) The hydrophobic interaction is long range, decaying exponentially with distance. *Nature*, 300, 341-342.
- ISRAELACHVILI, J., WENNERSTROM, H. (1996) Role of hydration and water structure in biological and colloidal interactions. *Nature*, 379, 219-225.
- ISRAELACHVILI, J. N. (1991) *Intermolecular and surface forces*. 2nd ed., Academic Press.
- IZZARD, C. S., LOCHNER, L.R. (1976) Cell-to-substrate contacts in living fibroblasts: an interference reflexion study with an evaluation of the technique. *J. Cell Sci.*, 21, 129-159.
- JANUSZ, W., PATKOWSKI, J., CHIBOWSKI, S. (2003) Competitive adsorption of Ca²⁺ and Zn(II) ions at monodispersed SiO₂/electrolyte solution interface. *J. Coll. Int. Sci.*, 266, 259-268.
- JOHNSON, S. B., DRUMMOND, C.J., SCALES, P.J., NISHIMURA, S. (1995) Comparison of techniques for measuring the electrical double-layer properties of surfaces in aqueous solution: hexadecyltrimethylammonium bromide self-assembly structures as a model system. *Langmuir*, 11, 2367-2375.
- JOPP, J., GRULL, H., YERUSHALMI-ROZEN, R. (2004) Wetting behaviour of water droplets on hydrophobic microtextures of comparable size. *Langmuir*, 20, 10015-10019.
- KATZ, B., ZAMIR, E., BERSHADSKY, Z.K., YAMADA, K.M., GEIGER, B. (2000) Physical state of the extracellular matrix regulates the structure and molecular composition of cell-matrix adhesions. *Mol. Biol. Cell*, 11, 1047-1060.
- KAVERINA, I., KRYLYSHKINA, O., SMALL, J.V. (2002) Regulation of substrate adhesion dynamics during cell motility. *Int J Bioche Cell Biol*, 34, 746-761.
- KIHIRA, H., RYDE, N., MATIJEVIC, E. (1992) Kinetics of heterocoagulation. Part 2. The effect of the discreteness of surface charge. *J. Chem. Soc. Faraday Trans.*, 88, 2379-2386.
- KRUPENKIN, T. N., TAYLOR, J.A., SCHNEIDER, T.M., YANG, S. (2004) From rolling ball to complete wetting: the dynamic tuning of liquids on nanostructured surfaces. *Langmuir*, 20, 3824-3827.

- KWOK, D. Y., GIETZELT, T., GRUNDKE, K., JACOBASCH, H., NEUMANN, A.W. (1997) Contact angle measurements and contact angle interpretation. 1. Contact angle measurements by axisymmetric drop shape analysis and a goniometer sessile drop technique. *Langmuir*, 13, 2880-2894.
- KWOK, D. Y., LIN, R., NEUMANN, A.W. (1996) Low-rate dynamic and static contact angles and the determination of solid surface tensions. *Colloids and surfaces A*, 116, 63-77.
- LAFUMA, A., QUERE, D. (2003) Superhydrophobic states. *Nature Mat.*, 2, 457-460.
- LAM, C. N. C., WU, R., LI, D., HAIR, M.L., NEUMANN, A.W. (2002) Study of the advancing and receding angles: liquid sorption as a cause of contact angle hysteresis. *Adv. Coll. Int. Sc.*, 96, 169-191.
- LANGLOIS, W. (1964) *Slow Viscous Flow*, New York, Macmillan.
- LAU, K. K. S., BICO, J., TEO, K.B.K., CHHOWALLA, M., AMARATUNGA, G.A.J., MILNE, W.I., MCKINLEY, G.H., GLEASON, K.K. (2003) Superhydrophobic carbon nanotube forest. *NanoLetters*, 3, 1701-1705.
- LECKBAND, D., ISRAELACHVILI, J. (2001) Intermolecular forces in biology. *Q. Rev. Biophys.*, 34, 105-267.
- LEE, J., PATANKAR, N.A. (2005) A roughness-based wettability switching membrane device for hydrophobic surfaces. *J. Micromech. Microeng.*, 15, 591-600.
- LI, S., BHATIA, S., HU, Y., SHIU, Y., LI, Y., USAMI, S., CHIEN, S. (2001) Effects of morphological patterning on endothelial cell migration. *Biorheology*, 38, 101-108.
- LIM, J. Y., LUI, X., VOGLER, E.A., DONAHUE, H.J. (2004) Systematic variation in osteoblast adhesion and phenotype with substratum surface characteristics. *J. Biomed. Mater. Res.*, 68A, 504-512.
- LO, C. H., WANG, H.B., DAMBO, M., WANG, Y.L. (2000) Cell movement is guided by the rigidity of the substrate. *Biophys. J.*, 79, 144-152.
- LU, J. R., SU, T.J., THOMAS, R.K. (1999) Structural conformation of bovine serum albumin layers at the air-water interface studied by neutron reflection. *J. Coll. Int. Sc.*, 213, 426-437.
- MAHESHWARI, G., BROWN, G., LAUFFENBURGER, D.A., WELLS, A., GRIFFITH, G.G. (2000) Cell adhesion and motility depend on nanoscale RGD clustering. *J. Cell Sci.*, 113, 1677-1686.
- MAO, M., ZHANG, J., YOON, R., DUCKER, W.A. (2004) Is there a thin film of air at the interface between water and smooth hydrophobic solids? *Langmuir*, 20, 1843-1849.
- MARMUR, A. (2003) Wetting on hydrophobic rough surfaces: to be heterogeneous or not to be? *Langmuir*, 19, 8343-8348.
- MARMUR, A. (2004) The Lotus Effect: superhydrophobicity and metastability. *Langmuir*, 20, 3517-3519.
- MARTINES, E., SEUNARINE, K., MORGAN, H., GADEGAARD, N., WILKINSON, C.C.D., RIEHLE, M. (2005) Super-hydrophobicity and super-hydrophilicity of regular nanopatterns. *Nano Letters*, 5, 2097-2103.

- MASSIA, S. P., HUBBELL, J.A. (1991) An RGD spacing of 440 nm is sufficient for integrin avb3-mediated fibroblast spreading and 140 nm for focal contacts and stress fiber formation. *J. Cell Bio.*, 114, 1089-1100.
- MCCLARY, K. B., UGAROVA, T., GRAINGER, D.W. (2000) Modulating fibroblast adhesion, spreading and proliferation using self-assembled monolayer films of alkylthiolates on gold. *J. Biomed. Mater. Res.*, 50, 428-439.
- MCHALE, G., SHIRTCLIFFE, N.J., AQIL, S., PERRY, C.C., NEWTON, M.I. (2004) Topography driven spreading. *Phys. Rev. Lett.*, 93, 036102-1.
- MEAGHER, L. (1992) Direct measurement of forces between silica surfaces in aqueous CaCl₂ solutions using an atomic force microscope. *J. Coll. Int. Sci.*, 152, 293-295.
- MEIRON, T. S., MARMUR, A., SAGUY, I.S. (2004) Contact angle measurement on rough surfaces. *J. Coll. Int. Sci.*, 274, 637-644.
- MEREDITH, D. O., ESCHBACH, L., WOOD, M.A., RIEHLE, M.O., CURTIS, A.S.G., RICHARDS, R.G. (2005) Human fibroblasts reactions to standard and electropolished titanium and Ti-6Al-7Nb, and electropolished stainless steel. *J Biomed Mat Res*, 75A, 541-555.
- MEREDITH, J. E., FAZELI, B., SHWARZ, M.A. (1993) The extracellular matrix as a cell survival factor. *Mol Biol Cell*, 4, 953-961.
- MIWA, M., NAKAJIMA, A., FUJISHIMA, A., HASHIMOTO, K., WATANABE, T. (2000) Effects of the surface roughness on sliding angles of water droplets on superhydrophobic surfaces. *Langmuir*, 16, 5754-5760.
- MUNSON, B., YOUNG DF, OKIISHI TH (1990) *Fundamentals of Fluid Mechanics*, New York, John Wiley & Sons, Inc.
- NAKAE, H., INUI, R., HIRATA, Y., SAITO, H. (1998) Effects of surface roughness on wettability. *Acta Mater.*, 46, 2313-2318.
- NEINHUIS, C., BARTHLOTT, W. (1997) Characterization and distribution of water-repellent, self-cleaning plant surfaces. *Annals of Botany*, 79, 667-677.
- NIKLASON, L. E., GAO, J., ABBOTT, W.M., HIRSHI, K.K., HOUSER, S., MARINI, R., LANGER, R. (1999) Functional arteries grown In vitro. *Science*, 284, 489-493.
- NINHAM, B. W. (1999) On progress in forces since the DLVO theory. *Adv. Coll. Int. Sc.*, 83, 1-17.
- OHARA, P. T., BUCK, R.C. (1979) Contact guidance in vitro. *Exp. Cell Res.*, 121, 235-249.
- ONDA, T., SHIBUICHI, S., SATOH, N., TSUJII, K. (1996) Super-water-repellent fractal surfaces. *Langmuir*, 12, 2125-2127.
- ONER, D., MCCARTHY, T.J. (2000) Ultrahydrophobic Surfaces. Effects of topography length scales on wettability. *Langmuir*, 7777-7782.
- OSTUNI, E., CHAPMAN, R.G., LIANG, M.N., MELULENI, G., PIER, G., INGBER, D.E., WHITESIDES, G.M. (2001) Self-assembled monolayers that resist the adsorption of proteins and the adhesion of bacterial and mammalian cells. *Langmuir*, 17, 6336-6343.
- OTTEN, A., HERMINGHAUS, S. (2004) How plants keep dry; a physicist's point of view. *Langmuir*, 20, 2405-2408.

- PALACEK, S. P., LOFTUS, J.C., GINSBERG, M.H., LAUFFENBERGER, D.A., HORWITZ, A.F. (1997) Integrin-ligand binding properties govern cell migration speed through cell-substratum adhesiveness. *Nature*, 385, 537-540.
- PARKER, J. L., CLAEISSON, P.M., ATTARD, P. (1994) *J. Phys. Chem.*, 98, 8468.
- PATANKAR, N. A. (2003) On the modeling of hydrophobic contact angles on rough surfaces. *Langmuir*, 19, 1249-1253.
- PATANKAR, N. A. (2004a) Mimicking the Lotus effect: influence of double roughness structures and slender pillars. *Langmuir*, 20, 8209-8213.
- PATANKAR, N. A. (2004b) Transition between Superhydrophobic states on rough surfaces. *Langmuir*, 20, 7097-7102.
- PELHAM, R. J. J., WANG, Y. (1997) Cell locomotion and focal adhesions are regulated by substrate flexibility. *PNAS*, 94, 13661-13665.
- PERTSIN, A. J., GRUNZE, M. (2000) Computer simulation of water near the surface of oligo(ethylene glycol)-terminated alkanethiol self-assembled monolayers. *Langmuir*, 16, 8829-8841.
- PETRIE, R. J., BAILEY, T., GORMAN, C.B., GENZER, J. (2004) Fast directed motion of "fakir" droplets. *Langmuir*, 20, 9893-9896.
- PIERRES, A., BENOLIEL AM, BONGRAND P (1996) Measuring bonds between surface-associated molecules. *J Immun Meth*, 196, 105-120.
- POMPE, T., RENNER, L., WERNER, C. (2005) Nanoscale features of fibronectin fibrillogenesis depend on protein-substrate interaction and cytoskeleton structure. *Biophys J*, 88, 527-534.
- POYTON, R., BRANTON D (1970) A multipurpose microperfusion chamber. *Exp Cell Res*, 60, 109-114.
- PRANDTL, L. (1952) *Essentials of Fluid Dynamics*, London, Blackie and Son Ltd.
- QUERE, D. (2002) Rough ideas on wetting. *Physica A*, 313, 32-46.
- QUERE, D. (2004) Model droplets. *Nature Materials*, 3, 79-80.
- QUERE, D., LAFUMA, A., BICO, J. (2003) Slippery and sticky microtextured solids. *Nanotech.*, 14, 1109-1112.
- RASBAND, W. S. (1997-2005) *Image J*. Bethesda, Maryland, USA, U.S. National Institutes of Health.
- READ, N. D., KELLOCH, L.J., COLLINS, T.J., GUNDLACH, A.M. (1997) Role of topography sensing for infection-structure differentiation in cereal rust fungi. *Planta*, 202, 163-170.
- RICHTER, G. M., STAMPFL, U., STAMPFL, S., REHNITZ, C., HOLLER, S., SCHNABEL, P., GRUNZE, M. (2005) A new polymer concept for coating of vascular stents using PTFEP (poly(bis(trifluoroethoxy)phosphazene) to reduce thrombogenicity and late in-stent stenosis. *Investigative Radiology*, 40, 210-218.
- RIEDEL, M., MULLER, B., WINTERMANTEL, E. (2001) Protein adsorption and monocyte activation on germanium nanopyramids. *Biomaterials*, 22, 2307-2316.
- RIEHLE, M. O. (2003) Cell behaviour of rat calvaria bone cells on surfaces with random nanometric features. *Mat. Sci. Eng. C*, 23, 337-340.

- ROURA, P., FORT, J. (2002) Comments on "Effects of the surface roughness on sliding angles of water droplets on superhydrophobic surfaces". *Langmuir*, 18, 566-569.
- ROVENSKI, Y. A. (1998) Cellular and molecular mechanisms of tumor invasion. *Biochemistry (Moscow)*, 63, 1029-1043.
- ROVENSKI, Y. A., DOMNINA, L.V., IVANOVA, O.Y., VASILIEV, J.M. (1999) Locomotory behaviour of epitheliocytes and fibroblasts on metallic grids. *J. Cell Sci.*, 112, 1273-1282.
- ROZLOSNIK, N., GERSTENBERG, M.C., LARSEN, N.B. (2003) Effect of Solvents and Concentration on the Formation of a Self-Assembled Monolayer of Octadecylsiloxane on Silicon (001). *Langmuir*, 19, 1182.
- RUARDY, T. G., MOORLAG, H.E., SCHAKENRAAD, J.M., VAN DER MEI, H.C., BUSSCHER, H.J. (1997) Growth of fibroblasts and endothelial cells on wettability gradient surfaces. *J. Coll. Int. Sci.*, 188, 209-217.
- RYAN, W. L., HEMMINGSEN, E.A. (1998) Bubble formation at porous hydrophobic surfaces. *J. Coll. Int. Sc.i*, 197, 101-107.
- SAWHNEY, R. K., HOWARD, J. (2002) Slow local movements of collagen fibers by fibroblasts drive the rapid global self-organization of collagen gels. *J. Cell Bio.*, 157, 1083-1091.
- SHIBUICHI, S., ONDA, T., SATOH, N., TSUJII, K. (1996) Super water-repellent surfaces resulting from fractal structures. *J. Phys. Chem.*, 100, 19512-19517.
- SHIRTCLIFFE, N. J., MCHALE, G., NEWTON, M.I., CHABROL, G., PERRY, C.C. (2004) Dual-scale roughness produces unusually water-repellent surfaces. *Adv. Mater.*, 16, 1929-1932.
- SHIRTCLIFFE, N. J., MCHALE, G., NEWTON, M.I., PERRY, C.C. (2005) Wetting and wetting transitions on copper-based super-hydrophobic surfaces. *Langmuir*, 21, 937-943.
- SHIU, J., KUO, C., MOU, C. (2004) Fabrication of tunable superhydrophobic surfaces by nanosphere lithography. *Chem. Mater.*, 16, 561-564.
- SNOSWELL, D. R. E., DUAN, J., FORNASIERO, D., RALSTON, J. (2003) Colloid stability and the influence of dissolved gas. *J. Phys. Chem B*, 107, 2986-2994.
- SNOSWELL, D. R. E., DUAN, J., FORNASIERO, D., RALSTON, J. (2005) Colloid stability of synthetic titania and the influence of surface roughness. *J. Coll. Int. Sci.*, 286, 526-535.
- SPARNAAY, M. J. (1983) Four notes on van der Waals forces. *J. Coll. Int. Sci.*, 91, 307-319.
- SPIJKER, H. T., BOS, R., BISSCHER, H.J., VAN KOOTEN T.G., VAN OEVEREN, W. (2002) Platelet adhesion and activation on a shielded gradient prepared on polystyrene. *Biomaterials*, 23, 757-766.
- SPRING, K., HOPE A (1978) Size and shape of the lateral intercellular spaces in a living epithelium. *Science*, 200, 54-57.
- STAVRIDIS, M., KATSIKOIANNI, M., MISSIRLIS, Y.F. (2003) The influence of surface patterning and/or sterilization on the hemocompatibility of polycaprolactones. *Mat. Sci. Eng. C*, 23, 359-365.
- SUH, K. Y., JON, S. (2005) Control over wettability of polyethylene glycol surfaces using capillary lithography. *Langmuir*, 21, 6836-6841.

- SUN, N., WALZ, J.Y. (2001) A model for calculating electrostatic interactions between colloidal particles of arbitrary surface topology. *J. Coll. Int. Sci.*, 234, 90-105.
- SURESH, L., WALZ J.Y. (1996) Effect of surface roughness on the interaction energy between a colloidal sphere and a flat plate. *J. Coll. Int. Sci.*, 183, 199-213.
- SURESH, L., WALZ, JY. (1997) Direct measurement of the effect of surface roughness on the colloidal forces between a particle and flat plate. *J. Coll. Int. Sci.*, 196, 177-190.
- TISSOT, O., PIERRES A, FOA C, DELAAGE M, BONGRAND P (1992) Motion of cells sedimenting on a solid surface in a laminar shear flow. *Biophys J*, 61, 204-215.
- TODD, B. A., EPPELL, S.J. (2004) Probing the limits of the Derjaguin approximation with scanning force microscopy. *Langmuir*, 20, 4892-4897.
- TOIKKA, G., HAYES, R.A., RALSTON, J. (1996) Surface forces between spherical ZnS particles in aqueous electrolyte. *Langmuir*, 12, 3783-3788.
- TORTORA, G., GRABOWSKI SR (2000) *Principles of Anatomy and Physiology*, John Wiley&Sons, Inc.
- TSURUTA, D., JONES, J.C.R. (2003) The vimentin cytoskeleton regulates focal contact size and adhesion of endothelial cells subjected to shear stress. *J. Cell Sci.*, 116, 4977-4984.
- TURNER, A. M. P., DOWELL, N., TURNER, S.W.P., KAM, L., ISAACSON, M., TURNER, J.N., CRAIGHEAD, H.G., SHAIN, W. (2000) Attachment of astroglial cells to microfabricated pillar arrays of different geometries. *J Biomed Mater Res*, 51, 430-441.
- TURNER, S., KAM, L., ISAACSON, M., CRAIGHEAD, H.G., SHAIN, W., TURNER, J. (1997) Cell attachment on silicon nanostructures. *J. Vac. Sci. Tech. B*, 15, 2848-2854.
- TYRRELL, J. W. G., ATTARD, P. (2001) Images of nanobubbles on hydrophobic surfaces and their interaction. *Phys. Rev. Lett.*, 87, 176104-1.
- VAN BREE, J. L. M. J., POULIS, J.A., VERHAAR, B.J., SCHRAM, K. (1974) The influence of surface irregularities upon the Van der Waals forces between macroscopic bodies. *Physica*, 78, 187-190.
- VAN KOOTEN, T., SCHAKENRAAD JM, VAN DER MEI HC, BUSSCHER HJ (1992) Development and use of a parallel-plate flow chamber for studying cellular adhesion to solid surfaces. *J. Biomed. Mat. Res.*, 26, 725-738.
- VERWEY, E. J. W., OVERBEEK, J.TH.G. (1948) *Theory of the stability of lyophobic colloids*, Dover.
- VIGIL, G., XU, Z., STEINBERG, S., ISRAELACHVILI, J. (1994) Interactions of Silica Surfaces. *J. Coll. Int. Sci.*, 165, 367-385.
- VOGLER, E. A. (1998) Structure and reactivity of water at biomaterial surfaces. *Adv. Coll. Interf. Sc.*, 74, 69-117.
- WALZ, J. Y. (1998) The effect of surface heterogeneities on colloidal forces. *Adv. Coll. Int. Sc.*, 74, 119-168.
- WATSON, G. S., WATSON, J.A. (2004) Natural nano-structures on insects-possible functions of ordered arrays characterized by atomic force microscopy. *Appl. Surf. Sci.*, 235, 139-144.

- WEBSTER, T. J., ERGUN, C., DOREMUS, R.H., SIEGEL, R.W., BIZIOS, R. (2000) Specific proteins mediate enhanced osteoblast adhesion on nanophase ceramics. *J. Biomed. Mat. Res.*, 51, 475-483.
- WEISS, P. (1934) In vitro experiments on the factors determining the course of the outgrowing nerve fiber. *J. Exp. Zool.*, 68, 393-418.
- WEISS, P. (1945) Experiments on cell and axon orientation in vitro: the role of colloidal exudates in tissue organization. *J. Exp. Zool.*, 100, 353-86.
- WENZEL, R. N. (1936) Resistance of solid surfaces to wetting by water. *Ind. Eng. Chem.*, 28, 988-994.
- WERNER, C., KORBER, H., ZIMMERMANN, R., DUHKIN, S., JACOBASCH, H. (1998) Extended electrokinetic characterization of flat solid surfaces. *J. Coll. Int. Sci.*, 208, 329-346.
- WIELAND, M., CHEHROUDI, B., TEXTOR, M., BRUNETTE, D.M. (2002) Use of Ti-coated replicas to investigate the effects on fibroblast shape of surfaces with varying roughness and constant chemical composition. *J Biomed Mater Res*, 60, 434-444.
- WIELAND, M., TEXTOR, M., CHEHROUDI, B., BRUNETTE, D.M. (2005) Synergistic interaction of topographic features in the production of bone-like nodules on Ti surfaces by rat osteoblasts. *Biomaterials*, 26, 1119-1130.
- WILKINSON, C., RIEHLE M, WOOD, MA GALLAGHER JO, CURTIS ASG (2002) The use of materials patterned on a nano- and micro-metric scale in cellular engineering. *Mat Sci Eng*, 19, 263-263.
- WOJCIAK, B., CROSSAN J., CURTIS A.S.G., WILKINSON C.D.W. (1995) Grooved substrata facilitate In vitro healing of completely divided flexor tendons. *J Mat Sc: Materials in Medecine*, 6, 266-271.
- WOJCIAK-STOTHARD, B., CURTIS A.S.G., MONAGHAN, W., MACDONALD, K., WILKINSON, C.D.W. (1996) Guidance and activation of murine macrophages by nanometric scale topography. *Exp. Cell Res.*, 223, 426-435.
- WOJCIAK-STOTHARD, B., CURTIS, A.S.G., MONAGHAN, W., MCGRATH, M., SOMMER, I., WILKINSON, C.D.W. (1995a) Role of the cytoskeleton in the reaction of fibroblasts to multiple grooved substrata. *Cell Motility and the Cytoskeleton*, 31, 147-158.
- WOJCIAK-STOTHARD, B., MADEJA, Z., KOROHODA, W., CURTIS, A.S.G., WILKINSON, C.D.W. (1995b) Activation of macrophage-like cells by multiple grooved substrata. Topographical control of cell behaviour. *Cell Biol Int*, 19, 485-489.
- WU, Z., ZHANG, X., ZHANG, X., LI, G., SUN, J., ZHANG, Y., LI, M., HU, J. (2005) Nanobubbles influence on BSA adsorption on mica surface. *Surf. Interf. Anal.*, 37, 797-801.
- YANG, J., BOS R, POORTINGA A, WIT PJ, BELDER GF, BUSSCHER HJ (1999) Comparison of particle deposition in a parallel plate flow chamber and a stagnation point flow chamber. *Langmuir*, 15, 4671-4677.
- YOSHIMITSU, Z., NAKAJIMA, A., WATANABE, T., HASHIMOTO, K. (2002) Effects of surface structure on the hydrophobicity and sliding behaviour of water droplets. *Langmuir*, 18, 5818-5822.
- YOUNG, T. (1805) *Phil. Trans. R. Soc. London*, 95, 65.

YU, N., POLYCARPOU, A.A. (2004) Adhesive contact based on the Lennard-Jones potential: a correction to the value of the equilibrium distance as used in the potential. *J. Coll. Int. Sci.*, 278, 428-435.

ZAMIR, E., GEIGER, B. (2001) Molecular complexity and dynamics of cell-matrix adhesions. *J. Cell Sci.*, 114, 3583-3590.

Publications

PUBLISHED BY THE AMERICAN CHEMICAL SOCIETY

A JOURNAL DEDICATED
TO NANOSCIENCE AND
NANOTECHNOLOGY

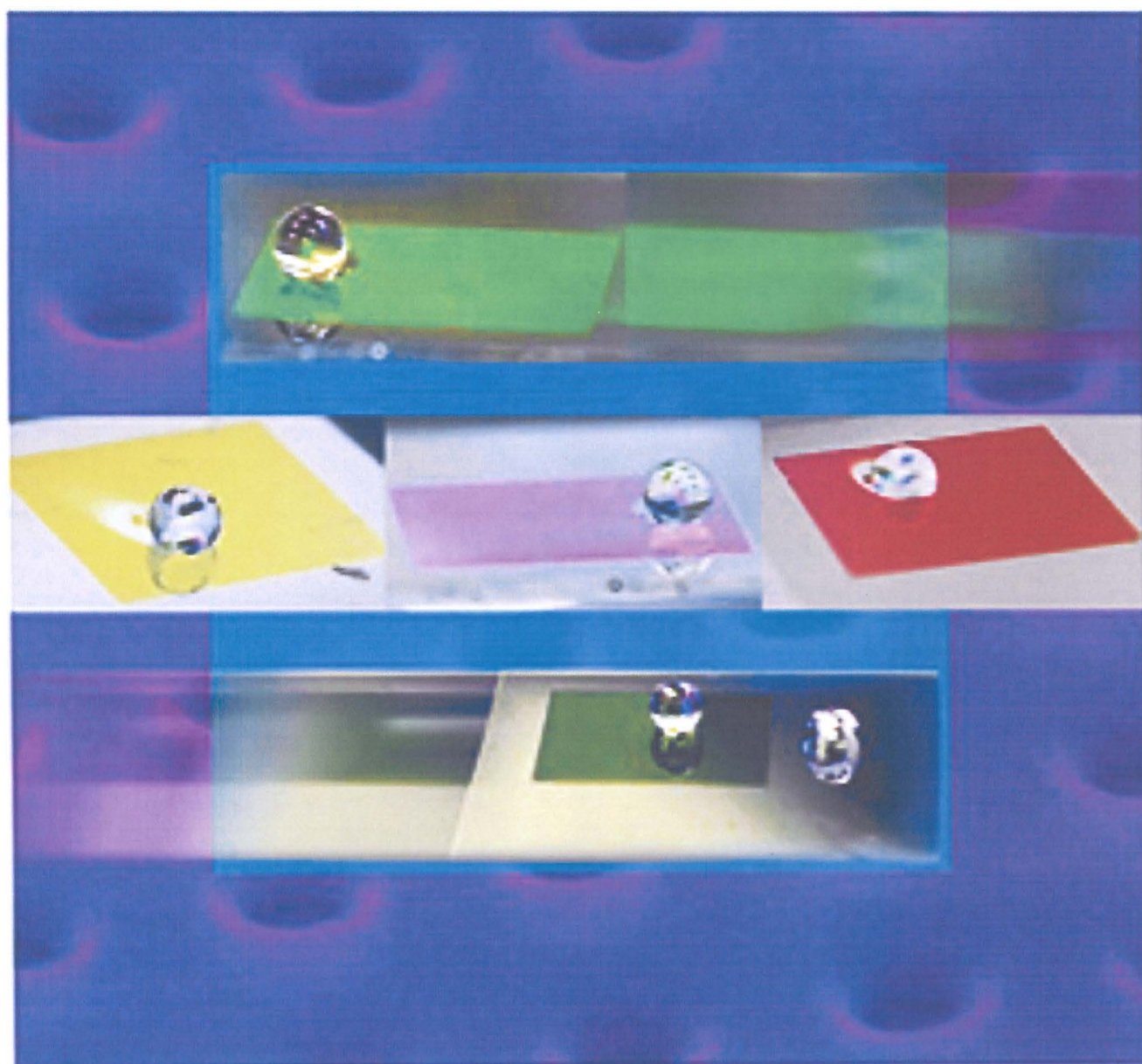
NANO

<http://pubs.acs.org/NanoLett>

VOLUME 5, NUMBER 10

OCTOBER 2005

LETTERS



Water Drops on Regular Nanopatterns

Superhydrophobicity and Superhydrophilicity of Regular Nanopatterns

Elena Martinez,[†] Kris Seunarine,[‡] Hywel Morgan,[§] Nikolaj Gadegaard,[‡] Chris D. W. Wilkinson,[‡] and Mathis O. Riehle^{*†}

Centre for Cell Engineering, IBLs, University of Glasgow, Glasgow, G12 8QQ, U.K.,
Department of Electronics and Electrical Engineering, University of Glasgow,
Glasgow, G12 8QQ, U.K., and School of Electronics and Computer Science,
University of Southampton, S017 1BJ, U.K.

Received July 25, 2005

ABSTRACT

The hydrophilicity, hydrophobicity, and sliding behavior of water droplets on nanoasperities of controlled dimensions were investigated experimentally. We show that the “hemi-wicking” theory for hydrophilic SiO₂ samples successfully predicts the experimental advancing angles and that the same patterns, after silanization, become superhydrophobic in agreement with the Cassie–Baxter and Wenzel theories. Our model topographies have the same dimensional scale of some naturally occurring structures that exhibit similar wetting properties. Our results confirm that a forest of hydrophilic/hydrophobic slender pillars is the most effective superwetable/water-repellent configuration. It is shown that the shape and curvature of the edges of the asperities play an important role in determining the advancing angles.

Introduction. The wettability of solid surfaces is a subject that has raised great interest in the past few decades. The surface energy of a sample will determine if a given liquid drop will roll up or spread when deposited on it. Roughening the surface enhances its repellent or wetting properties,¹ resulting in “superhydrophobic” or “superhydrophilic” textures (this nomenclature applies if the liquid considered is water, as is the case in this work).

Many authors have contributed to the fabrication and understanding of superhydrophobic surfaces.^{2–14} Öner and McCarthy¹⁰ describe a superhydrophobic surface as one where the advancing angle, θ_{adv} , is very high (generally $>150^\circ$), and the receding angle, θ_{rec} , is such that the drop exhibits low hysteresis $\Delta\theta$ ($\Delta\theta = \theta_{adv} - \theta_{rec}$). Water drops form beads and roll off this kind of surface, cleaning it in the process. This phenomenon has been termed the “Lotus effect” because it is very pronounced on the leaves of the lotus plant (*Nelumbo nucifera*).^{14,15} These leaves exhibit a double-structured roughness, where submicrometric wax crystals cover a larger micrometric structure; even though double-scale roughness has been proven to enhance water repellency,¹⁶ it has been suggested that the small scale

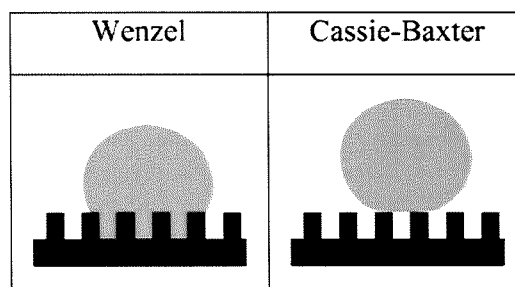


Figure 1. Schematic of roughness-filling by water according to the Wenzel and Cassie–Baxter models.

roughness plays an important role.¹² The wings of some insects (e.g., *Pflatoda claripennis* and in the family Rhinotermitidae) are also covered with nanometric structures that are thought to ensure water repellency as well as other properties;¹⁷ unlike the irregular topography of wax crystals, these surfaces are covered with ordered arrays of rounded protrusions.

The effect of surface roughness on hydrophobicity has been explained by two different theories. According to the model developed by Wenzel, it is assumed that the space between the protrusions on the surface is filled by the liquid³ (Figure 1); this model predicts that both hydrophobicity and hydrophilicity are reinforced by the roughness,

* Corresponding author. E-mail: m.riehle@bio.gla.ac.uk; tel: 0044-141-3302931; fax: 0044-141-3303730.

[†] Centre for Cell Engineering.

[‡] Department of Electronics and Electrical Engineering.

[§] University of Southampton.

according to the following relation

$$\cos \theta_W = r \cos \theta_Y \quad (1)$$

where θ_W is the apparent contact angle on a rough surface, θ_Y is the ideal contact angle (Young's angle) of water on a smooth surface of identical chemistry, and r is the roughness factor, which is defined as the ratio of actual surface area over the projected area.

The approach developed by Cassie and Baxter, however, assumes that air is trapped by the asperities² so that the drop sits on a composite surface made of air and solid (Figure 1); the relation between the apparent contact angle θ_{CB} and the ideal angle θ_Y is in this case described as

$$\cos \theta_{CB} = r_f f \cos \theta_Y + f - 1 \quad (2)$$

where r_f is the roughness factor of the wetted area, and f is the area fraction of the projected wet area. The product $r_f f$ is often called the solid fraction ϕ_s .

Both Wenzel and Cassie–Baxter relations were originally formulated for static drops at equilibrium; yet because it was shown that low-rate advancing angles and static angles are essentially identical,¹⁸ eqs 1 and 2 can be applied to advancing angles. Fewer attempts have been made to model the receding angles.^{11,19} It has been shown⁴ that a droplet can be in either a Cassie–Baxter or a Wenzel state on a rough hydrophobic surface depending on how it is formed. Because the advancing angles predicted by both the Cassie–Baxter and Wenzel theories can be very close to the experimental values, the receding angles can be used as a qualitative indication of the state of the drop: if θ_{rec} is high (i.e., the hysteresis is low), then the drop will be in a Cassie–Baxter (“slippy”) mode; if θ_{rec} is low, then the drop will be in a Wenzel (“sticky”) state. Therefore, obtaining a stable Cassie–Baxter drop is the ultimate goal for achieving superhydrophobicity by tailoring surface topography. The adhesive behavior of water on rough surfaces can also be assessed by sliding-angle measurements.^{5,6,9} The sliding angle is defined as the critical angle where a water droplet begins to slide down an inclined plate: a high sliding angle indicates a sticky Wenzel state, whereas a low sliding angle suggests a Cassie–Baxter regime (i.e., the drop will easily roll off a slightly tilted substrate).⁴

Much less work has been dedicated to the study of superhydrophilic (or more generally, superwetting) surfaces.^{1,20,21} Assuming that no air is trapped in the roughness of the hydrophilic surface (for the opposite case, see Abdelsalam et al.²²), the Wenzel model still applies, along with the hemi-wicking or “composite-drop” model,²³ where the drop is assumed to be sitting on a composite surface made of solid and water.

All of the above-mentioned theories for both hydrophobic and hydrophilic rough surfaces have been tested by preparing surfaces structured on the micrometer scale;^{5–7,9,10,14,16,20} only a few studies have been done recently on nanotopographies,^{8,22,24,25} mainly because of the difficulty of fabrication.

In the present study, we have fabricated ordered arrays of nanopits and nanopillars and investigated their dynamic wettability before and after chemical hydrophobization. Our model structures resemble the natural submicrometric features that ensure the water repellency of biological surfaces such as the lotus leaf and some insect wings.

Because of the accurate geometrical characterization of our nanopatterns, the validity of the analytical models currently available for predicting the wettability of rough surfaces can be verified, for both the hydrophilic and the hydrophobic case. To the best of our knowledge, this is the most extensive quantitative study of the wetting properties of small-scale topography reported so far.

Experimental Details. (A) *Fabrication.* Nanopatterns with increasing solid fraction (two samples with pits and four with pillars) were fabricated in silicon wafers (4 in., <100>, p-doped, $525 \pm 50 \mu\text{m}$ thick) across an area of $1 \times 1 \text{ cm}^2$. (1) Nanopillars. A 2-nm titanium layer was evaporated on the silicon (Plassys evaporator), and the samples were spin-coated immediately with a 60% NEB31A3–40% EC solvent (Sumitomo Chemical Co Ltd) at 3 krpm for 60 s (150-nm-thick coating). After a preexposure bake at 90 °C for 2 min, the wafers were exposed in the e-beam writer (Leica Microsystems EBP 5) with the desired pattern. After a postexposure bake at 85 °C for 2 min, we developed the samples in Microposit MF CD-26 for 20 s and rinsed them with reverse osmosis (RO) water; the titanium was etched (1 part HF: 26 parts RO water) for approximately 2–3 s, and the samples were rinsed in RO water. The silicon was then dry-etched using STS-ICP (Surface Technology Systems-Inductively Coupled Plasma) with C_4F_8 and SF_6 (unswitched gases) at an etch rate of 100 nm/min, and finally piranha-cleaned for 5 min. (2) Nanopits. The silicon wafers were spin-coated with 40% ZEP520A at 5 krpm (100-nm-thick coating) and baked at 180 °C for 1 h. The samples were then exposed in the e-beam writer, developed in *o*-xylene for 60 s, and dry-etched as for the pillars. Finally, the surfaces were piranha-cleaned for 5 min.

(B) *Surface Modification.* Prior to the measurements of contact angles on the hydrophilic nanopatterns, we cleaned all of the samples with an O_2 plasma for 15 min (BP80 RIE, flow rate 20 sccm, pressure 30 mT, RF power 100 W); the contact angles on these surfaces were measured within 24 h.

Subsequently, the same patterns were coated with octadecyltrichlorosilane (OTS) by modifying the procedure of Rosloznic et al.:²⁶ all of the samples were sonicated for 10 s in 1:1 water–ethanol and 10 s in IPA, then rinsed in chloroform and blow-dried. After a 15 min O_2 cleaning, we sonicated them for 10 s in chloroform and 10 s in IPA, rinsed them in 1:1 water–ethanol, rinsed them in RO water, and blow-dried them. The clean samples were then placed in a ceramic slide holder, which was gently tilted on the side at 90° so that the patterns were facing down. This technique ensured that if any OTS clusters formed in the solution, then they had less of a chance of being deposited on the patterned surfaces. The tilted holder was placed in a glass beaker filled with a 0.001% solution of OTS (Sigma) in heptane (Sigma).

After 3.5 h, we sonicated the holder three times for 1 min in copious amounts of heptane, then rinsed it in IPA, 1:1 water–ethanol, and RO water and finally blow-dried it.

(C) *Sample Characterization.* (1) Scanning Electron Microscopy. The surfaces were imaged with a Hitachi S4700 prior to and following hydrophobization. After contact angle measurements, we cleaved them and their SEM profiles were used to measure the dimensions of the asperities with ImageJ.²⁷ (2) Dynamic Contact Angle Measurements. Images of the advancing and receding contact angles of filtered Milli-Q water were captured at a rate of 2 images/s with a long-distance objective connected to a CCD camera and analyzed with the FTÅ200 software (First Ten Ångstroms, v2.0). Water drops were deposited and taken up through a 30-gauge flat-tipped needle, at a rate of 0.25 $\mu\text{L/s}$; the maximum volume of the drops was 5 μL on hydrophobic substrates and 4 μL on hydrophilic ones. The values reported are averages of at least five measurements made on different areas of the sample. All of the measurements were performed at room temperature on a vibration-free platform. (3) Sliding-Angle Measurements. For sliding-angle measurements on the hydrophobic samples, water drops of weight ranging from 5 to 40 mg were deposited gently on a horizontal plate fixed on a goniometer by means of a calibrated micropipet. The goniometer was rotated slowly until the drops started to slide. The sliding angle was determined on at least four different locations/sample.

Theoretical Models. (A) *Hydrophobic Surfaces.* For vertical structures with a flat top, assuming that the water does not invade the roughness, then $r_f = 1$ and $\phi_s = f$. In this work, ϕ_s always refers to the solid fraction of cylindrical pillars $\phi_s = \pi d^2/4l^2$, where d is the base diameter of the cylinders, and l is their center-to-center pitch. We applied the Cassie–Baxter and Wenzel formulas to different geometries. (1) The Cassie–Baxter relation was calculated for two cases:

cylindrical asperities:

$$\cos \theta_{\text{CB-c}} = -1 + \phi_s(\cos \theta_Y + 1) \quad (3)$$

hemispherical-top pillars:⁷

$$\cos \theta_{\text{CB-h}} = -1 + \phi_B(\cos \theta_Y + 1)^2 \quad (4)$$

where ϕ_B is the ratio of the area of the asperity bases over the total area. In our case, $\phi_B = \phi_s$. (2) Wenzel's relation was calculated for two cases:

cylindrical asperities:

$$\cos \theta_{\text{W-c}} = r \cos \theta_Y \quad (5)$$

hemispherical-top pillars:

$$\cos \theta_{\text{W-h}} = [1 + 4\phi_s(\frac{h}{d} - 0.25)] \cos \theta_Y \quad (6)$$

We also calculated the receding angle of composite drops by assuming that a receding drop leaves a film of water behind.¹⁹ In this way, Patankar¹¹ derived eq 7 to predict the receding angles on asperities with a flat top

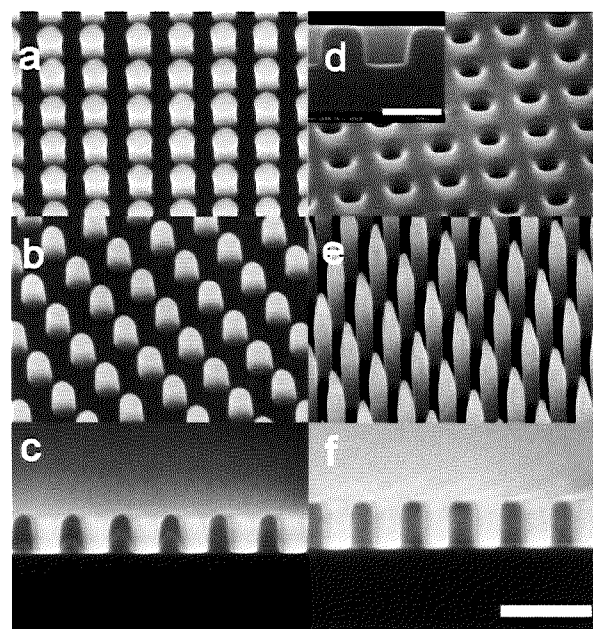


Figure 2. SEM images of (a) P22 before hydrophobization; (b) P22 after hydrophobization; (c) profile of P22; (d) sample H83 after hydrophobization, the insertion shows its profile; (e) P12 after hydrophobization; (f) profile of P21. The profiles were imaged with a 90° tilt, the other images were taken at 45°, scale bar = 500 nm (a–f) and 200 nm (inset in d), respectively.

Table 1. Dimensions of the Nanopatterns^a

	H90	H83	P22	P21	P13	P12
d (nm)	105	138	157	156	124	117
h (nm)	116	141	239	286	268	792
l (nm)	300	300	300	300	300	300

^a All dimensions were measured with ImageJ (± 5 nm). In case of hollow asperities (H), h indicates the depth. In case of pillars (P), h indicates the maximum distance from the base to the top.

($r_f = 1$). We applied eq 7 to cylindrical pillars

$$\cos \theta_{\text{rec-c}} = 2\phi_s - 1 \quad (7)$$

In the case of hemispherical asperities, eq 7 becomes

$$\cos \theta_{\text{rec-h}} = \phi_s(2 + 2 \cos \theta_Y + \sin^2 \theta_Y) - 1 \quad (8)$$

(B) *Hydrophilic Surfaces.* We applied the composite-drop (or hemi-wicking) and the Wenzel formulas to different geometries. (1) The composite-drop relation was calculated for two cases:

cylindrical asperities:²³

$$\cos \theta_{\text{comp-c}} = 1 + \phi_s(\cos \theta_Y - 1) \quad (9)$$

hemispherical-top pillars:

$$\cos \theta_{\text{comp-h}} = \phi_s(2 \cos \theta_Y + 3 \cos^2 \theta_Y - 1) + 1 \quad (10)$$

(2) Wenzel's relation was applied to the case of cylindrical pillars, as in eq 5.

Table 2. Experimental Angles of Water on Hydrophobic (5 μL Drop) and Hydrophilic (4 μL Drop) Nanopatterns^a

		flat	H90	H83	P22	P21	P13	P12
hydrophobic	$\theta_{\text{adv}}(\text{deg})$	114 ± 1	125 ± 2	129 ± 3	155 ± 2	159 ± 2	161 ± 2	164 ± 2
	$\theta_{\text{rec}}(\text{deg})$	100 ± 3	92 ± 2	89 ± 2	0	140 ± 2	150 ± 2	163 ± 2
	model		W-c	W-c	W-h	CB-h	CB-h	CB-h
hydrophilic	$\theta_{\text{adv}}(\text{deg})$	35 ± 3	36 ± 3	35 ± 3	12 ± 3	19 ± 3	11 ± 3	0
	$\theta_{\text{rec}}(\text{deg})$	0	0	0	0	0	0	0
	model		comp-c	comp-c	comp-c	comp-c	comp-c	comp-h

^a Advancing and receding angles are shown, along with the best theoretical agreement (model): (W) Wenzel, (CB) Cassie–Baxter and (comp) composite-drop, with (-c) cylindrical and (-h) hemispherical top.

Results and Discussion. (A) *Sample Characteristics.* SEM images of the patterns immediately after fabrication showed perfectly cylindrical nanopillars and nanopits, except for sample P12, where the tall pillars had a cusped top. The edges of the pillars were rounded after hydrophobization because of sonication. This is summarized in Figure 2a–b. In particular, sample P22 has pillars with a hemispherical top (Figure 2c), and the others look like cylinders with smooth edges (Figure 2f), except P12 whose shape was unchanged after coating (Figure 2e). The pitted samples (Figure 2d) had a cylindrical profile. The different patterns were named after their solid fraction percentage (H designates a hollow pattern, i.e., pits, P a protruding pattern, i.e., pillars; P22 indicates a pillared sample where 22% of the apparent area is wet by the drop, assuming a cylindrical top). Table 1 shows the dimensions of the patterns (base diameter d , height h , center-to-center pitch l). The contact angle measured on the OTS-coated flat silicon was $114 \pm 1^\circ$, which indicates that a monolayer was formed (a contact angle for total coverage was reported to be 115°).²⁶

(B) *Hydrophilic Patterns: Experiments and Predictions.* The experimental advancing and receding angles (θ_{adv} and θ_{rec}) on hydrophilic silicon are shown in Table 2. The experimental advancing angles along with the theoretical predictions are plotted in Figure 3. Because all of the structures (except P12) were perfectly cylindrical, the Wenzel and composite-drop curves were plotted for this geometry; the composite-drop curve for hemispherical-top pillars is also shown for comparison with the experimental advancing angle on P12. Young's angle for these substrates was taken as the angle measured on the flat control ($\theta_Y = 35 \pm 1^\circ$). The receding drops on these substrates were pinned ($\theta_{\text{rec}} = 0^\circ$), as predicted by Quere.²³

Figure 3 shows that the composite-drop formula for cylindrical asperities is in excellent agreement with the experimental values, except for sample P12 where $\theta_{\text{adv}} = 0^\circ$. It should be noted that both the Wenzel formula for cylinders and the composite-drop formula for hemispherical tops (eq 10) always predict an apparent angle of 0° , which is theoretically unattainable because $\cos \theta > 1$. Therefore, the topography-induced superhydrophilicity of sample P12 was due to the high aspect ratio, h/d , of the protrusions, which acted as a reservoir for the fast spreading of the liquid front,²³ a spreading much faster than that on the flat surface.²¹ Because the composite-drop relation does not depend on the aspect ratio of the features, this formula predicts that hemispherical-top pillars will always be superhydrophilic.

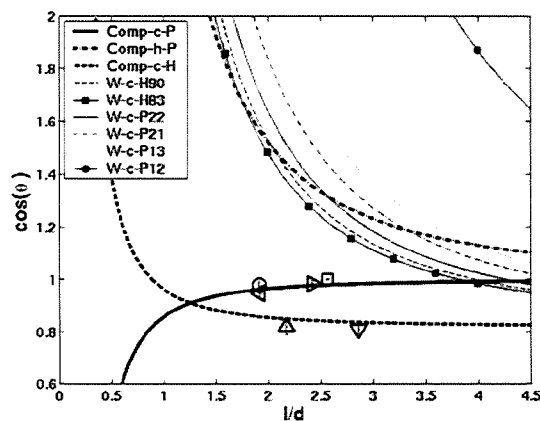


Figure 3. Plot of the apparent advancing angles of a 4- μL drop of water on hydrophilic patterns as a function of structure geometry. composite drop (comp-) and Wenzel (W-) curves for cylindrical (-c) and hemispherical (-h) asperities are shown. The Wenzel curves were plotted for cylindrical asperities only. The composite drop curves for pillars, P, and pits, H, are different because of a different dependence on l/d . Individual points indicate experimental data: (Δ) H90; (∇) H83; (\circ) P22; (left-facing triangle) P21; (right-facing triangle) P13; (\square) P12.

In this context, it would be interesting to investigate the effect of height variation on the reservoir-effect of such structures.

(C) *Hydrophobic Patterns: Experiments and Predictions.* The experimental advancing and receding angles (θ_{adv} and θ_{rec}) on hydrophobic silicon are shown in Table 2. Young's angle for these substrates was taken as the advancing angle measured on the flat control ($\theta_Y = 114^\circ \pm 1$). The experimental advancing angles along with the theoretical predictions are plotted in Figure 4.

Because the end-geometries of the hydrophobized pillars were somewhat between cylindrical and hemispherical, the Cassie–Baxter and Wenzel curves were plotted for both geometries (eqs 3 and 5 in Figure 4a, and eqs 4 and 6 in Figure 4b), whereas the pits were always modeled as perfect cylinders (eqs 3 and 5). The sliding angles in Figure 5 were used as a means to test the predictions derived from Figure 4 concerning the “state” of the drops (i.e., Cassie–Baxter or Wenzel).

In the following paragraphs, we discuss our results within the framework of Patankar's criterion for designing superhydrophobic surfaces.¹¹ Briefly, this method consists of obtaining a stable Cassie–Baxter drop by fabricating structures, which, given the highest possible aspect ratio, h/d , have a dimensionless spacing, l/d , such that $\cos \theta_{\text{CB}} > \cos \theta_{\text{W}}$, or

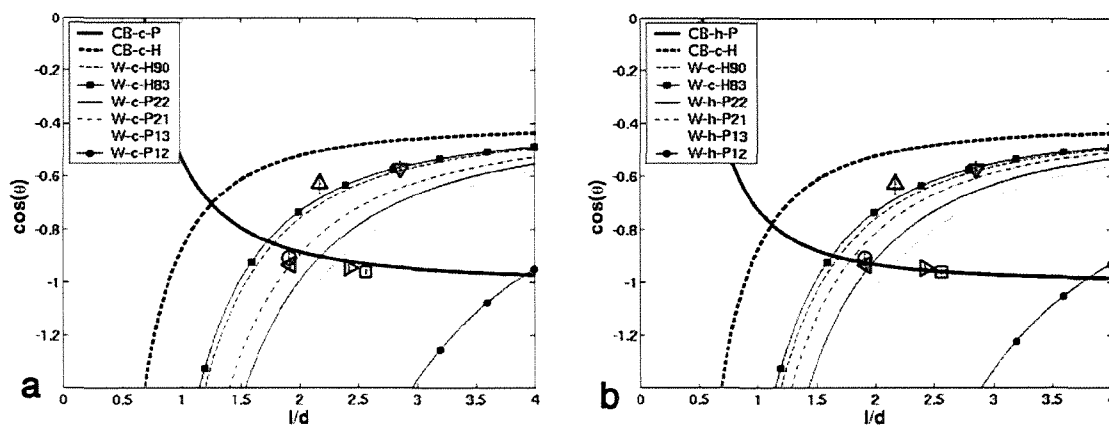


Figure 4. Plot of the apparent advancing angles of a 5- μ L drop of water on hydrophobic patterns as a function of structure geometry. (a) Cassie–Baxter (CB-) and Wenzel (W-) curves for cylindrical asperities (-c-). (b) Cassie–Baxter (CB-) and Wenzel (W-) curves for cylindrical asperities (-c-) and cylinders with hemispherical tops (-h-). The CB and W curves for pits H90 and H83 are the same (W-c-H) in a and b, whereas the CB and W curves for pillars are different: in a the pillars (P) are modeled as cylinders; in b they are modeled as cylinders with hemispherical tops. Note that the dependence of the CB curve on l/d for pillars and pits (CB-c-H and CB-c-P) is different. Individual points indicate experimental data: (Δ) H90; (∇) H83; (\circ) P22; (left-facing triangle) P21; (right-facing triangle) P13; (\square) P12.

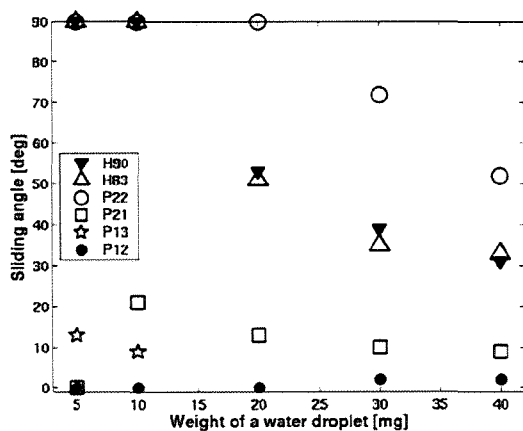


Figure 5. Sliding angles of water droplet on hydrophobic patterns as a function of drop weight. The points at 90° indicate pinned drops.

a value of $|\cos \theta_W - \cos \theta_{CB}|$ as high as possible; the first condition ensures that a Cassie–Baxter drop will have lower energy than a Wenzel drop for the given geometry; the second condition means that even if $\cos \theta_{CB} < \cos \theta_W$, then the energy barrier between the two states should be as high as possible to avoid transitions from a metastable Cassie–Baxter drop to a lower-energy Wenzel state.

The experimental values of the advancing angles on the pitted samples (H90 and H83) were in agreement with their respective Wenzel curves for cylindrical pits (same W-c-H in both Figure 4a–b). This was supported by sliding-angle measurements, where 5–10 mg drops were completely pinned (Figure 5). This result goes against theoretical expectations because the Cassie–Baxter curve for pits (CB-c-H) is always at a lower energy than the Wenzel one (W-c-H), that is, $\cos \theta_{CB-c-H} > \cos \theta_{W-c-H}$. However, the Cassie–Baxter regime for pits is stabilized only for $l/d < 1.54$ (H90) and $l/d < 1.48$ (H83), which are the critical values at which the corresponding Wenzel angles become unattainable ($\cos \theta_W < -1$); it is therefore possible to obtain a higher

energy configuration with our topography. However, this predicts the occurrence of stable Cassie drops on pitted surfaces with a high density of pits of large diameters.

The best agreement with the experimental data for pillars was found with the models using a hemispherical top (Figure 4b), even when the tops were not perfectly hemispherical (e.g., as in Figure 2f). This underlines the importance of the curvature of the edges in determining the advancing angles. From now on, we will refer to the results plotted in Figure 4b.

Samples P22 and P21 had practically the same ϕ_S values, but different roughness values, r . Their experimental advancing angles were close to the intersection between the Cassie–Baxter curve for pillars and their Wenzel curves. In this case, the receding angles should allow us to distinguish if the drops were in either a Wenzel or a Cassie–Baxter state. On receding, the water droplets were pinned on P22 ($\theta_{rec} = 0^\circ$) because the receding angle never attained a steady state. The sliding-angle measurements showed that drops of up to 20 mg were pinned on this substrate (upper 90° values in Figure 5). This result suggests that P22 is in a Wenzel state; this could be explained by the fact that P22 is the shallowest of the four protruding patterns and it has truly hemispherical edges: both factors make the Cassie–Baxter regime more unlikely to happen because sharp edges and a high aspect ratio are important conditions to ensure air trapping.⁷ Öner and McCarthy¹⁰ showed that the receding angles depended on the three-phase contact line structure, whereas the advancing angles were unaffected by it. We suggest that the unusual pinning on sample P22 might be due to the curvature of the hemispherical tops (see Figure 2c) because the contact line could be pinned by greater solid–liquid contact and indeed a hemispherical top will have more solid–liquid contact than a flat top with the same height ($\Delta\phi_S = 4\%$ for P22). However, a receding angle of 0° was unexpected, and we have no explanation for this; between the possible reasons we cannot exclude a differential hydrophobization of the

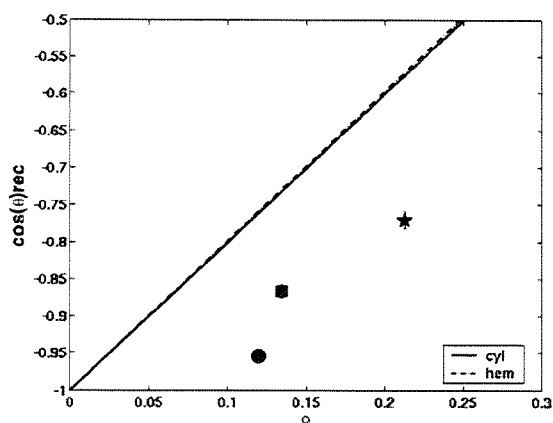


Figure 6. Receding angles of water on hydrophobic patterns as a function of the solid fraction, ϕ_s . The experimental values ((★) P21; (■) P13; (●) P12) are plotted with eq 7 (cyl) and eq 8 (hem).

bottom surface compared to the top of the asperities, which would have affected the receding angles on the Wenzel samples; still, only P22 showed this behavior.

Unlike P22, sample P21 had a high receding angle, showing that it was in a Cassie state. Its closeness to the critical point would imply that a transition to the Wenzel state would need very little energy; this hypothesis was confirmed by the tilting angle measurements, which showed a sudden jump from 0 to 21° when the drop weight was increased from 5 to 10 mg. The increased weight forced the water inside the texture, and the 10-mg drop transitioned to the Wenzel state.

For sample P13, a Wenzel state would have a lower energy, but the energy barrier to overcome is bigger than that in P21. In this case, an increase in drop weight from 5 to 10 mg caused a decrease in sliding angle, confirming the Cassie–Baxter state of the 5- μL droplet.

Sample P12 had the best water-repellent configuration not only because the Cassie–Baxter state was at lower energy than the Wenzel state and the energy barrier between the two was very high but also because the Wenzel angle corresponding to this geometry is unattainable ($\cos \theta_w < -1$). Tilting angles on P12 were $0 \pm 2^\circ$ throughout the whole range of drop weights, making it impossible to deposit a drop smaller than 30 μL . This finding is coherent with Patankar's prediction that a forest of nanopillars would be the most effective water-repellent structure,¹² confirming that for a given spacing, l , increasing the aspect ratio, h/d , will stabilize the Cassie–Baxter regime, as was also illustrated by Yoshimitsu et al.⁵ Sample P12 was superwetable when its surface was hydrophilic: this similarity not only shows that roughness with the highest possible aspect ratio, h/d , will dramatically enhance the wettability of a surface, whether hydrophilic or hydrophobic, but it also entails the ambivalence of topography-enhanced wetting/dewetting, as highlighted already by McHale et al.²¹

Having verified the validity of the Cassie–Baxter model for our submicrometric structures, we investigated Patankar's¹² suggestion that the epicuticular wax crystalloids on the Lotus leaf (200 nm–1 μm) play a significant role in

repelling water droplets. We tested this hypothesis by applying the Cassie–Baxter formula for hemispherical tops to our superhydrophobic surfaces (P21, P13, and P12), assuming an ideal contact angle of cuticular wax $\theta_Y = 100^\circ$:²⁸ the Cassie–Baxter formula predicts apparent contact angles of 150, 155, and 157°, respectively. This result is only indicative because the morphology of the wax crystalloids is very different from those of our model structures. However, we can confirm Patankar's hypothesis that roughness at this scale might stabilize or even be the primary cause of the hydrophobicity of dual-scale topographies. It would be even more interesting for us to compare our results with experimental contact angles of insect wings because our models closely resemble the ordered arrays of nanometric structures shown by Watson et al.¹⁷ Unfortunately, this data is not available at present.

Finally, we verified that the current theoretical predictions for receding angles agree with our experimental values. The experimental receding angles of our Cassie–Baxter drops (P21, P13, and P12) were plotted with eqs 7 and 8 (Figure 6). Our values show a trend similar to the theoretical curves for cylindrical and hemispherical-ended pillars, but more work will have to be done in order to obtain better quantitative predictions.

Conclusions. Regular nanopatterns were fabricated in silicon wafers, and the behavior of water droplets on these surfaces was evaluated before and after chemical hydrophobization. From our results, we conclude that the composite-drop (hemi-wicking) model successfully predicts the advancing angles on hydrophilic patterns. Analogously, the Cassie–Baxter and Wenzel models gave accurate estimates of the advancing angles on hydrophobic patterns. These models are very sensitive to even small variations in the asperity profile, and we show that if the edges of the cylindrical pillars are not sharp, a geometry considering a hemispherical-top rather than a flat one will predict the advancing experimental angles more accurately; we suggest that the same might be true for receding angles. In accordance with Patankar's criterion for designing a superhydrophobic surface, we confirmed that a forest of slender pillars is the most stable water-repellent texture; this same topography exhibited superhydrophilicity, confirming the ambivalence of topography-enhanced wetting/dewetting. Finally, our findings support the suggestion that the epicuticular wax crystalloids of the lotus leaf play a main role in its water-repellent behavior.

Acknowledgment. Many thanks to Adam S. G. Curtis, F. Madani, V. Koutsos, L. Csaderova, N. Blondiaux, M. Robertson, and S. Borzı. The partial support by the EC-funded project NaPa (contract no. NMP4-CT-2003-500120) is gratefully acknowledged. The content of this work is the sole responsibility of the authors.

References

- (1) Bico, J.; Thiele, U.; Quere, D. *Colloids Surf., A* **2002**, *206*, 41–46.
- (2) Cassie, A. B. D.; Baxter, S. *Trans. Faraday Soc.* **1944**, *40*, 546.
- (3) Wenzel, R. N. *Ind. Eng. Chem.* **1936**, *28*, 988–994.
- (4) Quere, D.; Lafuma, A.; Bico, J. *Nanotechnology* **2003**, *14*, 1109–1112.
- (5) Yoshimitsu, Z.; Nakajima, A.; Watanabe, T.; Hashimoto, K. *Langmuir* **2002**, *18*, 5818–5822.

- (6) Shibuichi, S.; Onda, T.; Satoh, N.; Tsujii, K. *J. Phys. Chem.* **1996**, *100*, 19512–19517.
- (7) Bico, J.; Marzolin, C.; Quere, D. *Europhys. Lett.* **1999**, *47*, 220–226.
- (8) Lau, K. K. S.; Bico, J.; Teo, K. B. K.; Chhowalla, M.; Amaratunga, G. A. J.; Milne, W. I.; McKinley, G. H.; Gleason, K. K. *Nano Lett.* **2003**, *3*, 1701–1705.
- (9) Miwa, M.; Nakajima, A.; Fujishima, A.; Hashimoto, K.; Watanabe, T. *Langmuir* **2000**, *16*, 5754–5760.
- (10) Oner, D.; McCarthy, T. J. *Langmuir* **2000**, 7777–7782.
- (11) Patankar, N. A. *Langmuir* **2003**, *19*, 1249–1253.
- (12) Patankar, N. A. *Langmuir* **2004**, *20*, 8209–8213.
- (13) Marmur, A. *Langmuir* **2004**, *20*, 3517–3519.
- (14) Furstner, R.; Barthlott, W.; Neinhuis, C.; Walzel, P. *Langmuir* **2005**, *21*, 956–961.
- (15) Barthlott, W.; Neinhuis, C. *Planta* **1997**, *202*, 1–8.
- (16) Shirtcliffe, N. J.; McHale, G.; Newton, M. I.; Perry, C. C. *Langmuir* **2005**, *21*, 937–943.
- (17) Watson, G. S.; Watson, J. A. *Appl. Surf. Sci.* **2004**, *235*, 139–144.
- (18) Kwok, D. Y.; Lin, R.; Neumann, A. W. *Colloids Surf., A* **1996**, *116*, 63–77.
- (19) Roura, P.; Fort, J. *Langmuir* **2002**, *18*, 566–569.
- (20) Bico, J.; Tordeux, C.; Quere, D. *Europhys. Lett.* **2001**, *55*, 214–220.
- (21) McHale, G.; Shirtcliffe, N. J.; Aqil, S.; Perry, C. C.; Newton, M. I. *Phys. Rev. Lett.* **2004**, *93*, 036102–1.
- (22) Abdelsalam, M. E.; Bartlett, P. N.; Kelf, T.; Baumberg, J. *Langmuir* **2005**, *21*, 1753–1757.
- (23) Quere, D. *Physica A* **2002**, *313*, 32–46.
- (24) Burton, Z.; Bhushan, B. *Nano Lett.* **2005**, *5*, 1607–1613.
- (25) Suh, K. Y.; Jon, S. *Langmuir* **2005**, *21*, 6836–6841.
- (26) Rozlosnik, N.; Gerstenberg, M. C.; Larsen, N. B. *Langmuir* **2003**, *19*, 1182.
- (27) Rasband, W. S. U.S. National Institutes of Health: Bethesda, MD, 1997–2005.
- (28) Holloway, P. J. *Ann. Appl. Biol.* **1969**, *63*, 145–153.

NL051435T

A Parallel-Plate Flow Chamber to Study Initial Cell Adhesion on a Nanofeatured Surface

Elena Martines*, Kieran McGhee, Chris Wilkinson, and Adam Curtis

Abstract—Cells in the human body come across many types of information, which they respond to. Both material chemistry and topography of the surface where they adhere have an effect on cell shape, proliferation, migration, and gene expression. It is possible to create surfaces with topography at the nanometric scale to allow observation of cell-topography interactions. Previous work has shown that 100-nm-diameter pits on a 300-nm pitch can have a marked effect in reducing the adhesion of rat fibroblasts in static cultures. In the present study, a flow of cell suspension was used to investigate cell adhesion onto nanopits in dynamic conditions, by means of a parallel-plate flow chamber. A flow chamber with inner nanotopography has been designed, which allows real-time observation of the flow over the nanopits. A nanopitted pattern was successfully embossed into polymethylmethacrylate to meet the required shape of the chamber. Dynamic cell adhesion after 1 h has been quantified and compared on flat and nanopitted polymethylmethacrylate substrates. The nanopits were seen to be significantly less adhesive than the flat substrates ($p < 0.001$), which is coherent with previous observations of static cultures.

Index Terms—Cell adhesion, embossing, flow, nanotopography, polymethylmethacrylate, topography

I. INTRODUCTION

THE ADHESION of cells to their surroundings is of crucial importance in governing a range of cell functions in physiology, pathology, and biotechnological applications. Tissue engineers are interested in cell adhesion onto artificial biomaterials, since a better knowledge of cell behavior can be applied in clinical trials: there is a need for designing prosthetic devices whose surface triggers a specific cell response, e.g., giving control over the phenotype and activity of the cells, or reducing inflammation around the implant.

An important factor in cell adhesion is the shape of the surface (“topography”) to which they adhere: different surface patterns have been shown to affect cell adhesion, morphology, and gene expression [1], [2].

By modifying the topography of surfaces, it is possible to study cell reaction to a variety of patterns. Surfaces with topographies at the micrometric [3], [4] and nanometric scale [5]–[9] can be created to allow observation of cell–surface interactions *in vitro*; it is interesting to investigate the impli-

cations of varying such a system, since the reaction of cells depends strongly on cell type and feature aspect ratio [2], [5], [8], [10]–[12].

The fabrication of nanopatterned substrates can be achieved with high-precision techniques like photolithography and electron beam lithography; both are used in-house. The electron beam lithography yields a lateral resolution as high as 5–10 nm, but unfortunately, although very precise, it is also expensive and time consuming, especially if large areas need to be patterned. To overcome these inconveniences, it is possible to replicate the substrate topography by embossing a mold into polymers, which also allows the combination of the topography with different materials in a cheap and reliable way [9], [13], [14].

Previous work has shown that 60–150-nm-diameter pits on a 300-nm pitch in polycaprolactone (PCL) can have a marked effect in reducing epitenon cell adhesion in static cultures [11], [15]. It is interesting to note that also some biological surfaces show functional nanometric patterns that prevent contamination and biofouling [16], [17].

The work of Gallagher *et al.* [15] was carried out in static conditions, where Brownian motion, gravity, and perhaps convection are the main acting forces. We wanted to build a system where hydrodynamic forces play the biggest role; the reason behind this is that cell adhesion under flow conditions has a very important role in many physiological functions, e.g., in the immune and developmental system. In the living body many cells are always surrounded or transported by actively moving fluids. Making cells flow onto a substrate can change their adhesion process, binding strength, and morphology with respect to a static culture [18]–[21]. Not only it is, perhaps, physiologically correct to culture cells in a flow, but it allows us to investigate phenomena (e.g., the rolling motion of leukocytes [22] or the migration of granulocytes [23]) whose mechanisms are still poorly understood. A number of flow chambers have been developed through the years, including parallel-plate flow chambers and stagnation-point flow chambers, that have been used to study, among others, cell adhesion, bacterial adhesion, microsphere deposition, and receptor–ligand bonds [18], [19], [21], [22], [24]–[28]; in a parallel-plate flow chamber, the motion of a sphere in laminar flow can be predicted with high approximation, and cell trajectories, speed, and adhesion can be monitored.

This study combines the use of a parallel-plate flow chamber and of nanopatterned polymethylmethacrylate surfaces: as a result, the cells flow steadily over nanopits 100 nm in diameter on a 300-nm pitch. This system allows observation and counting of cells, reproducibility of the experiment, and easy assembly of the nanotopography inside the chamber. Cell adhesion after 1-h flow was quantified.

Manuscript received March 2, 2004; revised March 15, 2004. This work was supported by the Engineering and Physical Sciences Research Council. *Asterisk indicates corresponding author.*

*E. Martines is with the Centre for Cell Engineering, Institute of Biomedical and Life Sciences, University of Glasgow, Glasgow G12 8QQ, U.K. (e-mail: elena@mblab.gla.ac.uk).

K. McGhee and C. Wilkinson are with the Department of Electronics and Electrical Engineering, University of Glasgow, Glasgow G12 8QQ, U.K.

A. Curtis is with the Centre for Cell Engineering, Institute of Biomedical and Life Sciences, University of Glasgow, Glasgow G12 8QQ, U.K.

Digital Object Identifier 10.1109/TNB.2004.828268

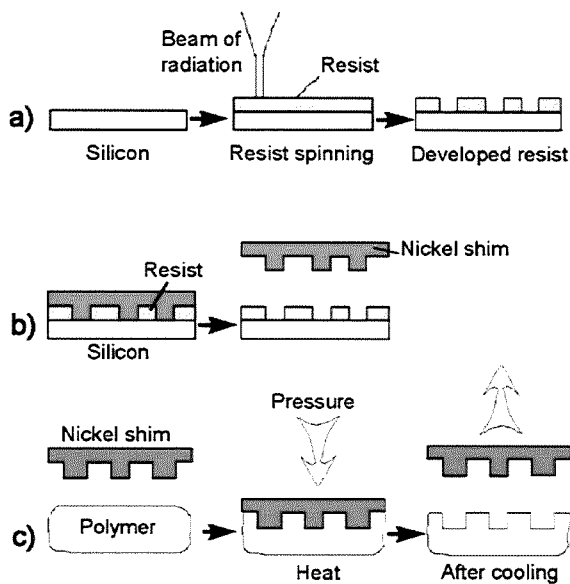


Fig. 1. Fabrication of nanopatterned PMMA. (a) Electron-beam lithographic process. (b) Electroplating. (c) Embossing of the nickel shim into the polymer.

II. MATERIALS AND METHODS

A. Fabrication of the Substrate

Samples of polymethylmethacrylate (PMMA) (GoodFellow Cambridge Ltd., Huntingdon, U.K., 1-mm thickness) were patterned following three steps (Fig. 1).

- 1) The pitted pattern (100-nm-diameter pits on a 300-nm pitch) was written by electron beam lithography (Leica EBPG5-HR) in the resist onto a silicon master [15].
- 2) A nickel shim was electroplated on the developed resist [9]; thus, the shim was the mold which carried the negative image of the nanopatterned resist.
- 3) The nickel shim was embossed into a sheet of solid PMMA in an embossing machine (Nanoimprinter, Obducat, Malmö, Sweden). The pattern on the PMMA is the same as on the resist.

PMMA was chosen because of its biocompatibility and physical properties (transparent, suitable melting temperature). In the Nanoimprinter, the shim is pressed against the polymer, which is heated above its glass transition temperature (approximately 90 °C). The polymer flows in the nanocavities of the shim, and is then cooled (with an injected flow of cold nitrogen) and separated.

A square nanopitted pattern ($15 \times 15 \text{ mm}^2$) was embossed in the middle of rectangular PMMA sheets at 180 °C under 15 bars for 300 s; these samples were used as the bottom wall of the flow chambers (Fig. 2).

1) *Observation of the Replicas:* The embossed PMMA substrates were sputter coated with AuPd, then examined by a Hitachi S800 scanning electron microscope at a voltage of 10 keV.

B. Flow Chamber

The embossed PMMA substrates were sonicated in ethanol for 1 min and in Millipore water for 2 min, and then further

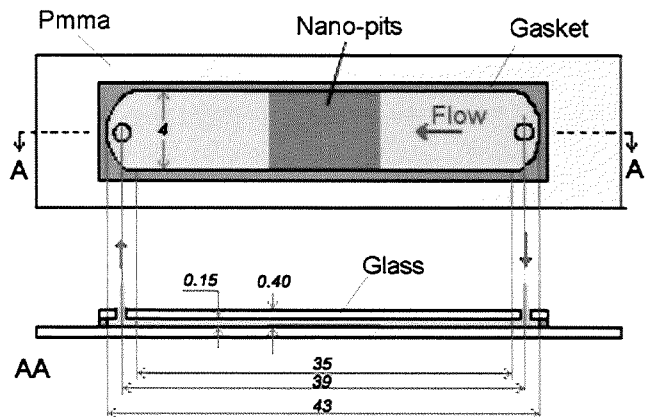


Fig. 2. Flow chamber (dimensions in millimeters).

rinsed in water twice. The glass slides were cleaned by sonicating in Opticlear, acetone, iso-propanol and water. A sheet of thermoplastic polymer (Nescofilm, Bando Chemical Ind. Ltd., Osaka, Japan) was cut (around a metal master) to create a waterproof gasket for the flow chamber. A parallel-plate flow chamber (Fig. 2) was constructed by clamping the thermoplastic gasket between a glass slide and the patterned PMMA substrate. The chamber was sealed by melting the gasket at 50 °C for 12 h using glass coverslips (0.17 mm thick) as spacers. Two circular holes in the glass slide provided the inlet and outlet of the flow. The chamber is designed to create a laminar flow over the substrate (see Appendix for calculations). The cells interacted with the PMMA topography on the lower wall of the chamber.

C. Cell Culture

Rat epitenon fibroblasts were cultured from laboratory stocks (described by Wojciak *et al.* [29]) in HECT complete medium (hepes-buffered Glasgow-modified Eagle's medium (Biowest, Ringmer, East Sussex, U.K.) supplemented with 3% bicarbonate (Gibco, Paisley, U.K.), 10% calf serum (Gibco), 3% antibiotics (Gibco), 10% tryptose broth (Sigma, Dorset, U.K.), 2.85 mM glutamine). Before reaching confluence, the cells were rinsed with hepes/saline and detached for 3 min in 0.01% trypsin in versene. After addition of medium, centrifugation, and counting, a suspension of 10^6 cells/ml was prepared.

D. Flow Apparatus

The flow chamber was inserted in a flow cell, to which the pipes were connected (Fig. 3). A 5-ml syringe containing 3 ml of cell suspension generated the flow from a translational syringe-pump (CFP, Chesterfield, U.K.). The flow rate Q depends on the diameter of the syringe (the diameter of a 5-ml syringe is 11.12 mm) and on the translational velocity of the pump V_{syringe} . Table I shows the experimental conditions used for this study.

The flow reached the flow cell through polyvinyl chloride (PVC) pipes (of bore diameter 0.5 mm, Altec, Alton Hants, U.K.), then the inside of the chamber through the circular inlet. The flow chamber was rinsed with a flow of 70% ethanol for 10 min, Millipore water for 10 min, then with ECT growth medium (same as HECT, but not hepes-buffered) for 10 min.

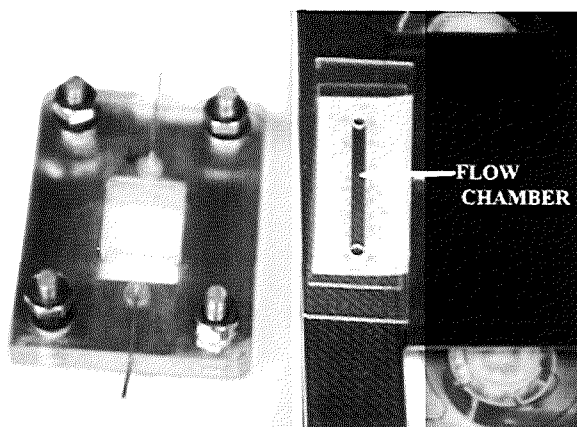


Fig. 3. Flow cell and flow chamber.

TABLE I
CHARACTERISTICS OF THE FLOW GENERATED BY A
5-ML SYRINGE AT THE PUMP SPEED V_{syringe} OF 1.32 $\mu\text{M/S}$

Dimensions (Lxbx2h)	35x4x0.17 mm ³
μ_{HECT} (viscosity)	0.7734x10 ⁻³ N-s/m ²
ρ_{HECT} (density)	1.012 g/ml
γ_{wall} (shear rate)	7 s ⁻¹
Re (Reynolds number)	0.02
l_c (entrance length)	0.6 μm

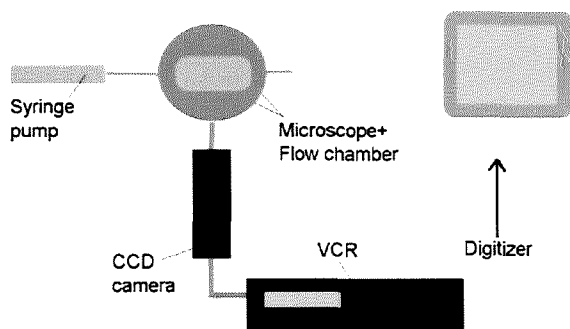


Fig. 4. Flow and recording apparatus.

The flow of suspended epitenon cells (10^6 cells/ml) in HECT medium was allowed for 1 h, then the chamber was rinsed with 4% formaldehyde in phosphate-buffered saline (PBS) for 15 min. The formalin fixed the cells that had adhered to the substrate, while washing off the others. When no free-flowing cells were visible, images were acquired for cell counting. All experiments were carried out at 37 °C. New PVC pipes and a new flow chamber were used at each experiment.

The chamber was observed under an inverted microscope (Leitz Diavert, Wetzlar, Germany). A charge-coupled device (CCD) camera (Panasonic VW-BL600) captured bright-field images with a 2.5 X objective, which were recorded on a Panasonic AG-6720A videorecorder and shown on a monitor (Fig. 4). Between 11 and 24 frames per experiment were acquired within a $15 \times 4 \text{ mm}^2$ area (the visible patterned area) on four controls and six pitted substrates. The images were digitized with NIH Image (National Institute of Health, Washington, DC) and the adhering cells were counted manually; the

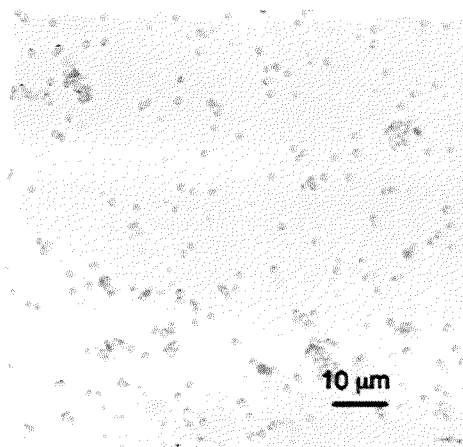


Fig. 5. Cells fixed in the flow chamber (after 1-h flow).

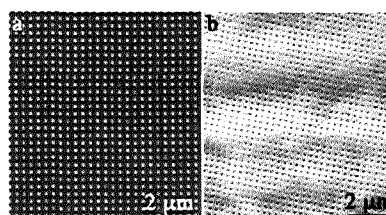


Fig. 6. Scanning electron microscopy images: (a) Nickel shim. (b) Nanopits embossed in PMMA.

cells gathering into clumps were counted as individual ones (Fig. 5).

Two-tailed *t*-test (assuming unequal variances) was used to compare the statistical significance of cell adhesion on the patterned substrates against the flat control.

III. RESULTS

Embossing was found to be a suitable technique to obtain transparent, thin sheets (approximately 1.2 mm) for the assembling of this flow chamber. Scanning electron microscopy showed that the nanopatterns were successfully embossed, reproducing the original topography of the resist (Fig. 6). The embossed PMMA samples are suitable for observation under a light microscope, since their transparency yields a very good image quality.

A flow chamber has been designed, which allows real-time, unobtrusive imaging of cells flowing onto a symmetrical nanopatterned substrate. The small height of the chamber makes sure that the flow is laminar and steady over the nanopits (see Appendix for more detail); in such a flow regime it is possible to quantify cell motion by measurements of cell trajectory and speed.

As far as cell adhesion is concerned, Fig. 7 shows the results yielded by this experiment. Epitenon cells adhere much less to the nanopits than to the flat controls. The *t*-test indicates that these results are statistically significant. Rolling motion and short-time arrests were observed, as reported by Pierres *et al.* [24]. Cell clumps formed on both patterned and flat surfaces, suggesting that cells adhere more easily to other cells rather than to the substrate, or simply that an adhered cell constitutes an obstacle for a flowing one, thus starting the nucleation of clumps (Fig. 5).

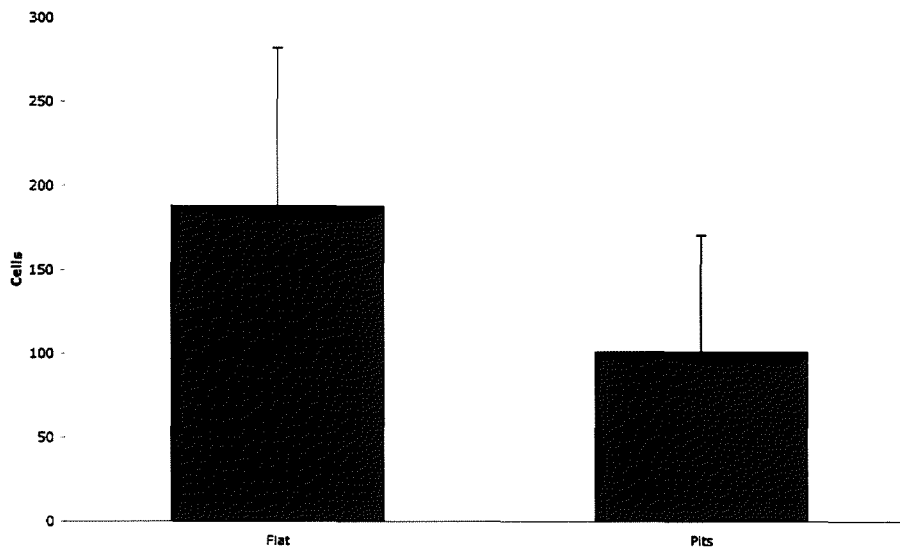


Fig. 7. Graphs of cell counts for epitenon cells on flat control (1, $n = 71$) and nanopitted substrates (2, $n = 97$). Results are mean \pm standard deviation. Statistics by t-test ($p < 0.001$).

IV. DISCUSSION

By producing replicas it is possible to create a large number of inexpensive nanotopographies in a variety of polymers (PMMA, PCL, polycarbonate, etc.). PMMA proved to be the best option for this application, since its glass transition temperature is higher than the one required to seal the flow chamber. The nanopits were successfully embossed in the polymer. Other biocompatible materials should be tried in the future.

This flow chamber proved to be a reliable way of observing a cell flow. It is easily reproducible, cost effective, and of simple assemblage.

The next step in the system design involves the fabrication of a flow cell and chamber where only the patterned PMMA is replaced at each experiment, instead of the whole chamber. This would prevent the time-consuming problems encountered with leaking and/or stress concentration at the circular inlet.

Also, the whole system could be improved by the use of a different flow supply: although the flow can be kept for up to 14 h at a flow rate of 28 s^{-1} , the cells sediment in the syringe, which means that after approximately 1 h, only growth medium is flowing into the chamber. For this reason, only the initial adhesion was quantified. As a consequence, a morphological analysis of the adhered cells (i.e., quantification of cytoskeletal orientation, area, perimeter of the cells) is not possible because the adhered cells need at least 3 h to spread on the substrate.

Previous work has shown that some nanopatterned surfaces prevent or reduce static epitenon cell adhesion *in vitro* [15]. The purpose of the present study was to investigate cell adhesion on the nanopits, but in dynamic conditions, which is a much more physiological-resembling situation than the static culture. The present results showed again a significant effect of the nanopits in reducing cell adhesion, meaning that in the interplay of hydrodynamic and interfacial forces, the pattern has still a strong influence. It can be concluded that the cells can "sense" the nanotopography even when undergoing much stronger mechanical forces.

There are reasons to believe that the interfacial forces of some nanopitted surfaces are responsible for the cell adhesion

changes, and different hypothesis have been made to explain this phenomenon [11], [30]. One of the most appealing explanations is that the changes in wettability induced by the pattern [31] selectively change the protein adsorption at the surface, thus affecting the formation of receptor–ligand bonds [30], [32]. Theoretical models could help understanding the change in interfacial energy that are caused by the surface topography; many attempts have been made to model the colloidal interactions between rough surfaces and micrometric spheres [33], [34]. Although these idealized systems do not compare directly to the cell–surface interactions, the case of convex asperities (dots) has been successfully addressed by Suresh *et al.* [33], suggesting that surface roughness might increase the attraction that causes the flocculation of particles. The case of hollow asperities (pits) has been treated by Herman *et al.* [34].

Our next experiment involves the variation of the flow speed to quantify initial cell adhesion on nanopits at different shear rates. Also, a morphological analysis of cells will be carried out by letting the flow run for longer times. Furthermore, since the reaction of cells to nanofeatures has been shown to be cell type dependent, it would be interesting to reproduce these experiments with other cell types; in particular, the behavior of human blood cells at physiological blood shears ($>100 \text{ s}^{-1}$ [37]) on nanotopography should be investigated.

APPENDIX

There are a very few known cases for which the equations of viscous flow can be solved without approximation; one of them is the flow of an incompressible fluid between two parallel infinite plates [38]. For this geometry the fluid particles move in the x direction parallel to the plates, and there is no velocity in the y and z direction (Fig. 8). In the case of steady flow, the Navier–Stokes equations are easily solved and, if the two plates are fixed, the velocity distribution becomes

$$u_x = \frac{1}{2\mu} \left(\frac{\partial p}{\partial x} \right) (y^2 - h^2) \quad (1)$$

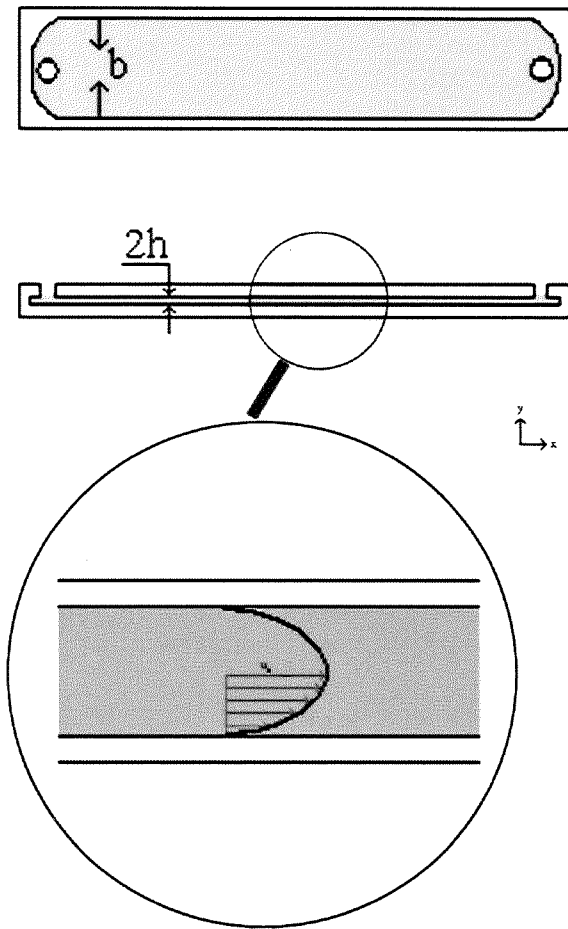


Fig. 8. The flow chamber in this project is a rectangular duct.

where μ is the dynamic viscosity of the fluid, p is the hydrodynamic pressure, and h is the half height of the chamber. Equation (1) shows that the velocity profile u_x between the two fixed plates is parabolic (Fig. 8), i.e., the flow is laminar (characterized by the “slipping motion of layers of fluid over other layers” [39]). In the case of rectangular ducts, such as the flow chamber in this project, the equations cannot so easily be solved, and the solution is more complex [40]. Because of two pair of sidewalls, the velocity profile is a paraboloid.

However, in this chamber the width b is 23 times greater than the height h , so that the two slides have been considered as two infinite (wide) parallel plates. The flow is also assumed to be steady and incompressible, and the fluid Newtonian. For this model, three parameters have been calculated (Table I): 1) the Reynolds number (Re); 2) the entrance length l_e ; and 3) the wall shear rate γ_{wall} .

A. Reynolds Number

A way to predict if the flow is going to be laminar or not is to calculate the dimensionless Re, which is the ratio between the inertial forces and the viscous forces due to the flow (2). If $\text{Re} \ll 1$, the viscous forces are predominant, so the flow will be laminar

$$\text{Re} = \frac{\rho V D}{\mu} \quad (2)$$

$$D = \frac{4bh}{b + 2h} \quad (3)$$

where (3) is the hydraulic diameter for rectangular pipes [38], ρ is the density of the fluid, V is the mean velocity of the flow, h is half the height of the chamber, and b is the width of the chamber.

The dynamic viscosity μ of the suspension can be calculated as to Happel and Brenner [41], and in the case of our dilute system, it can be approximated to the viscosity of the HECT medium, which has been measured with a 27 942 ASTM-IP Ostwald viscometer. At 37 °C

$$\begin{aligned} \rho_{\text{HECT}} &= 1.012 \text{ g/ml} \\ \mu_{\text{HECT}} &= 0.7734 \times 10^{-3} \text{ N} \cdot \text{s/m}^2. \end{aligned}$$

Calculations of Re for this flow chamber show that the viscous effects are predominant ($\text{Re} = 0.02$), which is not surprising due to the small height of the chamber.

B. Entrance Length

When the flow is entering the chamber, it needs a certain length before it becomes fully developed, i.e., before the velocity profile becomes parabolic. This is the so-called entrance length l_e . Different correlations have been accepted to calculate the entrance length [38], [39]; for this chamber, [38, eq. (4)] has been used, where D is the hydraulic diameter:

$$l_e = 0.065 \text{ Re } D. \quad (4)$$

The turbulent effects due to the geometry have not been considered (the flow pattern represents a sharp-edged “source and sink” configuration [39]), which means that the entrance length is longer than calculated. However, the distance between the inlet and the centre of the chamber is 19.5 mm, which is 10^4 times bigger than the calculated entrance length ($l_e = 0.6 \mu\text{m}$): it seems, then, reasonable to assume that the flow in the middle is fully developed.

C. Wall Shear Rate

The most commonly cited hemodynamic factor implicated in cell adhesion defects, disease initiation, and ligand-receptor bond dissociation is the wall shear stress τ_{wall} , while the wall shear rate $\gamma_{\text{wall}} (= \tau_{\text{wall}}/\mu)$ seems to affect bond formation [42]. The shear rate γ quantifies the speed of deformation of a flowing fluid, and it is inversely proportional to the viscosity μ . The wall shear rate is calculated from the velocity distribution in a Newtonian fluid flowing between two wide, parallel plates [38] (5)

$$\gamma_{\text{wall}} = \frac{3Q}{2bh^2} \quad (5)$$

where Q is the flow rate. In this flow chamber, $\gamma_{\text{wall}} = 7 \text{ s}^{-1}$.

ACKNOWLEDGMENT

The authors would like to thank Dr. N. Gadegaard, Dr. M. Riehle and Prof. H. Morgan for discussion, and Mr. A. McGregor, Mr. G. Baxter (IBLS Mechanical Workshop,

Glasgow, U.K.), and Mr. K. Piechowiak (Electronics Mechanical Workshop, Glasgow, U.K.) for technical assistance.

REFERENCES

- [1] A. Curtis and C. D. W. Wilkinson, "Topographical control of cells," *Biomaterials*, vol. 18, pp. 1573–1583, 1997.
- [2] M. Dalby, S. J. Yarwood, M. O. Riehle, H. J. H. Johnstone, S. Affrossman, and A. S. G. Curtis, "Increasing fibroblast response to materials using nanotopography: Morphological and genetic measurements of cell response to 13-nm-high polymer demixed islands," *Exp. Cell Res.*, vol. 276, pp. 1–9, 2002.
- [3] B. Chehroudi and D. M. Brunette, "Effects of surface topography on cell behavior," in *Encyclopedic Handbook of Biomaterials and Bioengineering. Part S: Materials*, D. Donald, L. Wise, D. E. Altobelli, M. J. Yaszewski, J. D. Gresser, and E. R. Schwartz, Eds. New York: Marcel Dekker, 1995.
- [4] D. L. Rovenski YA, O. Y. Ivanova, and J. M. Vasiliev, "Locomotory behavior of epitheliocytes and fibroblasts on metallic grids," *J. Cell Sci.*, vol. 112, pp. 1273–1282, 1999.
- [5] P. Clark, P. Connolly, A. S. G. Curtis, J. A. T. Dow, and C. D. W. Wilkinson, "Cell guidance by ultrafine topography *in vitro*," *J. Cell Sci.*, vol. 99, pp. 73–77, 1991.
- [6] C. Wilkinson, M. Riehle, M. A. Wood, J. O. Gallagher, and A. S. G. Curtis, "The use of materials patterned on a nano- and micro-metric scale in cellular engineering," *Mater. Sci. Eng.*, 2001.
- [7] M. Dalby, M. O. Riehle, S. Affrossman, and A. S. G. Curtis, "In vitro reaction of endothelial cells to polymer demixed nanotopography," *Biomaterials*, vol. 23, pp. 2945–2954, 2002.
- [8] C. Wilkinson, A. S. G. Curtis, and J. Crossan, "Nanofabrication in cellular engineering," *J. Vac. Sci. Tech. B*, vol. 16, pp. 3132–3136, 1998.
- [9] N. Gadegaard, S. Thoms, D. S. Macintyre, K. McGhee, J. O. Gallagher, B. Casey, and C. D. W. Wilkinson, "Arrays of nano-dots for cellular engineering," *Microelectron. Eng.*, vol. 67–68, pp. 162–168, 2003.
- [10] A. Curtis and C. D. W. Wilkinson, "Topographical control of cell migration," in *Motion Analysis of Living Cells. Techniques in Modern Biomedical Microscopy*, D. Soll and D. Wessels, Eds. New York: Wiley-Liss, 1998, pp. 141–156.
- [11] A. Curtis, B. Casey, J. O. Gallagher, D. Pasqui, M. A. Wood, and C. D. W. Wilkinson, "Substratum nanotopography and the adhesion of biological cells. Are symmetry or regularity of nanotopography important?," *Biophys. Chem.*, vol. 94, pp. 275–283, 2001.
- [12] M. Riehle, "Cell behavior of rat calvaria bone cells on surfaces with random nanometric features," *Mater. Sci. Eng. C*, vol. 23, pp. 337–340, 2003.
- [13] Y. Xia, J. A. Rogers, K. E. Paul, and G. M. Whitesides, "Unconventional methods for fabricating and patterning nanostructures," *Chem. Rev.*, vol. 99, pp. 1823–1848, 1999.
- [14] L. Heyderman, H. Schiff, C. David, J. Gobrecht, and T. Shweizer, "Flow behavior of thin polymer films used for hot embossing lithography," *Microelectron. Eng.*, vol. 54, pp. 229–245, 2000.
- [15] J. O. Gallagher, K. F. McGhee, C. D. W. Wilkinson, and M. O. Riehle, "Interaction of animal cells with ordered nanotopography," *IEEE Trans. Nanobiosci.*, vol. 1, pp. 24–28, Mar. 2002.
- [16] W. Barthloot and C. Neinhuis, "Purity of the sacred lotus, or escape from contamination in biological surfaces," *Planta*, vol. 202, pp. 1–8, 1997.
- [17] C. Baum, W. Meyer, R. Stelzer, L. G. Fleisher, and D. Siebers, "Average nanorough skin surface of the pilot whale (*globicephala melas, delphinidae*): Considerations on the self-cleaning abilities based on nanoroughness," *Marine Biol. Online*, 2001.
- [18] P. Bongrand, P. M. Claesson, and A. S. G. Curtis, *Studying Cell Adhesion*. Heidelberg, Germany: Springer-Verlag, 1994.
- [19] J. Doroszewski, J. Skierski, and L. Prządka, "Interaction of neoplastic cells with glass surface under flow conditions," *Exp. Cell Res.*, vol. 104, pp. 335–343, 1977.
- [20] T. Van Kooten, J. M. Schakenraad, H. C. Van der Mei, and H. J. Busscher, "Development and use of a parallel-plate flow chamber for studying cellular adhesion to solid surfaces," *J. Biomed. Mater. Res.*, vol. 26, pp. 725–738, 1992.
- [21] M. Stavridi, M. Katsikogianni, and Y. F. Missirlis, "The influence of surface patterning and/or sterilization on the hemocompatibility of polycaprolactones," *Mater. Sci. Eng. C*, vol. 23, pp. 359–365, 2003.
- [22] O. Tissot, A. Pierres, C. Foa, M. Delaage, and P. Bongrand, "Motion of cells sedimenting on a solid surface in a laminar shear flow," *Biophys. J.*, vol. 61, pp. 204–215, 1992.
- [23] J. Doroszewski and A. Kiwala, "Adhesion and locomotion of granulocytes under flow conditions," *J. Cell Sci.*, vol. 90, pp. 335–340, 1988.
- [24] A. Pierres, A. M. Benoliel, and P. Bongrand, "Measuring bonds between surface-associated molecules," *J. Immunol. Methods*, vol. 196, pp. 105–120, 1996.
- [25] R. Poyton and D. Branton, "A multipurpose microperfusion chamber," *Exp. Cell Res.*, vol. 60, pp. 109–114, 1970.
- [26] J. Dvorak and W. Stotler, "A controlled-environment culture system for high resolution light microscopy," *Exp. Cell Res.*, vol. 68, pp. 144–148, 1971.
- [27] K. Spring and A. Hope, "Size and shape of the lateral intercellular spaces in a living epithelium," *Science*, vol. 200, pp. 54–57, 1978.
- [28] J. Yang, R. Bos, A. Poortinga, P. J. Wit, G. F. Belder, and H. J. Busscher, "Comparison of particle deposition in a parallel plate flow chamber and a stagnation point flow chamber," *Langmuir*, vol. 15, pp. 4671–4677, 1999.
- [29] B. Wojciak, J. Crossan, A. S. G. Curtis, and C. D. W. Wilkinson, "Grooved substrata facilitate *In vitro* healing of completely divided flexor tendons," *J. Mater. Sci.: Mater. Med.*, vol. 6, pp. 266–271, 1995.
- [30] T. Webster, C. Ergun, R. H. Doremus, R. W. Siegel, and R. Bizios, "Specific proteins mediate enhanced osteoblast adhesion on nanophase ceramics," *J. Biomed. Mater. Res.*, vol. 51, pp. 475–483, 2000.
- [31] J. Bico, C. Tordeux, and D. Quere, "Rough wetting," *Europhys. Lett.*, vol. 55, pp. 214–220, 2001.
- [32] T. Ruardy, H. E. Moorlag, J. M. Schakenraad, H. C. Van der Mei, and H. J. Busscher, "Growth of fibroblasts and endothelial cells on wettability gradient surfaces," *J. Colloid Interface Sci.*, vol. 188, pp. 209–217, 1997.
- [33] L. Suresh and J. Y. Walz, "Effect of surface roughness on the interaction energy between a colloidal sphere and a flat plate," *J. Colloid Interface Sci.*, vol. 183, pp. 199–213, 1996.
- [34] M. Herman and K. D. Papadopoulos, "A method for modeling the interactions of parallel flat plate systems with surface features," *J. Colloid Interface Sci.*, vol. 142, pp. 331–342, 1991.
- [35] W. Bowen and A. O. Sharif, "Hydrodynamic and colloidal interactions effects on the rejection of a particle larger than a pore in microfiltration and ultrafiltration membranes," *Chem. Eng. Sci.*, vol. 53, pp. 879–890, 1998.
- [36] E. Kokkoli and C. F. Zokoski, "Surface pattern recognition by a colloidal particle," *Langmuir*, vol. 17, pp. 369–376, 2001.
- [37] A. Hoeks, S. K. Samijo, P. J. Brands, and R. S. Reneman, "Noninvasive determination of shear-rate distribution across the arterial lumen," *Hypertension*, vol. 26, pp. 26–33, 1995.
- [38] B. Munson, D. F. Young, and T. H. Okiishi, *Fundamentals of Fluid Mechanics*, 3rd ed. New York: Wiley, 1990.
- [39] L. Prandtl, *Essentials of Fluid Dynamics*. London, U.K.: Blackie, 1952.
- [40] W. Langlois, *Slow Viscous Flow*. New York: Macmillan, 1964.
- [41] J. Happel and H. Brenner, *Low Reynolds Number Hydrodynamics*. New York: Prentice-Hall, 1965.
- [42] S. Chen and T. A. Springer, "Selectin receptor–ligand bonds: Formation limited by shear rate and dissociation governed by the Bell model," *Proc. Nat. Acad. Sci.*, vol. 98, no. 3, pp. 950–955, Jan. 30, 2001.

Elena Martines received the M.Eng. degree from the Institut National des Sciences Appliquées (INSA), Lyon, France, in 2001. She is currently working toward the Ph.D. degree in the Centre for Cell Engineering, University of Glasgow, Galsgow, U.K.

Her research interests include the use of nanotopographic surfaces to study cell adhesion, microfluidic systems, and surface forces modeling.

Kieran McGhee, photograph and biography not available at the time of publication.

Chris Wilkinson, photograph and biography not available at the time of publication.

Adam Curtis, photograph and biography not available at the time of publication.



**THESIS
CONTAINS
CD/DVD**